

Continuum modelling of cell growth and nutrient transport in a perfusion bioreactor

Muhammad Shakeel

Thesis submitted to The University of Nottingham
for the degree of Doctor of Philosophy

January 2011

*Dedicated to my beloved parents for their
love, endless support and encouragement*

Abstract

Tissue engineering aims to regenerate, repair or replace organs or tissues which have become defective due to trauma, disease or age related degeneration. This engineering may take place within the patient's body or tissue can be regenerated in a bioreactor for later implantation into the patient. Regeneration of soft tissue is one of the most demanding applications of tissue engineering. Producing proper nutrient supply, uniform cell distribution and high cell density are the important challenges. Many experimental models exist for tissue growth in a bioreactor. It is important to put experiments into a theoretical framework. Mathematical modelling in terms of physical and biochemical mechanisms is the best tool to understand experimental results.

In this work a mathematical model of convective and diffusive transport of nutrients and cell growth in a perfusion bioreactor is developed. A cell-seeded porous scaffold is placed in a perfusion bioreactor and fluid delivers the nutrients to the cells for their growth. The model describes the key features of the tissue engineering processes which includes the interaction between the cell growth, variation of material porosity, flow of fluid through the material and delivery of nutrients to the cells. The fluid flow through the porous scaffold is modelled by Darcy's law, and the delivery of nutrients to the cells is modelled by the advection-diffusion equation. A non-linear reaction diffusion system is used to model the cell growth. The cell diffusion depends on the cell density and growth of cells is modelled by logistic growth. The effect of shear stress on nutrient consumption and cell growth is also included in the model. COMSOL (a commercial finite element solver) is used to numerically solve the model. The results show that the distribution of cells and total cell number in the scaffold depends on the initial cell density and porosity. We suggest various seeding strategies and scaffold designs to improve the cell growth rate and total cell yield.

Acknowledgements

First of all I would like to praise and thank to almighty Allah the most merciful and knowledgeable who enabled me to complete my doctorate. I bow my head with all submission and humility by way of gratitude to almighty Allah. I thank to Allah almighty for making my dream come true. The day that I dreamt of to acquire my PhD degree has finally come.

I feel honored of being supervised by Dr Paul Matthews, Dr Richard Graham (both from The University of Nottingham) and Dr Sarah Waters (University of Oxford). This thesis would not have been completed without the help, support, guidance, and efforts of my supervisors. I would like to offer my sincerest gratitude and thanks to all my supervisors, who have supported me throughout my PhD studies with their patience and knowledge. I attribute the level of my PhD degree to their encouragement and effort because without them this thesis, too, would not have been completed or written. One simply could not wish for better or friendlier supervisors.

I would also like to express my thanks to the School of Mathematical Sciences, and IT department of The University of Nottingham for providing me support and computing facilities to produce and complete my thesis. Special thanks to Professor David Grant and Loïuse France for their helpful suggestions and fruitful discussions. I am also thankful to the Higher Education Commission of Pakistan for providing me financial support for my PhD studies.

I would like to thank my late parents for all their love and encouragements. They raised me with love and supported me in all my pursuits. They have been a constant source of inspiration throughout my life. I will forever indebted to my parents for their support and encouragement when it was required.

My final, and most heartfelt, acknowledgment must go to my wife Shazia Shakeel. Her support, encouragement, and companionship helped me throughout my studies. For all that, and for being everything I am not, she has my everlasting love.

Contents

1	Tissue engineering: Introduction and literature review	1
1.1	Introduction	1
1.2	Regenerative medicine	2
1.2.1	Cellular therapy	2
1.2.2	Tissue engineering	3
1.2.2.1	Tissue engineering background	4
1.3	Key components of tissue engineering	6
1.3.1	Cells	6
1.3.2	Scaffold	8
1.3.3	Growth factors	11
1.3.4	Bioreactor	12
1.3.4.1	Spinner flask bioreactor	13
1.3.4.2	Rotating wall vessel bioreactor	13
1.3.4.3	Perfusion bioreactor	14
1.4	Mechanotransduction	16
1.5	Limitations of nutrient supply in tissue engineering	17
1.6	Mathematical modelling in tissue engineering	18
1.7	Objective of thesis and structure	26
2	Flow in porous materials	28
2.1	Introduction	28
2.2	Geometry and governing equations	30

2.3	Nondimensionalization	31
2.4	Permeability distribution	32
2.5	Numerical solution	34
2.5.1	Case I : $\lambda_n = 0$	34
2.5.2	Case II : $\lambda_n \neq 0$	35
2.5.2.1	Solution of X dependent equation	35
2.5.2.2	Solution of Y dependent equation	37
2.6	Analytical solution	41
2.6.1	Case I : Permeability function of two spatial coordinates	41
2.6.1.1	Case I : $\lambda_n = 0$	41
2.6.1.2	Case II : $\lambda_n \neq 0$	42
2.6.2	Case II : Permeability function of one spatial coordinate	46
2.6.3	Case III : Constant permeability	47
2.6.4	Case IV : Permeability and velocity boundary conditions both functions of spatial coordinates	47
2.7	Comparison of Numerical and Analytical Results	48
2.7.1	Case I : Permeability function of two spatial variables, Constant inflow and outflow velocities.	48
2.7.2	Case II : Permeability function of one spatial variable, Constant inflow and outflow velocities	50
2.7.3	Case III : Constant permeability, Constant inflow and outflow velocities	51
2.7.4	Case IV : Permeability, inflow and outflow velocities functions of spatial coordinates	52
2.8	Summary and conclusions	53
3	Mathematical modelling of cell growth in a perfusion bioreactor	54
3.1	Introduction	54
3.2	Conceptual Model	55
3.3	Geometry and Model Equations	56

3.3.1	Flow Field	57
3.3.2	Nutrient Transport	58
3.3.3	Cell Growth	58
3.3.4	Cell feedback on permeability	59
3.3.5	Consumption and Proliferation Rate	59
3.4	Nondimensionalization	60
3.4.1	Dimensionless equations and boundary conditions	61
3.5	Numerical solution	65
3.5.1	Parameter values	66
3.6	Results and discussion	68
3.6.1	Uniform initial seeding and initial permeability	68
3.6.2	Non-uniform initial seeding, uniform initial permeability	70
3.6.3	Non-uniform initial seeding and permeability	72
3.6.4	Effect of parameters	74
3.7	Analytical solution	76
3.7.1	Case I: Initial time solution	78
3.7.2	Case II: Steady state solution	83
3.8	Stability of steady state solution	85
3.9	Fixing flow rate	87
3.10	Conclusions	89
4	Fisher-Kolmogorov equation with non-linear diffusion	90
4.1	Introduction	90
4.2	One dimensional Fisher equation with non-linear diffusion	93
4.3	Nondimensionalization	95
4.4	Travelling wave solution	96
4.4.1	Phase plane analysis	97
4.4.2	Stability of fixed points	98
4.4.3	Selection of initial condition	101

4.5	Numerical solution	102
4.5.1	Parameter values	103
4.5.2	Case I : $\chi = 1.3217$	104
4.5.3	Case II : $\chi = 13.2173$	105
4.5.4	Case III : $\chi = 132.1739$	106
4.5.5	Case IV : $\chi = 0$	107
4.6	Numerical minimum wave speed	108
4.7	Accuracy of numerical method	110
4.8	Two dimensional Fisher equation with density dependent diffusion . . .	111
4.9	Summary and Conclusions	116
5	2-D coupled model of fluid flow, nutrient transport and cell growth in a per- fusion bioreactor	118
5.1	Introduction	118
5.2	Geometry and model constraints	119
5.2.1	Model geometry	119
5.2.2	Model assumptions	121
5.3	Model equations	121
5.3.1	Cell feedback equation	122
5.3.2	Flow field	123
5.3.2.1	Fixed flow rate	124
5.3.2.2	Fluid shear stress	125
5.3.3	Nutrient Transport	126
5.3.4	Cell Growth	127
5.3.5	Nutrient consumption and cell proliferation rates	128
5.4	Nondimensionalization	133
5.5	Dimensionless equations and boundary conditions	134
5.5.1	Cell feedback	134
5.5.2	Flow field	134
5.5.2.1	Fixed flow rate	135

5.5.2.2	Fluid shear stress	135
5.5.3	Nutrient transport equation	135
5.5.4	Cell growth equation	136
5.6	Parameter values	139
5.6.1	Geometric parameters	139
5.6.2	Cell parameters	139
6	Effect of initial seeding and channeling on cell growth	142
6.1	Introduction	142
6.2	Solution method	145
6.3	Convergence	147
6.3.1	Fixed Δt_{cell} and t_{update} and different number of mesh points.	147
6.3.2	Fixed number of mesh points and t_{update} and different Δt_{cell}	149
6.3.3	Fixed number of mesh points and Δt_{cell} and different t_{update}	150
6.4	Initial seeding strategy	152
6.4.1	Uniform initial cell density	153
6.4.2	Central blob	155
6.4.3	Off-Centre blob	157
6.4.4	Layer of cells opposite to nutrient source	159
6.4.5	Layer of cells on all the boundaries of the scaffold	161
6.4.6	Layer of cells on three boundaries of scaffold	163
6.4.7	Layer of cells at side walls of the scaffold	164
6.4.8	Comparison of results of initial cell seeding strategy	166
6.5	Effect of porosity	168
6.5.1	Adjacent scaffolds of different porosities	169
6.5.2	High porosity vertical tubes	171
6.5.3	High porosity vertical tubes along side walls	173
6.5.4	High porosity diagonal tubes	175
6.5.5	High porosity diagonal and vertical tubes	177

6.5.6	Comparison of results of porosity distribution	179
6.5.7	Combined effects of initial seeding and initial porosity	180
6.6	Effect of flow rate on cell growth	181
6.6.1	High flow rate	183
6.6.2	Reduced flow rate	184
6.7	Summary and conclusions	185
7	Summary and conclusions	187
7.1	Summary	187
7.2	Conclusions	189
7.3	Future work	192
A	Notation guide	195
B	COMSOL modelling guide	198
B.1	Introduction	198
B.2	Modelling using graphical user interface (GUI)	198
B.2.1	Model Navigator	198
B.2.2	Options and Settings	199
B.2.3	Geometry Modelling	200
B.2.4	Coupling variables	200
B.2.5	Poisson's Equation	201
B.2.6	Convection and Diffusion	202
B.2.7	Heat Equation(hteq)	202
B.2.8	Mesh Generation	203
B.2.9	Computing the solution	203
B.2.10	Post processing and visualization	204
B.2.11	Exporting data to COMSOL script or MATLAB	205
B.2.12	Data Extraction in MATLAB	205
C	Finite element method(FEM)	207

C.1 Basic concepts	207
C.2 Worked Example	209
D Specific rate equations for microbial growth	219
D.1 Michaelis-Menton model	219
D.2 Moser's Model	220
D.3 Monod's Model	220
D.4 Tiesser's Model	220
D.5 Contois Model	220
References	222

List of Tables

3.1	Summary of dimensionless model equations, boundary and initial conditions.	64
3.2	Model parameters and values used in this work.	67
4.1	Model parameters used in this work	104
4.2	Values of γ and δ for $\chi = 1.3217$	104
4.3	Values of γ and δ for $\chi = 13.2173$	105
4.4	Values of γ and δ for $\chi = 132.1739$	106
4.5	Numerical minimum wave speed v_{num}	108
4.6	Table shows numerical results of v_{min} and N_{total} as a function of time. N_{init} , Δt and t_{new} are same as in Figure 4.5. The other parameter values are $\gamma = 2$, $\delta = 0.013976$, $\chi = 132.173$. Table shows v_{min} and N_{total} at $t = 0.6$ for fixed (a) $\Delta t = 0.001$ and $t_{new} = 0.01$ and different mesh size (b) mesh size and $t_{new} = 0.01$ and different Δt (c) mesh size and $\Delta t = 0.001$ and different t_{new}	110
4.7	Numerical results of minimum wave speed v_{min} of modified two dimensional Fisher equation (4.8.5). The initial conditions and parameters values used in the simulation are same as in Figure 4.13.	115
5.1	Summary of dimensional model equations, boundary and initial conditions	132
5.2	Summary of dimensionless model equations, boundary and initial conditions	138
5.3	Model parameters and values used in the simulation	140
5.4	Values of dimensionless parameters	141

6.1 Parameter values 182

List of Figures

1.1	Classification of regenerative medicine based on the use of scaffold. . . .	2
1.2	Principles of Tissue Engineering	3
1.3	Tissue engineering scaffold. Poly(lactic-coglycolic acid) porous scaffold for bone tissue engineering produced by melt casting and particulate leaching	8
1.4	Spinner flask bioreactor.	13
1.5	Rotating wall vessel bioreactor.	14
1.6	Perfusion bioreactor.	15
2.1	Reference geometry. Flow of fluid through a porous material. Fluid is pumped in at the boundary $y^* = L^*$ and pumped out at $y^* = -L^*$. No fluid flux through the boundaries $x^* = \pm L^*$	30
2.2	Discretization of interval $x_0 \leq x \leq x_{N_g-1}$. x_{-1} and x_{N_g} are ghost points. .	36
2.3	Analytical results of (a) flow of fluid through the porous material with permeability $k(x, y) = e^{x+y}$. Inflow and outflow velocities are constant <i>i.e.</i> $f(x) = g(x) = 1$. The arrows indicate the direction of flow and lines indicate the pressure contours. (b) y component fluid velocity at different spatial locations.	49
2.4	Numerical results of (a) flow of fluid through the porous material with permeability $k(x, y) = e^{x+y}$. Inflow and outflow velocities are constant <i>i.e.</i> $f(x) = g(x) = 1$. The arrows indicate the direction of flow and solid lines indicate the pressure contours. (b) y component of fluid velocity at different spatial locations.	49

2.5	Analytical results of (a) flow of fluid through the porous material with permeability $k(x, y) = e^x$. Inflow and outflow velocities are constant <i>i.e.</i> $f(x) = g(x) = 1$. The arrows indicate the direction of flow and solid lines indicate the pressure contours. (b) y component of fluid velocity at different spatial locations.	50
2.6	Numerical results of (a) fluid flow through a porous material for constant permeability and constant inflow and outflow velocities. The arrows indicate the direction of flow and horizontal lines indicate the pressure contours. (b) y component of fluid velocity at different spatial locations.	52
2.7	Analytical results of (a) flow of fluid through the porous material with permeability $k(x, y) = e^{x+y}$. Inflow and outflow velocities are $f(x) = g(x) = 1 - x^2$. The arrows indicate the direction of flow and lines indicate the pressure contours. (b) y component of fluid velocity at different spatial locations.	52
2.8	Numerical results of (a) flow of fluid through the porous material with permeability $k(x, y) = e^{x+y}$. Inflow and outflow velocities are $f(x) = g(x) = 1 - x^2$. The arrows indicate the direction of flow and lines indicate the pressure contours. (b) y component of fluid velocity at different spatial locations.	53
3.1	Interacting phenomena in perfusion bioreactor.	55
3.2	A perfusion bioreactor. Scaffold of length $2L^*$ and width $2L^*$ is placed within the bioreactor. Fluid is pumped in at the boundary $y^* = L^*$ and pumped out at $y^* = -L^*$. There is no fluid flux through the boundaries $x^* = \pm L^*$. Pressure at top and bottom boundaries are p_0^* and p_1^* respectively.	56
3.3	Schematic diagram of solution.	65
3.4	Snapshots of the cell density N , nutrient concentration S and velocity \mathbf{u} at times $t = 2$ and $t = 5$. The initial cell density $N_{init}(x, y)$ and initial permeability $k_0(x, y)$ both are uniform <i>i.e.</i> $N_{init}(x, y) = 0.1$ and $k_0(x, y) = 1$. The values of dimensionless parameters used in the simulation are $D_s = 0.001$, $R_s = 0.5$, $\Gamma = 0.1$ and $\eta = 0.5$. The cell update time $t_{update} = 0.25$ and $\Delta t_{cell} = 0.025$	69

3.5	Cross section plot of (a) nutrient concentration S and (b) cell density N , at times $t = 0.5 : 0.5 : 5$ when initial seeding and initial permeability both are uniform. The values of dimensionless parameters are same as in Figure 3.4.	70
3.6	Non-uniform initial cell density.	70
3.7	Snapshots of cell density N , nutrient concentration S and velocity \mathbf{u} at times $t = 2$ and $t = 5$ when initial cell density is non-uniform and initial permeability is uniform <i>i.e.</i> $N_{init}(x, y) = 0.1793 \exp(-x^2 - y^2)$ and $k_0(x, y) = 1$. The values of dimensionless parameters are same as in Figure 3.4.	71
3.8	Cross section plot of (a) nutrient concentration S and (b) cell density N , at times $t = 0.5 : 0.5 : 5$ when initial seeding is non-uniform and initial permeability is uniform. The values of dimensionless parameters are same as in Figure 3.4.	72
3.9	Snapshots of cell density N , nutrient concentration S and velocity \mathbf{u} at times $t = 0.5 : 0.5 : 5$ when initial seeding and initial permeability are both non-uniform <i>i.e.</i> $N_{init} = 0.17 \exp(-x^2 - y^2)$ and $k_0 = \exp(x + y)$. The values of dimensionless parameters are same as in Figure 3.4.	73
3.10	Cross section plot of (a) nutrient concentration S and (b) cell density N are plotted for different times when initial cell density and initial permeability are both non-uniform. The values of dimensionless parameters are same as in Figure 3.4.	74
3.11	Snapshots of cell density N , nutrient concentration S and velocity \mathbf{u} at time $t = 5$. Initial seeding, initial permeability, t_{update} and Δt_{cell} are same as in Figure 3.4. In this case perfusion velocity $U_c^* = 3 \times 10^{-4} m/sec$. The values of dimensionless parameters are $D_s = 0.0005$, $R_s = 0.25$, $\Gamma = 0.1$ and $\eta = 0.5$	75
3.12	Snapshots of cell density N , nutrient concentration S and velocity \mathbf{u} at time $t = 5$. Initial seeding, initial permeability, t_{update} and Δt_{cell} are same as in Figure 3.4. In this case perfusion velocity $U_c^* = 7.5 \times 10^{-5} m/sec$. The values of dimensionless parameters are $D_s = 0.002$, $R_s = 1$, $\Gamma = 0.1$ and $\eta = 0.5$	76

3.13 Snapshots of cell density N , nutrient concentration S and velocity \mathbf{u} at time $t = 5$. Initial seeding, initial permeability, t_{update} , Δt_{cell} and the values of dimensionless parameters except η (in this case $\eta = 0.8$) are same as in Figure 3.4. 76

3.14 Analytical solution (3.7.9) and numerical results of profile of nutrient concentration S at time $t = 1$. The parameter values used in the simulation are $D_s = 0.1$, $R_s = 0.5$, $\eta = 0.01$, $k_0(x, y) = 1$ and $N_{init} = 0.1$ 79

3.15 $\blacklozenge y = 1$, $\blacklozenge y = 0.5$, $\blacklozenge y = 0$, $\blacklozenge y = -0.5$, $\blacklozenge y = -1$. Analytic solution (3.7.12) and numerical results of cell density N for various values of y at times $0 \leq t \leq 1$. Solid lines represents the numerical solution and * represents the analytical solution. Initial cell density $N_{init} = 0.1$ and initial permeability $k_0(x, y) = 1$. The parameter values used in the simulation are $D_s = 0.1$, $R_s = 0.5$, $\eta = 0.01$ 80

3.16 Analytic solution (3.7.9) of profile of nutrient concentration S for times $0 \leq t \leq 1$ when cells are not updated and numerical results of the profile of nutrient concentration S when cells are updated after each time $t_{update} = 0.1$. * represents the analytic solution and solid lines represents the numerical results of nutrient concentration. Arrow indicates that graph is being read from top to bottom. The parameter values used in the simulation are $D_s = 0.1$, $R_s = 0.5$, $\eta = 0.01$, $N_{init} = 0.1$ and $k_0(x, y) = 1$ 81

3.17 $\blacklozenge y = 1$, $\blacklozenge y = 0.5$, $\blacklozenge y = 0$, $\blacklozenge y = -0.5$, $\blacklozenge y = -1$. Dotted lines represents the analytic results and solid lines represents numerical results. Analytic solution of equation (3.7.12) (when cells are not updated) and numerical results (when cells are updated after each time step $t_{update} = 0.1$) of cell density N for times $0 \leq t \leq 1$ are plotted. The parameter values used in the simulation are $D_s = 0.1$, $R_s = 0.5$, $\eta = 0.01$, $N_{init} = 0.1$ and $k_0(x, y) = 1$ 82

3.18 Analytic solution (3.7.15) and numerical solution of profile of nutrient concentration S at steady state. * represent the analytical result and solid line represent the numerical result. The parameter values used in the simulation are $D_s = 0.1$, $R_s = 0.5$, $\eta = 0.01$, $N_{init} = 0.1$ and $k_0(x, y) = 1$. 84

3.19 Cell density N for the various values of y approaching to steady state. The parameter values used in the simulation are $D_s = 0.1$, $R_s = 0.1$, $\eta = 0.01$, $N_{init} = 0.1$ and $k_0(x, y) = 1$ 85

3.20	Stability of numerical solution at steady state. The parameter values used in the simulation are $D_s = 0.1$, $R_s = 0.5$, $\eta = 0.1$, and $N_{init} = 1 + 0.1 \sin(\pi y/2)$	86
3.21	Analytic solution and numerical results of profile of nutrient concentration for original and rescaled problem. The parameter values used in the simulation are $D_s = 0.1$, $R_s = 0.5$	88
4.1	Phase plane trajectories of equation (4.4.11). Here parameter values are $\chi = 132.1739$, $\delta = 0.0139$ $\gamma = 2$ and $v = 1.5 > v_c$	100
4.2	Phase plane trajectories of equation (4.4.11). Here parameter values are $\chi = 132.1739$, $\delta = 0.0139$ $\gamma = 2$ and $v = 0.5 < v_c$	100
4.3	Phase plane trajectories of equation (4.4.11) for different values of $v \geq v_c$. The other parameter values are same as in Figure 4.1. Colored lines represents the different values of speed v e.g.  $v = 1$,  $v = 1.5$,  $v = 2$,  $v = 2.5$ and  $v = 3$	101
4.4	Phase plane trajectories of equation (4.4.11) for different values of $v < v_c$. The other parameter values are same as in Figure 4.1. Colored lines represents the different values of speed v e.g.  $v = 0.8$,  $v = 0.7$,  $v = 0.6$ and  $v = 0.5$	101
4.5	Numerical results of profile of cell density N at different times and for different values of γ and δ when $\chi = 1.3217$. Initial cell density is $N_{init}(x) = N_0 H(r^2 - x^2)$, where $N_0 = 0.25$, and $r^2 = 0.1$. The time step size $\Delta t = 0.001$ and cell update time $t_{new} = 0.01$. The Figure shows the cell distribution after each time t_{new} and final time is $t = 0.3$	105
4.6	Numerical results of profile of cell density N at different times and for different values of γ and δ when $\chi = 13.2173$. N_{init} , Δt and t_{new} are same as in Figure 4.5. In this case the final time is $t = 0.6$	106
4.7	Numerical results of profile of cell density N at different times and for different values of γ and δ when $\chi = 132.1739$. N_{init} , Δt and t_{new} are same as in Figure 4.5.	107
4.8	Numerical results of profile of cell density N at different time without growth term. N_{init} , Δt and t_{new} are same as in Figure 4.5.	108

4.9 Phase plane trajectories of equation (4.4.14) for different values of $v \geq v_c$. The other parameter values are $\chi = 132.1739$, $\gamma = 3$ and $\delta = 0.037990$. Colored lines represents the different values of speed v e.g. ♠ $v = 1.15$, ♣ $v = 1.2$, ♥ $v = 1.3$, and ♦ $v = 1.5$ 109

4.10 Phase plane trajectories of equation (4.4.14) for different values of $v < v_c$. The other parameter values are $\chi = 132.1739$, $\gamma = 3$ and $\delta = 0.037990$. Colored lines represents the different values of speed v e.g. ♣ $v = 1$, ♦ $v = 1.02$, ♥ $v = 1.05$ and ♠ $v = 1.09$ 109

4.11 Shape of growth front at time $t = 0.3$ for fixed $\chi = 132.1739$ and value of δ for corresponding value of γ are given in Table 4.4. N_{init} , Δt and t_{new} are same as in Figure 4.5. 110

4.12 Numerical results of total cell density N as a function of time for fixed (a) $\Delta t = 0.001$ and $t_{new} = 0.01$ and different mesh size (b) mesh size and $t_{new} = 0.01$ and different Δt (c) mesh size and $\Delta t = 0.001$ and different t_{new} . Here $\gamma = 2$, $\delta = 0.013976$, $\chi = 132.173$ and N_{init} , Δt and t_{new} are same as in Figure 4.5. 111

4.13 Numerical solution of modified 2-D Fisher equation (4.8.5). Color represents the cell density N at different spatial locations for different time. Initial cell density is $N_{init}(x, y) = N_0 H(r^2 - x^2 - y^2)$, where $N_0 = 0.25$ and $r^2 = 0.05$. The values of the parameter used in the simulation are $\gamma = 1$, $\chi = 13.2173$, $\delta = 0.05141$, $\Delta t = 0.001$ and $t_{new} = 0.01$ 114

4.14 Cross section plot $y = 0$ of cell density N for same times and parameter values used in Figure 4.13. 115

5.1 Schematic diagram of perfusion bioreactor system. A porous scaffold of length $2L^*$ and width $2L^*$ is placed within the bioreactor. Fresh fluid is drawn from the reservoir B by the actions of the pump. The fluid is then pumped into the porous scaffold. After exiting from the scaffold it returns to the medium reservoir A. Reservoir B is continuously filled with the fresh medium. 120

5.2 Schematic diagram of the progression of cells from quiescence phase to proliferative phase and then to zero proliferation phase. 130

5.3 Schematic diagram of the progression of nutrient consumption from quiescence phase to proliferative phase and then to zero proliferation phase. 131

6.1	Schematic diagram of model equations and solution. All the notations are described in 5 and appendix A	144
6.2	Example of a coarse mesh. In this figure there are 851 mesh points, 1600 mesh elements out of which 100 are boundary elements and the system is solved for 9903 degrees of freedom.	145
6.3	Total cell number for different number of mesh points but fixed step sizes Δt_{cell} and time t_{update} . The initial cell density is $N_{init}(x, y) = 0.344H(0.0365 - x^2 - y^2)$. The values of parameters used are $\rho = 1$, $D_s = 6 \times 10^{-6}$, $R_s = 1.488$, $\delta = 0.13976$, $\beta = 13.2173$, $\gamma = 2$, $\sigma_{c1} = 3$ and $\sigma_{c2} = 15$, $g = 60$ and $k_1 = 5$	148
6.4	Difference between total cell number for different number of mesh points but fixed step size Δt_{cell} and time t_{update} . The green line is the difference between total cell number for mesh points 3301 and 851. The red line is the difference between total cell number for mesh points 13001 and 3301.	148
6.5	Total cell number for different step sizes Δt_{cell} but fixed mesh size and time t_{update} . The initial cell density and parameter values are the same as in Figure 6.3	150
6.6	Total cell number for different t_{update} but fixed mesh size and step size Δt_{cell} . The initial cell density and parameter values are the same as in Figure 6.3.	151
6.7	Snapshots of the cell density N , nutrient concentration S , fluid velocity \mathbf{u}_r and the shear stress σ at time $t = 0.5, 1.5, 2.5$ when initial cell density is uniform. The parameter values used in the simulation are given in Table 5.4.	154
6.8	Form of initial cell distribution when a blob of cells is placed at the centre of the scaffold. Mathematically $N_{init} = 0.346 \times H(0.0365 - x^2 - y^2)$	155
6.9	Snapshots of the cell density N , nutrient concentration S , fluid velocity \mathbf{u}_r and the shear stress σ at time $t = 0.5, 1.5, 2.5$ when initially a blob of cells placed at the centre of scaffold. The parameter values are same as in Figure 6.7.	156
6.10	Form of initial cell distribution when a blob of cells is placed away from the nutrient source. Mathematically $N_{init} = 0.346 \times H(0.0365 - x^2 - (y + 0.5)^2)$	158

6.11	Snapshots of the cell density N , nutrient concentration S , fluid velocity \mathbf{u}_r and the shear stress σ at time $t = 0.5, 1.5, 2.5$ when initially a blob of cells placed away from the nutrient source. The parameter values are the same as in Figure 6.7.	159
6.12	Form of initial cell distribution when a layer of cells is placed away from the nutrient source. Mathematically $N_{init} = 0.2 \times H(-0.9 - y)$	160
6.13	Snapshots of the cell density N , nutrient concentration S , fluid velocity \mathbf{u}_r and the shear stress σ at time $t = 0.5, 1.5, 2.5$ when initially a layer of cells is placed away from the nutrient source. The parameter values are same as in Figure 6.7.	161
6.14	Form of initial cell distribution when cells are placed on all the boundaries of the scaffold.	162
6.15	Snapshots of the cell density N and fluid velocity \mathbf{u}_r at time $t = 0.5, 1.5, 2.5$ when initially layer of cells is placed on the periphery of the scaffold. The parameter values are same as in Figure 6.7.	163
6.16	Form of initial cell distribution when cells are placed on all the boundaries of the scaffold except the inlet boundary.	163
6.17	Snapshots of the cell density N and fluid velocity \mathbf{u}_r at time $t = 0.5, 1.5, 2.5$ when initially cells are seeded on all the boundaries of the scaffold except inlet boundary. The parameter values are same as in Figure 6.7.	164
6.18	Form of initial cell distribution when layers of cells are placed on the side walls of the scaffold.	165
6.19	Snapshots of the cell density N and fluid velocity \mathbf{u}_r at time $t = 0.5, 1.5, 2.5$ when initially layer of cells is placed on the side walls of the scaffold. The parameter values are same as in Figure 6.7.	165
6.20	Comparison of the time evolution of total cell number for various initial seeding strategies.	167
6.21	Comparison of the time evolution of the total cell number for four different initial seeding strategies. Color represents the different seeding strategies. Solid and dotted lines represent the total cell number when threshold shear stresses are $\sigma_{c1} = 3$, $\sigma_{c2} = 15$ and $\sigma_{c1} = 2.5$, $\sigma_{c2} = 4.5$ respectively.	169

6.22 Scaffold having different porosity in different regions. Initial porosity of scaffold $\phi_0 = 0.60$ in one half and $\phi_0 = 0.90$ in the other half.	170
6.23 Snapshots of the cell density N , nutrient concentration S , fluid velocity \mathbf{u}_r and the shear stress σ at time $t = 0.5, 1.5, 2.5$ when the initial cell density is uniform and initial porosity of the scaffold is high in one half and low in the other half. The parameter values are the same as in Figure 6.7.	171
6.24 Scaffold with three high porosity vertical tubes. Initial porosity of tubes is 0.95 and initial porosity of other sections is 0.70.	172
6.25 Snapshots of the cell density N , nutrient concentration S , fluid velocity \mathbf{u}_r and the shear stress σ at time $t = 0.5, 1.5, 2.5$ when the initial cell density is uniform and three high porosity vertical parallel tubes are inserted in the scaffold. The parameter values are the same as in Figure 6.7. . . .	173
6.26 Scaffold with three high porosity vertical tubes along side walls. Initial porosity of tubes is 0.95 and initial porosity of other sections of scaffold is 0.70.	174
6.27 Snapshots of the cell density N and fluid velocity \mathbf{u}_r at time $t = 0.5, 1.5, 2.5$ when the initial cell density is uniform and three high porosity vertical tubes are inserted in the scaffold. The parameter values are the same as in Figure 6.7.	175
6.28 Scaffold with high porosity diagonal tubes. Initial porosity of tubes is 0.95 and initial porosity of other sections of scaffold is 0.70.	175
6.29 Snapshots of the cell density N , nutrient concentration S , fluid velocity \mathbf{u}_r and the shear stress σ at time $t = 0.5, 1.5, 2.5$ when the initial cell density is uniform and two high porosity diagonal tubes are inserted in the scaffold. The parameter values are the same as in Figure 6.7.	176
6.30 Scaffold with high porosity diagonal and vertical tubes. Initial porosity of tubes is 0.95 and initial porosity of other sections of scaffold is 0.70. . .	177
6.31 Snapshots of the cell density N , nutrient concentration S , fluid velocity \mathbf{u}_r and the shear stress σ at time $t = 0.5, 1.5, 2.5$ when the initial cell density is uniform and two high porosity diagonal and one vertical tubes are inserted in the scaffold. The parameter values are the same as in Figure 6.7.	178

6.32	Comparison of the time evolution of total cell number for various initial porosities of scaffold. The initial cell density is uniform throughout the scaffold. Dashed curves are our previous results, from Section 6.4.8 included for comparison.	179
6.33	Comparison of the time evolution of total cell number for optimal case of initial cell density, initial porosity distribution and combined effects of initial seeding and initial porosity.	181
6.34	Snapshots of the cell density N , nutrient concentration S , fluid velocity \mathbf{u}_r and the shear stress σ at time $t = 0.5, 1.5, 2.5$ when the initial cell density is uniform and flow rate $U_c^* = 0.05m/sec$, $D_s = 3 \times 10^{-6}$ and $R_s = 0.744$. The other parameter values are the same as in Figure 6.7. . .	183
6.35	Snapshots of the cell density N , nutrient concentration S , fluid velocity \mathbf{u}_r and the shear stress σ at time $t = 0.5, 1.5, 2.5$ when the initial cell density is uniform and flow rate $U_c^* = 0.0125m/sec$, $D_s = 1.2 \times 10^{-5}$ and $R_s = 2.976$. The other parameter values are the same as in Figure 6.7.	185
6.36	Comparison of the time evolution of total cell number for different perfusion velocities. The initial cell density is uniform throughout the scaffold.	186
C.1	Discretization of finite element domain	210
C.2	Finite element solution of flow field and pressure contours	218

Tissue engineering: Introduction and literature review

1.1 Introduction

Tissue engineering, the regeneration of organs or tissues in the laboratory for the replacement of damaged or lost tissue, is a multidisciplinary science since it aims to apply the principles of engineering and life sciences to reinstate the functions of devastated organs or tissues. Tissue engineering faces several challenges of which achieving significant cell growth in the supporting scaffold is one. To achieve the optimal cell density tissue engineers must ensure adequate delivery of nutrients to the inner region of the scaffold and uniform cell distribution. During cell growth biochemical and physical mechanisms interact in a very complex manner. To understand the complex interacting phenomena of these mechanisms in the scaffold-bioreactor system a number of mathematical models have been developed. Translating complex biological systems into mathematical equations with well defined parameters we aim to provide a better understanding of these systems. The crucial benefit of mathematical modelling is that a simple mathematical model can help to predict and analyze the complex mechanisms involved in the system. Due to these reasons mathematical models of pathological and physiological processes have already been developed in various areas *e.g.* solid tumor growth (Britton, 2003). We focus here on developing mathematical models for tissue growth in bioreactors, which will not only enhance the understanding of the mass transfer and cell growth processes but, will also demonstrate the utility and potential of computational models in choosing the various parameters for optimal cell growth.

1.2 Regenerative medicine

Regenerative medicine is an emerging multidisciplinary field which aims to restore the functions of damaged or lost tissue due to accident, trauma, disease or age related degeneration by a variety of approaches, from cell based therapies. This technology uses the principles of bioengineering and life sciences to treat the diseased tissue. Broadly, there are two approaches used in regenerative medicine both of which make use of human cells to regrow or treat damaged or lost tissue. One approach is called "cellular therapy" which does not involve the use of scaffold and the other approach which uses a scaffold is called "tissue engineering". Figure 1.1 shows the classification of regenerative medicine depending on the use of scaffold.

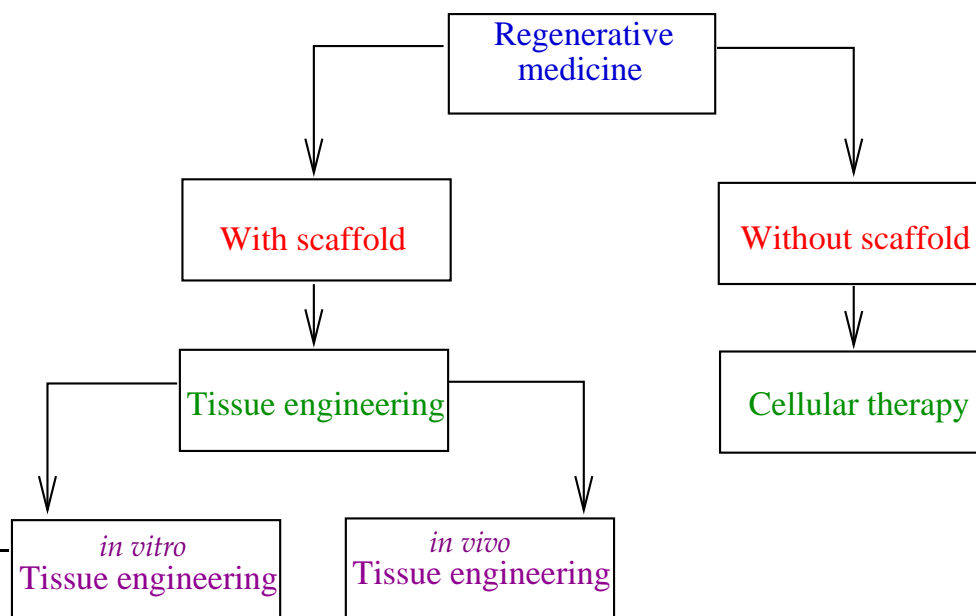


Figure 1.1: Classification of regenerative medicine based on the use of scaffold.

1.2.1 Cellular therapy

The replacement of damaged or diseased cells with healthy functioning ones is called "cell therapy" or "cellular therapy". This regenerative medicine technique describes the process of introducing new cells into a tissue to treat a disease. Whole blood transfusions, packed red cell transfusions, platelet transfusions, bone marrow transplants, and organ transplants are all forms of cell therapy. In some limited cases, injections of cells to patients is sufficient for the medical treatment. However, in many other cases where lost tissues or organs have a large size with a distinct three-dimensional structure, cell

injection alone is not effective as a cure because of the quick scattering of injected cells from the site of injection. In such cases, a support is required for cells to adhere, expand, differentiate, and produce extra cellular matrix for neo-tissue formation.

1.2.2 Tissue engineering

The regenerative medicine technique in which the treatment of damaged or lost tissue involves the use of scaffold is called "tissue engineering". In *in vivo* tissue engineering the tissue is grown in the patient's body. In *in vitro* tissue engineering the tissue is grown in the laboratory for later transplant into the patient's body. In this thesis we will focus on *in vitro* tissue engineering. A common strategy to regenerate new tissues in the laboratory involves different phases: (1) isolation of specific cells through a small biopsy from a patient or donor, (2) *in vitro* expansion of cells isolated from the biopsy, (3) seeding of cells onto 3-D scaffolds to support cell adhesion and proliferation, (4) appropriate cell culture using a bioreactor (closed culture environment) to mimic the conditions *in vivo*, (5) delivery of the construct to the desired site in the patient's body. These phases are illustrated in Figure 1.2.

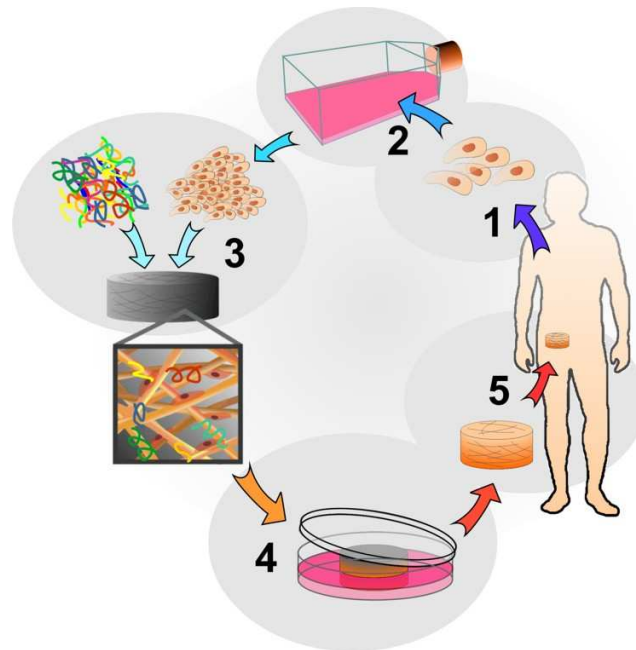


Figure 1.2: Principles of tissue engineering.

(Source: http://www.centropede.com/UKSB2006/ePoster/images/background/TE_model_large.jpg)

1.2.2.1 Tissue engineering background

Tissue engineering is a relatively new field which aims to bring together chemical and material engineering, cell biology and medicine, and theoretical and computational modelling. The main aim of tissue engineering is to regenerate or recreate human tissue in the laboratory for the repair and replacement of damaged or lost tissue as a result of an accident, trauma or cancer, age related degeneration or to correct congenital structural anomalies. Living, physiological three dimensional tissues can be fabricated in the laboratory by utilizing a suitable combination of cells, scaffold and cell signalling, both chemical and mechanical (Griffith, 2002). Tissue engineering approaches may be used to recreate skin, muscle or bone tissue or may involve regeneration of entire organs such as heart, kidney or liver *etc.* It is a cell based therapy that enables the restoration of function to a variety of tissues and organs (Freed et al., 1994). Scientists working in the field of tissue engineering believe that in the near future patients with liver/kidney failure will be cured with implanted neo-organs made from the patient's own liver/kidney cells and fibres. Tissue engineers are anticipating that in the near future insulin dependent diabetic patients will not require frequent insulin injections because they will have semi-synthetic replacement pancreases, and kidney dialysis machines will no longer be needed because patients with damaged or failed kidneys will have the option of replacing their damaged or failed kidneys with new ones grown from their very own cells (Scientific American, 1999).

The term "tissue engineering" was first introduced by the participants of a National Science Foundation meeting held in 1987 in the USA. In this meeting researchers from all over the world gathered to discuss the future of bioengineering, and coined a new term "Tissue engineering" (Ikada, 2006b). Early developments in this interdisciplinary field are discussed in Langer and Vacanti (1993). In this paper the authors demonstrate how the principles of engineering and life sciences can be applied to regenerate a biological substitute that restores the functions of damaged or lost tissue. Tissue engineering defined by Langer and Vacanti (Langer and Vacanti, 1993) as "an interdisciplinary field that applies the principles of engineering and life sciences toward the development of biological substitutes that restore, maintain, or improve tissue functions or a whole organ".

Tissue and organ damage or loss as a result of trauma, infection, disease or age related degeneration is a major human health problem (Whitaker et al., 2001a). Limited healing capacity of some tissues/organs is a major clinical problem. Certain tissues and organs cannot heal satisfactorily by themselves and require treatment to reinstate their

functions *e.g.* articular cartilage which is a relatively simple structural tissue with only one main function (load bearing) and has very limited ability for self-repair. However none of the available treatments can restore the functions of articular cartilage.

At present artificial organs and organ transplantation are the techniques available to treat patients who need to reinstate diseased or damaged organs or tissues. However a number of problems are associated with the use of artificial organs and transplantation as discussed below. Currently used artificial organs and mechanical devices do not repair the organ functions and are not intended to become a part of the host tissue. Artificial organs can produce an inflammatory response in the host tissue (Maguire Jr et al., 1987) and there is also a great concern over the long term performance of the artificial organs (Chapekar, 2000). In the past decade advances in biomedical engineering has improved artificial organs, but still they need better biofunctionality and biocompatibility (Ikada, 2006a). Alternatively, whole organ transplantation is one of the few options currently available. During the past century many obstacles to organ transplantation were overcome, including the use of immunosuppressive drugs, advanced surgical techniques, and improved postoperative care (care after transplantation) (Ikada, 2006a, Saltzman, 2004). Due to these developments the transplantation of liver, kidney, heart, blood vessels and all major organs have become a daily reality. Despite the excellent results of these transplantation techniques this technology has some major problems such as donor site morbidity and tissue rejection. Furthermore, the supply of donor tissue is not enough compared to the number of patients requiring transplantation. With the increase in population size and consequently an increase in demand for organ transplantation, this problem will become more severe in time. Tissue engineering offers a promising alternative. A characteristic feature which distinguishes tissue engineering from the other techniques is that it can regenerate tissue by using the patient's own cells which are entirely free of severe immune rejection, poor biocompatibility, low biofunctionality and viral infection (Stock and Vacanti, 2001).

Tissue engineering applications can be classified into *therapeutic applications*, where tissue is grown *in vivo* or *in vitro* and later transplanted into the patient, and *diagnostic applications*, where the tissue is fabricated *in vitro* and is used for testing different chemical reactions, including drug metabolism and uptake (Griffith, 2002).

Successful *in vitro* tissue engineering examples include the fabrication of tissue engineered autologous bladders for the replacement of patients with end stage bladder disease (Atala et al., 2006) and transplantation of tissue engineered airway (Macchiarini et al., 2008). We discuss the key aspects of *in vitro* tissue engineering in turn below.

1.3 Key components of tissue engineering

Tissue reconstruction is based on four fundamental components: appropriate cell type, development of a suitable scaffold to support cell attachment, growth factors, and bioreactors. The cells construct the matrix of the new tissue, while the scaffold provides the cells a structure on which to grow. The growth factors facilitate the cells to regenerate new tissue (Ikada, 2006a) and bioreactors provide a controlled environment to allow the cells to grow and differentiate to generate the required tissue. Careful consideration must be given to all the aspects of *in vitro* tissue engineering including the source of cells, scaffold construction, mechanical properties and cell seeding strategy.

1.3.1 Cells

The body is composed of several organs and tissues. An organ contains several tissues and each tissue is an assembly of one or more cell types. Cells are one of the most basic and important materials for tissue engineering. Cells are chosen mainly for their ability to proliferate, differentiate, undergo cell-to-cell signalling and perform biological activities *e.g.* extracellular matrix production. The starting point for any attempt to engineer a tissue or organ is a consideration of the types of cells to be employed. The cell source can be autologous (cells taken from the patient), allogeneic (cells from other human sources), or xenogeneic (cells from different species). Alternatively stem cells may be used collected from either autologous, allogeneic or xenogeneic sources (Griffith and Naughton, 2002). There are both advantages and disadvantages of each of these. Autologous cells have no legal problems with their use and there is no problem of immune rejection. The patient will not reject the engineered tissue because it is synthesized by their own cells and the patient will not have to take immunosuppressive drugs. However the problems associated with the use of autologous cells are (1) they may be unhealthy and (2) it may be difficult to harvest a sufficient amount of cells in a reasonable time (Curtis and Riehle, 2001). If the number of cells are insufficient for clinical use it is first necessary to expand the number of cells by cell culture. This procedure not only requires a clean cell processing centre but it is also time consuming. Thus to get the sufficient amount of autologous cells we have to wait for a long time (Curtis and Riehle, 2001). On the other hand allogeneic cells have the problem of immune rejection but are available in sufficient amounts to rebuild the tissue. Xenogeneic cells not only have the problem of immune rejection but there may be problems with animal virus transmission (Lanza et al., 2007). The frequency of pig use as a cell source

has dramatically reduced after the report which indicated the presence of porcine endogenous retrovirus (Patience et al., 1997).

By definition stem cells are pluripotent which means that they have the ability to differentiate virtually into every cell type. Modern research on stem cells has contributed significantly to the progress of tissue engineering. Stem cells may be derived from either fetal tissue or from adult tissue. The use of fetal tissue raises immunological and ethical issues so recent studies have focused on cells derived from adult tissue (Stock and Vacanti, 2001). Isolation of several adult stem cells, including mesenchymal, hematopoietic, neural and hepatic stem cells, have opened a new avenue for obtaining a sufficient supply of cells to rebuild the tissue (Chapekar, 2000). Currently stem cell-based technology has been used to engineer several tissues including epithelia (skin, cornea) and skeletal tissues (Bianco et al., 2001).

There are two basic approaches to cell harvest. The first approach which is used to obtain autologous cells is by biopsy. This approach can be applied to most organs *e.g.* heart, liver, skin, bone marrow, cartilage and blood vessels. But for some tissues or organs, such as heart valves, direct biopsy is not feasible and related harvest sites must be considered. For heart valves peripheral vein segments are considered to be a suitable cell source. In neural tissues *e.g.* spinal cord and peripheral nerve, neither direct or indirect biopsies are feasible (Stock and Vacanti, 2001). One way to counter this cell source difficulty is to isolate stem cells.

The small numbers of cells isolated from biopsies must be expanded before they are seeded on a scaffold. 2-D cell culture is an excellent method for increasing the number of cells. 2-D monolayer cell culture on a flat plate substrate is the most common method to increase the number of cells. In this method cells are allowed to grow in one plane under space limiting conditions. This results in an artificial growth environment which is completely different from the *in vivo* environment and the cells may lose their functional behaviour. In the human body most cells occur in a 3-D environment so 3-D culture has been preferred to 2-D culture (Abbott, 2003). Many cellular processes including morphogenesis and organogenesis occur exclusively when cells are organized in 3-D fashion. In 3-D culture at high cell density enhance cell-cell interaction which is favorable for extra cellular matrix (ECM) production. 3-D culture is poor for cell expansion. Cells in 3-D culture are surrounded with a substrate from multiple directions. However 2-D culture may change to 3-D culture once cells begin to be surrounded by the matrix produced by the cells themselves (Ikada, 2006a).

1.3.2 Scaffold

When a tissue is severely damaged or lost not only are a large number of functional cells damaged but the extra cellular matrix (ECM) is lost. In this situation we need artificial or biologically derived ECM for the cells to synthesize a neo-tissue. In tissue engineering we call this ECM template a "scaffold" (Ikada, 2006b). The cells must be implanted or seeded onto an artificial structure capable of supporting three-dimensional tissue formation. The scaffold provides an architecture on which seeded cells can organize and develop into the desired organ or tissue prior to transplantation. Cell attachment is the first step in starting cell growth and neo-tissue formation. There are many different types of scaffolds, and Figure 1.3 shows an example of a tissue engineering scaffold.

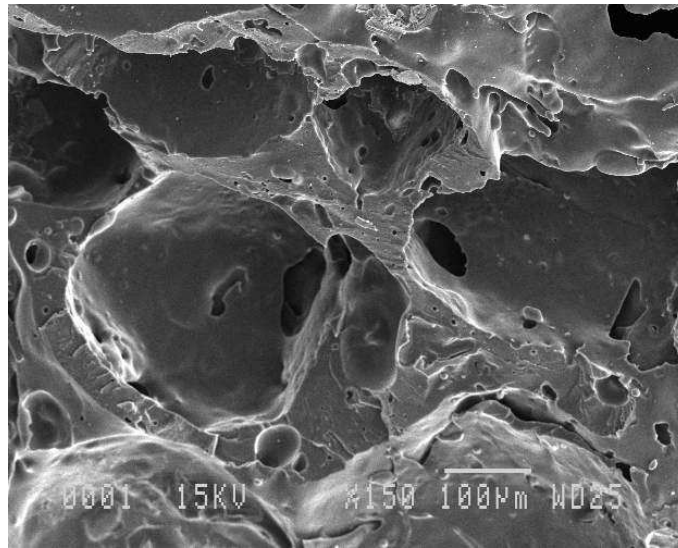


Figure 1.3: Tissue engineering scaffold. Poly(lactic-coglycolic acid) porous scaffold for bone tissue engineering produced by melt casting and particulate leaching. (Source: <http://www.msm.cam.ac.uk/ccmm/research/vam27.html>)

To achieve the goal of tissue reconstruction, scaffolds must meet some specific requirements.

1. The scaffold should be highly porous with adequate pore size having interconnected micro pores, so that the seeded cells can migrate into the inner region of scaffold and increase the cell number there. The importance of large porosity is that the nutrients can reach the cells very easily and it also provides the space for the cells to grow. The micro pores are responsible for vascular formation and transport of nutrients and growth factors in and out of the scaffold (Ikada, 2006a).

2. The scaffold material should be bio-compatible (the material is compatible with living cells and poses no risk of injury, toxicity and immune rejection) and bio-degradable because it is essential that scaffold should degrade with the passage of time without the necessity of surgical removal (Chapekar, 2000, Stock and Vacanti, 2001). The rate of degradation of scaffold material must coincide as much as possible with the rate of new tissue formation (Griffith and Naughton, 2002, Hutmacher, 2000). This means that while cells are fabricating their own natural matrix structure around themselves, the scaffold is able to provide structural integrity and maintain the mechanical strength within the body until tissue regeneration is almost completed and eventually it will break down leaving the newly formed tissue which will take over the mechanical load (Chapekar, 2000, Ikada, 2006b). If the scaffold material remains for a longer time than desired then the remaining scaffold material may slow down the tissue formation rather than promote it. Premature degradation of scaffold material combined with slow development of replacement tissue may result in reduced mechanical strength, which may lead to its failure (Chapekar, 2000). Thus the rate of scaffold degradation is crucial to the success of tissue formation.

Generally the first step in tissue engineering is the seeding of cells into the porous scaffold, which plays an important role in determining the progression of tissue formation (Vunjak-Novakovic et al., 1998). Achieving a high cell density and the desired cell distribution in the scaffold are the main challenges of cell seeding technologies in tissue engineering. Seeding cells into the scaffold at high densities has been associated with enhanced tissue formation in the 3-D construct (Holy et al., 2000). Furthermore the initial distribution of cells within scaffold has been shown to influence the distribution of tissue subsequently formed within the engineered construct. If the number of seeded cells is small then the tissue formation is poor. If the density of the seeded cells into scaffold is low, then the distance between the neighboring cells is large; the resulting tissue that forms is then poor because of insufficient communication between the cells (Ikada, 2006b).

Formation of tissue with desirable properties is entirely dependent on the scaffold mechanical properties at both the macroscopic and microscopic level. Macroscopically the scaffold should be able to provide stability to the tissue. At the microscopic level cell growth, differentiation and the ultimate tissue formation are dependent on the local mechanical environment and mechanical properties of scaffold such as elasticity, compressibility, tensile strength *etc.* are key.

Various materials have been used for the construction of scaffolds in tissue engineering. Scaffold materials for tissue engineering must be bio-compatible and biodegradable. Poly(α -hydroxyacid), especially lactide and glycolide polymers, have widely been used as biomaterials (Whitaker et al., 2001b). A general criterion for selecting a polymer as a biomaterial is to correlate mechanical properties and degradation time to the needs of the application (Middleton and Tipton, 2000). Several different materials have been evaluated as potential scaffold materials for tissue engineering. These include biodegradable synthetic polymers such as polyesters, polyurethane, polydioxane etc., and naturally derived polymers such as collagen, glycosaminoglycan, chitosan and hyaluronic acid. Other materials such as metals (e.g. titanium) and ceramics (e.g. hydroxyapatite) have also been in use over the last century, but most of these materials are not biodegradable and have limited process abilities. Most of the commercially available biodegradable materials used for tissue engineering are polyesters, derived from lactic acid, glycolic acid and their co-polymers. These polymeric materials are being investigated worldwide for applications in fields of surgery (e.g. surgical sutures, pins and screws), pharmacology (drug delivery system) and tissue regeneration (e.g. scaffolds for orthopaedics tissue engineering, cartilage, bone skin, ligaments etc). This is due to their biocompatibility, variable and controlled degradability and approval by the Food and Drug Administration (Boccaccini and Blaker, 2005).

To process the polymers into desirable, 3-D structure with interconnected pores suitable for *in vivo* or *in vitro* tissue engineering, a variety of fabrication techniques have been employed for scaffold production (Hutmacher, 2000). Current techniques include solvent casting and particulate leaching, fibre extrusion and bonding, solid-free fabrication, phase separation and emulsion freeze-drying, gas and supercritical fluid foaming. Supercritical fluid (SCF) technology has been seen as a promising alternative to the other techniques (Rose and Oreffo, 2002, Woods et al., 2004). This is due to the absence of co-solvents and thermal processing that may be harmful to adherent cells, nearby tissues and biologically active factors. Therefore, SCFs offer ideal conditions for several tissue engineering applications such as the incorporation of growth factors within polymeric scaffolds, used to stimulate or inhibit the cell growth, differentiation, migration and extracellular matrix (ECM) production. Osteoconductive materials, such as hydroxyapatite and tricalcium phosphate, can also be incorporated within polymeric scaffolds to minimize the mechanical competence concerns. Furthermore this technology avoids the use of traditional salt leaching methods to improve the porosity and interconnectivity or even additional drying steps for solvent removal as required by most of the current techniques.

In addition to the above techniques, in recent years, sophisticated technologies have been employed for scaffold fabrication. They include solid free prototype and electrospinning scaffold. Electrospinning scaffold does not require an expensive apparatus but solid free prototype needs high cost apparatus. Some special type of scaffolds such as naturally derived scaffolds, injectable scaffolds, elastic scaffolds, inorganic scaffolds and composite scaffolds are fabricated for specific tissue engineering applications. Scaffolds have also been produced for individuals via custom 3-D printing using a laser stereo lithography technique (Howard et al., 2008). This allows the scaffold to be built from computed 3-D information derived from patient scans or from computer simulations (Antonov et al., 2005).

1.3.3 Growth factors

A variety of proteins play a key role in promoting or preventing the cell growth, differentiation, migration, adhesion and motility (Whitaker et al., 2001b). These proteins are called the growth factors (Ikada, 2006a). Within the body these proteins can be generated by the cells themselves (autocrine) or as a result of communication with the neighbouring cells (paracrine). There are several characteristic properties of growth factors. A growth factor can be produced by the variety of cell types and the same growth factor can act on many cell types with a diverse range of effects (Babensee et al., 2000, Whitaker et al., 2001b). Growth factors can be secreted by many cell types and typically act as signalling molecules between cells (Rose and Oreffo, 2002). For optimized tissue formation growth factors should be presented to the cells for a limited period of time in the correct local environment (Babensee et al., 2000, Lanza et al., 2007). The growth factors that have frequently been applied to tissue engineering include bone morphogenetic proteins (BMPs), basic fibroblasts growth factors (BFGF), epidermal growth factor (EGF), nerve growth factor (NGF), vascular endothelial growth factor (VEGF) and transforming growth factor- β (TGF- β) (Ikada, 2006a, Whitaker et al., 2001b). Some growth factors such as platelet derived growth factors (PDGF), epidermal growth factor (EGF) and hepatocyte growth factors act as powerful agents to stimulate the mitosis of cell proliferation whereas others such as nerve growth factor (NGF) stimulate cell migration (Whitaker et al., 2001b).

Growth factors are important for successful repair and regeneration of tissue and, hence, they play a central role in tissue engineering strategies (Nimni, 1997, Whitaker et al., 2001b). Application of growth factors in tissue engineering requires enhancement of their activities *in vitro* by means of adequate delivery system. The method

with which the growth factors are delivered to the site of action is also very critical to the success of tissue engineering. The delivery methods include bolus injection; release of growth factors directly on scaffold surfaces; in collagen sponge or porous coating; constant delivery via osmotic pump; and controlled release of growth factors trapped in an absorbable polymer. In tissue engineering there are two potential delivery systems. Firstly growth factors can be applied directly into the scaffold at or after fabrication (Fournier and Doillon, 1996, Tabata et al., 1999). Growth factors delivered to a biodegradable scaffold system are released as the scaffold degrades. The growth factor, directly incorporated into a scaffold, is released by a diffusion-controlled mechanism (Whang et al., 1998). Secondly, the growth factor delivery device in the form of microparticles, nanoparticles, fibres or injectable complexes can be incorporated into the scaffold (Mooney et al., 1996).

A single growth factor can be used for the tissue engineering of one tissue but a combination of growth factors can be used for the enhancement of tissue regeneration (Ikada, 2006a). For the supply of sufficient nutrients to the cells involved in the tissue regeneration, tissue engineers are working to induce neovascularization using different growth factors.

1.3.4 Bioreactor

After cell seeding onto the scaffold, it is necessary to allow cell growth *in vitro* prior to transplantation. This may be done by culturing the scaffold in a system which aims to provide the same conditions as *in vivo*. A bioreactor is a closed culture environment in which biological and/or biochemical processes develop under controlled environmental and operating conditions (Ellis et al., 2005). The main aim of bioreactor is to control the biochemical and biomechanical environment. The variables that are controlled include: pH, temperature, pressure, nutrient supply, waste removal, media flow rate, shear stress, mechanical and hydrodynamic forces. The functions of bioreactors are to provide suitable nutrient, growth factors and oxygen delivery to the cells in the scaffold, and to remove waste products such as lactate and carbon dioxide from the scaffold (Martin et al., 2004). Different techniques have been used for cell culture in a bioreactor, but seeding efficiencies are not yet at optimal levels. Lower seeding densities affect the amount of time and resources required to obtain scaffolds ready for implantation. The most commonly used seeding method is the static loading of cells onto a scaffold, but the main disadvantage of this technique is the low seeding efficiencies and non-uniform cell distribution within scaffolds (Kim et al., 1998).

We can classify the bioreactors by their main mode of operation, *e.g.* spinner flask, rotating wall and perfusion bioreactors.

1.3.4.1 Spinner flask bioreactor

A mechanically stirred flask is considered one of the simplest bioreactors and the most common mechanically stirred bioreactor is the spinner flask bioreactor (Ellis et al., 2005). Scaffolds are attached to needles hanging from the cover of the flask and suspended within a stirred suspension of cells. During seeding cells are transported onto and into the scaffold by convection (Freed and Vunjak-Novakovic, 1997). During culture, medium stirring enhances mass transfer. This method has favorable results but the main disadvantages of the technique includes the amount of time required for seeding, low efficiency at low cell concentrations, non-uniform cell distribution and undesirable high shear rates which can damage the cells (Ikada, 2006a, Wendt et al., 2003). The degree of shear stress depends on the stirring speed and morphology of scaffold. Figure 1.4 shows a simple spinner flask bioreactor.

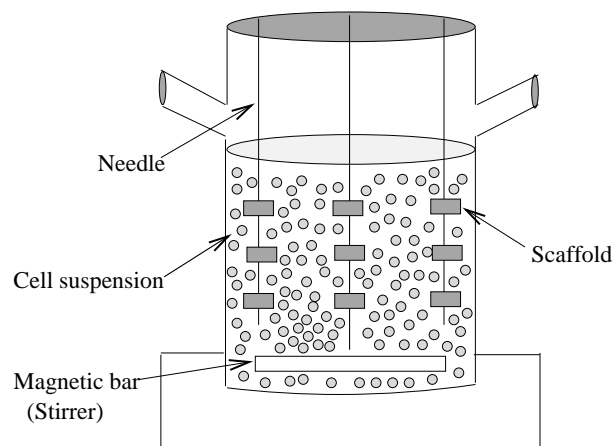


Figure 1.4: Spinner flask bioreactor.

1.3.4.2 Rotating wall vessel bioreactor

This is composed of two cylinders and the scaffolds are placed in the annular region between the two cylinders. The inner cylinder is stationary and gas exchange is allowed through the inner cylinder while the outer cylinder is impermeable and rotates in a controlled fashion. The vessel is initially seeded with the suspension of cells in culture media. As the bioreactors turns, the cells continuously fall through the culture media and, over a period of time, cells self assemble to form a 3-D tissue construct. Scaffolds

may be added to the vessel at the same time when the cell suspension is introduced to act as a substrate where cells can adhere (Lappa, 2003, Waters et al., 2006). This bioreactor provides dynamic culture environment to the constructs, with two beneficial factors: efficient mass transfer rate and low shear stress (Martin et al., 2004). The vessel walls are rotated at a controlled rotation rate which enables the net gravitational force, drag force and centrifugal force acting on the scaffold to be balanced. Figure 1.5 shows a simple rotating wall bioreactor.

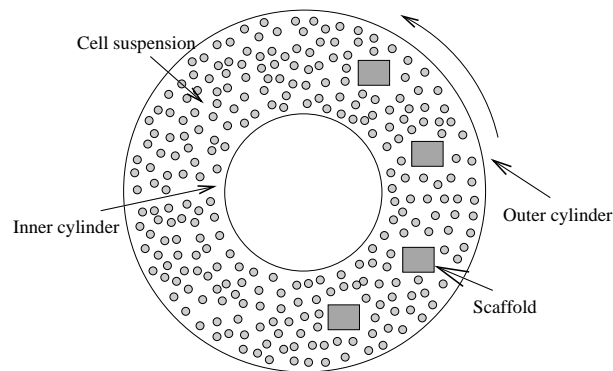


Figure 1.5: Rotating wall vessel bioreactor.

1.3.4.3 Perfusion bioreactor

In this type of bioreactor a pump is used to force the medium through the interconnected pores of the scaffold rather than around the edges. During seeding cells are transported directly into the pores of the scaffold. During culture the availability of fresh medium through the construct enhances mass transfer not only at the surface of the construct but also within the internal porous network.

The perfusion bioreactor has one problem of non-uniform cellular secretions through the thickness of the construct along with damage to some of the cells. If the fluid is flowing from one end of the scaffold then the front surface has high shear stress due to incoming fluid, while the back side does not feel the force except for inside the pores. Due to this reason a thicker matrix will be formed at the front surface as compared to the back surface. Figure 1.6 shows an example of perfusion bioreactor.

Using the principles of convective transport for scaffold seeding, the flow of a cell suspension directly through the pores of a 3-D scaffold produces more uniformly seeded scaffolds compared with static seeding (Li et al., 2001). Higher seeding efficiencies and more uniform cell distributions were achieved as compared with either static seeding

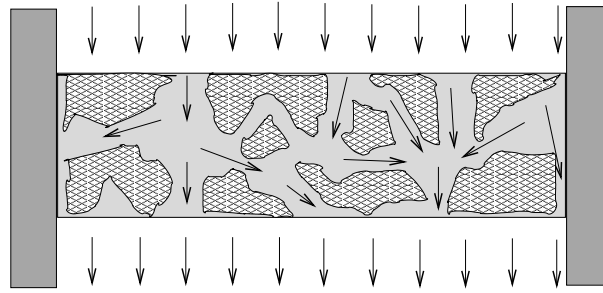


Figure 1.6: Perfusion bioreactor.

or stirred flask bioreactor when direct perfusion was incorporated into a bioreactor capable of performing both 3-D scaffold seeding and subsequent cell culture.

In the early days of bioreactor use in tissue engineering the main aim of the bioreactor was to provide the nutrient to the inner region of the construct but presently bioreactors not only control the supply of nutrients to the cells but also control the temperature, pH, medium flow rate, shear stress, waste removal, pressure, hydrodynamic and mechanical forces. Most commonly used bioreactors are rotating wall and perfusion bioreactor systems. In rotating wall bioreactors the cell-seeded scaffold are suspended in the cylindrical chamber that allow the construct to fall through the medium but they do not hit the sides. In a perfusion bioreactor the medium is pumped into the construct. Both systems apply mechanical force for example shear stress exerted on the cells and allow nutrient transport. In these bioreactor systems stresses and strains applied to cells are not experimentally measurable. These mechanical forces can influence the tissue formation and bioreactor performance, so it is necessary to understand the affect of these forces between the cells and ECM to produce a functional tissue.

Regenerating tissue in the laboratory is a complex process and several mechanical and biochemical forces are in operation during the growth of tissue. It has been demonstrated that the bioreactor environment has a profound impact on tissue morphology and mechanical environment. So it is very important to identify the effect of these forces during the formation of tissue. Very little is known about either how these forces should be applied for specific tissue or how these forces are used by the cells (Martin et al., 2004). For the successful growth of a tissue *in vitro* it is very important to tissue engineers to study the effect of biochemical, mechanical or hydrodynamic forces during the tissue formation.

1.4 Mechanotransduction

Mechanotransduction is the study of the mechanism by which mechanical forces for example between cells, between cells and the scaffold, and forces exerted on cells by fluid shear stress are converted into biochemical signals and how cells respond to these signals. Externally applied mechanical forces can effect cell proliferation, cell orientation, gene activity and cell viability (Butler et al., 2000). For example Akhyari et al. (2002) found that cyclic mechanical stretch enhances the proliferation and matrix organization of human heart cells seeded on a gelatin -matrix scaffold. Several groups have studied the mechanical effects induced by the fluid flow (Girard and Nerem, 1995, Ives et al., 1986). There is also evidence that during *in vitro* tissue growth the mechanical input (*i.e.* hydrostatic pressure and shear stress induced by fluid flow) gives tissue that has characteristics very similar to *in vivo* tissue structures (Ellis et al., 2005).

To understand the molecular basis for mechanotransduction we need a detailed knowledge of the distribution of forces experienced by an individual cell. Currently we have sufficient knowledge to measure molecular level forces in only a few cases. The discovery of the way in which these forces influence the cellular response will open a new avenue for many tissue engineering applications. Several authors have used different techniques to stimulate the individual cell mechanically, but they found that the cellular response is multifaceted and diverse. Similarly there are likely to be a variety of sensing mechanisms and locations in the cells where forces can be converted from a mechanical to biochemical signal. Theoretically both continuum and microstructural approaches can be used to determine the force distribution. For a detailed description of cell mechanics and mechanotransduction pathways readers are directed to Huang et al. (2004).

In vitro static culture for cell monolayers and small explants has been employed for many years. These techniques can provide sufficient nutrients to tissues with a thickness less than few hundred micrometers. Due to limitation of diffusion of nutrients and waste products throughout the tissue engineered construct, when considering the formation of large tissue such as muscle or breast, it is found that the cell density increases at the periphery of the construct where the nutrient concentration is high and a necrotic core can form in the internal regions of the construct (Cartmell and El-Haj, 2005). To overcome this problem bioreactors capable of perfusion are widely used. These bioreactors not only increases the mass transfer to the internal regions of the construct but can also provide controlled mechanical stimuli such as flow-mediated shear stresses and hydrostatic pressure (Cartmell et al., 2003, Freed and Vunjak-Novakovic, 1995). It

has been documented that fluid induced shear stress is proportional to perfusion velocity. Fluid flow can have harmful effect on the tissue regeneration. Several authors studied effect of fluid flow on the tissue regeneration and found that stimulation via fluid shear stress enhances tissue regeneration (Bakker et al., 2004, Klein-Nulend et al., 1995, You et al., 2000, 2001). Cartmell and El-Haj (2005) studied the effect of mechanical forces applied via fluid induced shear stresses. They applied different patterns of fluid flow (unidirectional, bi-directional) and different modes of shear stimulus to cells. They also found that when the cells experience a given force they respond by upregulating the cell's proteins and genes. The tissue engineering construct thus formed has more strength than the non-mechanically stimulated counterparts. The mechanical stimuli acts in a similar fashion to the growth factors approach (Cartmell and El-Haj, 2005). It has been found experimentally that the magnitude of the shear stress effects tissue regeneration. Tissue regeneration is unaffected by low shear stress but intermediate values of shear stress enhances tissue regeneration. It has been found that high shear stresses are responsible for the cell death (Cartmell et al., 2003).

To summarize we can say that mechanical stimuli are crucial for formation of tissue outside the body in the laboratory. Several studies proved that mechanical effects can enhance the structural and functional properties of engineered tissue (Martin et al., 2004). Very little is known about the specific mechanical forces that can stimulate the particular tissue. It is therefore a great challenge for tissue engineers to discover these mechanisms either experimentally or theoretically so that appropriate methods can be employed *in vitro* to fabricate the functional tissue for implantation. The bioreactor can be very important to study the effect of mechanical forces in developing the engineered tissue and also the response of engineered tissue to mechanical forces.

1.5 Limitations of nutrient supply in tissue engineering

An important step in the success of tissue engineering is the transport of oxygen and nutrient to the cells (Kellner et al., 2002). If oxygen concentrations are inadequate, cell proliferation ceases and viability begins to break down. Indeed, under hypoxic (low oxygen concentration) conditions the oxygen required for metabolism is very low, and in this situation cells convert glucose to lactic acid (Boutilier and St-Pierre, 2000). In this process each glucose molecule gives only 2 ATP molecules (the basic energy unit). On the other hand under aerobic condition one molecule of glucose produces up to 36 molecules of ATP (Stephanopoulos et al., 1998). That means under hypoxic conditions

glucose utilization increases which causes a decrease in glucose concentration and an increase in lactate concentration causes a decrease in pH. If the glucose concentration becomes too low or the lactate concentration becomes too high then cells begin to die (Boutilier and St-Pierre, 2000). Tolerance to hypoxic conditions differs widely between cell types. Some cells can live under the mild hypoxic conditions for several hours but in the complete absence of nutrients cells can survive only for a few minutes (Boutilier and St-Pierre, 2000).

In the case of large tissue formation a significant issue is the supply of nutrients to the cells. The very high cell density in most soft tissues often combined with large implant dimensions, means that the supply of nutrients is a critical factor in the success or failure of soft tissue scaffold (Croll et al., 2005). Due to the constraint of oxygen transport in the case of cortical bone and cartilage, which are relatively avascular tissues, scientists have only been able to synthesize functional tissue in the laboratory with a thickness less than few hundred micrometers (Kellner et al., 2002). In liver tissue engineering, a very low initial density of $10^6 / mL$ of rat liver cells are seeded on a $5mm$ thick PLGA (poly lactic co-glycolic acid) foam scaffold and cultured under static conditions. It was found that liver cells lost 50% of their DNA contents after 12 days (Hasirci et al., 2001). When the cells are seeded uniformly throughout the scaffold then the cells near the oxygen source consume oxygen and proliferate very quickly; but cells in the deeper sections of the scaffold will not get enough oxygen for growth and they experience hypoxic conditions. The cell density becomes non-uniform giving more cells near the oxygen source and very few cells in the deeper sections of the scaffold.

Existing techniques to improve the nutrient delivery to, and waste removal from, cells seeded onto 3-D scaffolds take advantage of the scaffold structure. Scaffolds are often highly porous with pore size ranging from $250\mu m$ to $600\mu m$. The nutrients are delivered to the cells via a liquid called the culture medium. Nutrients that the cells need to perform their functions include oxygen, glucose, ascorbic acid (vitamin C) and various salts. The cells produce waste products *e.g.* lactic acid and carbon dioxide, which lowers the pH of the surrounding medium which can be harmful for the cells.

1.6 Mathematical modelling in tissue engineering

In this Section some mathematical models relevant to tissue growth within a dynamic culture environment are reviewed. Two different approaches can be considered in constructing mathematical models for dynamic cell culture. The first approach is to

formulate the model by considering the interactions of individual cells. In this case the position and velocity of each individual cell in the system is considered. The second approach considers the system as a continuum. In this case the position and velocity are assumed to be average quantities over some local region. The two approaches have different advantages and disadvantages. For example, individual cell-based modelling allows incorporation of rules governing cell behaviour, and gives detailed information about the dynamics of the cell population such as movement of each cell (Armstrong et al., 2006). Since individual cell-based models consider the behaviour of each individual cell these models are very complex and can only be solved by numerical techniques, which can be numerically expensive and time consuming if the number of cells are very large. Alternatively, continuum models can be expressed in terms of systems of coupled partial differential equations, which sometimes allows us to apply classical applied mathematics techniques such as asymptotic approximations to solve the system. Alternatively, where analytical solution does not exist we employ numerical techniques to solve the continuum model which are computationally quicker and easy to implement.

Slime-mold *dictyostelium discoideum* is a widely used individual based model system. Individual based model of this organism have been developed to study several basic developmental processes, including cell-cell signaling, signal transduction, pattern formation, aggregation and cell motility. Palsson and Othmer (2000) and Palsson (2001) presented an individual based model for motile *dictyostelium discoideum* cells. The basic properties of each individual cell include that each cell is in contact with the neighboring cell, each cell can generate active forces and the cells may deform. The authors determined that the individual behaviour of a cell depends on the internal parameter state and information it receives from the external environment which includes a mechanism for interaction between the neighboring cells and ECM . They calculated the net force on the cell by adding all the forces acting on the cell due to the surrounding medium. The collective movement of the entire tissue is given by the net movement of all the cells, which move according to an equation of motion.

There are several classes of discrete tissue models. The most simple are lattice-based or cellular-automaton models, where cells are forced to lie on a regular grid. In such models only one cell can exist at one spatial location. It is possible to model cell proliferation and cell-cell adhesion. Loeffler et al. (1986) introduced the first comprehensive model analysis of the 2-D cell layer in the murine crypt. Later several authors discussed similar models independently (Finney et al., 1989, Isele and Meinzer, 1998). These models were based on a 2-D rigid lattice with rectangular cell layout. In these models rules

are set up for cell interaction, division and movement. There are several weaknesses in these models, firstly, lattice-based tissue models cannot explain the continuous growth and migration of individual cells as their movement is restricted to discrete spatial locations. Secondly these models do not reflect the effect of polygonal packing arrangements in crypts. Finally, in these models cell movement and cell mitosis are directly coupled in spite of the observation that migration can be observed even after complete mitotic arrest (Kaur and Potten, 1986).

To overcome these limitations lattice-free model have been developed. These models can be classified in two categories, cell-centre models and vertex models. In cell-centre models the location of each cell is given by a single point, and the point may be considered to be located at the centre of the cell nucleus. The total force on any cell is a function of the set of cell centres. In vertex models each cell is polygonal and defined by the location of a finite set of vertices (Pathmanathan et al., 2009, Walter, 2009). The lattice-free model for cell division in a small intestinal crypt is presented by Meineke et al. (2001). In this model the cell location is not restricted to a grid framework, as in Loeffler et al. (1986). The model differs from the earlier approaches in using a dynamic movement on a lattice-free cylindrical surface. It is a cell-centre model. The authors used a Voronoi diagram to divide the plane into regions. They assumed that cells will keep a constant distance between them and captured the distance between the cells through the series of damped springs. Cells are not allowed to move out of the crypt from the bottom boundary but the cells that move beyond the upper boundary are removed. The authors compared the model results with experimental data and found that the both results are in excellent agreement when a complete ring of sixteen stem cells is considered to reside immediately above the Paneth cells. Using a similar Voronoi diagram approach Morel et al. (2001) formulated a model for proliferation control in a generalized epithelium. This model incorporated both cell growth and differentiation factors. The authors found the effect of the micro environment upon the cell proliferation. A multiscale model for proliferation in the intestinal crypt has been presented by Van Leeuwen et al. (2009). Pathmanathan et al. (2009) studied the mechanical behaviour of a discrete tissue model. They used a discrete cell-centre approach to model the evolution of a collection of cells. Osborne et al. (2010) compared the results of cell-vertex model, cell-centre model and an analogous continuum model of cell proliferation and migration in a crypt. The authors found that the conclusions are independent of the modelling approach and also cell based models are more convenient to investigate however they are computationally expensive for large numbers of cells. On the other hand continuum models are computationally quicker and easy to

implement.

We will now discuss the continuum models. Obradovic et al. (2000) developed a simple mathematical continuum model to study the synthesis of glycosaminoglycans(GAG) and local oxygen concentration in a polyglycolic acid (PGA) scaffold seeded with bovine chondrocytes. The oxygen concentration and GAG were modelled by using a simple diffusion equation,

$$\frac{\partial S_i}{\partial t} = D_i \nabla^2 S_i - Q_i, \quad (1.6.1)$$

where species 1 and 2 represents O_2 and GAG respectively, S_i is the concentration and D_i is the diffusion of each species. Q_i is consumption of O_2 and G. The Q_{O_2} is modelled by Michaelis Menton kinetics and Q_G is modelled as follows,

$$Q_G = N_G \cdot k_G \left(1 - \frac{S_G}{S_\infty} \right) S_{O_2}, \quad (1.6.2)$$

where N is the cell density, k_G represents the rate of GAG synthesis and S_∞ is the maximum GAG concentration. Calculated GAG concentrations were qualitatively and quantitatively consistent with experimental data. They concluded that the spatial variation of oxygen concentration gives heterogeneities in the GAG concentration.

Several mathematical models for cellular proliferation and the diffusion of oxygen inside a scaffold, where the cells are distributed uniformly or non uniformly, were discussed by Galban and Locke (1997). They used the volume averaging method to derive an average reaction diffusion equation for the nutrient concentration in a two phase system (cellular and void). In the volume averaging method the total amount of a quantity (say cell or nutrient concentration) of certain volume is averaged over the entire volume. They also determined the effective diffusion coefficient and reaction rate as a function of local cell volume fraction and local cell volume fraction is determined as a function of time by using the suitable mass balance equation. Particular attention was paid to the diffusion coefficient, which was taken to change by an order of magnitude between regions full of cells and those without, but in this work cell motility is neglected.

Malda et al. (2004b) developed a mathematical model of the oxygen gradient in the absence of perfusion. They used the simple diffusion equation to model the concentration of oxygen in the scaffold. They identified the oxygen gradient in the tissue engineering construct and predicted the oxygen profiles during the *in vitro* culture. The oxygen consumption rate is modelled by Monod kinetics (see appendix D for details). They

found that oxygen gradients occur inside the construct, due to slow diffusion of oxygen and consumption of oxygen by cells. These gradients are higher in the regions of high cell concentration. However this model did not account for the cell proliferation.

Lewis et al. (2005) developed a model of the spatial and temporal distribution of oxygen concentration and cell proliferation and compared the results with the experimental data of Malda et al. (2004b). They considered the cell proliferation rate as a linear function of nutrient concentration and cell number density. The oxygen consumption rate was assumed to be proportional to cell proliferation rate. They found that for the first 14 days the behaviour can be explained well with the mathematical model. They concluded that the cells which only depend on diffusion for the supply of oxygen produce a proliferation dominated region at the scaffold edge closest to the oxygen source, which decreases in thickness as time progresses. They considered only diffusion for the transport of oxygen to the cells.

Croll et al. (2005) developed a model of oxygen diffusion and cell growth during the early stages of implantation in a dome-shaped PLGA scaffold. The cell's oxygen consumption was described by Monod's model. They described the effective diffusivity by Maxwell's equation for porous media. Croll et al. (2005) concluded that a homogeneous cell density seeding strategy, even with moving oxygen source provided via vascularization (formation of vessels, especially blood vessels), gives rise to hypoxic (deficiency in the amount of oxygen reaching body tissues) conditions in some regions of the scaffold for an unacceptable period of time. They proposed that heterogeneous seeding strategy is better than the homogeneous seeding for large scale tissue engineering. In heterogeneous seeding a small amount of native tissue is placed near the blood supply for the implantation of a large scaffold.

Landman and Cai (2007) extended the work of Croll et al. (2005) and Lewis et al. (2005). They developed and investigated a one dimensional model of oxygen concentration, cell proliferation and cell migration inside a scaffold in which the arteriovenous loop is placed inside a scaffold, in order to form a vascularizing network within a scaffold. The cell proliferation rate is described by Heaviside step function $H(C - C_h)$, where C_h is the minimum concentration required for the cells to survive. They considered the additional effects of vascular growth, homogeneous and heterogeneous seeding, diffusion of cells and critical hypoxic oxygen concentration.

In all the models discussed above the the transport of nutrients is only by diffusion. This transport mechanism is useful when the thickness of tissue is less than the few millimeters. However for soft tissue engineering when the size of the tissue is large

then the supply of nutrients is limited to the exterior of the scaffold and cells in the internal regions of the scaffold become hypoxic very quickly. One way to overcome the diffusion limitations is to exploit advective transport. A mathematical model of nutrient concentration and cell proliferation inside a scaffold is an important tool for assessing and planning tissue engineering outcomes. Several authors have developed a number of mathematical models to study the fluid dynamics and nutrient distribution in the perfusion bioreactor.

Coletti et al. (2006) developed a comprehensive mathematical model of convection and diffusion in a perfusion bioreactor. The fluid dynamics of the medium flow inside the bioreactor is described through the Navier-Stokes equations for incompressible fluid while convection through the scaffold is modeled by Brinkmans extension to Darcy's Law for porous materials. The nutrient uptake rate is described by Michaelis Menton kinetics and cell growth is modeled as a function of nutrient concentration through the Contois equation, accounting for contact inhibition.

Chung et al. (2007) developed a mathematical model to investigate the cell growth, nutrient uptake and culture medium circulation within a porous scaffold under direct perfusion. They proposed a three layer model consisting of porous scaffold sandwiched between two fluid layers. The nutrient uptake rate was described by Michaelis Menton kinetics and cell growth was described by the modified Contois function. The fluid flow outside the cell scaffold construct was modeled by the Navier-Stokes equation while the fluid dynamics within the cell scaffold construct is modeled by the Brinkmann equation for porous media. To examine the media perfusion they also included time dependent porosity and permeability changes due to the cell growth. They concluded that cell growth can be enhanced by media perfusion. In addition to enhancement of cell growth perfusion also gives more uniform spatially distributed cells as compared to static culture. In a subsequent model Chung et al. (2008) proposed a compact single layer model consisting of only scaffold construct. They studied the cell growth and nutrient distribution and compared the results with the three layer model. They found that the single layer model predicts the cell growth and nutrient distribution as accurately as the three layer model (Chung et al., 2007) developed earlier.

To improve the delivery of nutrients and removal of waste products (lactate acid and carbon dioxide) a fluid known as the culture medium is forced through the pores of the scaffold. For tissue with the thickness of few millimeters these method are successful compared to static culture (Cartmell et al., 2003, Glowacki et al., 1998). Perfusion bioreactors have been used to develop a variety of tissue types. For small tissue types

direct perfusion techniques are shown to be successful however the problem arises when tissue size is large. Forcing the fluid through the pores of the scaffold alone is not sufficient for the transport of nutrients throughout the construct. In order to deliver the nutrients and remove waste from the centre of the construct in addition to perfusion of the medium through the scaffold two porous biodegradable polyglycolic acid (PLGA) fibres can also be incorporated into the scaffold. These fibres deliver the nutrients to the interior regions of the scaffold. Whittaker et al. (2009) in a Mathematical medicine study group meeting (MMSG 2006) studied the problem of delivery of nutrients to, and removal of waste product from the interior region of the scaffold. They developed a mathematical model to study this problem. But they did not study the oxygen concentration profiles and cell growth in this model.

A weakness of the above models is that they did not consider the multiphase nature of tissue growth. These models neither address the mechanical forces generated in the tissue as a result of tissue growth nor do these models include the possibility of cell migration (except Landman and Cai (2007)) through the scaffold. Obradovic et al. (2000) and Lewis et al. (2005) modelled the tissue as a homogeneous mass, however, tissue is a composite material formed of a "collection of cells and ECM" (Cowin, 2000) as well as accompanying fluid. In many biological systems there is a complex interaction between these materials. The tissue composition may change over time due to mitosis, necrosis and apoptosis (Lemon et al., 2006). A multiphase model is one in which each phase (*e.g.* cells, fluid, and ECM) are considered as a separate phase with constitutive laws describing its material properties and interaction with neighbouring phase.

Lemon et al. (2006) developed a general multiphase model, consisting of an arbitrary number of phases, of *in vitro* tissue growth using multiphase porous flow mixture theory. The model consists of mass and force balance equations for each tissue component, together with appropriate relations defining the material deformation in response to stresses. They considered the intraphase (cell-cell interaction) and interphase pressures (cell-scaffold interactions) and gave their appropriate forms. They used a linear stability technique to analyze the dynamics of different phases in the tissue and considered the mechanical forces acting between the different phases of the tissue.

In a subsequent paper Lemon and King (2007) presented a comprehensive multiphase model of nutrient limited engineered tissue growth and examined the multiphase nature of tissue mechanics and nutrient transport. They presented a three phase case of motile cells, water and scaffold. They considered two idealized seeding techniques, static seeding and dynamic seeding and used the multiphase model for *in vitro* tissue

growth developed by Lemon et al. (2006) to analyze the growth processes as a result of the above two seeding techniques. They also compared the theoretical results with experimental data of Malda et al. (2004b) for chondrocytes seeded onto a scaffold.

Byrne and Preziosi (2003) developed a two-phase model (cell and liquid phase) of avascular tumour to investigate the influence of the cells environment on their proliferative rate in the context of tumour growth. The proliferation of tumour was dependent on the nutrient concentration and cell density. The main features of the model include the dependence of proliferation rate on cellular stress and incorporation of mass exchange between the solid and fluid phase. They found that as the value of the parameter which measures the reduction in cell proliferation due to cell stress, crosses the critical value the tumour is eliminated.

O'Dea et al. (2008) developed a mathematical model of tissue growth in a perfusion bioreactor and analyzed the effect of an imposed flow and mechanotransduction (mechanics by which forces are converted into biochemical signals). They used the multiphase formulation of Lemon et al. (2006) restricted to two phases (cell population and culture medium) and examined the mechanical forces acting on the tissue and subsequent morphology of tissue. They also considered the complex interaction involved in the tissue without considering the precise microscopic details. Later the authors extended their model to include the third phase as the porous scaffold (O'Dea et al., 2010). The inclusion of third phase allowed the interaction between the cells and porous scaffold. They observed a different cell behaviour depending upon the relative importance of cell aggregation and repulsion. They also studied the mechanotransduction effects due to cell density, pressure and fluid shear stress on tissue growth. All of these multiphase models described above model the macroscopic effects of the microscopic processes using the constitutive laws.

Waters et al. (2006) developed mathematical models to investigate the morphology of tissue construct formed from single-cell suspension in culture media, within a rotating bioreactor. They modelled the construct as a viscous fluid drop surrounded by an extensible membrane in a viscous fluid. The viscous drop is assumed to be more dense than the surrounding fluid. They considered both thin-disk and slender-pipe bioreactors and obtained a series of spatially 2-D problems. They found that construct morphology is the result of mechanical forces it experiences and the instability is driven by the density difference between two fluids. They also studied the effects of rotation, gravitational field, material and geometrical properties on the stability.

In this thesis we have developed a mathematical model of cell growth and nutrient

transport in a perfusion bioreactor. The nutrients are delivered to the cells by two mechanisms advection and diffusion. The cells grow according to a logistic law and spread in the domain via diffusion. The model includes the key features of tissue engineering processes such as fluid flow, nutrient transport, cell growth, porosity and permeability changes due to cell growth and effect of mechanical forces such as fluid shear stress on cell growth and nutrient consumption rates. We include non-linear cell diffusion in our model while none of the models discussed above have considered non-linear cell diffusion. The model is sensitive to choice of initial seeding strategy and initial porosity of the scaffold thus we can consider various initial seeding and initial porosity functions. We also maintain the constant volumetric flow rate in our model.

1.7 Objective of thesis and structure

The main objective of this study is to develop a mathematical model of fluid flow, nutrient concentration and cell growth in a perfusion bioreactor. One of the challenges tissue engineering currently faces is the delivery of nutrients into the internal region of the construct. Cells near the nutrient source grow quickly due to high concentration of nutrients and cells away from the nutrient source grow slowly due to lack of nutrient concentration. Our aim is to develop a mathematical model which can predict the initial conditions required for a uniform cell distribution in the final construct. This may be achieved by improving the delivery of nutrients in the internal region of the scaffold.

Mathematical modelling of fluid flow through a porous material is presented in Chapter 2. Darcy's law governs the flow of fluid through the porous material. We assume that the permeability of the scaffold is spatially varying. We employ both numerical and analytical techniques to find the solution of governing equations. Analytic results are presented for particular choices of permeability for which the solution exists but numerical results are presented for more general choices of permeability. We present comparisons of the numerical and analytical results.

In Chapter 3 we present a simple coupled model of fluid flow, nutrient concentration and cell growth in the perfusion bioreactor. We assume that permeability of the scaffold depends on the spatial coordinates and also on the cell density. We model the permeability by an exponential function of cell density and spatial coordinates. The fluid flow through the porous scaffold is governed by Darcy's law. Nutrients are delivered to the cells by two mechanisms *i.e.* diffusion and advection, and the advection-

diffusion equation is used to model the delivery of nutrients. The growth of cells is modelled by a reaction-diffusion equation. The solution of the flow equation gives the flow field which is substituted into the advection diffusion equation to obtain the nutrient concentration which is further substituted into the cell growth equation to obtain the cell density. We update the cell density in the permeability equation and solve the entire system again for updated cell density. This process continues until system gets close to steady state. The model is solved numerically by finite element solver COMSOL. To validate the numerical results we solve the model analytically subject to some simplifying assumptions. We compare analytic and numerical results and find excellent agreement. We also check the stability of steady state solution numerically and analytically.

In Chapter 4 we model the cell growth with non-linear diffusion. The Fisher equation governs the cell growth with non-linear diffusion. We investigate travelling wave solutions and use phase plane analysis to find the minimum wave speed of the growth front. We conclude that when the diffusion is linear or weakly non-linear the travelling wave moves with minimum wave speed but in the case of highly non-linear diffusion the wave speed increases with increasing non-linearity.

In Chapter 5 we further extend the model presented in the Chapter 3 to accommodate non-linear cell diffusion, mechanical stimuli in the form of shear stress induced by the fluid and also we maintain a constant volumetric flow rate. In this model we assume that the permeability of the scaffold is a function of porosity, and porosity is the function of cell density and spatial coordinates. We use the same steps as discussed in Chapter 3 to solve the coupled system.

In Chapter 6 we present the results for different initial seeding strategies and initial porosity. Employing a numerical method we conclude that the total cell density in the scaffold depends on the initial seeding strategy and initial porosity of the scaffold. By keeping the initial porosity constant and examining various initial seeding strategies we conclude that when a layer of cell is placed away from the nutrient source then it spreads in the entire scaffold uniformly and we get a highest total cell density by using this initial seeding technique. By keeping the initial seeding uniform and examining different initial porosities we find that if we put three parallel tubes of high porosity in the scaffold then nutrients will reach to the internal regions of the scaffold and we get a largest cell yield.

In Chapter 7 we summarize the main conclusions of the thesis and we outline possible extensions of the model.

Flow in porous materials

2.1 Introduction

To model the flow of fluid through the porous material, we must define suitable parameters which characterize the material's structure and properties of the fluid. The two important parameters for the porous material are the dimensionless porosity ϕ (ratio of empty to filled space in the material) and the permeability k^* (ability of porous material to transmit fluid through its pores) of the material. Stars are used to denote the dimensional quantities throughout. For an inhomogeneous material porosity ϕ may depend on both space and time. The permeability k^* depends upon the porosity and geometric properties of the material. The permeability is often estimated using the Kozeny equation (Bear, 1988),

$$k^* = \frac{\epsilon^{*2}\phi^3}{180(1-\phi)^2}, \quad (2.1.1)$$

where ϵ^{*2} is the mean pore diameter. The two important parameters for the fluid are dynamic viscosity μ^* and effective viscosity $\bar{\mu}^*$. Dynamic viscosity μ^* measures the fluid resistance to flow. It is the ratio of the shear stress exerted on the surface of the fluid to the velocity gradient. Effective viscosity $\bar{\mu}^*$ is a function of dynamic viscosity μ^* and the material structure. $\bar{\mu}^*$ may differ from μ^* and is likely to depend upon the tortuosity (a twisted path) of the medium. For a dilute suspension of particles $\bar{\mu}^*$ is approximated by Einstein's law $\bar{\mu}^* = \mu^*(1 + 2.5\phi)$ (Brinkman, 1949, Goyeau et al., 2003). For a more dense suspension $\bar{\mu}^*$ is approximated by $\bar{\mu}^* = \mu^*(1 - 2.5\phi)$ (Goyeau et al., 2003).

In 1856 Henry Darcy derived an empirical law known as Darcy's law, that relates the velocity of fluid through a porous material to the pressure drop across it. The law

was formulated on the basis of the results of experiments on the flow of water through beds of sand. In the absence of gravitational forces, the Darcy's law commonly used in modern texts is

$$\mathbf{u}^* = -\frac{k^*}{\mu^*} \nabla^* p^*, \quad (2.1.2)$$

where \mathbf{u}^* is the mean velocity and not the true velocity of the fluid. Equation (2.1.2) is a modified version of Darcy's law. It is also known as "Hazen-Darcy equation"; because in the original Darcy's law the effect of viscosity was neglected. However modern texts refer to this as Darcy's law (Bear, 1988, Bear and Buchlin, 1991). Equation (2.1.2) is valid only when flow is incompressible and a Newtonian fluid flows through an isotropic, homogeneous porous material at low Reynolds number. The effect of inertial forces and viscous shear stresses, caused by the interaction between fluid and porous medium, on the flow is neglected. The retention of only the damping force due to porous material, $\mu^* \mathbf{u}^* / k^*$, is a good approximation for small k^* ; however it breaks down as k^* becomes large (Brinkman, 1949).

Brinkman (1949) addressed the limitation of large k^* and considered the viscous forces exerted by the fluid flowing through the porous material having large permeability. For high porosity porous media the Darcy-Brinkman equation is a governing equation with an extra viscous term known as Brinkman term added to the Darcy equation,

$$-\nabla^* p^* + \bar{\mu}^* \nabla^{*2} \mathbf{u}^* = \frac{\mu^*}{k^*} \mathbf{u}^*, \quad (2.1.3)$$

where \mathbf{u}^* is the mean velocity and $\bar{\mu}^*$ is the effective viscosity. Equations (2.1.2) and (2.1.3) are the most widely used equations in modelling the flow of fluid through the porous media.

In this Chapter we study the flow of a Newtonian fluid through a 2-D porous material. We use the simple Darcy's law given by equation (2.1.2) to model the flow of fluid through the porous material. We assume that the permeability k^* of the porous material is a function of spatial coordinates. Fluid enters into the porous material with a certain velocity from one end and leaves it from the other end with certain velocity. Inlet and outlet velocities may differ but total inflow and outflow fluxes are the same. Results are presented for different choices of permeability k^* and inlet and outlet velocities. We see that the Darcy's law can be solved numerically for any choice of permeability k^* but analytically it is not possible to solve Darcy's law for every choice of permeability k^* . Analytic and numerical results are compared for particular choices of permeability k^* .

2.2 Geometry and governing equations

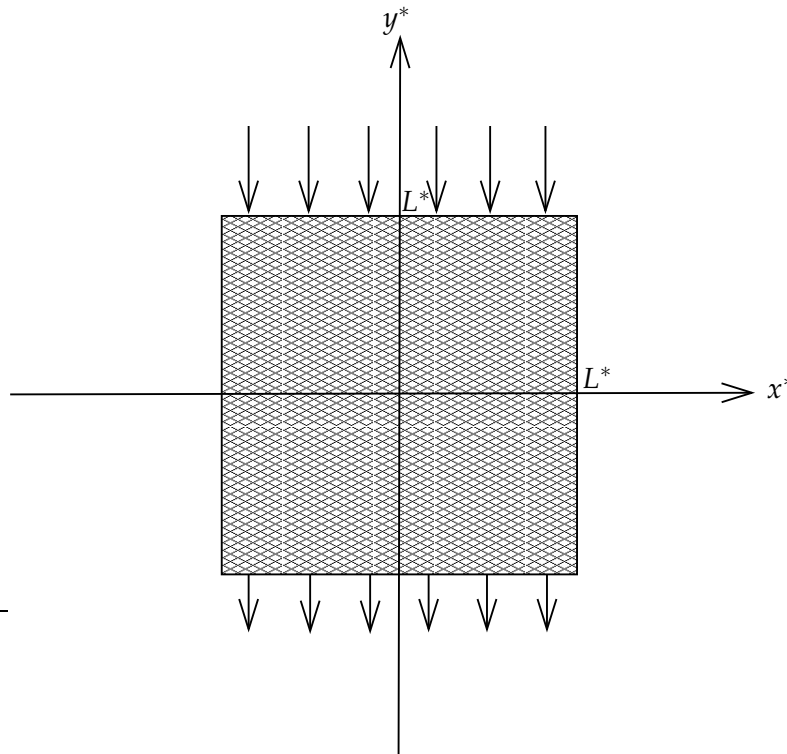


Figure 2.1: Reference geometry. Flow of fluid through a porous material. Fluid is pumped in at the boundary $y^* = L^*$ and pumped out at $y^* = -L^*$. No fluid flux through the boundaries $x^* = \pm L^*$.

Let us consider a Cartesian coordinate system (x^*, y^*) aligned with the porous material of length $2L^*$ and width $2L^*$. We assume that the permeability k^* of the porous material is spatially varying so that

$$k^* = k^*(x^*, y^*). \quad (2.2.1)$$

We also assume that flow is incompressible and a Newtonian fluid is flowing through the porous material. Fluid velocities are assumed to be sufficiently small that inertia can be neglected. Fluid is pumped into the porous material at the boundary $y^* = L^*$ and drawn out of the porous material at the boundary $y^* = -L^*$ as shown in Figure 2.1. If the scaffold has a large number of pores and the fluid velocity in the pores is not very high then the pore Reynolds number is not too large. For low Reynolds number we can use Darcy's law to model the flow of fluid through the porous scaffold (Batchelor, 2000, Bear, 1988). Darcy's law relates the Darcy velocity \mathbf{u}^* to the interstitial pressure

p^* . The Darcy velocity is the average of the interstitial velocity, taken over the entire volume that includes solid scaffold and pore network. The interstitial pressure is the average fluid pressure in the pores of the scaffold. We write

$$\mathbf{u}^* = -\frac{k^*(x^*, y^*)}{\mu^*} \nabla^* p^*, \quad (2.2.2)$$

where μ^* is the dynamic viscosity of the fluid. The continuity equation is

$$\nabla^* \cdot \mathbf{u}^* = 0. \quad (2.2.3)$$

We assume that no fluid is flowing through the boundaries at $x^* = \pm L^*$. Mathematically we write

$$\mathbf{u}^* \cdot \hat{\mathbf{n}} = 0 \quad \text{at } x^* = \pm L^*, \quad -L^* \leq y^* \leq L^*. \quad (2.2.4)$$

Fluid is pumped into the porous material with velocity $f^*(x^*)$ at the boundary $y^* = L^*$ and leaves the porous material with velocity $g^*(x^*)$ from the boundary $y^* = -L^*$. Mathematically we write

$$\mathbf{u}^* \cdot \hat{\mathbf{n}} = -f^*(x^*) \quad \text{at } y^* = L^*, \quad -L^* \leq x^* \leq L^*, \quad (2.2.5)$$

$$\mathbf{u}^* \cdot \hat{\mathbf{n}} = g^*(x^*) \quad \text{at } y^* = -L^*, \quad -L^* \leq x^* \leq L^*, \quad (2.2.6)$$

where $\hat{\mathbf{n}}$ is the outward unit normal vector, $f^*(x^*)$ and $g^*(x^*)$ are the fluid velocities at the inlet boundary $y^* = L^*$ and the outlet boundary $y^* = -L^*$ respectively. Also

$$\int_{-L^*}^{L^*} f(x^*) dx^* = \int_{-L^*}^{L^*} g(x^*) dx^*$$

i.e. inflow and outflow fluxes are the same.

2.3 Nondimensionalization

We nondimensionalize all lengths with L^* and permeability with respect to a typical permeability k_c^* , so that

$$x^* = L^* x, \quad y^* = L^* y, \quad \nabla^* = \frac{1}{L^*} \nabla, \quad (2.3.1)$$

$$k^*(x^*, y^*) = k_c^* k(x, y). \quad (2.3.2)$$

We nondimensionalize velocity and pressure as follows

$$\mathbf{u}^* = f_{max}^* u, \quad p^* = \frac{\mu^* f_{max}^* L^*}{k_c^*} p, \quad (2.3.3)$$

$$f^*(x^*) = f_{max}^* f(x), \quad g^*(x^*) = f_{max}^* g(x), \quad (2.3.4)$$

where f_{max}^* is the maximum value of the prescribed inlet velocity. Darcy's law and the continuity equation can then be written in dimensionless form as

$$\mathbf{u} = -k(x, y) \nabla p, \quad (2.3.5)$$

$$\nabla \cdot \mathbf{u} = 0. \quad (2.3.6)$$

Substituting equation (2.3.5) into the continuity equation (2.3.6) we get

$$\nabla \cdot (k(x, y) \nabla p) = 0. \quad (2.3.7)$$

Solution for p always include a constant. The dimensionless boundary conditions are

$$\hat{\mathbf{n}} \cdot \nabla p = 0 \quad \text{at} \quad x = \pm 1, \quad -1 \leq y \leq 1, \quad (2.3.8)$$

$$k(x, y) \hat{\mathbf{n}} \cdot \nabla p = f(x) \quad \text{at} \quad y = 1, \quad -1 \leq x \leq 1, \quad (2.3.9)$$

$$k(x, y) \hat{\mathbf{n}} \cdot \nabla p = -g(x) \quad \text{at} \quad y = -1, \quad -1 \leq x \leq 1. \quad (2.3.10)$$

2.4 Permeability distribution

In equation (2.3.7) the permeability $k(x, y)$ of porous material can be any function of spatial coordinates. For simplicity and convenience we assume that $k(x, y)$ is separable *i.e.*

$$k(x, y) = k_1(x)k_2(y), \quad (2.4.1)$$

which allows us to seek a separable solution of the form

$$p(x, y) = X(x)Y(y). \quad (2.4.2)$$

Substituting assumptions (2.4.1) and (2.4.2) into equation (2.3.7) and rearranging the terms, we get

$$\frac{1}{X(x)k_1(x)} \left[k_1(x) \frac{d^2 X(x)}{dx^2} + \frac{dk_1(x)}{dx} \frac{dX(x)}{dx} \right] = -\frac{1}{Y(y)k_2(y)} \left[k_2(y) \frac{d^2 Y(y)}{dy^2} + \frac{dk_2(y)}{dy} \frac{dY(y)}{dy} \right]. \quad (2.4.3)$$

The left hand side of (2.4.3) is a function of x only and right hand side is a function of y only. This is possible only when both sides are equal to a constant. We suppose that the constant is given by $-\lambda_n^2$, and the corresponding solutions for $X(x)$ and $Y(y)$ are given by $X_n(x)$ and $Y_n(y)$ (where n is an integer). Then we have

$$\frac{1}{X_n(x)k_1(x)} \left[k_1(x) \frac{d^2 X_n(x)}{dx^2} + \frac{dk_1(x)}{dx} \frac{dX_n(x)}{dx} \right] = -\lambda_n^2, \quad (2.4.4)$$

$$-\frac{1}{Y_n(y)k_2(y)} \left[k_2(y) \frac{d^2 Y_n(y)}{dy^2} + \frac{dk_2(y)}{dy} \frac{dY_n(y)}{dy} \right] = -\lambda_n^2, \quad (2.4.5)$$

which may be rewritten in the form

$$k_1(x) \frac{d^2 X_n(x)}{dx^2} + \frac{dk_1(x)}{dx} \frac{dX_n(x)}{dx} + k_1(x) \lambda_n^2 X_n(x) = 0, \quad (2.4.6)$$

$$k_2(y) \frac{d^2 Y_n(y)}{dy^2} + \frac{dk_2(y)}{dy} \frac{dY_n(y)}{dy} - k_2(y) \lambda_n^2 Y_n(y) = 0. \quad (2.4.7)$$

We solve equation (2.4.6) subject to boundary conditions (2.3.8) which can be written as,

$$\frac{dX_n}{dx} = 0 \quad \text{at} \quad x = \pm 1. \quad (2.4.8)$$

Since boundary conditions are equal to zero so this is an eigenvalue problem. Solution of equation (2.4.6) gives the eigenvalues $-\lambda_n^2$ and eigenfunctions $X_n(x)$.

Orthogonality of eigenfunctions

Equation (2.4.6) can be rewritten in the form

$$\frac{d}{dx} \left[k_1(x) \frac{dX_n(x)}{dx} \right] + \lambda_n^2 k_1(x) X_n(x) = 0. \quad (2.4.9)$$

Multiplying (2.4.9) by $X_m(x)$ and integrating with respect to x between -1 and 1 we get

$$\int_{-1}^1 k_1(x)X_n(x)X_m(x)dx = 0, \quad \text{when } m \neq n. \quad (2.4.10)$$

Equation (2.4.10) is the orthogonality condition for the eigenfunctions. Integrating equation (2.4.9) with respect to x between -1 and 1 gives

$$\int_{-1}^1 k_1(x)X_n(x)dx = 0. \quad (2.4.11)$$

From the solution of (2.4.6) and (2.4.7) we get the functions $X_n(x)$ and $Y_n(y)$. Then using these functions in equation (2.4.2) we can find the pressure p .

In the next Section we will formulate a numerical method for general $k_1(x)$ and $k_2(y)$ to solve equations (2.4.6) and (2.4.7). Note that it is not possible to solve these equations analytically for every choice of functions $k_1(x)$ and $k_2(y)$. In Section 2.6 we will present an analytical solution of equations (2.4.6) and (2.4.7) for some suitable functions $k_1(x)$ and $k_2(y)$ for which analytical solution exists. In Section 2.7 we will compare numerical and analytical results.

2.5 Numerical solution

In this Section we solve equations (2.4.6) and (2.4.7) numerically for functions $k_1(x)$ and $k_2(y)$. Let us consider the two different cases of λ_n , *i.e.* $\lambda_n = 0$ and $\lambda_n \neq 0$.

2.5.1 Case I: $\lambda_n = 0$

Since $\lambda_n = 0$ corresponds to only one solution so we replace $X_n(x)$ and $Y_n(y)$ in equation (2.4.6) and (2.4.7) by $X(x)$ and $Y(y)$. For $\lambda_n = 0$ equation (2.4.6) reduces to the form

$$\frac{d}{dx} \left[k_1(x) \frac{dX(x)}{dx} \right] = 0,$$

whose solution subject to boundary conditions (2.4.8) is given by

$$X(x) = b,$$

where b is an arbitrary constant. Similarly for $\lambda_n = 0$ equation (2.4.7) reduces to the form

$$\frac{d}{dy} \left[k_2(y) \frac{dY(y)}{dy} \right] = 0,$$

whose general solution is

$$Y(y) = c \int_{-1}^y \frac{1}{k_2(\tilde{y})} d\tilde{y} + d,$$

where c and d are constants. Substituting values of $X(x)$ and $Y(y)$ into equation (2.4.2) we obtain,

$$p = a_0 \int_{-1}^y \frac{1}{k_2(\tilde{y})} d\tilde{y} + b_0,$$

where $a_0 = bc$ and $b_0 = bd$ are arbitrary constants.

2.5.2 Case II : $\lambda_n \neq 0$

2.5.2.1 Solution of X dependent equation

Dividing each term of equation (2.4.6) by $k_1(x)$ we get

$$X_n''(x) + \frac{k_1'(x)}{k_1(x)} X_n'(x) + \lambda_n^2 X_n(x) = 0, \quad (2.5.1)$$

where primes denote differentiation with respect to x . We solve equation (2.5.1) subject to boundary conditions (2.4.8), by using a finite difference method. Finite difference approximations for $X_n''(x)$ and $X_n'(x)$ are given by

$$X_n''(x) = \frac{X_n^{(m-1)} - 2X_n^m + X_n^{(m+1)}}{h^2} + O(h^2), \quad (2.5.2)$$

$$X_n'(x) = \frac{X_n^{m+1} - X_n^{m-1}}{2h} + O(h^2), \quad (2.5.3)$$

where X_n^m denotes the value of $X_n(x)$ at $x_m = x_0 + mh$, ($m = 0, 1, 2, \dots, N_g - 1$), $x_0 = -1$, $x_{N_g-1} = 1$ and h is the step size which is given by

$$h = \frac{2}{N_g - 1}.$$

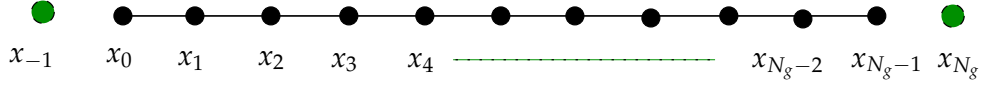


Figure 2.2: Discretization of interval $x_0 \leq x \leq x_{N_g-1}$. x_{-1} and x_{N_g} are ghost points.

N_g is the total number of grid points. Substituting these approximations into equation (2.5.1) gives a linear system of equations.

$$\left[\frac{1}{h^2} - \frac{1}{2h} \frac{k_1'(x)}{k_1(x)} \right] X_n^{(m-1)} + \left[\lambda_n^2 - \frac{2}{h^2} \right] X_n^m + \left[\frac{1}{h^2} + \frac{1}{2h} \frac{k_1'(x)}{k_1(x)} \right] X_n^{(m+1)} = 0. \quad (2.5.4)$$

This holds at each grid point except the boundaries $x = -1$ and $x = 1$. So these are $(N_g - 2)$ equations.

At the boundaries $x = -1$ and $x = 1$ we have Neumann boundary conditions. To deal with this type of boundary condition we introduce the new points x_{-1} and x_{N_g} , which by virtue of their being outside the domain of problem, are called a ghost points as shown in the Figure 2.2. At the boundaries $x = -1$ and $x = 1$ for Neumann boundary conditions we use equation (2.5.3).

At $x = -1$ we have

$$\frac{X_n^1 - X_n^{-1}}{2h} = 0 \Rightarrow X_n^1 = X_n^{-1} \quad (2.5.5)$$

At $x = 1$ we have

$$\frac{X_n^{N_g} - X_n^{N_g-2}}{2h} = 0 \Rightarrow X_n^{N_g} = X_n^{N_g-2} \quad (2.5.6)$$

At the boundaries $x = -1$, and $x = 1$ we need to evaluate X_n^{-1} and $X_n^{N_g}$ respectively. Substituting $m = 0$ and $m = N_g - 1$ in equation (2.5.4) respectively, and using equations (2.5.5) and (2.5.6) we get two more linear equations,

$$\left[\lambda_n^2 - \frac{2}{h^2} \right] X_n^{(0)} + \frac{2}{h^2} X_n^{(1)} = 0, \quad (2.5.7)$$

$$\frac{2}{h^2} X_n^{(N_g-2)} + \left[\lambda_n^2 - \frac{2}{h^2} \right] X_n^{(N_g-1)} = 0. \quad (2.5.8)$$

So we have in total N_g linear equations which can be written in matrix form as

$$(A + \lambda_n^2 I) \mathbf{X}_n(x) = 0 \quad (2.5.9)$$

where

$$A = \begin{pmatrix} Q & -Q & 0 & 0 & 0 & \cdots & \cdots & \cdots & \cdots & 0 \\ M_1 & Q & R_1 & 0 & 0 & \cdots & \cdots & \cdots & \cdots & 0 \\ 0 & M_2 & Q & R_2 & 0 & \cdots & \cdots & \cdots & \cdots & 0 \\ 0 & 0 & M_3 & Q & R_3 & \cdots & \cdots & \cdots & \cdots & \cdots \\ \vdots & \vdots & \vdots & \ddots & \ddots & \ddots & \vdots & \vdots & \vdots & \vdots \\ \vdots & \vdots & \vdots & \vdots & \ddots & \ddots & \ddots & \vdots & \vdots & \vdots \\ \vdots & \vdots & \vdots & \vdots & \vdots & \ddots & \ddots & \ddots & \vdots & \vdots \\ \vdots & \vdots & \vdots & \vdots & \vdots & \vdots & M_{N_g-3} & Q & R_{N_g-3} & 0 \\ 0 & 0 & \cdots & \cdots & \cdots & 0 & 0 & M_{N_g-2} & Q & R_{N_g-2} \\ 0 & 0 & \cdots & \cdots & \cdots & 0 & 0 & 0 & -Q & Q \end{pmatrix}, \quad (2.5.10)$$

is an $(N_g \times N_g)$ matrix and I is an $(N_g \times N_g)$ unit matrix. Also

$$Q = -\frac{2}{h^2}, \quad M_m = \frac{1}{h^2} - \frac{k'_1(x_m)}{k_1(x_m)} \frac{1}{2h},$$

$$R_m = \frac{1}{h^2} + \frac{k'_1(x_m)}{k_1(x_m)} \frac{1}{2h}, \quad \text{where } m = 1, 2, \dots, N_g - 2$$

To find eigenvalues $-\lambda_n^2$ we solve

$$\det(A + \lambda_n^2 I) = 0,$$

and the corresponding eigenfunctions $X_n(x)$ can be found by substituting the values of $-\lambda_n^2$ into the equation (2.5.9).

2.5.2.2 Solution of Y dependent equation

Dividing equation (2.4.7) throughout by $k_2(y)$ we get

$$Y_n''(y) + \frac{k'_2(y)}{k_2(y)} Y_n'(y) - \lambda_n^2 Y_n(y) = 0, \quad (2.5.11)$$

where primes denote the differentiation with respect to y . The above equation is a second-order ordinary differential equation and will have two linearly independent solutions $Y_{n1}(y)$ and $Y_{n2}(y)$. Any linear combinations of these solutions is also a solution of equation (2.5.11). We need to evaluate two linearly independent solutions $Y_{n1}(y)$ and $Y_{n2}(y)$.

Solution $Y_{n1}(\mathbf{y})$

To find a solution $Y_{n1}(y)$ of the equation (2.5.11) we impose temporary boundary conditions

$$Y'_{n1}(1) = 1, \quad Y'_{n1}(-1) = 0, \quad (2.5.12)$$

Using finite difference approximations for $Y''_n(y)$ and $Y'_n(y)$ and boundary conditions (2.5.12) in equation (2.5.11) we get linear system of equations

$$\begin{aligned} \left[\frac{1}{h^2} - \frac{1}{2h} \frac{k'_2(y)}{k_2(y)} \right] Y_n^{(m-1)} + \left[-\lambda_n^2 - \frac{2}{h^2} \right] Y_n^m + \\ \left[\frac{1}{h^2} + \frac{1}{2h} \frac{k'_2(y)}{k_2(y)} \right] Y_n^{m+1} = 0. \end{aligned} \quad (2.5.13)$$

where Y_n^m denotes the value of $Y_n(y)$ at $y_m = y_0 + mh$, ($m = 0, 1, 2, \dots, N_g - 1$), $y_0 = -1$, $y_{N_g-1} = 1$ and h is the step size which is given by

$$h = \frac{2}{N_g - 1}.$$

Notice that again at the boundaries $y = -1$ and $y = 1$ we have Neumann boundary conditions. Hence follow the same steps, as we did in the X dependent equation, to find the value of $Y_{n1}(y)$ at the boundaries $y = 1$ and $y = -1$. At the boundaries $y = -1$ and $y = 1$ we get two linear equations given by

$$\left[-\lambda_n^2 - \frac{2}{h^2} \right] Y_n^{(0)} + \frac{2}{h^2} Y_n^{(1)} = 0. \quad (2.5.14)$$

$$\frac{2}{h^2} Y_n^{(N_g-2)} + \left[-\lambda_n^2 - \frac{2}{h^2} \right] Y_n^{(N_g-1)} = -2h \left[\frac{1}{h^2} - \frac{k'_2(1)}{k_2(1)} \frac{1}{2h} \right]. \quad (2.5.15)$$

The linear system of N_g equations can be written in the matrix form as

$$A_1 \mathbf{Y} = \mathbf{C}_1, \quad (2.5.16)$$

where A_1 is an $(N_g \times N_g)$ matrix given by

$$A_1 = \begin{pmatrix} T & \frac{2}{h^2} & 0 & 0 & 0 & \cdots & \cdots & \cdots & \cdots & 0 \\ U_1 & T & V_1 & 0 & 0 & \cdots & \cdots & \cdots & \cdots & 0 \\ 0 & U_2 & T & V_2 & 0 & \cdots & \cdots & \cdots & \cdots & 0 \\ 0 & 0 & U_3 & T & V_3 & \cdots & \cdots & \cdots & \cdots & \cdots \\ \vdots & \vdots & \vdots & \ddots & \ddots & \ddots & \vdots & \vdots & \vdots & \vdots \\ \vdots & \vdots & \vdots & \vdots & \ddots & \ddots & \ddots & \vdots & \vdots & \vdots \\ \vdots & \vdots & \vdots & \vdots & \vdots & \ddots & \ddots & \ddots & \vdots & \vdots \\ \vdots & \vdots & \vdots & \vdots & \vdots & \vdots & U_{N_g-3} & T & V_{N_g-3} & 0 \\ 0 & 0 & \cdots & \cdots & \cdots & 0 & 0 & U_{N_g-2} & T & V_{N_g-2} \\ 0 & 0 & \cdots & \cdots & \cdots & 0 & 0 & 0 & \frac{2}{h^2} & T \end{pmatrix}, \quad (2.5.17)$$

and

$$T = -\frac{2}{h^2} - \lambda_n^2, \quad U_m = \frac{1}{h^2} - \frac{k'_2(y_m)}{k_2(y_m)} \frac{1}{2h},$$

$$V_m = \frac{1}{h^2} + \frac{k'_2(y_m)}{k_2(y_m)} \frac{1}{2h}, \quad \text{where } y_m = y_0 + mh \quad m = 1, 2, \dots, N_g - 2,$$

and C_1 is a $(N_g \times 1)$ column matrix given by

$$C_1 = \begin{pmatrix} 0 \\ 0 \\ 0 \\ \vdots \\ 2h \left[\frac{1}{h^2} - \frac{k'_2(1)}{k_2(1)} \frac{1}{2h} \right] \end{pmatrix}.$$

Solution Y_{n2}

To determine a second solution $Y_{n2}(y)$ of the equation (2.5.11) we impose the boundary conditions

$$Y'_{n2}(1) = 0, \quad Y'_{n2}(-1) = 1. \quad (2.5.18)$$

Using the finite difference approximations for $Y_n''(y)$ and $Y_n'(y)$ and boundary conditions (2.5.18) in equation (2.5.11) we get linear system of N_g equations, which can be written in the matrix form as

$$A_1 \mathbf{Y} = \mathbf{C}_2, \quad (2.5.19)$$

where A_1 is given by the equation (2.5.17), and

$$\mathbf{C}_2 = \begin{pmatrix} -2h \left[\frac{1}{h^2} + \frac{k_2'(-1)}{k_2(-1)} \frac{1}{2h} \right] \\ 0 \\ 0 \\ \vdots \\ 0 \end{pmatrix}.$$

Hence

$$Y_n(y) \approx C_n Y_{n1}(y) + D_n Y_{n2}(y) \quad (2.5.20)$$

We are now in a position to determine the fluid pressure. Substituting the values of $X_n(x)$ and $Y_n(y)$ in equation (2.4.2) we get

$$p \approx a_0 \int_{-1}^y \frac{1}{k_2(\tilde{y})} d\tilde{y} + b_0 + \sum_{n=1}^{\infty} X_n(x) [C_n Y_{n1}(y) + D_n Y_{n2}(y)]. \quad (2.5.21)$$

By applying the boundary conditions (2.3.9) and (2.3.10) and using orthogonality conditions (2.4.10) and (2.4.11) we can find the values of unknowns *i.e.*

$$\begin{aligned} a_0 &\approx \frac{\int_{-1}^1 f(x) dx}{\int_{-1}^1 k_1(x) dx}, \\ C_n &\approx \frac{1}{k_2(1)} \frac{\int_{-1}^1 f(x) X_n(x) dx}{\int_{-1}^1 k_1(x) X_n^2 dx}, \\ D_n &\approx \frac{1}{k_2(-1)} \frac{\int_{-1}^1 g(x) X_n(x) dx}{\int_{-1}^1 k_1(x) X_n^2 dx}. \end{aligned}$$

We approximate the integrals appearing in a_0 , C_n and D_n by using trapezoidal rule. Now the only unknown left is b_0 , which can be calculated by using the condition

$$p(0,0) = 0.$$

Apply this condition on equation (2.5.21) we get

$$b_0 = -a_0 \int_{-1}^0 \frac{1}{k_2(\tilde{y})} d\tilde{y} - \sum_{n=1}^{\infty} X_n(0) [C_n Y_{n1}(0) + D_n Y_{n2}(0)].$$

2.6 Analytical solution

In this Section we will solve equations (2.4.6) and (2.4.7) analytically. To find the analytic solution of equations (2.4.6) and (2.4.7) for general functions $k_1(x)$ and $k_2(y)$ is a difficult task. For simplicity and convenience we consider different forms of functions $k_1(x)$ and $k_2(y)$ for which analytic solution exists.

2.6.1 Case I: Permeability function of two spatial coordinates

We assume that

$$k_1(x) = e^x, \quad \text{and} \quad k_2(y) = e^y.$$

For these values of $k_1(x)$ and $k_2(y)$ equations (2.4.6) and (2.4.7) can be written as

$$\frac{d^2 X_n(x)}{dx^2} + \frac{dX_n(x)}{dx} + \lambda_n^2 X_n(x) = 0, \quad (2.6.1)$$

$$\frac{d^2 Y_n(y)}{dy^2} + \frac{dY_n(y)}{dy} - \lambda_n^2 Y_n(y) = 0. \quad (2.6.2)$$

The solution of (2.6.1) subject to boundary conditions (2.4.8) gives eigenvalues λ_n and eigenfunctions $X_n(x)$. We consider two cases for λ_n .

2.6.1.1 Case I: $\lambda_n = 0$

When $\lambda_n = 0$ the solution of equation (2.6.1) subject to boundary conditions (2.4.8) is

$$X = b.$$

Similarly when $\lambda_n = 0$ equation (2.6.2) reduces to the form

$$\frac{d^2 Y(y)}{dy^2} + \frac{dY(y)}{dy} = 0,$$

whose general solution is

$$Y(y) = ce^{-y} + d.$$

Substituting $X(x)$ and $Y(y)$ in equation (2.4.2) we get

$$p = a_0e^{-y} + b_0.$$

where $a_0 = bc$ and $b_0 = bd$ are arbitrary constants.

2.6.1.2 Case II : $\lambda_n \neq 0$

Solution of X dependent equation

For $\lambda_n \neq 0$ equation (2.6.1) is a second order ordinary differential equation. The general solution of equation (2.6.1) is given by

$$X_n(x) = e^{-x/2} [C_n \cosh(\omega_n x) + D_n \sinh(\omega_n x)], \quad (2.6.3)$$

where

$$\omega_n = \frac{\sqrt{1 - 4\lambda_n^2}}{2}. \quad (2.6.4)$$

Using the boundary conditions (2.4.8) we get two linear equations in C_n and D_n .

$$\left[-\frac{1}{2}C_n + \omega_n D_n \right] \cosh(\omega_n) + \left[-\frac{1}{2}D_n + \omega_n C_n \right] \sinh(\omega_n) = 0, \quad (2.6.5)$$

$$\left[-\frac{1}{2}C_n + \omega_n D_n \right] \cosh(\omega_n) - \left[-\frac{1}{2}D_n + \omega_n C_n \right] \sinh(\omega_n) = 0. \quad (2.6.6)$$

Adding and subtracting these equations gives

$$\left[-\frac{1}{2}C_n + \omega_n D_n \right] \cosh(\omega_n) = 0, \quad (2.6.7)$$

$$\left[-\frac{1}{2}D_n + \omega_n C_n \right] \sinh(\omega_n) = 0. \quad (2.6.8)$$

From equations (2.6.7) if $\cosh(\omega_n) = 0$ then from equation (2.6.8) we must have $-\frac{1}{2}D_n + \omega_n C_n = 0$, which implies that

$$\omega_n = i(2n + 1)\frac{\pi}{2} \quad \text{where } n = \pm 1, \pm 2, \dots \quad \text{and } D_n = 2\omega_n C_n.$$

Hence

$$X_{n1}(x) = C_n e^{-x/2} \left[\cos \left((2n+1) \frac{\pi}{2} x \right) - (2n+1)\pi \sin \left((2n+1) \frac{\pi}{2} x \right) \right]. \quad (2.6.9)$$

From equation (2.6.8) if $\sinh(\omega_n) = 0$ then from equation (2.6.7) we must have $-\frac{1}{2}C_n + \omega_n D_n = 0$, which implies that

$$\omega_n = in\pi, \quad \text{and} \quad C_n = 2\omega_n D_n.$$

Hence

$$X_{n2}(x) = -E_n e^{-x/2} [2n\pi \cos(n\pi x) + \sin(n\pi x)]. \quad (2.6.10)$$

To summarize we can say that

$$\lambda_{n1}^2 = \frac{1}{4} [1 + (2n+1)^2 \pi^2] \quad \text{when} \quad \omega_{n1} = i(2n+1) \frac{\pi}{2}.$$

and

$$\lambda_{n2}^2 = \frac{1}{4} (1 + 4n^2 \pi^2) \quad \text{when} \quad \omega_{n2} = in\pi.$$

where $X_{n1}(x)$ are the eigenfunction corresponding to λ_{n1}^2 and $X_{n2}(x)$ are the eigenfunction corresponding to λ_{n2}^2 .

Solution of Y dependent equation

For $\lambda_n \neq 0$ the general solution of equation (2.6.2) is given by

$$Y_n(y) = e^{-y/2} [A \cosh(v_n y) + B \sinh(v_n y)]. \quad (2.6.11)$$

where

$$v_n = \frac{\sqrt{1 + 4\lambda_n^2}}{2} \quad (2.6.12)$$

Since equation (2.6.2) is a second order ordinary differential equation, we need two linearly independent solutions $Y_{n1}(y)$ and $Y_{n2}(y)$. We apply two sets of temporary boundary conditions to find the two linearly independent solutions $Y_{n1}(y)$ and $Y_{n2}(y)$.

Solution $Y_{n1}(y)$

For solution $Y_{n1}(y)$ of the equation (2.6.2) we impose boundary conditions (2.5.12). The solution of equation (2.6.2) subject to boundary conditions (2.5.12) is

$$Y_{n1}(y) = \frac{e^{-y/2}e^{1/2}}{4v_n^2 - 1} \left[\left(\frac{2v_n}{\sinh v_n} + \frac{1}{\cosh v_n} \right) \cosh(v_n y) + \left(\frac{1}{\sinh v_n} + \frac{2v_n}{\cosh v_n} \right) \sinh(v_n y) \right]. \quad (2.6.13)$$

Solution $Y_{n2}(y)$

For solution $Y_{n2}(y)$ of the equation (2.6.2) we impose the boundary conditions (2.5.18). The solution of equation (2.6.2) subject to boundary conditions (2.5.18) is

$$Y_{n2}(y) = \frac{e^{-y/2}e^{-1/2}}{4v_n^2 - 1} \left[\left(-\frac{2v_n}{\sinh v_n} + \frac{1}{\cosh v_n} \right) \cosh(v_n y) + \left(-\frac{1}{\sinh v_n} + \frac{2v_n}{\cosh v_n} \right) \sinh(v_n y) \right]. \quad (2.6.14)$$

Hence

$$Y_n(y) = A_n Y_{n1}(y) + B_n Y_{n2}. \quad (2.6.15)$$

Now we are in position to find p . Substituting $X_n(x)$ and $Y_n(y)$ in equation (2.4.2) we get

$$p = a_0 e^{-y} + b_0 + \sum_{n=1}^{\infty} X_n(x) [A_n Y_{n1}(y) + B_n Y_{n2}]. \quad (2.6.16)$$

Applying the boundary conditions (2.3.9) and (2.3.10), with $f(x)$ and $g(x)$ both 1, we get

$$a_0 = -\frac{1}{\sinh 1}, \quad (2.6.17)$$

$$A_n = \frac{\int_{-1}^1 X_n(x) dx}{e \int_{-1}^1 e^x X_n^2(x) dx}, \quad (2.6.18)$$

$$B_n = \frac{\int_{-1}^1 X_n(x) dx}{e^{-1} \int_{-1}^1 e^x X_n^2(x) dx}. \quad (2.6.19)$$

A_n and B_n depend on the $X_n(x)$, which in turn depends on the values of ω_n . We can therefore consider two different cases

$$\omega_{n1} = i(2n + 1)\frac{\pi}{2}$$

$$A_{n1} = \frac{8(2n + 1)\pi \sin(2n + 1)\frac{\pi}{2} \cosh(1/2)}{eC_n(1 + (2n + 1)^2\pi^2)^2}, \quad (2.6.20)$$

and

$$B_{n1} = \frac{8e(2n + 1)\pi \sin(2n + 1)\frac{\pi}{2} \cosh(1/2)}{C_n(1 + (2n + 1)^2\pi^2)^2}. \quad (2.6.21)$$

$$\omega_{n2} = in\pi$$

$$A_{n2} = \frac{-16n\pi \cos(n\pi) \sinh(1/2)}{eE_n(1 + 4n^2\pi^2)^2}, \quad (2.6.22)$$

and

$$B_{n2} = \frac{-16en\pi \cos(n\pi) \sinh(1/2)}{E_n(1 + 4n^2\pi^2)^2}. \quad (2.6.23)$$

hence we can write

$$p = a_0e^{-y} + b_0 + \sum_{n=1}^{\infty} X_{n1}(x) \left[A_{n1}Y_{n1}^{(\omega_{n1})}(y) + B_{n1}Y_{n2}^{(\omega_{n1})}(y) \right] + \sum_{n=1}^{\infty} X_{n2}(x) \left[A_{n2}Y_{n1}^{(\omega_{n2})}(y) + B_{n2}Y_{n2}^{(\omega_{n2})}(y) \right]. \quad (2.6.24)$$

In the above equation $Y_{n1}^{(\omega_{n1})}$, $Y_{n2}^{(\omega_{n1})}$ are the solutions of equation (2.6.2) corresponding to $\omega_{n1} = i(2n + 1)\frac{\pi}{2}$ and $Y_{n1}^{(\omega_{n2})}$, $Y_{n2}^{(\omega_{n2})}$ are solutions of equation (2.6.2) corresponding to $\omega_{n2} = in\pi$.

Also $X_{n1}(x)$, $X_{n2}(x)$, A_{n1} , B_{n1} , A_{n2} and B_{n2} are given by the equations (2.6.9), (2.6.10), (2.6.20), (2.6.21), (2.6.22) and (2.6.23) respectively.

The only unknown left in equation (2.6.24) is b_0 which can be evaluated by using the condition

$$p(0, 0) = 0.$$

Applying this condition on equation (2.6.24) we get

$$b_0 = -a_0 - \sum_{n=1}^{\infty} \left[X_{n1}(0) \left\{ A_{n1} Y_{n1}^{(\omega_{n1})}(0) + B_{n1} Y_{n2}^{(\omega_{n1})}(0) \right\} + X_{n2}(0) \left\{ A_{n2} Y_{n1}^{(\omega_{n2})}(0) + B_{n2} Y_{n2}^{(\omega_{n2})}(0) \right\} \right].$$

2.6.2 Case II : Permeability function of one spatial coordinate

Consider the case when $k_1(x) = e^x$ and $k_2(y) = 1$, then from equations (2.4.6) and (2.4.7) we have

$$\frac{d^2 X_n(x)}{dx^2} + \frac{dX_n(x)}{dx} + \lambda_n^2 X_n(x) = 0, \quad (2.6.25)$$

$$\frac{d^2 Y_n(y)}{dy^2} - \lambda_n^2 Y_n(y) = 0. \quad (2.6.26)$$

For $\lambda_n = 0$ solution of equations (2.6.25) and (2.6.26) subject to boundary conditions (2.4.8) is

$$p = a_0 y + b_0. \quad (2.6.27)$$

For $\lambda_n \neq 0$ solution of equations (2.6.25) subject to boundary conditions (2.4.8) is given by equations (2.6.9) and (2.6.10). Solution Y_{n1} and Y_{n2} of (2.6.26) subject to temporary boundary conditions (2.5.12) and (2.5.18) is given by

$$Y_{n1} = \frac{1}{\lambda(e^{4\lambda} - 1)} \left[e^{(3+y)\lambda} + e^{(1-y)\lambda} \right], \quad (2.6.28)$$

$$Y_{n2} = -\frac{1}{\lambda(e^{4\lambda} - 1)} \left[e^{(1+y)\lambda} + e^{(3-y)\lambda} \right]. \quad (2.6.29)$$

So

$$Y(y) = C_n Y_{n1} + D_n Y_{n2}. \quad (2.6.30)$$

By substituting the values of $X(x)$ and $Y(y)$ in equation (2.4.2) we get

$$p = a_0 y + b_0 + \sum_{n=1}^{\infty} \left[X_{n1}(x) \left\{ A_{n1} Y_{n1}^{(\omega_1)}(y) + B_{n1} Y_{n2}^{(\omega_1)}(y) \right\} + X_{n2}(x) \left\{ A_{n2} Y_{n1}^{(\omega_2)}(y) + B_{n2} Y_{n2}^{(\omega_2)}(y) \right\} \right]. \quad (2.6.31)$$

where X_{n1} and X_{n2} are given by equations (2.6.9) and (2.6.10) respectively. Also applying the boundary conditions (2.3.9) and (2.3.10), with $f(x)$ and $g(x)$ both 1, we get

$$\begin{aligned} a_0 &= \frac{1}{\sinh 1}, \\ A_{n1} &= B_{n1} = \frac{8\pi(2n+1) \sin((2n+1)\frac{\pi}{2}) \cosh(1/2)}{C_n(1+4n^2\pi^2 + \pi^2 + 4n\pi^2)^2}, \\ A_{n2} &= B_{n2} = \frac{-16n\pi \cos(n\pi) \sinh(1/2)}{E_n(1+4n^2\pi^2)^2}, \end{aligned}$$

and

$$\begin{aligned} b_0 &= - \sum_{n=1}^{\infty} \left[X_{n1}(0) \left\{ A_{n1} Y_{n1}^{(\omega_1)}(0) + B_{n1} Y_{n2}^{(\omega_1)}(0) \right\} \right. \\ &\quad \left. + X_{n2}(0) \left\{ A_{n2} Y_{n1}^{(\omega_2)}(0) + B_{n2} Y_{n2}^{(\omega_2)}(0) \right\} \right]. \end{aligned}$$

2.6.3 Case III : Constant permeability

When permeability is uniform everywhere *i.e.* $k(x, y) = \text{constant}$ then equation (2.3.7) reduces to

$$\nabla^2 p = 0.$$

Solution of this equation subject to boundary conditions (2.3.8), (2.3.9) and (2.3.10) is given by

$$p = y + d. \tag{2.6.32}$$

where d is an arbitrary constant. The value of $d = 0$ when we use the condition $p(0,0) = 0$ in the above equation.

2.6.4 Case IV : Permeability and velocity boundary conditions both functions of spatial coordinates

Let the permeability be a function of two spatial variables *e.g.*

$$k(x, y) = e^x e^y,$$

and inflow and outflow velocities vary *e.g.*

$$f(x) = g(x) = 1 - x^2,$$

then in that case we have the solution of the form (2.6.16) where

$$\begin{aligned} a_0 &= -\frac{2}{3 \sinh 1}, \\ A_n &= \frac{\int_{-1}^1 (1 - x^2) X_n dx}{e \int_{-1}^1 e^x X_n^2 dx}, \\ B_n &= e \frac{\int_{-1}^1 (1 - x^2) X_n dx}{\int_{-1}^1 e^x X_n^2 dx}. \end{aligned}$$

A_n and B_n can be calculated by using the MAPLE.

2.7 Comparison of Numerical and Analytical Results

In this Section we will compare the numerical and analytical results. We consider in detail different cases for the permeability $k(x, y)$ and inflow and outflow velocity.

2.7.1 Case I : Permeability function of two spatial variables, Constant inflow and outflow velocities.

Consider the case when permeability is a function of two spatial variables x and y . Also we assume that inflow and outflow velocities are constant *i.e.*

$$k_1(x) = e^x, \quad k_2(y) = e^y, \quad f(x) = 1, \quad g(x) = 1.$$

Analytical and numerical results of fluid pressure p and fluid velocity \mathbf{u} are plotted in Figure 2.3 and 2.4 respectively.

Figures 2.3(a) and 2.4(a) show analytic and numerical results of pressure contours and fluid velocity respectively. In this case the permeability of porous material is an exponential function of x and y , which means that material is less permeable near the boundary $x = -1$ and $y = -1$. Permeability of material increases as we move towards right along the x direction and upwards along the y direction. Hence the velocity of fluid is less near the left bottom corner of the porous material and fluid has highest velocity near the right upper corner. Also near the boundary $x = 1$ and $y = 1$ permea-

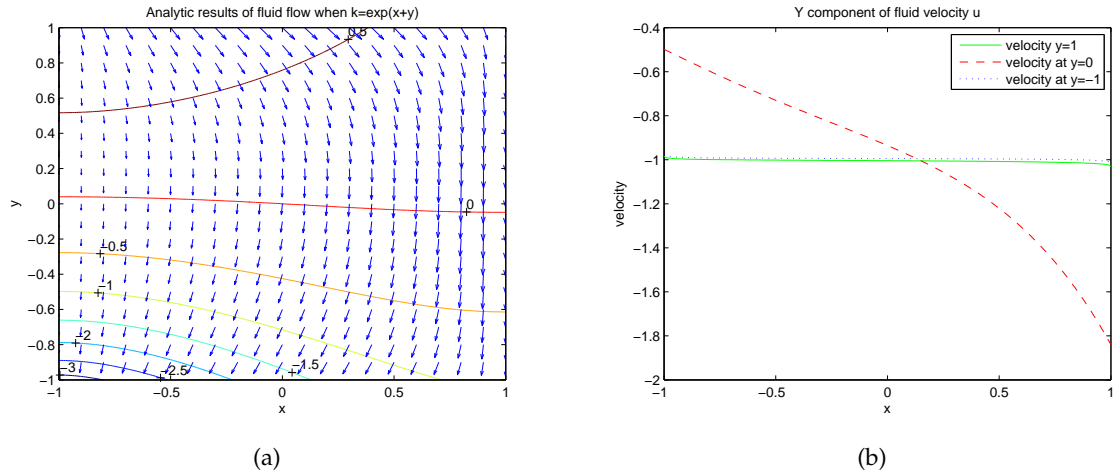


Figure 2.3: Analytical results of (a) flow of fluid through the porous material with permeability $k(x, y) = e^{x+y}$. Inflow and outflow velocities are constant *i.e.* $f(x) = g(x) = 1$. The arrows indicate the direction of flow and lines indicate the pressure contours. (b) y component fluid velocity at different spatial locations.

bility is maximum. Near the left bottom corner the pressure contours are very close which indicates that high pressure is needed to push the fluid through that region and also fluid velocity is low in this region. Near the top right corner fluid velocity is high. These features are evident from the Figures 2.3(a) and 2.4(a).

Figures 2.3(b) and 2.4(b) show the magnitude of the y component of fluid velocity at the boundaries and along the line $y = 0$. It is clear from the Figure that boundary conditions are satisfied *i.e.* inflow and outflow velocities are 1. Also along the line

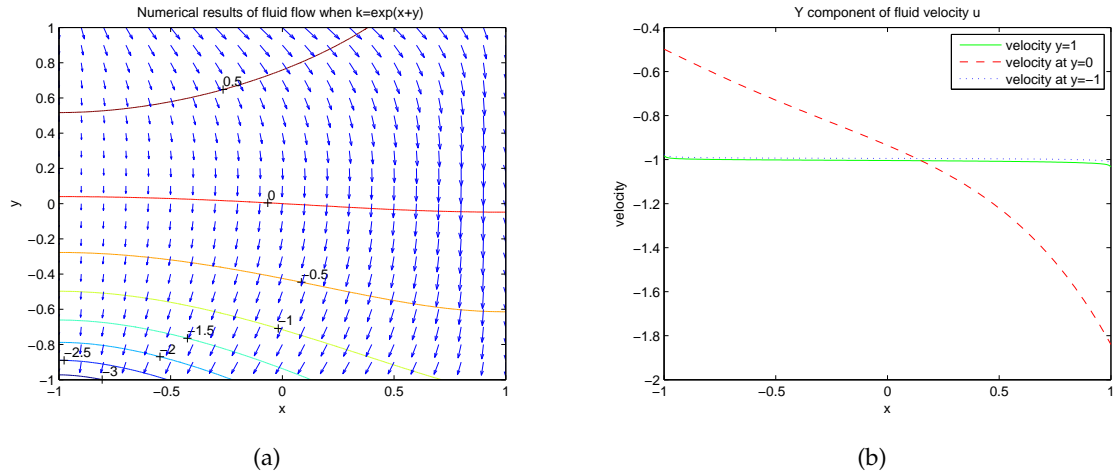


Figure 2.4: Numerical results of (a) flow of fluid through the porous material with permeability $k(x, y) = e^{x+y}$. Inflow and outflow velocities are constant *i.e.* $f(x) = g(x) = 1$. The arrows indicate the direction of flow and solid lines indicate the pressure contours. (b) y component of fluid velocity at different spatial locations.

$y = 0$ fluid velocity is low near the left boundary $x = -1$ and it increases as we move along this line towards the right boundary $x = 1$.

The maximum absolute and relative errors in pressure p are 0.0059 and 3.93×10^{-5} respectively showing that the analytic and numerical results are in good agreement. Since we are using second order central difference method error is $O(h^2)$.

2.7.2 Case II : Permeability function of one spatial variable, Constant inflow and outflow velocities

Consider the case when the permeability is a function of one spatial coordinate only *e.g.* x and inflow and out flow velocities are constant *i.e.*

$$k_1(x) = e^x, \quad k_2(y) = 1, \quad f(x) = 1, \quad g(x) = 1.$$

Analytical results of pressure contours and fluid velocities are plotted in Figures 2.5. In Figure 2.5(a) analytic results of pressure contours and fluid velocity are plotted respectively. Numerical results are identical to Figure 2.5(a), which are not included here. When the permeability is an exponential function of x , *i.e.* $k = e^x$ then material is less permeable near the boundary $x = -1$ and permeability increases as we move towards right boundary $x = 1$.

Permeability is minimum near the bottom left corner and maximum near the top right corner. In this case the fluid velocity should be low near the bottom left corner and it

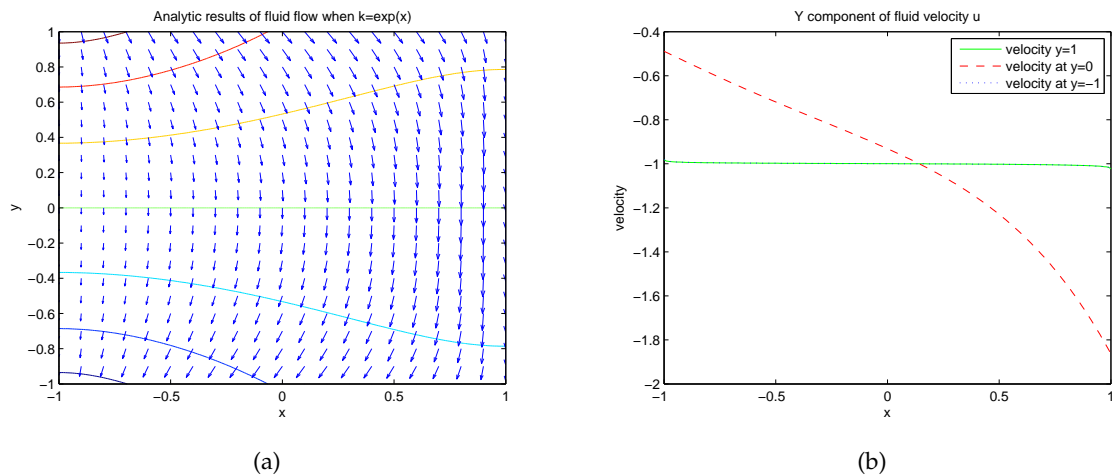


Figure 2.5: Analytical results of (a) flow of fluid through the porous material with permeability $k(x, y) = e^x$. Inflow and outflow velocities are constant *i.e.* $f(x) = g(x) = 1$. The arrows indicate the direction of flow and solid lines indicate the pressure contours. (b) y component of fluid velocity at different spatial locations.

should be high near the top right corner which is evident from the Figure 2.5(a). Also near the bottom left corner pressure contours are close together indicating that we need high pressure to push the fluid through the porous material near the boundary $x = -1$. Figure 2.5(b) shows the magnitude of fluid velocity \mathbf{u} in y direction at different spatial locations. It is clear from the Figure that at both the boundaries the velocity is 1 and along the line $y = 0$ velocity is low near the boundary $x = -1$ and velocity is high near the boundary $x = 1$. Numerical results are again identical to Figure 2.5(b), which are not shown here.

The maximum absolute and relative errors in pressure p are 0.0023 and 1.8×10^{-5} respectively. Since absolute and relative errors are small so we conclude that numerical and analytical results agree. Again the error is $O(h^2)$.

2.7.3 Case III : Constant permeability, Constant inflow and outflow velocities

Consider the case when permeability of the porous material is uniform everywhere and inflow and out flow velocities are also constant *i.e.*

$$k_1(x) = 1, \quad k_2(y) = 1, \quad f(x) = 1, \quad g(x) = 1.$$

Figure 2.6 shows the numerical results of fluid pressure p and fluid velocity \mathbf{u} . In Figure 2.6(a) solid horizontal lines represents pressure contour and arrow represents the fluid velocity.

From Figure 2.6(a) we observe that when permeability of the porous material is uniform then fluid velocity throughout the porous material remains uniform, which validates our analytical results given by equation (2.6.32). Also we observe from the Figure that pressure contours are equally spaced which indicates as expected that a uniform pressure gradient is needed to push the fluid through the material. From analysis we find that maximum absolute and relative errors in pressure p are given by 1.0468×10^{-10} and 1.0468×10^{-13} respectively. These numbers are very small which validates that numerical results of pressure p plotted in Figure 2.6(a) agree well with the analytical results.

Figure 2.6(b) shows magnitude of the fluid velocity at the top boundary $y = 1$, bottom boundary $y = -1$ and along the line $y = 0$. It is clear from the Figure that velocity boundary condition are satisfied at top and bottom boundaries, and fluid velocity is also 1 along the line $y = 0$. Analytically magnitude of the fluid velocity in the y direc-

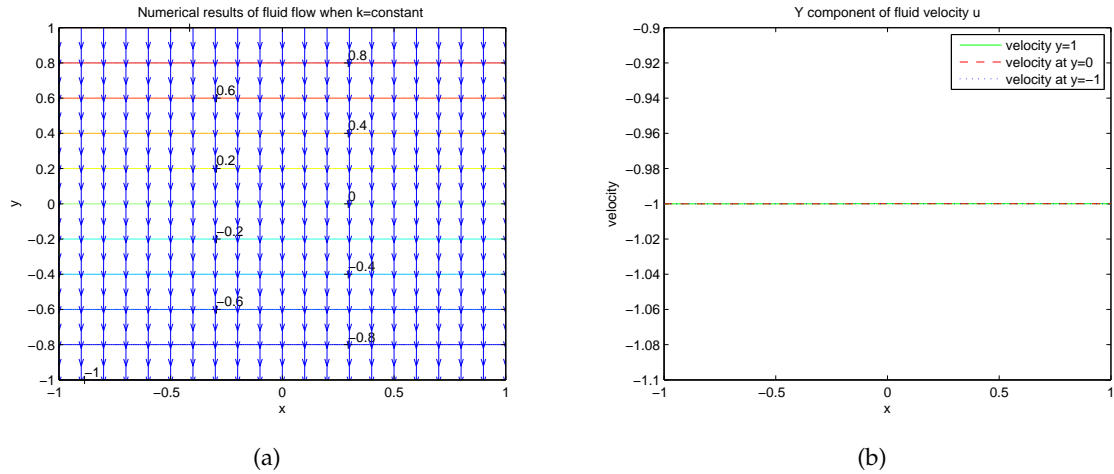


Figure 2.6: Numerical results of (a) fluid flow through a porous material for constant permeability and constant inflow and outflow velocities. The arrows indicate the direction of flow and horizontal lines indicate the pressure contours. (b) y component of fluid velocity at different spatial locations.

tion is 1 and numerically fluid velocity in the y direction is 1, which is evident from the Figure 2.6(b).

2.7.4 Case IV : Permeability, inflow and outflow velocities functions of spatial coordinates

Consider the case when the permeability is a function of two spatial variables and inflow and outflow velocities are functions of x *i.e.*

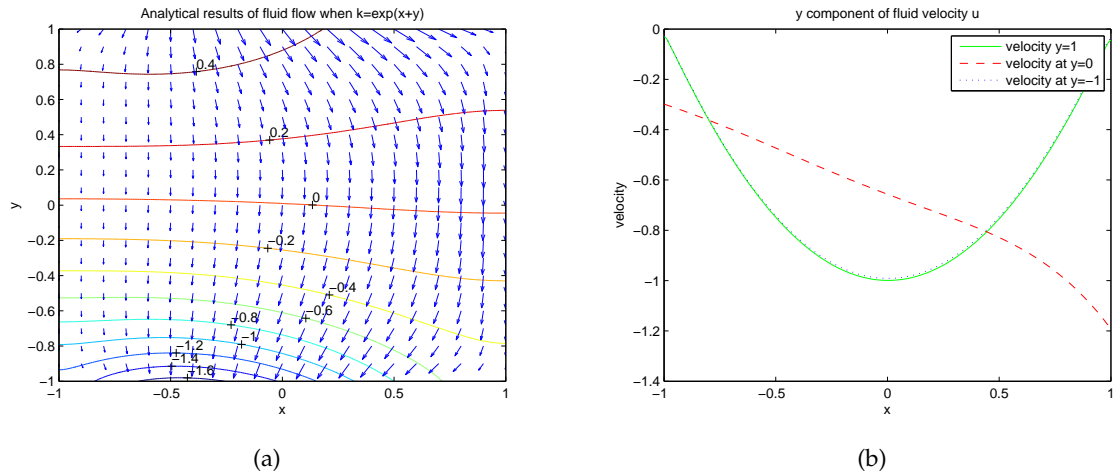


Figure 2.7: Analytical results of (a) flow of fluid through the porous material with permeability $k(x, y) = e^{x+y}$. Inflow and outflow velocities are $f(x) = g(x) = 1 - x^2$. The arrows indicate the direction of flow and lines indicate the pressure contours. (b) y component of fluid velocity at different spatial locations.

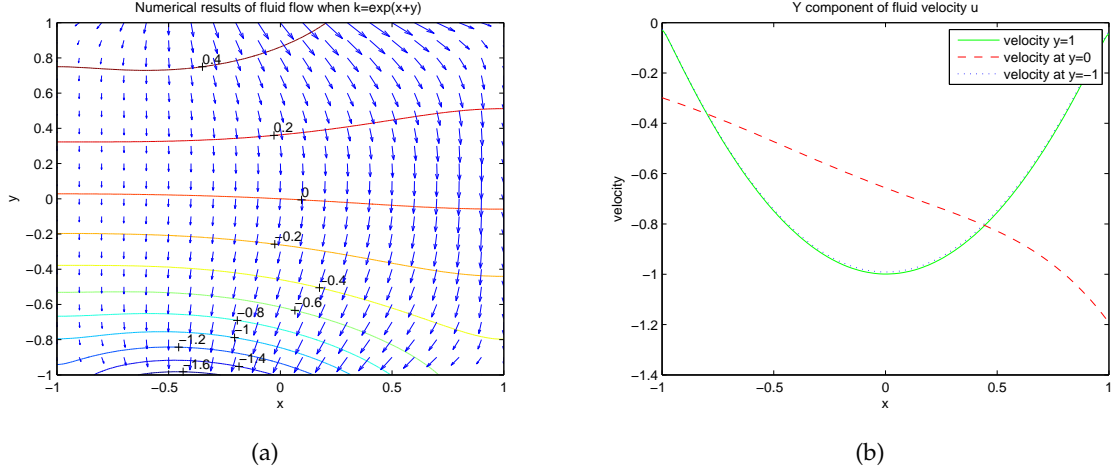


Figure 2.8: Numerical results of (a) flow of fluid through the porous material with permeability $k(x, y) = e^{x+y}$. Inflow and outflow velocities are $f(x) = g(x) = 1 - x^2$. The arrows indicate the direction of flow and lines indicate the pressure contours. (b) y component of fluid velocity at different spatial locations.

$$k_1(x) = e^x, \quad k_2(y) = e^y, \quad f(x) = 1 - x^2 = g(x).$$

Analytical and numerical results of pressure p and fluid velocity \mathbf{u} are plotted in Figure 2.7 and 2.8 respectively.

The maximum absolute and relative errors in pressure p are 1.2469 and 0.0130 respectively. Percentage relative error is 1.3. Since these numbers are small so we conclude that analytical and numerical results agree well. Again the error in this case is $O(h^2)$.

2.8 Summary and conclusions

In this Chapter we have studied the flow of fluid through the porous material. We used Darcy's law to model the flow of fluid through the porous material. We have assumed that the permeability $k(x, y)$ of the porous material is a separable function of the spatial coordinates. Numerical results are presented for generic $k(x, y)$ but analytic results are presented for some special $k(x, y)$ for which analytical solutions exist. We concluded that fluid flows with high velocity in the regions where the permeability is high and velocity of the fluid is small in the regions where permeability of porous material is small. We compared analytic and numerical results for different choices of permeability $k(x, y)$ and found that they agree well.

Mathematical modelling of cell growth in a perfusion bioreactor

3.1 Introduction

Tissue engineering aims to repair or replace the damage or lost tissue or organ by transplanting the biological substitutes that are grown outside the body in the laboratory. In Chapter 1 we have briefly discussed the currently available techniques and problems associated with these techniques. Several experimental and mathematical techniques have been developed to study the nutrient profile and spatial cell distribution in the bioreactor. Mathematical modelling can be used for better understanding of experimental results. In this Chapter we describe a simple coupled mathematical model of nutrient transport and cell growth in the bioreactor. The model includes the important features of the tissue engineering process including the fluid flow, nutrient transport, cell growth and permeability variation of the material due to cell growth. We solve the model numerically by using the finite element solver COMSOL. We apply some simplifying assumptions to the model equations to solve the model analytically. It is not possible to find a complete analytic solution of the model so we find the analytic results for nutrient concentration and cell density when time is small and at steady state. Numerical and analytic results are compared at initial and large times. We also study the stability of steady state solution analytically and numerically. As cells grow and block the scaffold pores it will affect the flow of fluid consequently the flow rate through the construct decrease continuously. In experiments constant volumetric flow rate is maintained through the construct so we will also discuss how mathematically a constant volumetric flow rate can be maintained through the construct. Our calculations confirm that the coupling between equations is correctly implemented in the

numerical routine.

Later in Chapter 5 we will consider the detailed model by including the effect of shear stress on nutrient consumption and cell growth, non-linear cell diffusion and constant volumetric flow rate.

3.2 Conceptual Model

Cell growth and nutrient transport are the two major phenomena taking place in the perfusion bioreactor. Apart from these two phenomena, during the cell growth different biochemical and mechanical forces are also in operation in a perfusion bioreactor and they influence the bioreactor performance. Figure 3.1 shows the main interacting phenomena taking place in a perfusion bioreactor when convective and diffusive transport of nutrient and cell growth take place within a scaffold. Nutrient transport is due to convection and diffusion and it affects the nutrient uptake rate *i.e.* if the nutrient transport is high then the nutrient uptake rate is also high and as a result cell growth will also be high. As cells grow and occupy the scaffold voids, the porosity and permeability of scaffold decreases from its initial value and the space left for the new cells is smaller. Due to the decrease in porosity the rate of diffusion of nutrients also decreases; on the other hand the decrease in permeability will have a direct effect on the convective velocity. Consequently the decrease in convective velocity and diffusion will influence the mass transfer and hence cell growth.

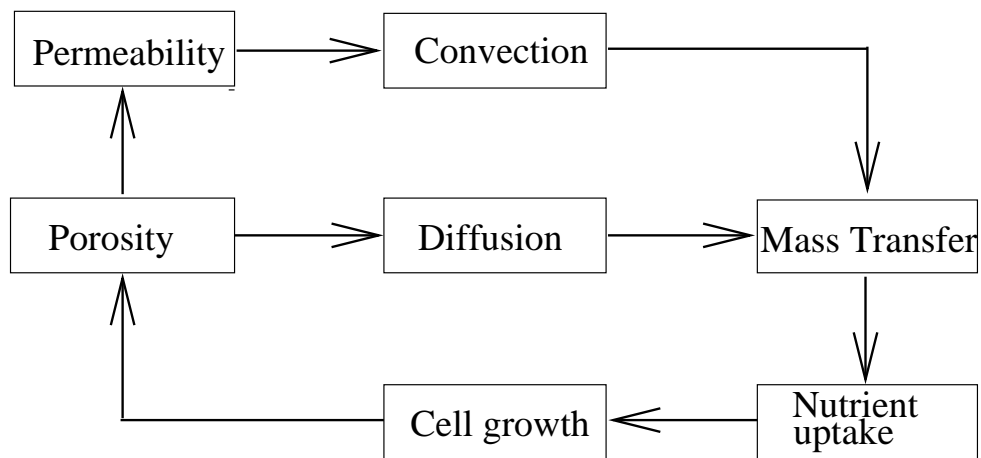


Figure 3.1: Interacting phenomena in perfusion bioreactor.

3.3 Geometry and Model Equations

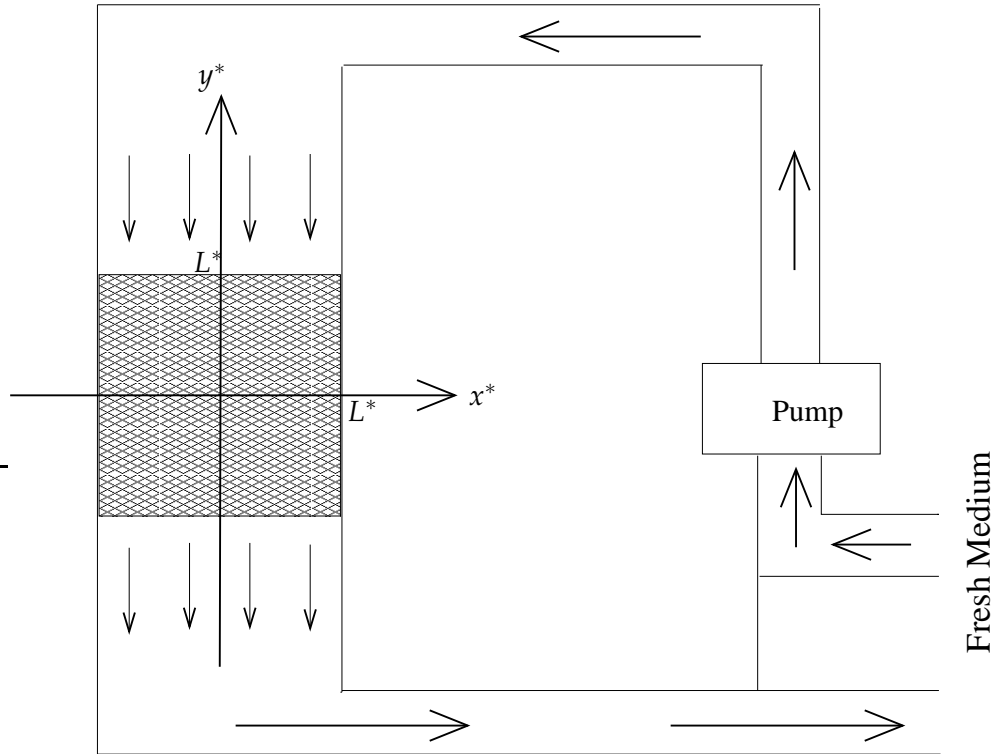


Figure 3.2: A perfusion bioreactor. Scaffold of length $2L^*$ and width $2L^*$ is placed within the bioreactor. Fluid is pumped in at the boundary $y^* = L^*$ and pumped out at $y^* = -L^*$. There is no fluid flux through the boundaries $x^* = \pm L^*$. Pressure at top and bottom boundaries are p_0^* and p_1^* respectively.

Let us assume that a cell-seeded porous scaffold consisting of interconnected porous network is placed in the bioreactor. Let the length and width of scaffold be $2L^*$ (Stars are used to denote dimensional quantities throughout). We consider a Cartesian coordinate system (x^*, y^*) aligned with the porous scaffold. The scaffold is characterized by the usual properties of porous material (porosity, void fraction and permeability). In this model we assume that the fluid is viscous, incompressible and Newtonian with viscosity $\mu^*(kg/m.sec)$. Fluid is pumped in at the boundary $y^* = L^*$ and drawn out at the boundary $y^* = -L^*$ as shown in Figure 3.2.

The model consist of three differential equations, the first representing the flow of fluid through the porous material, with the velocity denoted by $\mathbf{u}^*(m/sec)$ and pressure denoted by $p^*(kg/m.sec^2)$, the second representing convection and diffusion of nutrients, with the concentration of nutrient denoted by $S^*(moles/m^3)$, and the third representing the cell growth, in terms of cell density $N^*(x^*, y^*)(cells/m^3)$. Nutrients are assumed to move due to convection and diffusion, with a constant diffusion rate $D_s^*(m^2/s)$ and

to be consumed by the cells at the rate G_s^* (moles/ m^3sec). Cells are assumed to diffuse with a constant diffusion rate D_n^* and they grow in number at a rate Q_n^* (cells/ m^3sec). We assume that the initial cell density in the scaffold is $N_{init}^*(x^*, y^*)$, where the form of $N_{init}^*(x^*, y^*)$ is determined by cell seeding strategy *i.e.* uniform or non-uniform seeding and $k_0^*(x^*, y^*)$ is the permeability of scaffold without cells.

In the next Section we will describe the equations governing the fluid flow, nutrient delivery and cell growth together with appropriate boundary and initial conditions.

3.3.1 Flow Field

Suppose that the permeability k^* , of the porous material is spatially varying so that

$$k^* = k^*(x^*, y^*).$$

Fluid velocities are assumed to be sufficiently small that inertia can be neglected. The Darcy velocity \mathbf{u}^* is related to the interstitial pressure p^* by Darcy's law,

$$\mathbf{u}^* = -\frac{k^*(x^*, y^*)}{\mu^*} \nabla^* p^*, \quad (3.3.1)$$

where μ^* is the dynamic viscosity of the fluid. The continuity equation is

$$\nabla^* \cdot \mathbf{u}^* = 0. \quad (3.3.2)$$

At the boundaries $x^* = \pm L^*$ we assume that no fluid is flowing through these boundaries. Mathematically we write

$$\mathbf{u}^* \cdot \hat{\mathbf{n}} = 0 \quad \text{at } x^* = \pm L^*, \quad -L^* \leq y^* \leq L^*, \quad (3.3.3)$$

and at the boundaries $y^* = \pm L^*$ we apply pressure boundaries conditions

$$p^* = p_0^* \quad \text{at } y^* = L^*, \quad -L^* \leq x^* \leq L^*, \quad (3.3.4a)$$

$$p^* = p_1^* \quad \text{at } y^* = -L^*, \quad -L^* \leq x^* \leq L^*, \quad (3.3.4b)$$

where $\hat{\mathbf{n}}$ is the outward unit normal vector, p_0^* is the prescribed pressure at top boundary $y^* = L^*$ and p_1^* is the prescribed pressure at bottom boundary $y^* = -L^*$, and we assume that $p_0^* > p_1^*$.

3.3.2 Nutrient Transport

Transport of nutrient to the cells is due to convection and diffusion so that the conservation equation governing the transport and consumption of nutrient is

$$\mathbf{u}^* \cdot \nabla^* S^* = D_s^* \nabla^{*2} S^* + G_s^*, \quad (3.3.5)$$

where \mathbf{u}^* is the convective velocity, S^* is the molar concentration of nutrient, D_s^* is the diffusion coefficient of nutrient and G_s^* is the nutrient uptake rate. In this case D_s^* is constant and G_s^* is assumed to be a prescribed function of the cell density and nutrient concentration. We assume that there is no flux of nutrients through the boundaries at $x^* = \pm L^*$. Mathematically we write

$$\hat{\mathbf{n}} \cdot \nabla^* S^* = 0 \quad \text{at} \quad x^* = \pm L^*, \quad -L^* \leq y^* \leq L^* \quad (3.3.6)$$

If the diffusion coefficient D_s^* is very small then in that case the downstream boundary condition becomes unimportant because it only influences a small boundary layer near $y^* = -L^*$, so we assume that there is no diffusive flux of nutrients through the boundary at $y^* = -L^*$. This type of boundary condition was also used by Coletti et al. (2006). We assume that at the boundary $y^* = L^*$ we have a constant nutrient concentration S_0^* . Mathematically we write,

$$S^* = S_0^* \quad \text{at} \quad y^* = L^*, \quad -L^* \leq x^* \leq L^*, \quad (3.3.7a)$$

$$\hat{\mathbf{n}} \cdot \nabla^* S^* = 0 \quad \text{at} \quad y^* = -L^*, \quad -L^* \leq x^* \leq L^*. \quad (3.3.7b)$$

Mathematically boundary conditions (3.3.6) and (3.3.7b) looks the same but physically they have different meanings. Boundary conditions (3.3.6) says that there is neither convective nor diffusive flux through the boundaries $x^* = \pm L^*$ and boundary conditions (3.3.7b) says that there is no diffusive flux through the boundary $y^* = -L^*$.

3.3.3 Cell Growth

The equation governing the growth of cells is given by,

$$\frac{\partial N^*}{\partial t^*} - D_n^* \nabla^{*2} N^* = Q_n^*, \quad (3.3.8)$$

where D_n^* is the diffusion rate of cells. We assume that there is no flux of cells through the boundaries at $x^* = \pm L^*$ and $y^* = \pm L^*$ and the initial cell density is $N_{mit}^*(x^*, y^*)$ i.e.

$$\hat{n} \cdot \nabla^* N^* = 0 \quad \text{at} \quad x^* = \pm L^* \quad \text{and} \quad y^* = \pm L^*, \quad (3.3.9a)$$

$$N^*(x^*, y^*, 0) = N_{init}^*(x^*, y^*) \quad \text{at} \quad t^* = 0. \quad (3.3.9b)$$

Because the cell growth is a very slow process with respect to the time it takes Darcy's law and advection-diffusion to reach steady state. As a result Darcy's law and advection diffusion equations reach steady state very quickly as compared to the cell growth equation. Due to this reason in this model Darcy's law and advection diffusion equations are quasi static equations while the cell growth equation is a transient equation.

3.3.4 Cell feedback on permeability

When cells grow (over the time interval Δt^* small enough that cell density changes only by a small amount) they occupy the void spaces in the scaffold and so the permeability of the scaffold decreases from its initial value $k_0^*(x^*, y^*)$ as the cell density increases. We assume that the permeability of the scaffold is the function of cell density. Mathematically we write

$$k^*(x^*, y^*, N^*) = k_0^*(x^*, y^*) e^{-\eta^* N^*}, \quad (3.3.10)$$

where $k_0^*(x^*, y^*)$ is the permeability of scaffold without cells and η^* ($m^3/cell$) is a constant. η^* controls the change in permeability and is called the blocking parameter. The exponential function ensures that permeability will always remain positive, because negative permeability has no physical meaning. For small values of the cell density the permeability equation has linear behaviour.

3.3.5 Consumption and Proliferation Rate

An important part of the modelling is the prescription of the nutrient consumption and net cell growth rate functions G_s^* and Q_n^* respectively. Let λ^* be the proliferation rate of the cells. We suppose that the rate of proliferation of cells is only a function of nutrient concentration *i.e.* $\lambda^*(S^*)$ and the rate of nutrient consumption per cell is $\alpha^* \lambda^*(S^*)$, where α^* is constant.

The cell density changes only due to cell growth. Because the growth rate is much higher than the death rate so we assume that the cell death is negligible. We assume that the cells proliferate according to the logistic law. Thus the net growth rate $Q_n^* =$

$\lambda^*(S^*)N^*(1 - N^*/N_{max}^*)$, where N_{max}^* is the maximum carrying capacity. There is a significant discussion about the form of the proliferation rate $\lambda^*(S^*)$, e.g. McElwain and Ponzo (1977) used a piecewise linear behaviour; whereas Galban and Locke (1999) used more complex functions such as modified Contois, Moser and nth order heterogeneous models (see Appendix D). Coletti et al. (2006) also used a Contois function to describe the cell growth. Landman and Cai (2007) considered a Heaviside step functional form $H(S^* - S_h^*)$, where S_h^* is the hypoxic threshold for the nutrient concentration. Lewis et al. (2005) also used Heaviside step function to represent the proliferation rate $\lambda^*(S^*)$ but he used hypoxic threshold for the nutrient concentration $S_h^* = 0$ so proliferation rate $\lambda^*(S^*) = H(S^*)$. Michaelis-Menton (see Appendix D) type behaviour is used by Malda et al. (2004a). All these forms reduce to simple linear behaviour for small values of the concentration. The most commonly used functional form, linear and Michaelis-Menton functions can be chosen here to describe the proliferation rate $\lambda^*(S^*)$. For simplicity we consider a simple linear behaviour used by Jones et al. (2000) and Lewis et al. (2005). So we choose $\lambda^*(S^*) = \beta^*S^*$, where $\beta^*(m^3/mole.sec)$ is a constant. Thus

$$Q_n^* = \beta^*S^*N^*(1 - N^*/N_{max}^*). \quad (3.3.11)$$

We assume that the dominant mechanism for cell nutrient consumption is entirely dependent on the cellular growth. Hence the nutrient consumption rate

$$G_s^* = -\alpha^*S^*N^*, \quad (3.3.12)$$

where $\alpha^*(m^3/cell.sec)$ is a constant.

3.4 Nondimensionalization

We nondimensionalize all lengths with L^* and the permeability with respect to a typical permeability k_c^* , so that

$$x^* = L^*x, \quad y^* = L^*y, \quad \nabla^* = \frac{1}{L^*}\nabla, \quad k^*(x^*, y^*) = k_c^*k(x, y), \quad k_0^*(x^*, y^*) = k_c^*k_0(x, y).$$

We nondimensionalize velocity and pressure as follows,

$$\mathbf{u}^* = U_c^*\mathbf{u}, \quad p^* = (p_0^* - p_1^*)p + p_1^*,$$

where $(p_0^* - p_1^*)$ is the pressure difference between the top and bottom boundaries, and U_c^* is the characteristic velocity scale given by

$$U_c^* = \frac{(p_0^* - p_1^*)k_c^*}{\mu^*L^*}.$$

We nondimensionalize all cell densities N^* and N_{init}^* by maximum carrying capacity N_{max}^* and nutrient concentration S^* by initial concentration S_0^* respectively,

$$N^* = N_{max}^*N, \quad N_{init}^* = N_{max}^*N_{init}, \quad S^* = S_0^*S.$$

Finally, we nondimensionalize time by

$$t^* = T^*t,$$

where T^* is a typical time scale. The choice of T^* will be determined subsequently.

3.4.1 Dimensionless equations and boundary conditions

Darcy's law (3.3.1) and the continuity equation (3.3.2) can then be written in dimensionless form as

$$\mathbf{u} = -k(x, y)\nabla p, \tag{3.4.1}$$

$$\nabla \cdot \mathbf{u} = 0. \tag{3.4.2}$$

By combining above two equations we get,

$$\nabla \cdot (k(x, y)\nabla p) = 0. \tag{3.4.3}$$

The boundary conditions (3.3.3) and (3.3.4) in dimensionless form become,

$$\hat{\mathbf{n}} \cdot \nabla p = 0 \quad \text{at } x = \pm 1, \quad -1 \leq y \leq 1, \tag{3.4.4a}$$

$$p = 1 \quad \text{at } y = 1, \quad -1 \leq x \leq 1, \tag{3.4.4b}$$

$$p = 0 \quad \text{at } y = -1, \quad -1 \leq x \leq 1. \tag{3.4.4c}$$

The nutrient transport equation (3.3.5) can be written in the dimensionless form as,

$$\mathbf{u} \cdot \nabla S = D_s \nabla^2 S - R_s NS \tag{3.4.5}$$

and boundary conditions (3.3.6) and (3.3.7) in dimensionless form becomes,

$$\hat{\mathbf{n}} \cdot \nabla S = 0 \quad \text{at } x = \pm 1, \quad -1 \leq y \leq 1, \quad (3.4.6a)$$

$$S = 1 \quad \text{at } y = 1, \quad -1 \leq x \leq 1, \quad (3.4.6b)$$

$$\hat{\mathbf{n}} \cdot \nabla S = 0 \quad \text{at } y = -1, \quad -1 \leq x \leq 1, \quad (3.4.6c)$$

where

$$D_s = \frac{D_s^*}{U_c^* L^*}, \quad \text{and} \quad R_s = \frac{a^* L^* N_{max}^*}{U_c^*},$$

are dimensionless numbers. The parameter D_s is the inverse of the Peclet number and represents the ratio of nutrient diffusion to advection. We assume that the diffusion of nutrients is slow as compared to advective velocity so that the parameter D_s will be small which implies that the Peclet number is high. The parameter R_s represents the rate of nutrient consumption relative to advection. If advective velocity U_c^* is high as compared to rate of nutrient consumption then the parameter R_s is small which implies that cells are eating nutrients slowly. The dimensionless form of cell growth equation (3.3.8) is

$$\frac{1}{T^*} \frac{\partial N}{\partial t} - \frac{D_n^*}{L^{*2}} \nabla^2 N = \beta^* S_0^* S N (1 - N). \quad (3.4.7)$$

Now we can choose the time scale T^* in two ways. If we choose the growth rate time scale *i.e.* $T^* = 1/\beta^* S_0^*$, then the cell growth equation in dimensionless form becomes

$$\frac{\partial N}{\partial t} - \Gamma \nabla^2 N = S N (1 - N). \quad (3.4.8)$$

where $\Gamma = D_n^*/L^{*2} \beta^* S_0^*$ is a dimensionless number which represents the diffusion rate of cells relative to cellular growth. But if we choose the diffusion time scale *i.e.* $T^* = L^{*2}/D_n^*$ then the cell growth equation in dimensionless form becomes

$$\frac{\partial N}{\partial t} - \nabla^2 N = \frac{1}{\Gamma} S N (1 - N), \quad (3.4.9)$$

We will consider the growth rate time scale because we are interested in growth of cells. Lewis et al. (2005), who neglected cell diffusivity, and Landman and Cai (2007) both used the growth rate time scale.

Boundary conditions (3.3.9a) and initial condition (3.3.9b) in dimensionless form can

be written as,

$$\hat{n} \cdot \nabla N = 0, \quad \text{at all the four boundaries } x = \pm 1, \quad y = \pm 1, \quad (3.4.10a)$$

$$N = N_{init}(x, y) \quad \text{at } t = 0. \quad (3.4.10b)$$

The cell feedback equation (3.3.10) in dimensionless form becomes

$$k(x, y) = k_0(x, y) \exp(-\eta N), \quad (3.4.11)$$

where $\eta = N_{max}^* \eta^*$. Hence the dimensionless parameters in the model are,

$$D_s = \frac{D_s^*}{U_c^* L^*}, \quad R_s = \frac{a^* L^* N_{max}^*}{U_c^*}, \quad \Gamma = \frac{D_n^*}{L^{*2} \beta^* S_0^*}, \quad \text{and } \eta = N_{max}^* \eta^*.$$

Table 3.1 shows the brief summary of model equations, boundary and initial conditions.

Equations	Boundary conditions	Initial conditions
Permeability distribution $k(x, y, N) = k_0(x, y) \exp(-\eta N)$.		
Darcy's law $\mathbf{u} = -k(x, y, N) \nabla p$, $\nabla \cdot \mathbf{u} = 0$.	$\hat{\mathbf{n}} \cdot \nabla p = 0$, at $x = \pm 1$, $-1 \leq y \leq 1$, $p = 1$, at $y = 1$, $-1 \leq x \leq 1$, $p = 0$, at $y = -1$, $-1 \leq x \leq 1$.	
Nutrient Transport $\mathbf{u} \cdot \nabla S = D_s \nabla^2 S - R_s NS$.	$\hat{\mathbf{n}} \cdot \nabla S = 0$, at $x = \pm 1$, $-1 \leq y \leq 1$, $S = 1$, at $y = 1$, $-1 \leq x \leq 1$, $\hat{\mathbf{n}} \cdot \nabla S = 0$ at $y = -1$, $-1 \leq x \leq 1$.	
Cell growth $\frac{\partial N}{\partial t} - \Gamma \nabla^2 N = SN(1 - N)$.	$\hat{\mathbf{n}} \cdot \nabla N = 0$, at $x = \pm 1$, $y = \pm 1$.	$N = N_{init}(x, y)$ at $t = 0$.

$$D_s = \frac{D_s^*}{U_c^* L^*}, \quad R_s = \frac{\alpha^* L^* N_{max}^*}{U_c^*}, \quad \Gamma = \frac{D_n^*}{L^{*2} \beta^* S_0^*}, \quad \text{and} \quad \eta = N_{max}^* \eta^*.$$

Table 3.1: Summary of dimensionless model equations, boundary and initial conditions.

3.5 Numerical solution

The model proposed in the Section 3.4.1 consists of four coupled equations namely, cell feedback equation, quasi static Darcy's law, quasi static advection diffusion equation and the time dependent cell growth equation subject, to appropriate boundary and initial conditions. We assume that the permeability of the scaffold is the function of cell density and the cell feedback equation gives the permeability of the scaffold with the current cell density. First we solve the quasi static Darcy's law (3.4.3) for fluid velocities \mathbf{u} and pressure p and we substitute the fluid velocity \mathbf{u} into quasi-static advection diffusion equation (3.4.5) to solve for nutrient concentration S and then we substitute the nutrient concentration S into the cell growth equation (3.4.8) to solve for cell density N subject to appropriate boundary and initial conditions and finally we update the cell density in the permeability equation and solve the entire system again for updated cell density. This process continues until the system approaches steady state. As the cells grow and increase in numbers they invade the void spaces in the scaffold so the permeability of the scaffold decreases from its initial value and changes in permeability effect the flow field and hence nutrient transport and cell growth. The schematic diagram of solution is described in the Figure 3.3.

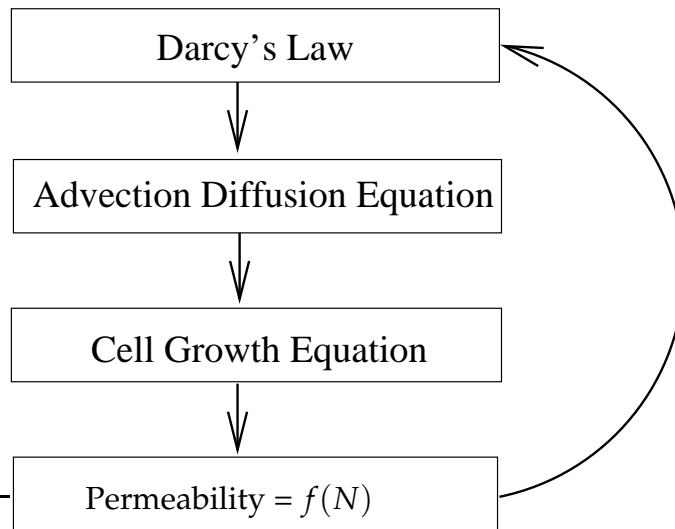


Figure 3.3: Schematic diagram of solution.

The set of three partial differential equations and boundary conditions are solved for 2-D Cartesian geometry using the commercially available finite element solver Femlab (Comsol). To get a meaningful results we need to take care of suitable meshing, finite element approximation (*e.g.* linear, quadratic or cubic) and numerical solution

parameters. To get the convergent results we have refined the mesh successively to increase the number of elements. The refined mesh gives 15680 elements out of which 240 are boundary elements. The total number of mesh vertices are 7961 and we have used the quadratic finite element approximation. We need to solve for three variables, pressure p , nutrient concentration S and cell density N . The system has 94803 (31601 \times 3) degrees of freedom, 31601 for each variable. In the system Darcy's law and the advection-diffusion equation are quasi-static. The only time dependent equation is cell growth equation. The cell growth equation is solved for time $t_0 : \Delta t_{cell} : t_{update}$, where $t_0 = 0$ is initial time, Δt_{cell} is the time step for cell growth equation and t_{update} is the time when we update the effect of cell density on cell feedback equation. We update the effect of cell density in the permeability equation after each time t_{update} and solve the entire system for updated cell density. This process continues until the system approaches the steady state.

3.5.1 Parameter values

The model presented in the Section 3.4 includes a number of parameters. Some parameters depend on the cell and nutrient type and some parameters depend on the scaffold geometry. Our model is a generic model and can be applied to any cell and nutrient type. We choose the cell type as Murine immortalized rat cell C_2C_{12} and we assume that growth of cell is limited to the supply of oxygen O_2 . Parameter values and their references for Murine immortalized rat cell C_2C_{12} are given in the Table 3.2.

Parameter	Description	Value	Units	Reference
L^*	Scaffold length	0.01	m	Rose et al. (2004)
U_c^*	Characteristic velocity	1.5×10^{-4}	m/sec	Rose et al. (2004)
N_{max}^*	Maximum Carrying capacity	4.7×10^{14}	$cells/m^3$	Coletti et al. (2006)
D_s^*	Diffusion coefficient of oxygen	1.5×10^{-9}	m^2/sec	Coletti et al. (2006)
$\alpha^* S_0^*$	Maximum oxygen consumption rate	1.86×10^{-18}	$moles/cell.sec$	Obradovic et al. (2000)
S_0^*	Initial nutrient concentration	0.119	$(moles/m^3)$	Coletti et al. (2006)
α^*	Constant in consumption rate	1.56×10^{-17}	$(m^3/cell.sec)$	
$\beta^* S_0^*$	Maximum cell growth rate	1.52×10^{-5}	$1/sec$	Coletti et al. (2006)
β^*	Constant in cell growth rate	1.27×10^{-4}	$m^3/mole.sec$	
D_n^*	Diffusion coefficient of cells	1.5×10^{-9}	m^2/sec	Ma et al. (2007)
η^*	Blocking parameter	1.06×10^{-15}	$m^3/cell$	
Values of dimensionless parameters				
D_s	Inverse Peclet number	0.001	–	
R_s	Ratio of nutrient consumption to advection	0.5	–	
Γ	Ratio of cell diffusion to cell growth rate	0.1	–	
η	Blocking parameter	0.5	–	

Table 3.2: Model parameters and values used in this work.

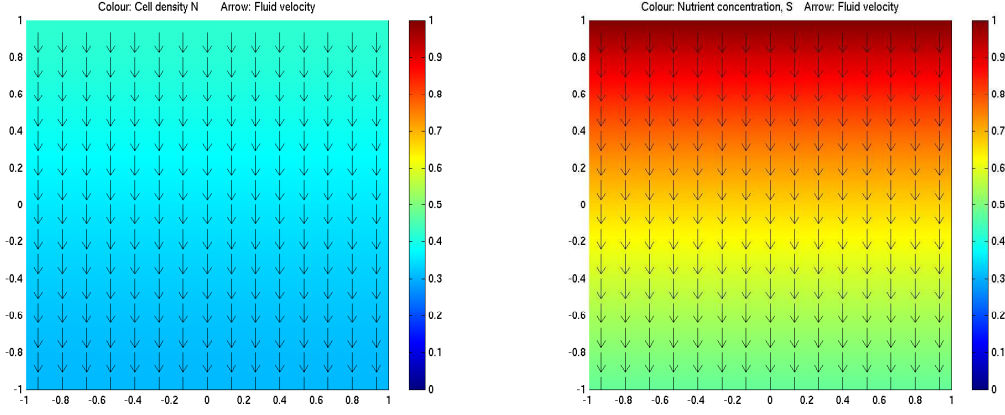
3.6 Results and discussion

In this Section we present the results of the model developed in Section 3.4.1 for various initial seeding and initial permeability functions. The growth of cells and concentration of nutrients in the scaffold is simulated using the model proposed in the Section 3.4. The evolution of velocity, nutrient concentration and cell density can be calculated at different growth rate times and at each spatial location. In the model initial cell density $N_{init}(x, y)$ and initial permeability of scaffold $k_0(x, y)$ are both generic functions of spatial coordinates x and y . We can consider any initial seeding strategy and initial permeability of scaffold. Results are discussed for various initial seeding strategies and initial permeability of scaffold. In Sections 3.6 to 3.9 all the results are presented for model with linear cell diffusion, constant pressure drop across the scaffold and neglecting the effect of shear stress induced by fluid on the cell growth and nutrient consumption.

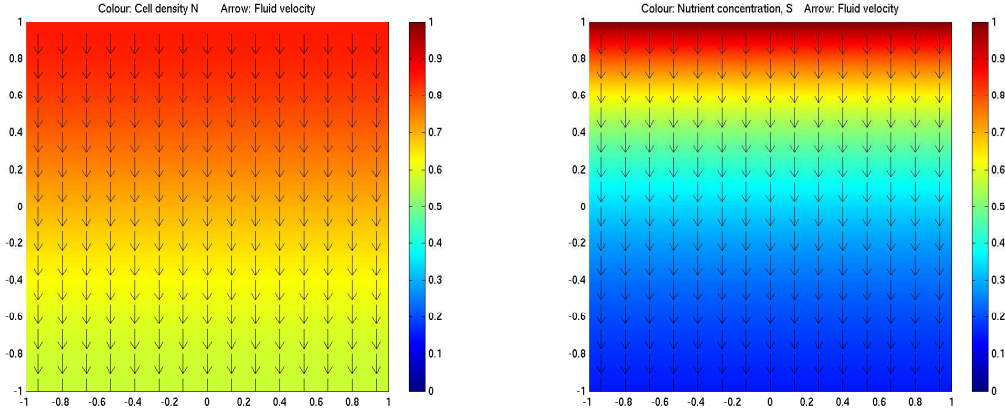
3.6.1 Uniform initial seeding and initial permeability

Let us consider the case when both initial seeding and initial permeability are uniform throughout the domain. We choose $N_{init}(x, y) = 0.1$ and $k_0(x, y) = 1$. Figure 3.4 shows a sequence of snapshots of fluid velocity (arrow plot) \mathbf{u} , nutrient concentration (color plot) S and cell density (color plot) N at times $t = 2$ and time $t = 5$. These times correspond to an intermediate point of transient solution and a point fairly close to steady state. We observe from the Figure 3.4 that initially the nutrients are distributed uniformly throughout the entire depth of scaffold but as time progresses the concentration of nutrients becomes non-uniform. The concentration of nutrients is high at the scaffold inlet wall $y = 1$ and it continuously decreases as we move away from the scaffold inlet wall. This decrease in nutrients also affects the cell growth. We know that the initial cell density is uniform and it remains uniform for initial times but as time progresses this becomes non-uniform giving more cells near the scaffold inlet wall where the nutrient concentration is high and fewer cells in the deeper sections of the scaffold where nutrient concentration is low. Since permeability of the scaffold is uniform so fluid will flow with uniform velocity through the scaffold at early times.

Figure 3.5 shows the cross section plot of nutrient concentration S and cell density N at $x = 0$ for different times. It is clear from the Figure 3.5 that at initial times nutrients are distributed uniformly throughout the scaffold but when cells start to grow nutrient concentration becomes non-uniform giving more nutrient concentration near the scaffold inlet wall and less nutrient concentration in the deeper sections of the scaffold.



(a) Cell density N and fluid velocity \mathbf{u} at $t = 2$. (b) Nutrient concentration S and fluid velocity \mathbf{u} at $t = 2$.



(c) Cell density N and fluid velocity \mathbf{u} at $t = 5$. (d) Nutrient concentration S and fluid velocity \mathbf{u} at $t = 5$.

Figure 3.4: Snapshots of the cell density N , nutrient concentration S and velocity \mathbf{u} at times $t = 2$ and $t = 5$. The initial cell density $N_{init}(x, y)$ and initial permeability $k_0(x, y)$ both are uniform *i.e.* $N_{init}(x, y) = 0.1$ and $k_0(x, y) = 1$. The values of dimensionless parameters used in the simulation are $D_s = 0.001$, $R_s = 0.5$, $\Gamma = 0.1$ and $\eta = 0.5$. The cell update time $t_{update} = 0.25$ and $\Delta t_{cell} = 0.025$.

Similarly initially cells are also distributed uniformly throughout the entire scaffold but it becomes non-uniform after a short time. Cell grow quickly near the scaffold inlet wall where high concentration of nutrient is available and growth of cells is slow in the deeper sections of the scaffold due to low nutrient concentration.

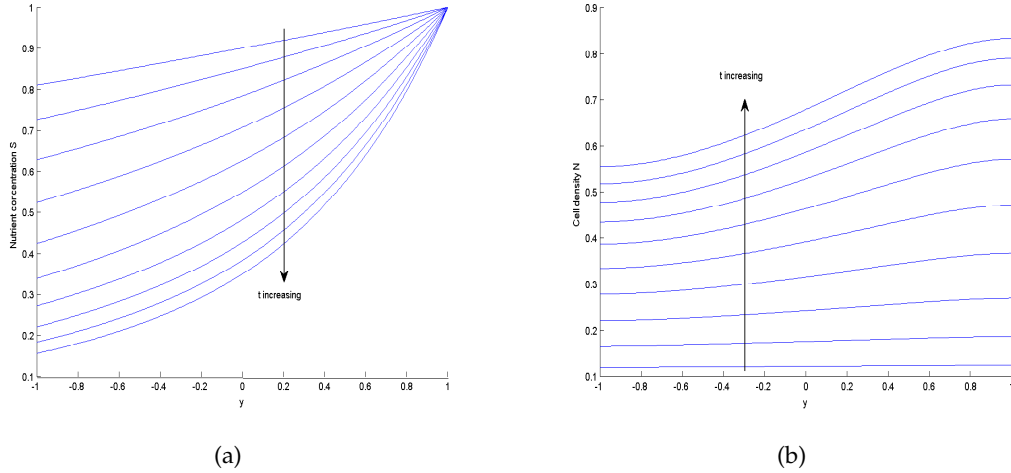


Figure 3.5: Cross section plot of (a) nutrient concentration S and (b) cell density N , at times $t = 0.5 : 0.5 : 5$ when initial seeding and initial permeability both are uniform. The values of dimensionless parameters are same as in Figure 3.4.

3.6.2 Non-uniform initial seeding, uniform initial permeability

Let us consider the case when the initial cell density is non-uniform and initial permeability of the scaffold is uniform. In this case initially we place the blob of cells at the centre of scaffold. Mathematically we represent the initial distribution of cells by

$$N_{init} = 0.17 \exp(-x^2 - y^2). \quad (3.6.1)$$

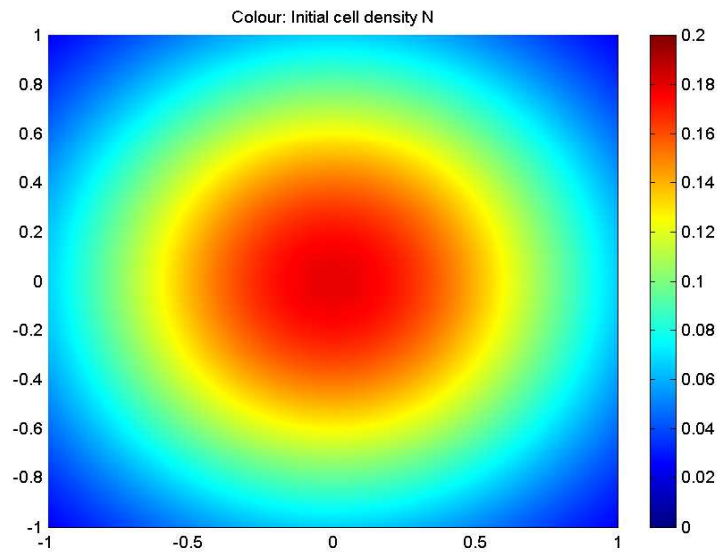
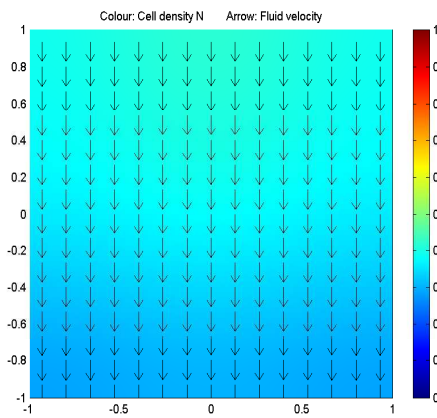


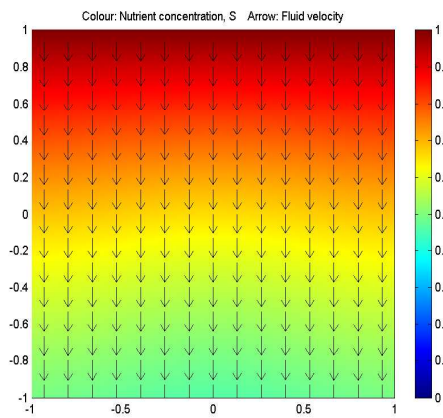
Figure 3.6: Non-uniform initial cell density.

Figure 3.6 shows the initial distribution of cells when a blob of cells is placed at the centre of the scaffold.

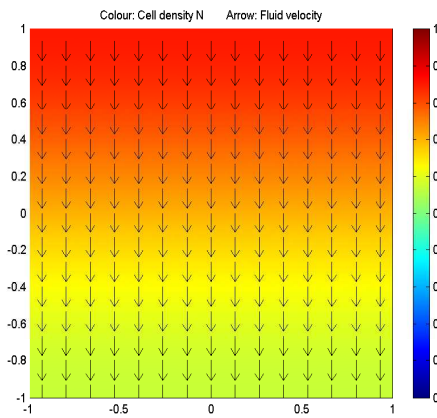
Figure 3.7 shows a sequence of snapshots of fluid velocity (arrow plot), nutrient concentration (color plot) and cell density (color plot) at different times when initial cell density is non-uniform and initial permeability of the scaffold is uniform. Initially nutrients are distributed uniformly throughout the entire depth of scaffold but as time progresses the concentration of nutrient decreases in the deeper sections of the scaffold. We observe from the Figure 3.7 that initially blob of cells is placed at the middle of the scaffold but after a few time units the blob of cell grows and spreads throughout



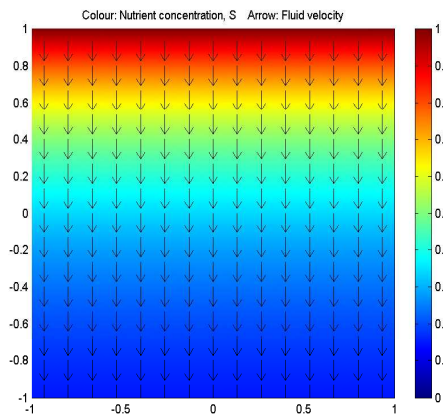
(a) Cell density N and fluid velocity \mathbf{u} at $t = 2$.



(b) Nutrient concentration S and fluid velocity \mathbf{u} at $t = 2$.



(c) Cell density N and fluid velocity \mathbf{u} at $t = 5$.



(d) Nutrient concentration S and fluid velocity \mathbf{u} at $t = 5$.

Figure 3.7: Snapshots of cell density N , nutrient concentration S and velocity \mathbf{u} at times $t = 2$ and $t = 5$ when initial cell density is non-uniform and initial permeability is uniform *i.e.* $N_{init}(x, y) = 0.1793 \exp(-x^2 - y^2)$ and $k_0(x, y) = 1$. The values of dimensionless parameters are same as in Figure 3.4.

the entire scaffold but distribution of cells remains non-uniform. When the blob of cells interacts with the boundaries of the scaffold then the nutrients will not pass easily through this region. The cells beyond this region will be hypoxic. The cells near the scaffold inlet wall grow very quickly due to presence of high nutrient concentration. Most of the nutrients are consumed very quickly by the cells near the inlet wall as a result nutrient concentration is low in the deeper sections of the scaffold.

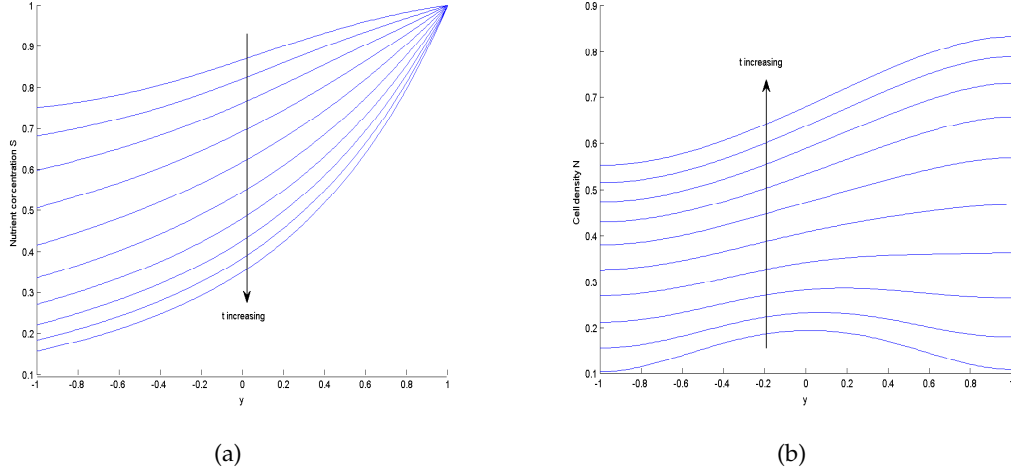


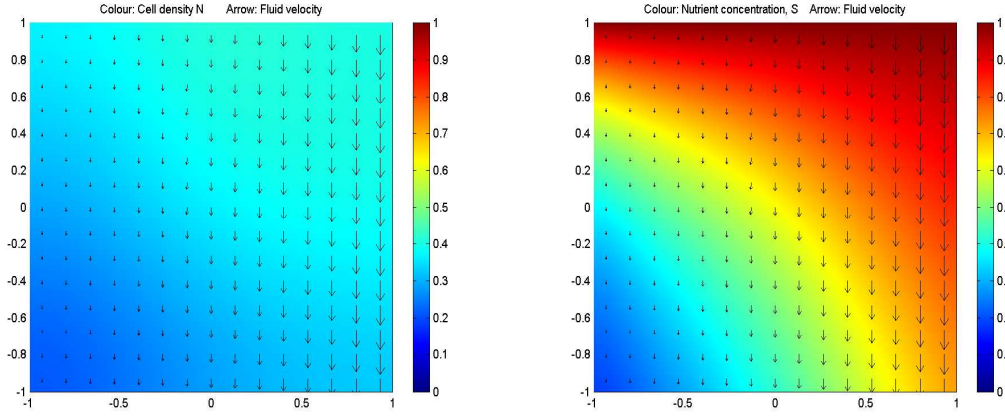
Figure 3.8: Cross section plot of (a) nutrient concentration S and (b) cell density N , at times $t = 0.5 : 0.5 : 5$ when initial seeding is non-uniform and initial permeability is uniform. The values of dimensionless parameters are same as in Figure 3.4.

Figure 3.8 shows the cross section plot of nutrient concentration S and cell density N at $x = 0$ for different times when initial cell density is non-uniform and initial permeability is uniform. It is clear from the Figure that the nutrient concentration is high near the scaffold inlet wall and low in the deeper sections of the scaffold. It also indicates that the cell density is high near the scaffold inlet wall due to presence of high nutrient concentration and the cell density decreases in the deeper sections of the scaffold due to low nutrient concentration.

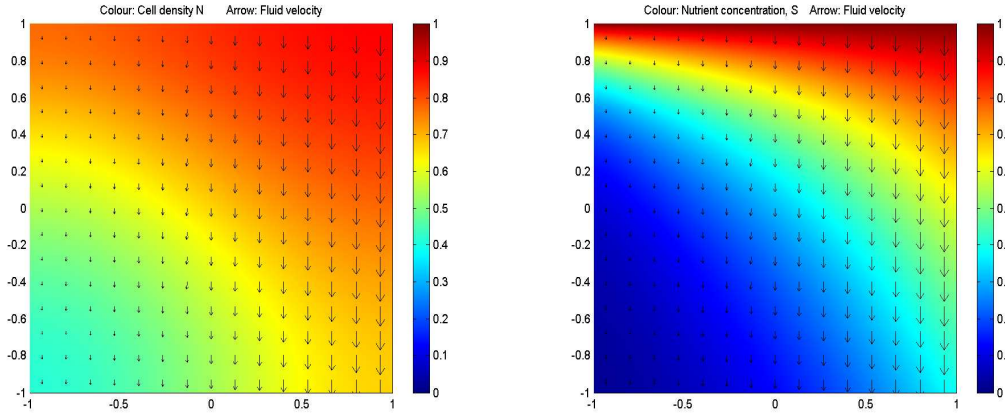
3.6.3 Non-uniform initial seeding and permeability

Consider the case when both initial cell density and initial permeability are non-uniform. We assume that the initial distribution of cell density is same as in shown in the Figure 3.6 and permeability of the scaffold without cells is the exponential function of spatial coordinates *i.e.* $k_0(x, y) = \exp(x + y)$.

Figure 3.9 shows the distribution of cell density and nutrient concentration at times $t = 2$ and $t = 5$ when both initial cell density and initial permeability are non-uniform.



(a) Cell density N and fluid velocity \mathbf{u} at $t = 2$. (b) Nutrient concentration S and fluid velocity \mathbf{u} at $t = 2$.



(c) Cell density N and fluid velocity \mathbf{u} at $t = 5$. (d) Nutrient concentration S and fluid velocity \mathbf{u} at $t = 5$.

Figure 3.9: Snapshots of cell density N , nutrient concentration S and velocity \mathbf{u} at times $t = 0.5 : 0.5 : 5$ when initial seeding and initial permeability are both non-uniform *i.e.* $N_{init} = 0.17 \exp(-x^2 - y^2)$ and $k_0 = \exp(x + y)$. The values of dimensionless parameters are same as in Figure 3.4.

We observe from the Figure 3.9 that cell density and nutrient concentration are high near the top right corner where the permeability is high and low near the bottom left corner where the permeability is small. We also observe that fluid velocity is high where the permeability is high and vice versa.

Figure 3.10 shows the cross section plot of nutrient concentration S and cell density N at $x = 0$ for different times when initial cell density and initial permeability are both non-uniform. We observe that the nutrient concentration in the deeper sections of the scaffold decreases with time. The cell density is high near the inlet wall and low in the deeper sections of the scaffold.

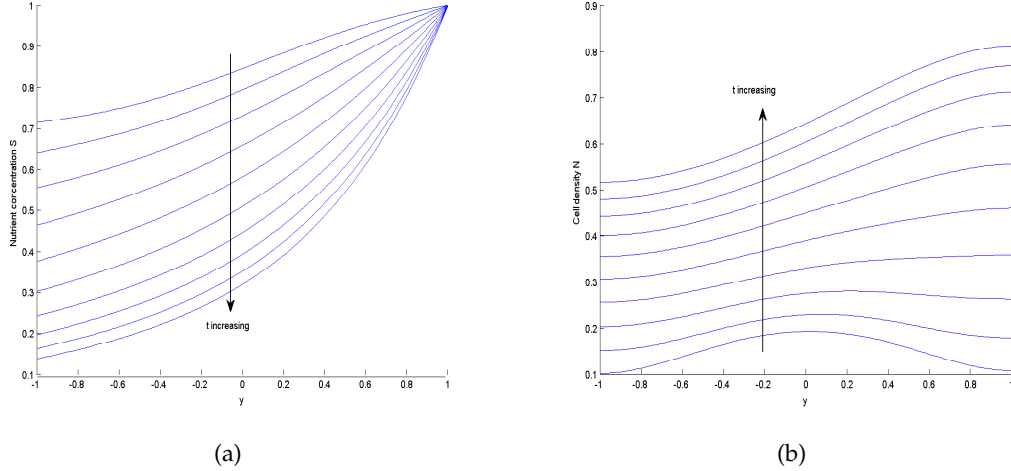
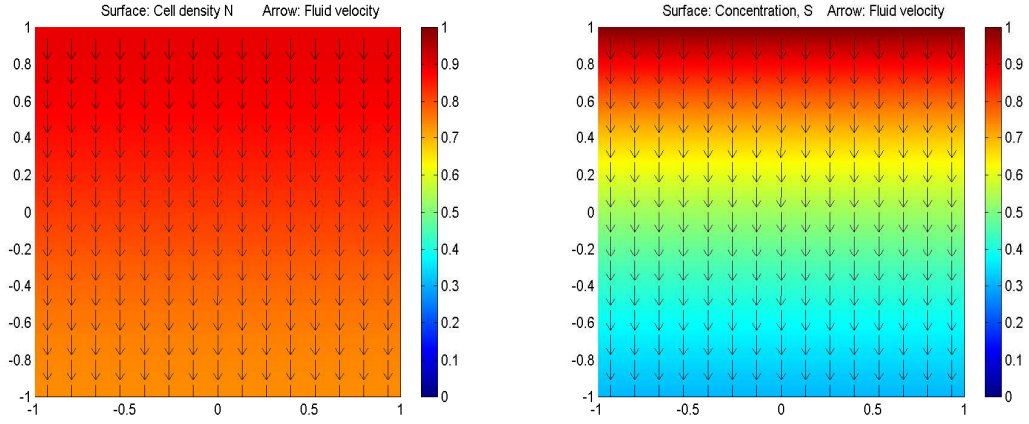


Figure 3.10: Cross section plot of (a) nutrient concentration S and (b) cell density N are plotted for different times when initial cell density and initial permeability are both non-uniform. The values of dimensionless parameters are same as in Figure 3.4.

3.6.4 Effect of parameters

The basic model developed in Section 3.4.1 is a generic model and can be easily employed to other geometric configurations, cell types or operating conditions. For example we can employ different values of flow rate U_c^* and blocking parameter η^* . In all the initial seeding and permeability techniques discussed above if we increase the value of flow rate U_c^* then the dimensionless parameters D_s and R_s both will decrease; since parameter D_s is the ratio of nutrient diffusion to advection and parameter R_s is the ratio of nutrient consumption to advection. Increase in flow rate U_c^* means that both nutrient diffusion and consumption decrease in comparison to advection. Due to decrease in nutrient consumption the growth rate in the deeper sections of the scaffold will increase. The increase in flow rate improves the delivery of nutrients in the deeper sections of the scaffold. Due to improved nutrient concentration away from the nutrient source the cell growth will also increase in these sections of the scaffold. However the decrease in flow rate increases the values of both parameters D_s and R_s . So both nutrient diffusion and consumption increase in comparison to advection. The high consumption rate of nutrients effects the cell growth. Due to high consumption rate most of the nutrients are eaten up very quickly near the inlet walls and cells away from the nutrient source becomes hypoxic and stop growing. However the high value of diffusion coefficient D_s does not help too much for the delivery of nutrients in the deeper sections of the scaffold.

Figure 3.11 shows the cell density N and nutrient concentration S at time $t = 5$ for



(a) Cell density N and fluid velocity \mathbf{u} at $t = 5$. (b) Nutrient concentration S and fluid velocity \mathbf{u} at $t = 5$.

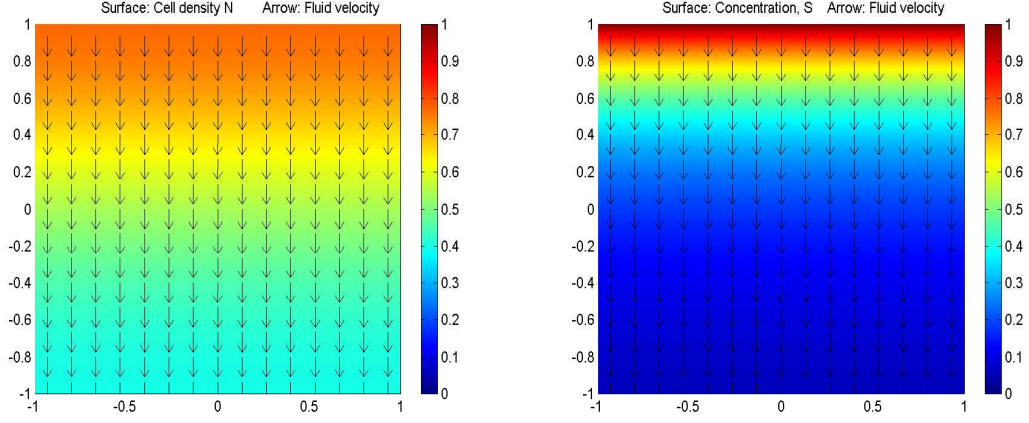
Figure 3.11: Snapshots of cell density N , nutrient concentration S and velocity \mathbf{u} at time $t = 5$. Initial seeding, initial permeability, t_{update} and Δt_{cell} are same as in Figure 3.4. In this case perfusion velocity $U_c^* = 3 \times 10^{-4} m/sec$. The values of dimensionless parameters are $D_s = 0.0005$, $R_s = 0.25$, $\Gamma = 0.1$ and $\eta = 0.5$.

high perfusion velocity. In this case the perfusion velocity U_c^* is double the perfusion velocity used to calculate the results in Figure 3.4. We can observe that the cell density has improved due to improvement in nutrient concentration.

Figure 3.12 shows the cell density N and nutrient concentration S at time $t = 5$ for low perfusion velocity. In this case the perfusion velocity U_c^* is half the perfusion velocity used to calculate the results in Figure 3.4. We can observe that the cell density decreases due to rapid decrease in nutrient concentration.

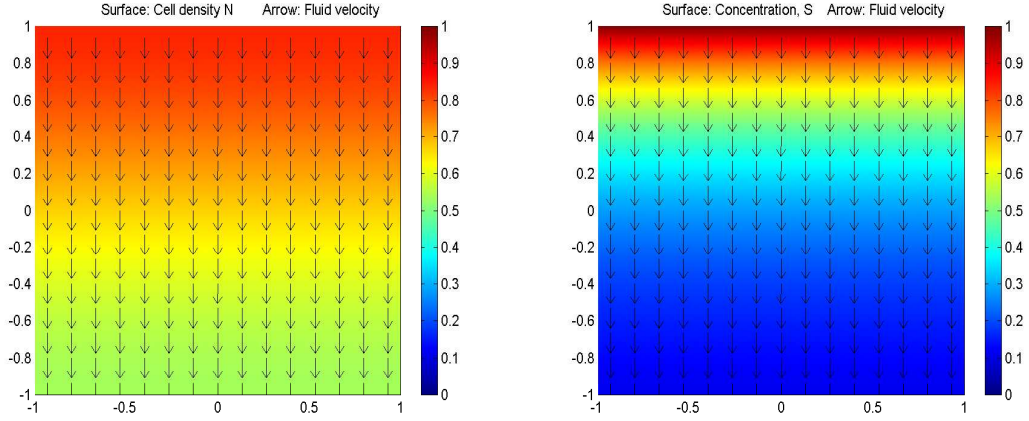
Next we fix all the other parameters as in Figure 3.4 and vary the value of parameter η ; this parameter controls the blocking of porous material. The increase in η decreases the permeability of the scaffold and *vice versa*. The parameter η also affects the growth of cells. This means that with an increase in the value of η , pores will block quickly which decreases the delivery of nutrients in the deeper sections of the scaffold and as a consequence cell growth also decreases in these sections of the scaffold.

Figure 3.13 shows the cell density N and nutrient concentration S at time $t = 5$ for high value of parameter η . It is evident from the Figure, in comparison with the Figure 3.4, that cell density lowers due to the larger value of η .



(a) Cell density N and fluid velocity \mathbf{u} at $t = 5$. (b) Nutrient concentration S and fluid velocity \mathbf{u} at $t = 5$.

Figure 3.12: Snapshots of cell density N , nutrient concentration S and velocity \mathbf{u} at time $t = 5$. Initial seeding, initial permeability, t_{update} and Δt_{cell} are same as in Figure 3.4. In this case perfusion velocity $U_c^* = 7.5 \times 10^{-5} m/sec$. The values of dimensionless parameters are $D_s = 0.002$, $R_s = 1$, $\Gamma = 0.1$ and $\eta = 0.5$.



(a) Cell density N and fluid velocity \mathbf{u} at $t = 5$. (b) Nutrient concentration S and fluid velocity \mathbf{u} at $t = 5$.

Figure 3.13: Snapshots of cell density N , nutrient concentration S and velocity \mathbf{u} at time $t = 5$. Initial seeding, initial permeability, t_{update} , Δt_{cell} and the values of dimensionless parameters except η (in this case $\eta = 0.8$) are same as in Figure 3.4.

3.7 Analytical solution

The model proposed in the Section 3.4 is a coupled model consisting of four equations. It is not possible to solve the model analytically. In this Section we will apply some simplifying assumptions on the nondimensional model proposed in the Section 3.4 so that we can solve the model analytically and compare the numerical and analytical results.

We assume that the initial permeability of the scaffold without cells is constant *i.e.* $k_0(x, y) = \text{constant}$, and the initial cell density $N_{init}(x, y)$ is uniform throughout the scaffold. From equation (3.4.11) we observe that the permeability of the scaffold is constant only when $N = N_{init}$ or $N = 1$ in the entire domain. This implies that permeability of the scaffold is constant only at initial times and at large times. Hence $k_j(x, y, N) = k_0(x, y) \exp(-\eta N_j)$ is constant, when $N_j = N_{init}, N_{max}$ or if $\eta = 0$. After these simplifying assumptions equation (3.4.3) reduces to

$$\nabla^2 p = 0. \quad (3.7.1)$$

Equation (3.7.1) is a second order partial differential equation which can be solved analytically subject to boundary conditions (3.4.4) using the method of separation of variables (See Chapter 2 Section 2.6.3). The analytic solution of equation (3.7.1) is

$$p = \frac{1}{2}(1 + y). \quad (3.7.2)$$

We conclude that when the permeability of the scaffold is constant then the pressure is a linear function of y only. Let $A_1 = k_0(x, y) \exp(-\eta N_j)$ then if we choose $k_0(x, y) = 1$ then by substituting the expression for p from equation (3.7.2) into equation (3.4.1) we get $\mathbf{u} = \left(0, -\frac{A_1}{2}\right)$ *i.e.* fluid is moving with uniform velocity in the direction of y .

Since the fluid velocity depends only on one spatial variable y and we apply zero flux boundary conditions on the side walls of the scaffold at $x = \pm 1$ for both nutrient transport and cell growth equations (3.4.5) and (3.4.8), consequently nutrient concentration S and cell density N are only functions of one spatial variable y . Hence the nutrient transport equation (3.4.5) reduces to

$$\mathbf{u} \cdot \nabla S(y) = D_s \nabla^2 S(y) - R_s S(y) N(y). \quad (3.7.3)$$

To solve equation (3.7.3) we need two boundary conditions given by

$$S = 1, \quad \text{at } y = 1, \quad -1 \leq x \leq 1, \quad (3.7.4a)$$

$$\frac{dS}{dy} = 0, \quad \text{at } y = -1 \quad -1 \leq x \leq 1. \quad (3.7.4b)$$

Substituting $\mathbf{u} = \left(0, -\frac{A_1}{2}\right)$ in equation (3.7.3) we obtain,

$$D_s \frac{d^2 S(y)}{dy^2} + \frac{A_1}{2} \frac{dS(y)}{dy} - R_s S(y) N(y) = 0. \quad (3.7.5)$$

Similarly, the cell density N is a function of y only and hence equation (3.4.8) reduces to a second order one dimensional time dependent reaction diffusion equation

$$\frac{\partial N(y, t)}{\partial t} = \Gamma \frac{\partial^2 N(y, t)}{\partial y^2} + SN(y, t)(1 - N(y, t)), \quad (3.7.6)$$

The boundary and initial conditions are

$$\frac{\partial N(y, t)}{\partial y} = 0, \quad \text{at } y = \pm 1, \quad (3.7.7a)$$

$$N = N_{init}, \quad \text{at } t = 0. \quad (3.7.7b)$$

Equations (3.7.5) and (3.7.6) are coupled equations and we solve this coupled system analytically when the permeability of the scaffold is constant. Permeability is constant only when $N = N_{init}$ or $N = 1$ and $\eta = 0$ so we consider two cases for the solution of this coupled system. First we consider the growth of cells at initial times *i.e.* very close to $t = 0$, before going on to the solution at large times *i.e.* when cell density N approaches its maximum limit 1.

3.7.1 Case I: Initial time solution

At initial time the cell density $N \approx N_{init}$, where N_{init} is constant. Then equation (3.7.5) can be approximated as

$$\frac{d^2 S(y)}{dy^2} + A \frac{dS(y)}{dy} - BS(y) = 0, \quad (3.7.8)$$

where

$$A = \frac{\exp(-\eta N_{init})}{2D_s} \quad \text{and} \quad B = \frac{R_s N_{init}}{D_s}.$$

Equation (3.7.8) is a second order, constant coefficient, homogeneous ordinary differential equation. The solution of equation (3.7.8) is,

$$S(y) = M_1 e^{\gamma_1 y} + M_2 e^{\gamma_2 y}, \quad (3.7.9)$$

where M_1 and M_2 are arbitrary constants and

$$\gamma_1 = \frac{-A + \sqrt{A^2 + 4B}}{2}, \quad \gamma_2 = \frac{-A - \sqrt{A^2 + 4B}}{2}. \quad (3.7.10)$$

The values of constants M_1 and M_2 can be found by using the boundary conditions (3.7.4), which gives

$$M_1 = -\frac{\gamma_2 e^{\gamma_1}}{(\gamma_1 e^{2\gamma_2} - \gamma_2 e^{2\gamma_1})}, \quad M_2 = \frac{\gamma_1 e^{\gamma_2}}{(\gamma_1 e^{2\gamma_2} - \gamma_2 e^{2\gamma_1})}.$$

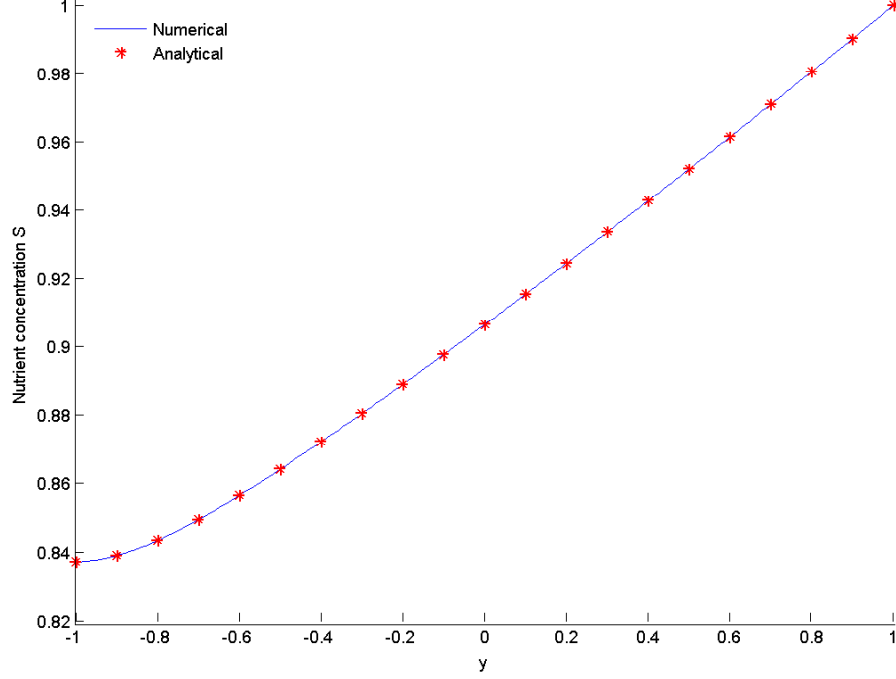


Figure 3.14: Analytical solution (3.7.9) and numerical results of profile of nutrient concentration S at time $t = 1$. The parameter values used in the simulation are $D_s = 0.1$, $R_s = 0.5$, $\eta = 0.01$, $k_0(x, y) = 1$ and $N_{init} = 0.1$.

Figure 3.14 shows the profile of nutrient concentration at time $t = 1$. Both the analytic solution (3.7.9) and numerical results of the nutrient concentration at time $t = 1$ are plotted on top of each other. At time $t = 1$ nutrient concentration is high near the scaffold inlet wall but it decreases continuously as we move towards the scaffold exit wall. The concentration of nutrients is low in the deeper sections of the scaffold as compared to the scaffold entrance. It is clear from the Figure 3.14 that the analytic and numerical results for the nutrient concentration S agree at time $t = 1$.

At initial times the cell density N is independent of y because the initial cell density in the entire scaffold is uniform. With this assumption equation (3.7.6) becomes,

$$\frac{dN(y, t)}{dt} = S(y)N(y, t)(1 - N(y, t)), \quad (3.7.11)$$

whose solution subject to initial condition (3.7.7b) is given by

$$N = \frac{B_1 \exp(S(y)t)}{1 + B_1 \exp(S(y)t)}, \quad (3.7.12)$$

where $B_1 = N_{init}/(1 - N_{init})$. Hence the cell density N grows exponentially and the change in cell density N depends on the available nutrient concentration S . Equation (3.7.12) indicates that if the nutrient concentration is high then the cell density N is high.

Figure 3.15 shows the analytic solution (3.7.12) and numerical results of cell density N for various value of y for times $0 \leq t \leq 1$. It is clear from the Figure that the growth of cells is high near the scaffold inlet wall $y = 1$ due to presence of high concentration of nutrients and the growth of cells decreases as we move away from the scaffold inlet wall because the concentration of nutrients also decreases in these sections of the scaffold. Analytic and numerical results for various values of y at times $0 \leq t \leq 1$ are in good agreement.

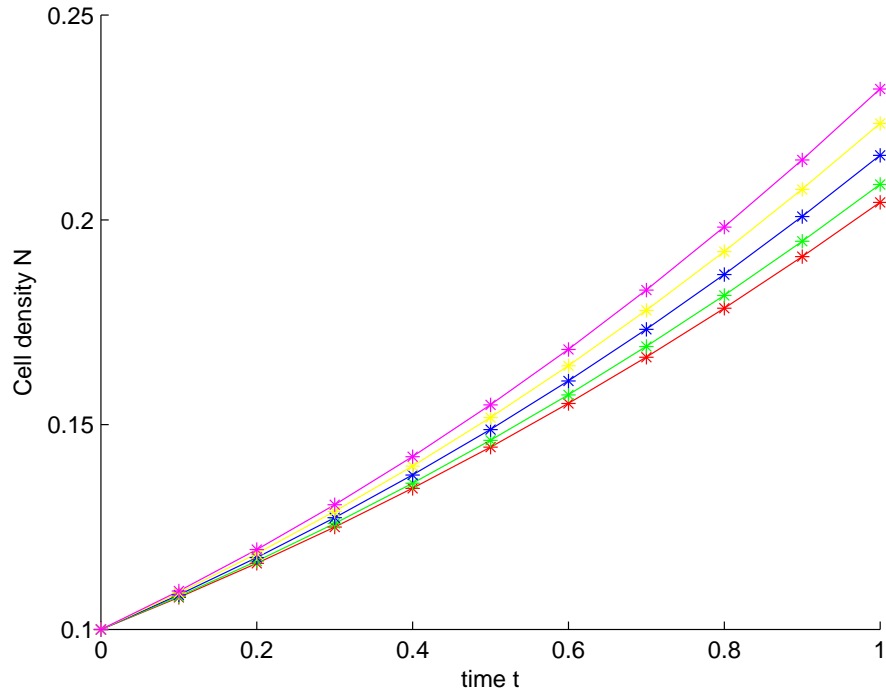


Figure 3.15: \blacklozenge $y = 1$, \blacklozenge $y = 0.5$, \blacklozenge $y = 0$, \blacklozenge $y = -0.5$, \blacklozenge $y = -1$. Analytic solution (3.7.12) and numerical results of cell density N for various values of y at times $0 \leq t \leq 1$. Solid lines represents the numerical solution and * represents the analytical solution. Initial cell density $N_{init} = 0.1$ and initial permeability $k_0(x, y) = 1$. The parameter values used in the simulation are $D_s = 0.1$, $R_s = 0.5$, $\eta = 0.01$.

To establish that the numerical coupling is properly implemented we did further checks. We assume that the coupled transport equation and time dependent cell growth equations are solved analytically for times $0 \leq t \leq 1$. In the analytical solution as the cells grow according to equation (3.7.12) we do not update the nutrient concentration S . But in the case of numerical coupled system we divide the interval $0 \leq t \leq 1$ into n time steps of length t_{update} . After each time t_{update} as the number of cells increase the system is solved for updated cell density or in other words we can say that numerical coupling is two directional. When the number of cells increase they consume more nutrients and as a result nutrient concentration decreases after each time t_{update} . Because the nutrient concentration decreases after each time t_{update} the rate of cell growth also decreases.

We compare the analytic results of nutrient concentration S and cell density N for various values of y for times $0 \leq t \leq 1$ (when the coupling is one directional) with the numerical results (when coupling is two directional). Figure 3.16 shows analytic solution (3.7.9) of profile of nutrient concentration for times $0 \leq t \leq 1$ (when the cells are not being updated) and numerical solution for the profile of nutrient concentra-

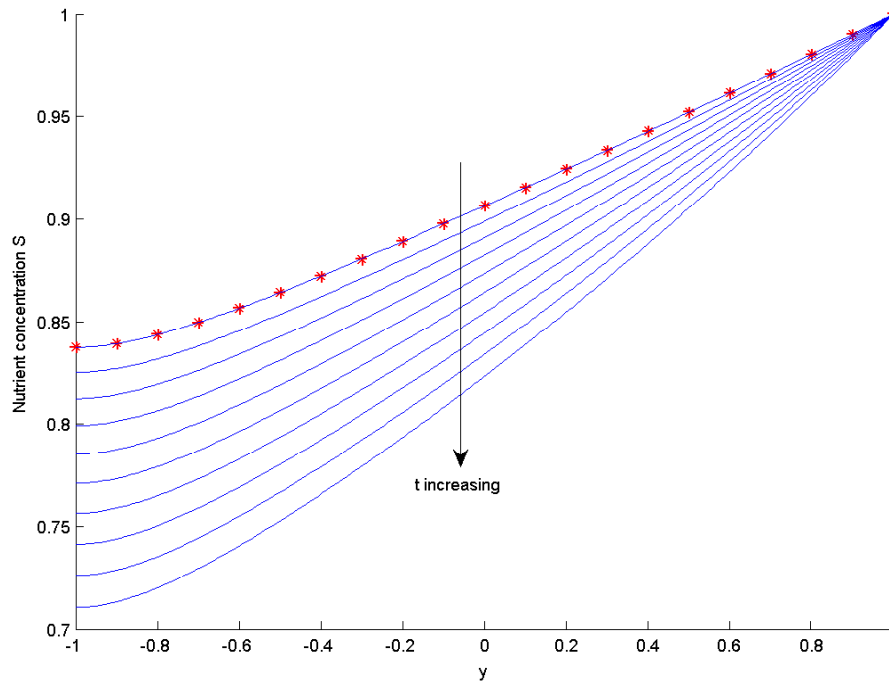


Figure 3.16: Analytic solution (3.7.9) of profile of nutrient concentration S for times $0 \leq t \leq 1$ when cells are not updated and numerical results of the profile of nutrient concentration S when cells are updated after each time $t_{update} = 0.1$. * represents the analytic solution and solid lines represents the numerical results of nutrient concentration. Arrow indicates that graph is being read from top to bottom. The parameter values used in the simulation are $D_s = 0.1$, $R_s = 0.5$, $\eta = 0.01$, $N_{init} = 0.1$ and $k_0(x, y) = 1$.

tion (when the cells are being updated after each time $t_{update} = 0.1$). It is evident from the Figure that initially when the cells are not updated both analytical and numerical solutions agree and after each time t_{update} , when the transport equation is solved for updated cell density, the nutrient concentration decreases after each time because with the increase in cell density the consumption of nutrient increases. As a result nutrient concentration decreases especially in the deeper sections of the scaffold which causes a decrease in cell growth.

Figure 3.17 shows the analytical solution (3.7.12) (when the cells are not updated) and numerical results (when the cells are updated after each time t_{update}) of cell density N at times $0 \leq t \leq 1$ for various values of y . In the numerical coupled system we solve for the flow field, nutrient transport and time dependent cell growth equation respectively. After each time t_{update} the system is solved again for updated cell density. When the number of cells increases they consume more nutrients for the growth so after each time step the cell growth decreases. This is because after each time step the available nutrient concentration is less than the previous step and cell density is more than the previous

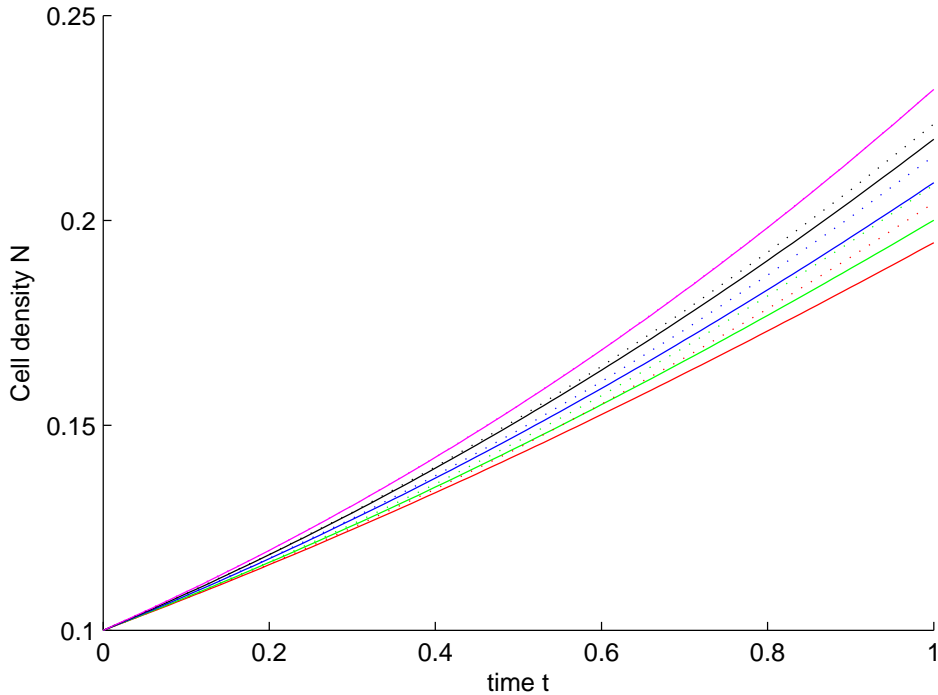


Figure 3.17: \blacklozenge $y = 1$, \blacklozenge $y = 0.5$, \blacklozenge $y = 0$, \blacklozenge $y = -0.5$, \blacklozenge $y = -1$. Dotted lines represents the analytic results and solid lines represents numerical results. Analytic solution of equation (3.7.12) (when cells are not updated) and numerical results (when cells are updated after each time step $t_{update} = 0.1$) of cell density N for times $0 \leq t \leq 1$ are plotted. The parameter values used in the simulation are $D_s = 0.1$, $R_s = 0.5$, $\eta = 0.01$, $N_{init} = 0.1$ and $k_0(x, y) = 1$.

step. That is why the numerical results deviate from the analytic results which indicates that our numerical coupling is working properly. We can see from the Figure 3.17 that both numerical and analytical results agree at the initial times but with the passage of time when numerical system is solved for updated cell density it starts deviating from the analytic results. But at the boundary $y = 1$ both the numerical and analytical results agree well because at the boundary $y = 1$ the available nutrient concentration remains constant. The deviation between analytical and numerical results increases as we move away from the scaffold inlet boundary $y = 1$ and this deviation is high at the boundary $y = -1$. This is because at the boundary $y = -1$ the available nutrient concentration is low.

3.7.2 Case II: Steady state solution

For steady state solution $\partial N/\partial t = 0$, then equation (3.7.6) reduces to,

$$\Gamma \frac{\partial^2 N(y)}{\partial y^2} + SN(y)(1 - N(y)) = 0, \quad (3.7.13)$$

$N(y) = 1$ satisfies the equation (3.7.13) and boundary conditions (3.7.7a).

For $N(y) = 1$, equation (3.7.5) becomes

$$\frac{d^2 S(y)}{dy^2} + \tilde{A} \frac{dS(y)}{dy} - \tilde{B} S(y) = 0, \quad (3.7.14)$$

where

$$\tilde{A} = \frac{\exp(-\eta)}{2D_s} \quad \text{and} \quad \tilde{B} = \frac{R_s}{D_s}.$$

The solution of equation (3.7.14) is

$$S(y) = \tilde{M}_1 e^{\eta_1 y} + \tilde{M}_2 e^{\eta_2 y}, \quad (3.7.15)$$

where \tilde{M}_1 and \tilde{M}_2 are arbitrary constants and

$$\eta_1 = \frac{-\tilde{A} + \sqrt{\tilde{A}^2 + 4\tilde{B}}}{2}, \quad \eta_2 = \frac{-\tilde{A} - \sqrt{\tilde{A}^2 + 4\tilde{B}}}{2}. \quad (3.7.16)$$

The values of constants \tilde{M}_1 and \tilde{M}_2 can be found by using the boundary conditions

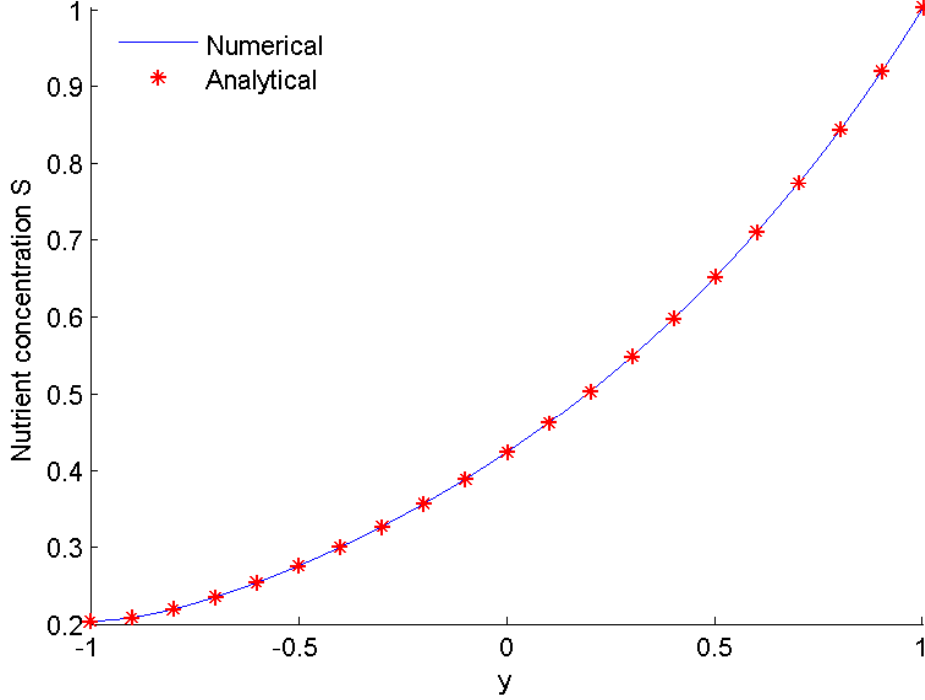


Figure 3.18: Analytic solution (3.7.15) and numerical solution of profile of nutrient concentration S at steady state. * represent the analytical result and solid line represent the numerical result. The parameter values used in the simulation are $D_s = 0.1$, $R_s = 0.5$, $\eta = 0.01$, $N_{init} = 0.1$ and $k_0(x, y) = 1$.

(3.7.4), which gives

$$\tilde{M}_1 = -\frac{\eta_2 e^{\eta_1}}{(\eta_1 e^{2\eta_2} - \eta_2 e^{2\eta_1})}, \quad \tilde{M}_2 = \frac{\eta_1 e^{\eta_2}}{(\eta_1 e^{2\eta_2} - \eta_2 e^{2\eta_1})}.$$

Figure 3.18 shows the analytical solution (3.7.15) and numerical results of profile of nutrient concentration at steady state. It is clear from the Figure 3.18 that at the steady state the concentration of nutrients is very low in the deeper sections of the scaffold. Numerical and analytic solution agree at the steady state. The length scale of nutrient penetration is $1/\eta_1$. In Figure 3.18 the length scale of nutrient penetration is 0.95.

Figure 3.19 shows that the cell density is approaching steady state for various values of y . Analytically at steady state $N = 1$ which is shown in the Figure 3.19. Numerically the system approaches steady state at different rates depending on the availability of nutrients in the various regions of the scaffold. The region close to the nutrient source gets to steady state quickly because near the nutrient source the availability of nutrients is high and as a result the rate of cell growth is high.

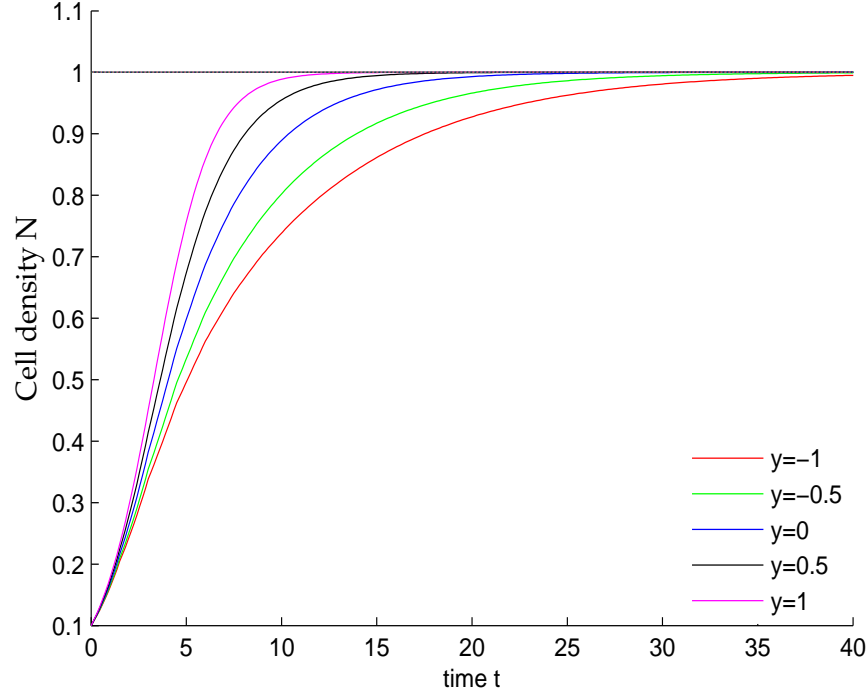


Figure 3.19: Cell density N for the various values of y approaching to steady state. The parameter values used in the simulation are $D_s = 0.1$, $R_s = 0.1$, $\eta = 0.01$, $N_{init} = 0.1$ and $k_0(x, y) = 1$.

3.8 Stability of steady state solution

The steady state solution $N = 1$ will be stable if every solution close to $N = 1$ decays to 1. To check the stability of steady state solution $N = 1$ we perturb the solution $N = 1$ from the equilibrium position and check that whether the perturbed solution decays to 1 or not. So we write,

$$N(y, t) = 1 + \epsilon N_1. \quad (3.8.1)$$

Substituting this solution into equation (3.7.6) and collecting $O(\epsilon)$ terms we get an ordinary differential equations in N_1 ,

$$\frac{\partial N_1}{\partial t} = \Gamma \frac{\partial^2 N_1}{\partial y^2} - S(y)N_1, \quad (3.8.2)$$

subject to boundary conditions,

$$\frac{\partial N_1}{\partial y} = 0 \quad \text{at} \quad y = \pm 1 \quad -1 \leq x \leq 1. \quad (3.8.3)$$

Substituting $N_1 = e^{\tilde{\lambda}t} f(y)$ into equation (3.8.2) we get,

$$\Gamma \frac{d^2 f(y)}{dy^2} - (\tilde{\lambda} + S(y))f(y) = 0. \quad (3.8.4)$$

Multiplying equation (3.8.4) by $f(y)$ and integrate from -1 to 1 we get,

$$\Gamma \int_{-1}^1 \left(\frac{df}{dy} \right)^2 dy + \int_{-1}^1 (\tilde{\lambda} + S(y))f^2(y)dy = 0. \quad (3.8.5)$$

Solving the equation (3.8.5) for $\tilde{\lambda}$ we get,

$$\tilde{\lambda} = - \frac{\Gamma \int_{-1}^1 \left(\frac{df}{dy} \right)^2 dy + \int_{-1}^1 S(y)f^2(y)dy}{\int_{-1}^1 f^2(y)dy}. \quad (3.8.6)$$

All the terms on the right hand side of equation (3.8.6) are positive, which implies that all the eigenvalues $\tilde{\lambda}$ are negative. Since eigenvalues are negative the solution N_1 is stable. Hence the steady state solution $N = 1$ is a stable solution. To check the stability

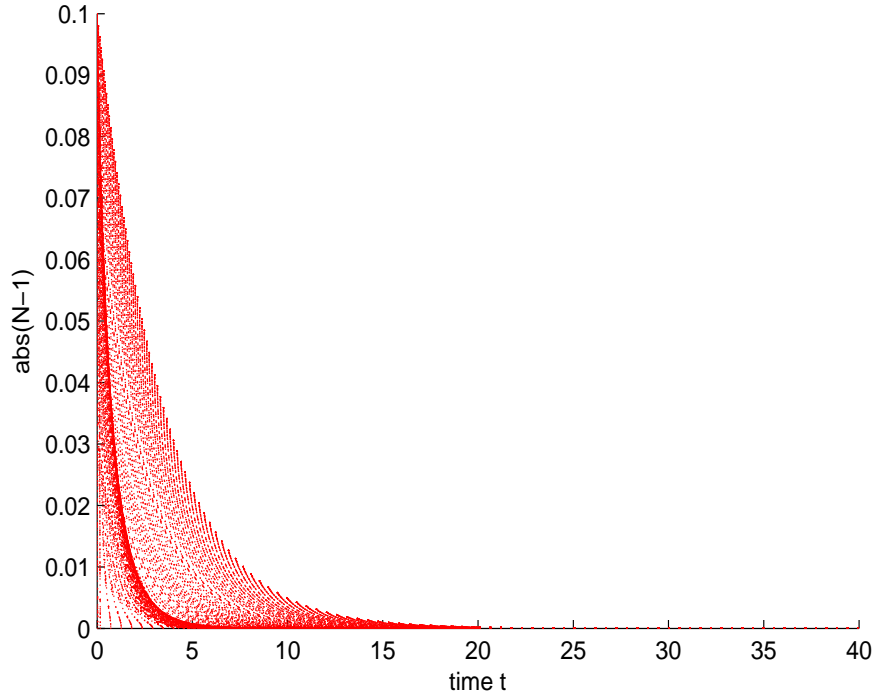


Figure 3.20: Stability of numerical solution at steady state. The parameter values used in the simulation are $D_s = 0.1$, $R_s = 0.5$, $\eta = 0.1$, and $N_{init} = 1 + 0.1 \sin(\pi y/2)$.

of numerical solution at the steady state we chose initial cell density N as

$$N_{init}(x, y) = 1 + \epsilon f(y) \quad (3.8.7)$$

where $\epsilon \ll 1$ is a very small number and $f(y)$ is any function of y which satisfies the boundary conditions. If we choose $\epsilon = 0.1$ and $f(y) = \sin(\frac{\pi y}{2})$ then we can see from the Figure 3.20 that all the solutions close to $N = 1$ decay exponentially to $N = 1$. This indicates that at the steady state the numerical solution is also stable.

3.9 Fixing flow rate

In experiments constant volumetric flow rate is maintained through the scaffold. In this Section we discuss how the real velocity is rescaled to keep the volumetric flow rate constant. When the cells grow and occupy the scaffold voids then permeability of scaffold decreases as a result velocity of the fluid flowing through the porous material decreases. The fluid velocity continuously decreases with the increase in cell density. The decrease in fluid velocity effects the delivery of nutrients to the cells. The growth of cells decreases with the decrease in nutrient concentration. To overcome this problem we fixed the flow rate and divide the Darcy's velocity by a constant that ensures that total flux across every line $y = d$ is constant. By the fixing flow rate delivery of nutrients to the cells especially in the deeper sections of the scaffold improves. The velocity \mathbf{u} obtained from the solution of Darcy's law, with zero-flux boundary conditions at the side walls of the scaffold, has only one component in the direction of y *i.e.* velocity $\mathbf{u} = (0, u_y)$. Since flow is incompressible and has zero-flux through the boundaries $x = \pm 1$. Therefore the total volumetric flux through $y = d$ is

$$u_d = \frac{1}{2} \int_{-1}^1 k(x, d, N) \frac{\partial P}{\partial y} dx, \quad (3.9.1)$$

which is independent of d . To keep the flow rate constant we rescale the velocity obtained from Darcy's law. To do this numerically we divide the actual velocity obtained from Darcy's law by the volumetric flux u_d at $y = d$, where $-1 \leq d \leq 1$ *i.e.*

$$\mathbf{u}_r = \frac{\mathbf{u}}{u_d},$$

where \mathbf{u}_r is the rescaled velocity, \mathbf{u} is the real velocity obtained from the Darcy's law and u_d is the flow rate at $y = d$. Let us calculate the rescaled velocity \mathbf{u}_r for uniform initial cell density and uniform initial permeability. For a constant initial permeability the flow rate at $y = d$ is given by

$$u_d = \frac{1}{2} \int_{-1}^1 \exp(-\eta N) \frac{\partial P}{\partial y} dx. \quad (3.9.2)$$

To keep the flow rate constant we do this rescaling whenever we update the cells. To

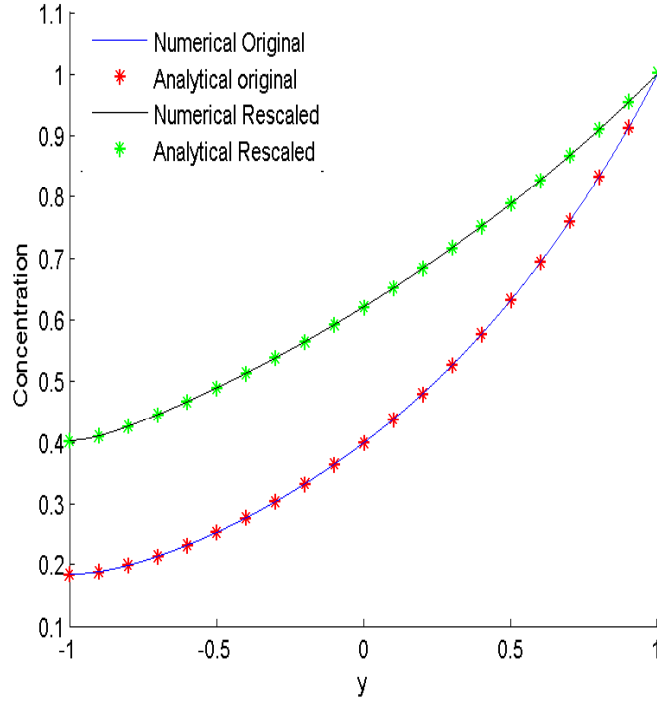


Figure 3.21: Analytic solution and numerical results of profile of nutrient concentration for original and rescaled problem. The parameter values used in the simulation are $D_s = 0.1$, $R_s = 0.5$.

check that numerical coupling is implemented properly we compare the numerical results with the analytic solution at the steady state.

We know that Darcy's velocity at the steady state is $\mathbf{u} = \left(0, -\frac{\exp(-\eta)}{2}\right)$. To calculate the rescaled velocity \mathbf{u}_r we divide \mathbf{u} by \mathbf{u}_d . From equation (3.9.2) and (3.7.2) we obtain

$$u_d = \frac{1}{2} \exp(-\eta N), \quad (3.9.3)$$

which implies that $\mathbf{u}_r = (0, -1)$. Alternatively if in the analytic solution at steady state we replace the pressure boundary conditions (3.3.4) with the velocity boundary conditions *i.e.*

$$\exp(-\eta) \frac{\partial p}{\partial y} = 1 \quad \text{at } y = \pm 1. \quad (3.9.4)$$

Solution of equation (3.7.1) subject to boundary conditions (3.9.4) is

$$p = \frac{1}{\exp(-\eta)} (1 + y). \quad (3.9.5)$$

If we choose $k_0(x, y) = 1$ then by substituting the expression for p from equation (3.9.5) into equation (3.4.1) we get $\mathbf{u}_r = (0, -1)$. Substituting $\mathbf{u}_r = (0, -1)$ in equation (3.7.3) we can calculate the nutrient concentration S at the steady state.

Figure 3.21 shows the analytic and numerical results of the profile of nutrient concentration for the original and rescaled problem. It is clear from the Figure that at the steady state when the flow rate is kept fixed the nutrient concentration in the deeper sections of the scaffold becomes high as compared to the original problem which are the expected results. The rescaled problem approaches the steady state quickly as compared to the original problem due to presence of high nutrient concentration in the deeper sections of the scaffold.

3.10 Conclusions

In this Chapter we have developed a simple mathematical model of fluid flow, nutrient concentration and cell growth in a perfusion bioreactor. The cell density in the final construct depends on the initial seeding technique and initial permeability of the scaffold. We present numerical results for uniform and non-uniform initial cell density and initial permeability of the scaffold. We observe from the results that the velocity of fluid and nutrient concentration are high in the regions where the permeability of the scaffold is high and *vice versa*. To solve the system analytically we apply some simplifying assumptions. We solve the system analytically for constant permeability. We observe that the analytical and numerical results for nutrient concentration S and cell density N agree at initial times as shown in the figures 3.14 and 3.15. Analytical and numerical results for nutrient concentration S and cell density N also agree at large times as shown in the Figures 3.18 and 3.19. We have solved the system analytically at initial times and at large times. It is not possible to solve the system analytically at intermediate times. Since analytic and numerical results agree for the initial times and at the large time (when system reaches steady state) so we conclude that the numerical coupling is properly implemented. We have also proved analytically and numerically that all the solutions close to steady state solution $N = 1$ decay to $N = 1$.

Later in Chapter 5 we will update the model developed in Section 3.4 by including the more complicated effects in the model, such as non-linear cell diffusion, effect of fluid induced shear stress on cell growth and nutrient consumption rates, and fixed flow rate.

Fisher-Kolmogorov equation with non-linear diffusion

4.1 Introduction

The process by which material spreads is called diffusion. It is a fundamental concept and important in biology and medicine, chemistry and geology, engineering and physics. Diffusion is the result of constant thermal motion of atoms, molecules and particles. It transports material from a region of high concentration to a region of low concentration. Thus the end result of diffusion would be a constant concentration, throughout space, of each of the components in the environment.

For a long time diffusion has been used as a model for spatial spread in many biological systems. Murray (1989) and Okubo (1980) used diffusion in invasion and pattern formation and Skellam (1991) studied diffusion in the field of ecology. For motile cell populations diffusion has been used in different situations. Chaplain and Stuart (1993) used diffusion to model the capillary growth network and Sherratt and Murray (1990) used it to model wound healing.

In biological models linear diffusion is an established model to study the movement of cell populations spatially. But it is not suitable for closely packed cell populations (Sherratt, 2000) such as epithelia, where one cell is in direct contact with its neighboring cell. For closely packed cells, a reaction diffusion equation can be used to model single population models (Chaplain and Stuart, 1991, Sherratt and Murray, 1990). But for different population models, a diffusion term would imply that populations can mix completely and movement of one cell type is not affected by the presence of the cells of other type. In reality this is entirely opposite, different cell populations cannot move

through one another; instead the cell will stop moving when it unexpectedly collides with another cell. This phenomenon is known as "contact inhibition of migration". This process has been well documented in many types of cells (Abercrombie, 1970).

In all biological systems the exchange of information at both inter- and intra- cellular level is almost continuous. In order to get sequential development and generation of the required pattern such communication is necessary *e.g.* for development and growth of an embryo. Propagating waveforms are one of the ways of conveying such biological information between the cells. Let us consider a simple one-dimensional diffusion equation

$$\frac{\partial N^*}{\partial t^*} = D^* \frac{\partial^2 N^*}{\partial x^{*2}}, \quad (4.1.1)$$

where N^* is chemical (cell or nutrient) concentration and D^* is diffusion coefficient. The time to exchange information in the form of changed concentration is $O(L^{*2}/D^*)$, where L^* is the length of domain. We can get this order by dimensional arguments of equation (4.1.1). At the early stage of growth of an organism the diffusion coefficient can be very small: values of order 10^{-9} to $10^{-11} \text{cm}^2 \text{sec}^{-1}$. If diffusion is the main process to convey the biological information then to cover the macroscopic distances of several millimeters requires a very long time. When the diffusion coefficient is $O(10^{-9}$ to $10^{-11} \text{cm}^2 \text{sec}^{-1})$ and L^* is order of 1mm then the time required to convey the information is $O(10^7 \text{ to } 10^9 \text{sec})$, which is very large in the early stages of growth of an organism. This means that simple diffusion is unlikely to be the main means of exchanging the information during embryogenesis. Kareiva (1983) and Tilman and Kareiva (1997) estimated the diffusion coefficient for insect dispersal in interacting population. About seventy years ago Fisher (1937) and Kolmogorov et al. (1937) introduced a classical model to describe the propagation of an advantageous gene in a one-dimensional habitat. The equation describing the phenomenon is a one-dimensional non-linear reaction-diffusion equation,

$$\frac{\partial N^*}{\partial t^*} = D^* \frac{\partial^2 N^*}{\partial x^{*2}} + \chi^* N^* (1 - N^*), \quad (4.1.2)$$

where N^* is chemical concentration, D^* is the diffusion coefficient and the positive constant χ^* represents the growth rate of the chemical reaction. Since then a great deal of work has been carried out to extend their model to take into account the other biological, chemical and physical factors. The equation (4.1.2) is also used in logistic growth models (Murray, 1977), neurophysiology (Tuckwell, 1988), flame propagation (Frank-

Kamenetskii, 1955), autocatalytic chemical reactions (Cohen, 1971, Fife and McLeod, 1977), and nuclear reactor theory (Canosa, 1969).

One of the extensions of the Fisher and Kolmogorov model is to introduce a non-linear diffusion coefficient, which can be taken as a non-linear Fick's law. The non-linearity can arise in terms of a space, time or density-dependent diffusion coefficient. In the Fisher and Kolmogorov model the reaction kinetics are coupled to diffusion which gives travelling waves of chemical concentration and it can affect the biological change very much faster as compared to the processes governed by simple diffusion without the kinetic term. In many biological populations density-dependent dispersal has been observed *e.g.* Myers and Krebs (1974) studied the population density cycles in small rodents, Carl (1971) observed that ground squirrels move from highly populated area to sparsely populated areas. Several mathematical models have been developed to describe the density-dependent dispersal systems. Gurney and Nisbet (1975, 1976) developed a first density-dependent diffusion model in ecological context by using a random walk approach and Montroll and West (1979) developed a one-dimensional model for single species by using the same approach. But there is not much work on the Fisher equation with non-linear diffusion. Sánchez-Garduño and Maini (1994) studied a travelling wave solution in a degenerate non-linear diffusion Fisher equation.

Although equation (4.1.2) is known as the Fisher-Kolmogorov equation, the discovery, investigation and analysis of travelling waves in chemical reactions was first reported by Luther (1906). He found that the wave speed is a simple consequence of the differential equations. He obtained the wave speed in terms of parameters associated with the reactions he was studying. The analytical form is the same as that found by Kolmogorov et al. (1937) and Fisher (1937).

Equation (4.1.2) has two homogeneous stationary states $N^* = 0$ and $N^* = 1$. A travelling wave solution of equation (4.1.2) describes a constant velocity front of transition from one homogeneous state to another. Kolmogorov et al. (1937) introduced a classical approach to investigate the travelling wave solution $N^*(x^*, t^*) = \phi(x^* - v^*t^*)$, of the reaction-diffusion system. In this case the original initial and boundary value problem is re-stated in terms of searching for a set of parameters which includes the speed v^* of the wave front for which the ordinary differential equation has trajectories connecting pairs of equilibrium points. These trajectories can be heteroclinic (a path in the phase plane which joins two different equilibrium points) and/or homoclinic (a path in the phase plane which joins an equilibrium point to itself). The boundary conditions are re-stated in terms of asymptotic behaviour of heteroclinic trajectories as

time t^* approaches to ∞ or to $-\infty$.

In this Chapter we study the growth of cells in one and two dimensional scaffolds in the presence of constant nutrients. The aim of this Chapter is to improve the modelling of cell growth in a perfusion bioreactor. To improve the existing models of cell growth in a perfusion bioreactor we have introduced the non-linear cell diffusion. We model a system in which cell growth and diffusion takes place simultaneously but the cell diffusion increases with the increase in cell density. The equation governing this system is a non-linear Fisher equation in which the diffusion coefficient depends on cell density. The non-linearity arises in the diffusion coefficient. We represent the diffusion coefficient as an exponential function of cell density. The form of non-linear diffusion captures the feature that it is very small for small cell density and increases with the increase in cell density and it is maximum when cells stop growing. However for linear diffusion cells spread immediately in the entire domain. Results are presented for different values of the parameters. The Fisher equation has such wide applicability in itself but also it is the prototype equation which admits travelling wavefront solutions. We study the travelling wave solution of this equation and find the approximation for the minimum wave speed. We find that the minimum wave speed depends on the model parameters and the method of finding the minimum wave speed using the eigenvalues of the stationary states gives the wrong answer when the diffusion is strongly non-linear.

4.2 One dimensional Fisher-Kolmogorov equation with non-linear diffusion

In this Section we describe a spatial and temporal one-dimensional mathematical model of cell growth in a bioreactor subject to uniform nutrient concentration. Consider the cells are seeded onto a porous scaffold with interconnected pores, which is placed in the bioreactor. The scaffold extends from $-L^* \leq x^* \leq L^*$, where x^* denotes the spatial coordinate. In this model we represent the cell density by N^* , initial cell density by N_{init}^* , maximum carrying capacity of the system by N_{max}^* and diffusion coefficient by D^* . We assume that the environment is inhomogeneous *i.e.* the cell density N^* and diffusion coefficient D^* depends on spatial coordinate x^* and time t^* , *i.e.* $N^* = N^*(x^*, t^*)$ and $D^* = D^*(N^*)$. We know that the cells require some nutrients such as oxygen and glucose *etc.* to live and perform specific functions. Suppose that the concentration of such nutrients remains uniform everywhere in the entire domain at all times. We want

to model a system in which the change in cell density is due to cell proliferation and cells disperse in the entire domain due to diffusion. We assume that when the cell density is small diffusion is also very small and when the cell density N^* reaches its maximum carrying capacity N_{max}^* the cell proliferation stops and cells spread in the entire domain via diffusion. For that we consider a logistic growth model in which the cell population spreads via diffusion. That means we have a coupled system of reaction kinetics and diffusion. The one-dimensional coupled reaction-diffusion equation is given by

$$\frac{\partial N^*}{\partial t^*} = \frac{\partial}{\partial x^*} \left[D^*(N^*) \frac{\partial N^*}{\partial x^*} \right] + \chi^* N^* \left(1 - \frac{N^*}{N_{max}^*} \right), \quad (4.2.1)$$

where N^* is cell density, χ^* is the growth rate of cells (maximum rate at which cells can proliferate), and $D^*(N^*)$ is the diffusion coefficient. $D^*(N^*)$ can be any function of cell density. According to our assumption $D^*(N^*)$ increases with increase in cell density so we choose the diffusion coefficient $D^*(N^*)$ to be an increasing function of cell density N^* , which is given by

$$D^*(N^*) = D_n^* \exp(\gamma^*(N^* - N_{max}^*)), \quad (4.2.2)$$

where parameter D_n^* is the cell diffusion when cell density N^* reaches its maximum carrying capacity N_{max}^* , so we can call this the maximum value of cell diffusion and the parameter γ^* controls how fast cells are spreading in the domain. The parameters D_n^* and γ^* have dimensions m^2/sec and $m^3/cell$ respectively. The exponential function in equation (4.2.2) ensures that cell diffusion will remain positive. The non-linear cell diffusion $D^*(N^*)$ has also its maximum value D_n^* when $\gamma^* = 0$. So we can say that non-linear cell diffusion is maximum either when cell density N^* reaches its maximum carrying capacity N_{max}^* or the value of parameter γ^* is zero. The non-linear diffusion becomes linear when $\gamma^* = 0$. It is also clear from the equation (4.2.2) that when there are no cells then in that case cell diffusion is $D_n^* \exp(-\gamma^* N_{max}^*)$, which is the minimum value of diffusion. So cell diffusion varies in the range,

$$D_n^* \exp(-\gamma^* N_{max}^*) \leq D^*(N^*) \leq D_n^*. \quad (4.2.3)$$

From equation (4.2.1) and the form of $D^*(N^*)$ defined by equation (4.2.2) we observe that cells grow in numbers due to second term on the right hand side of equation (4.2.1) and they disperse in the entire domain due to first term on the right hand side of equation (4.2.1). Initially when the cell density N^* is small, the diffusion coefficient $D^*(N^*)$

is also small and $D^*(N^*)$ increases with increasing cell density N^* but it always remains positive.

We apply zero flux boundary conditions at both the boundaries $x^* = \pm L^*$. The particular choice of boundary conditions reflects the assumption that the individual cells cannot leave the domain. Mathematically we write

$$\frac{\partial N^*}{\partial x^*} = 0, \quad \text{at } x^* = \pm L^*. \quad (4.2.4)$$

We assume that the initial cell density $N^*(x^*, 0)$ is given by

$$N^*(x^*, 0) = N_{init}^*(x^*), \quad (4.2.5)$$

where the form of $N_{init}^*(x^*)$ depends on initial seeding strategy.

4.3 Nondimensionalization

For convenience and to reduce the parameters in the equation we rescale all the variables to analyze the nondimensional form of the equation. We nondimensionalize all lengths by L^* and the cell density by the maximum carrying capacity N_{max}^* .

$$x^* = L^*x, \quad \nabla^* = \frac{1}{L^*}\nabla, \quad N^* = N_{max}^*N. \quad (4.3.1)$$

We nondimensionalize time by the speed of the growth front v^* , where v^* is given by equation (4.4.21) and will be determined later.

$$t^* = \frac{L^*}{v^*}t. \quad (4.3.2)$$

In the dimensionless form equation (4.2.1) and boundary conditions (4.2.4) can be written as

$$\frac{\partial N}{\partial t} = \delta \frac{\partial}{\partial x} \left[D(N) \frac{\partial N}{\partial x} \right] + \chi N(1 - N), \quad -1 \leq x \leq 1, \quad (4.3.3)$$

$$\frac{\partial N}{\partial x} = 0, \quad \text{at } x = \pm 1, \quad (4.3.4)$$

where $D(N) = \exp(\gamma(N - 1))$ and $\gamma = \gamma^*N_{max}^*$. The parameters δ and χ are dimensionless parameters in the model which are given by

$$\delta = \frac{D_n^*}{L^*v^*}, \quad \text{and } \chi = \frac{\chi^*L^*}{v^*}. \quad (4.3.5)$$

The parameter χ is the ratio of cell growth rate to speed of growth front and parameter δ is the ratio of maximum value of non-linear diffusion to the speed of growth front. The parameter δ controls the diffusion and the parameter χ controls the growth term. Also boundary condition (4.2.4) and the initial condition (4.2.5) in dimensionless form becomes

$$\frac{\partial N}{\partial x} = 0, \quad \text{at } x = \pm 1, \quad (4.3.6)$$

$$N(x, 0) = N_{init}(x). \quad (4.3.7)$$

Equation (4.3.3) can also be written as

$$\frac{\partial N}{\partial t} = \delta \frac{\partial D(N)}{\partial N} \left(\frac{\partial N}{\partial x} \right)^2 + \delta D(N) \frac{\partial^2 N}{\partial x^2} + \chi N(1 - N). \quad (4.3.8)$$

4.4 Travelling wave solution

In the spatially homogeneous situation equation (4.3.3) has two steady states $N = 0$ and $N = 1$, which are respectively unstable and stable. This suggests that we should look for a travelling wave solution of equation (4.3.3) for which $0 \leq N \leq 1$; negative cell density has no physical meaning. Since a travelling wave exists over the whole real line and has no boundaries, it is not sensible to consider L^* a boundary. Now L^* is interpreted as a typical length scale.

Before discussing the travelling wave solution we must decide what we mean by a travelling wave. A travelling wave is a wave which travels without change of shape. If $N(x, t)$ represents a travelling wave, the shape of the solution will be same for all times and the propagation speed v of this shape will also remain constant. If we observe this wave in the travelling frame moving at speed v it will appear stationary. Mathematically we can write

$$N(x, t) = N(x - vt) = N(\xi), \quad \xi = x - vt, \quad (4.4.1)$$

then $N(x, t)$ is travelling wave, and it moves in the positive x -direction with constant speed v . It is clear from equation (4.4.1) that if $x - vt$ is constant then N is constant, this means that coordinate system is moving with speed v in the positive x -direction.

If a travelling wave solution exists it can be written in the form

$$N(x, t) = \Phi(\xi), \quad \xi = x - vt, \quad (4.4.2)$$

where v is the wave speed. Since equation (4.3.3) is invariant if $x \rightarrow -x$, v may be negative or positive. To be specific we assume that $v \geq 0$. We have

$$\frac{\partial N}{\partial t} = -v \frac{d\Phi}{d\zeta}, \quad \frac{\partial N}{\partial x} = \frac{d\Phi}{d\zeta}, \quad \text{and} \quad \frac{\partial^2 N}{\partial x^2} = \frac{d^2\Phi}{d\zeta^2}. \quad (4.4.3)$$

Substituting the travelling wave solution (4.4.2) into equation (4.3.3) and using relations from equation (4.4.3) we get a second order ordinary differential equation,

$$\delta D(\Phi)\Phi'' + \delta \frac{dD(\Phi)}{d\Phi} \Phi'^2 + v\Phi' + \chi\Phi(1 - \Phi) = 0, \quad (4.4.4)$$

where

$$D(\Phi) = \exp(\gamma(\Phi - 1)), \quad (4.4.5)$$

where primes denote the differentiation with respect to ζ . A typical wave front solution is a solution such that Φ approaches one steady state as $\zeta \rightarrow -\infty$ and approaches the other steady state as $\zeta \rightarrow \infty$. Therefore the boundary conditions for travelling wave solution are usually

$$\lim_{\zeta \rightarrow -\infty} \Phi(\zeta) = 0, \quad \lim_{\zeta \rightarrow \infty} \Phi(\zeta) = 1. \quad (4.4.6)$$

4.4.1 Phase plane analysis

From equation (4.4.4) we observe that we have to determine the values of wave speed v such that a non-negative solution Φ of equation (4.4.4) exists. We use phase plane analysis to characterize solutions of equation (4.4.4) in the (Φ, Ψ) phase plane where,

$$\Phi' = \Psi, \quad \Psi' = \frac{1}{\delta D(\Phi)} \left[-v\Psi - \delta \frac{dD(\Phi)}{d\Phi} \Psi^2 - \chi\Phi(1 - \Phi) \right]. \quad (4.4.7)$$

The system of ordinary differential equations (4.4.7) is nearly singular at $\Phi = 0$, since $D(0) \approx 0$ for high values of parameter γ . To remove the near singularity we introduce a new parameter (Sánchez-Garduño and Maini, 1994), τ in such a way that

$$\frac{d\tau}{d\zeta} = \frac{1}{D(\Phi(\zeta))} \Rightarrow \tau(\zeta) = \int_0^\zeta \frac{ds}{D(\Phi(s))}. \quad (4.4.8)$$

Except at $\Phi = 0$, where $\frac{d\tau}{d\zeta}$ is not defined, $\frac{d\tau}{d\zeta} > 0$. Thus we have

$$\Phi(\zeta) = \Phi(\tau(\zeta)), \quad \Psi(\zeta) = \Psi(\tau(\zeta)). \quad (4.4.9)$$

and we obtain

$$\Phi'(\zeta) = \frac{d\Phi}{d\tau} \frac{d\tau}{d\zeta} \quad \text{and} \quad \Psi'(\zeta) = \frac{d\Psi}{d\tau} \frac{d\tau}{d\zeta}. \quad (4.4.10)$$

Substituting $\Phi'(\zeta)$ and $\Psi'(\zeta)$ into the system of equations (4.4.7) we get

$$\dot{\Phi} = D(\Phi)\Psi = f(\Phi, \Psi), \quad (4.4.11a)$$

$$\dot{\Psi} = \frac{1}{\delta} \left[-v\Psi - \delta \frac{dD(\Phi)}{d\Phi} \Psi^2 - \chi\Phi(1 - \Phi) \right] = g(\Phi, \Psi), \quad (4.4.11b)$$

where dot denotes the derivative with respect to τ .

The phase trajectories of (4.4.11) are solutions of

$$\frac{d\Psi}{d\Phi} = \frac{1/\delta \left[-v\Psi - \delta (dD(\Phi)/d\Phi) \Psi^2 - \chi\Phi(1 - \Phi) \right]}{D(\Phi)\Psi}. \quad (4.4.12)$$

The fixed points (Φ_s, Ψ_s) are the points where $f(\Phi, \Psi) = 0 = g(\Phi, \Psi)$, these are steady states. So in this case fixed points are $(0,0)$ and $(1,0)$. The local behaviour of the trajectories of system (4.4.11) can be obtained by analyzing the linear approximation of system (4.4.11) around each fixed point.

4.4.2 Stability of fixed points

The system of equations (4.4.11) has two fixed points, but which of these fixed points are stable? The local stability of a fixed point (Φ_s, Ψ_s) is determined by linearization of the dynamics at the intersection. If the functions $f(\Phi, \Psi)$ and $g(\Phi, \Psi)$ are analytic near the fixed points (Φ_s, Ψ_s) we can expand $f(\Phi, \Psi)$ and $g(\Phi, \Psi)$ in a Taylor series and, retaining only the linear terms, we get

$$f(\Phi, \Psi) = f(\Phi_s, \Psi_s) + \Phi \frac{\partial f}{\partial \Phi} + \Psi \frac{\partial f}{\partial \Psi}, \quad (4.4.13a)$$

$$g(\Phi, \Psi) = g(\Phi_s, \Psi_s) + \Phi \frac{\partial g}{\partial \Phi} + \Psi \frac{\partial g}{\partial \Psi}. \quad (4.4.13b)$$

So with the linear approximations the system of equations (4.4.11) becomes

$$\dot{\Phi} = \Phi \frac{\partial f}{\partial \Phi} + \Psi \frac{\partial f}{\partial \Psi} = a\Phi + b\Psi, \quad (4.4.14a)$$

$$\dot{\Psi} = \Phi \frac{\partial g}{\partial \Phi} + \Psi \frac{\partial g}{\partial \Psi} = c\Phi + d\Psi, \quad (4.4.14b)$$

which can be written in the matrix form as

$$\dot{\Omega} = A\Omega, \quad (4.4.15)$$

where

$$\dot{\Omega} = \begin{pmatrix} \dot{\Phi} \\ \dot{\Psi} \end{pmatrix}, \quad A = \begin{pmatrix} a & b \\ c & d \end{pmatrix} = \begin{pmatrix} \frac{\partial f}{\partial \Phi} & \frac{\partial f}{\partial \Psi} \\ \frac{\partial g}{\partial \Phi} & \frac{\partial g}{\partial \Psi} \end{pmatrix}, \quad \Omega = \begin{pmatrix} \Phi \\ \Psi \end{pmatrix}. \quad (4.4.16)$$

Let λ_1 and λ_2 be eigenvalues of A then we have

$$\det(A - \lambda I) = 0, \quad \Rightarrow \quad \lambda^2 - (a + d)\lambda + \det(A) = 0. \quad (4.4.17)$$

$$\lambda_{1,2} = \frac{(\Psi D'(\Phi) - v/\delta - 2\Psi D'(\Phi)) \pm \sqrt{(\Psi D'(\Phi) - v/\delta - 2\Psi D'(\Phi))^2 - 4 \det(A)}}{2} \quad (4.4.18)$$

Eigenvalues λ for the fixed points $(0,0)$ and $(1,0)$ are

$$(0,0) : \lambda = \frac{1}{2} \left[-\frac{v}{\delta} \pm \sqrt{\frac{v^2}{\delta^2} - \frac{4\chi D(0)}{\delta}} \right], \quad (4.4.19a)$$

$$(1,0) : \lambda = \frac{1}{2} \left[-\frac{v}{\delta} \pm \sqrt{\frac{v^2}{\delta^2} + \frac{4\chi D(1)}{\delta}} \right]. \quad (4.4.19b)$$

We know that $D(0) = \exp(-\gamma)$ and $D(1) = 1$. Using values of $D(0)$ and $D(1)$ in equation (4.4.19) we get

$$(0,0) : \lambda = \frac{1}{2} \left[-\frac{v}{\delta} \pm \sqrt{\frac{v^2}{\delta^2} - \frac{4\chi \exp(-\gamma)}{\delta}} \right], \quad (4.4.20a)$$

$$(1,0) : \lambda = \frac{1}{2} \left[-\frac{v}{\delta} \pm \sqrt{\frac{v^2}{\delta^2} + \frac{4\chi}{\delta}} \right]. \quad (4.4.20b)$$

It is clear from the equation (4.4.20a) that fixed point $(0,0)$ is a stable node if $v^2 > 4\chi\delta \exp(-\gamma) \Rightarrow v > v_c = 2\sqrt{\chi\delta \exp(-\gamma)}$, the case when $v = v_c$ giving a degenerate node. The fixed point $(0,0)$ is a stable spiral if $v^2 < 4\chi\delta \exp(-\gamma)$ or $v < v_c = 2\sqrt{\chi\delta \exp(-\gamma)}$; *i.e.* Φ oscillates in the vicinity of origin. When $v < 2\sqrt{\chi\delta \exp(-\gamma)}$ then it is not physically realistic because $\Phi(\xi) = N(x, t)$ cannot be negative. The fixed point $(1,0)$ is a saddle point. The solution of modified Fisher equation evolve to a travelling wave if the fixed point $(0,0)$ is a stable node and minimum wave speed of wave front is $v_c = 2\sqrt{\chi\delta \exp(-\gamma)}$. The condition that $(0,0)$ is a stable node is a necessary condition for travelling wave propagation but not sufficient. Sometimes it gives wrong answer as we shall in see Section 4.6. If the propagation speed of the front is determined

by the leading edge of the population distribution the non-linear fronts whose asymptotic propagation speed equals v_c is called a "pulled front". In this case the eigenvalues give the right answer because the wave speed is determined by what happens at the front edge where $\Phi \approx 0$. As above $v_c = 2\sqrt{\chi\delta \exp(-\gamma)}$ is determined by the eigenvalues thus we call v_c speed of pulled front. On the other hand if the speed of front is determined by the whole wave-front but not the behaviour of the leading edge the front is called the "Pushed front" (Rothe, 1981, Van Saarloos, 2003). In this case simply computing the eigenvalues gives the wrong answer for the minimum wave speed and the minimum wave speed is $v_{min} > v_c$.

Thus the wave speed for a pulled front is given by $v_c = 2\sqrt{\chi\delta \exp(-\gamma)}$. The wave speed v_c depends on the parameters χ , δ and γ , is directly proportional to the square root of the product of χ and δ , which implies that if the value of product $\chi\delta$ is high then the wave will move with high speed. In terms of the original dimensional equation (4.2.1) the wave speed v_c^* is

$$v_c^* = 2\sqrt{\chi^* D_n^* \exp(-\gamma^* N_{max}^*)}. \quad (4.4.21)$$

We observe from the system of equations (4.4.19) that for a general function $D(\Phi)$ the wave speed v_c is determined by $D(0)$. So in general the wave speed of the pulled front is $v_c = 2\sqrt{\chi\delta D(0)}$.

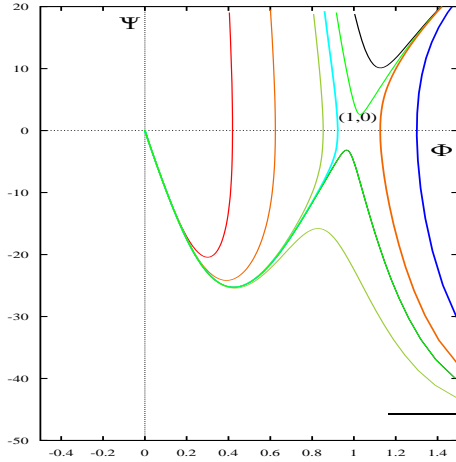


Figure 4.1: Phase plane trajectories of equation (4.4.11). Here parameter values are $\chi = 132.1739$, $\delta = 0.0139$, $\gamma = 2$ and $v = 1.5 > v_c$.

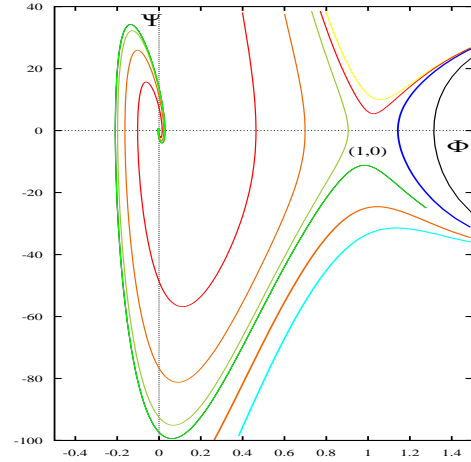


Figure 4.2: Phase plane trajectories of equation (4.4.11). Here parameter values are $\chi = 132.1739$, $\delta = 0.0139$, $\gamma = 2$ and $v = 0.5 < v_c$.

Figure 4.1 shows the phase plane sketch of the trajectories of equation (4.4.11) when $v > v_c$. We see that when $v > v_c$ the fixed point $(0, 0)$ is a stable node because all the

trajectories from $(1, 0)$ to $(0, 0)$ have the same limiting direction towards $(0, 0)$ and the fixed point $(1, 0)$ is a saddle point because there are two incoming trajectories and two outgoing trajectories and all the other trajectories in the neighborhood of the critical point $(1, 0)$ bypass $(1, 0)$. Similarly Figure 4.2 shows the phase plane sketch of the trajectories of equation (4.4.11) when $v < v_c$. We observe that when $v < v_c$ the fixed point $(0, 0)$ is a stable spiral because all the trajectories from $(1, 0)$ to $(0, 0)$ spiral around the point $(0, 0)$.

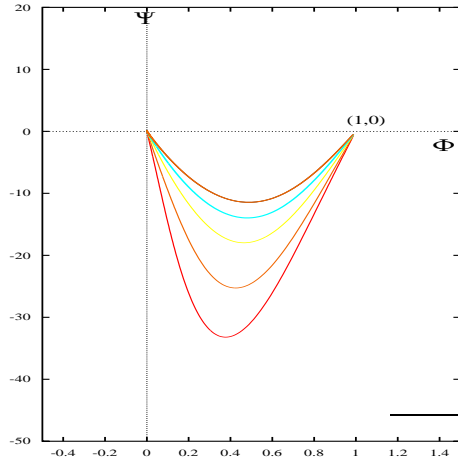


Figure 4.3: Phase plane trajectories of equation (4.4.11) for different values of $v \geq v_c$. The other parameter values are same as in Figure 4.1. Colored lines represents the different values of speed v e.g. $v = 1$, $v = 1.5$, $v = 2$, $v = 2.5$ and $v = 3$.

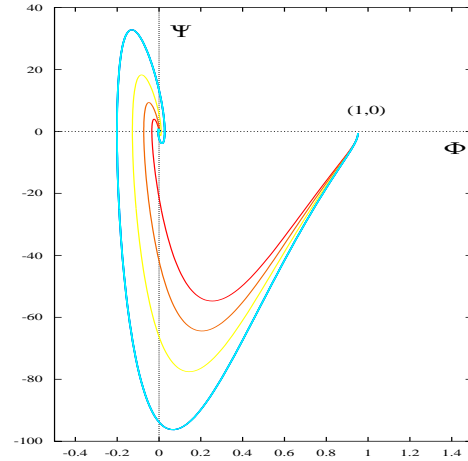


Figure 4.4: Phase plane trajectories of equation (4.4.11) for different values of $v < v_c$. The other parameter values are same as in Figure 4.1. Colored lines represents the different values of speed v e.g. $v = 0.8$, $v = 0.7$, $v = 0.6$ and $v = 0.5$.

Figures 4.3 and 4.4 show the phase plane sketch of trajectories of equation (4.4.11) for various wave speeds $v \geq v_c$ and $v < v_c$ respectively. We observe from the Figure 4.3 that when $v \geq v_c$ all the trajectories in the phase plane $(\Phi, \Phi' = \Psi)$ from $(1, 0)$ to $(0, 0)$ remain entirely in the quadrant where $\Phi \geq 0$ and $\Phi' \leq 0$, with $0 \leq \Phi \leq 1$ for all wave speeds $v \geq v_c$. Similarly from the Figure 4.4 we see that for all wave speeds $v < v_c$ the phase trajectories from $(1, 0)$ to $(0, 0)$ spiral around the fixed point $(0, 0)$. In this case Φ oscillates in the vicinity of the origin giving Φ negative which is unphysical.

4.4.3 Selection of initial condition

A very important question at this stage is what kind of initial condition $N(x, 0)$ will evolve into the travelling wave solution and if the travelling wave solution exists what is its wave speed v ? Fisher (1937) found that equation (4.3.3) has an infinite number of travelling wave solutions for which $0 \leq N(x, 0) \leq 1$ for all wave speeds $v \geq v_c$. Kol-

mogorov et al. (1937) proved that equation (4.3.3) has a travelling wavefront solution and the wave speed is $v \geq v_c$, if $N(x, 0)$ has compact support. A function $N(x, 0)$ is said to have a compact support if

$$N(x, 0) = N_{init}(x) \geq 0, \quad (4.4.22)$$

where

$$N_{init}(x) = \begin{cases} F(x) & \text{if } x_1 \leq x \leq x_2 \\ 0 & \text{if } x_1 \geq x \geq x_2 \end{cases}$$

where $x_1 < x_2$ and $N(x, 0) = N_{init}(x)$ is continuous in (x_1, x_2) . If the initial condition is other than (4.4.22) then solution depends on the behaviour of $N(x, 0)$.

If $D(\Phi) = 1$ then equation (4.4.4) reduces to

$$\delta\Phi'' + v\Phi' + \chi\Phi(1 - \Phi) = 0 \quad (4.4.23)$$

A travelling wave solution of equation (4.4.23) in explicit form for $\delta = \chi = 1$ was found by Ablowitz and Zeppetella (1979) for special wave speed $v = 5/\sqrt{6} \approx 2.041$,

$$\Phi(\xi) = \frac{1}{[1 + \exp(\xi/\sqrt{6})]^2}. \quad (4.4.24)$$

But if $D(\Phi)$ is not a constant then it is not possible to find the exact solution of equation (4.4.4). Solution of such non-linear problem can be approximated by perturbation theory or numerical investigation.

4.5 Numerical solution

Numerically we solve the modified Fisher equation (4.3.3) by using the commercial finite element solver COMSOL. We subdivide the domain $-1 \leq x \leq 1$ into a suitable number of mesh elements (intervals) of length Δx . The end points of each interval are called node points and the elements do not have to have the same length. But in this case the length Δx of each element is same. To obtain meaningful results care is required in the definition of a suitable number of mesh elements, finite element approximation and model parameters. Convergence can be achieved by successively refining the mesh elements. The refined mesh contains 30721 mesh vertices and 30720 mesh elements. The dependent variable N is approximated by a quadratic shape function and solved for 61441 degrees of freedom. We assume that at time $t = 0$ the cell density

is N_{init} and after the time $t = t_{new}$ the cell density is N_{new} . We start with initial cell density N_{init} and after each time t_{new} we replace N_{init} by N_{new} and solve the equation (4.3.3) again for updated cell density. The time from $t = 0$ to $t = t_{new}$ is subdivided as $t = 0 : \Delta t : t_{new}$, where Δt is the time step size from $t = 0$ to $t = t_{new}$ and t_{new} is the time when we update the cell density. The cell density N at each mesh point x is obtained for different times. To estimate the wave speed v_c numerically we look for the point x after each time t where the cell density is half of its maximum value *i.e.* $N = 1/2$ (maximum cell density). When cell density is half of its maximum value at time $t = t_1$, then $x = x_1$ and at time $t = t_2$, $x = x_2$. So we can estimate the total distance $\Delta x = x_2 - x_1$ traveled by the wave in the time interval $\Delta t = t_2 - t_1$. Hence

$$\text{wave speed} = \frac{\text{total distance}}{\text{total time}} = \frac{\Delta x}{\Delta t}. \quad (4.5.1)$$

Results are plotted for different values of dimensionless parameters χ and δ in Sections 4.5.2 to 4.5.5. In the next Section we discuss the parameter values used in the model.

4.5.1 Parameter values

The Fisher equation with non-linear diffusion (4.3.3) includes a number of parameters. Some parameters depend on the cell type and some parameters depend on scaffold geometry. Table 4.1 shows the values of the parameters used in the simulation. We assume that the length $2L^*$ of the scaffold is $0.02m$. Some quantities such as cell growth rate depend on the cell type cultured in the bioreactor. The above proposed model is a generic model and can be applied to any cell type. To compare the model with the experimental data the cells used in the simulations are Murine immortalized rat cell C_2C_{12} . The maximum cell growth rate χ^* for C_2C_{12} cells is 1.52×10^{-5} (Coletti et al., 2006). Since cell growth is a slow process we can choose that speed of growth front v^* is very small *e.g.* $(10^{-1} \text{ or } 1 \text{ or } 0.1)mm/day$. The value of dimensionless parameter χ can be obtained by using the values of dimensional parameters χ^* , L^* and v^* . The values of parameters γ and δ are not available in the literature. To estimate the value of these parameters we use the expression for dimensionless wave speed *i.e.* $v_c = 2\sqrt{\chi\delta \exp(-\gamma)}$. We choose that the theoretical wave speed $v_c = 1$. In the expression for v_c there are two unknowns δ and γ . In order to find the value of δ and γ we fix one of the parameters δ or γ in the expression for v_c . If we fix the parameter γ then using the expression for v_c we can find the value of parameter δ . We observe that the value of dimensionless parameter δ depends on the value of parameter γ . If the value of parameter γ is high then value of δ is also high. This means that cells will

diffuse more quickly for high values of parameter γ . Table 4.1 shows the values of the dimensional parameters used in the model.

Table 4.1: Model parameters used in this work

Parameter	Description	Value			unit
L^*	Scaffold length	0.01			m
N_{max}^*	Maximum carrying capacity	4×10^{17}			$cells/m^3$
χ^*	Maximum cell growth rate	1.52×10^{-5}			$1/sec$
v^*	Speed of growth front	10	1	0.1	mm/day
χ		1.3217	13.2173	132.1739	

We know that the initial cell density $N(x, 0) = N_{init}(x)$. The form of $N_{init}(x)$ can be determined from seeding strategy. We can use any form of $N_{init}(x)$. Let us assume that $N_{init}(x) = N_0 H(r^2 - x^2)$, where N_0 and r are constants and $H(\cdot)$ is the Heaviside step function.

In the following Section we consider various cases in which we fix the value of dimensionless parameter χ and vary the values of dimensionless parameter δ and parameter γ in such a way that the theoretical wave speed v_c remains 1.

4.5.2 Case I: $\chi = 1.3217$

In this case we fix the value of dimensionless parameter $\chi = 1.3217$ and find the values of parameter δ and γ such that theoretical speed of growth front v_c is 1. Table 4.2 shows the values of dimensionless parameter δ for corresponding values of parameter γ .

γ	0	1	2	3	4
δ	0.1891	0.5141	1.39760	3.7990	10.3269

Table 4.2: Values of γ and δ for $\chi = 1.3217$

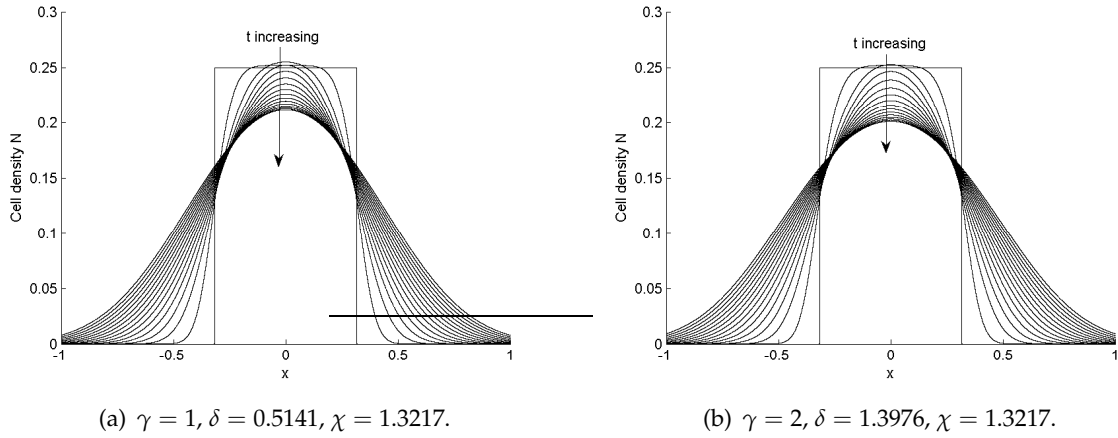


Figure 4.5: Numerical results of profile of cell density N at different times and for different values of γ and δ when $\chi = 1.3217$. Initial cell density is $N_{init}(x) = N_0H(r^2 - x^2)$, where $N_0 = 0.25$, and $r^2 = 0.1$. The time step size $\Delta t = 0.001$ and cell update time $t_{new} = 0.01$. The Figure shows the cell distribution after each time t_{new} and final time is $t = 0.3$.

Figure 4.5 shows the numerical solution of modified Fisher equation (4.3.3) for the parameter values given in the Table 4.2. We observe from Figure 4.5 that solution does not evolve to the travelling wave solution. Cell density N drops down because diffusion is bigger than the growth term, which means that the dimensionless parameter δ is bigger than the dimensionless parameter χ . Diffusion dominates in this simulation so we need to look at the case where diffusion is smaller and cell growth is larger, to find a travelling wave. Numerical results are plotted for $\gamma = 1$ and $\gamma = 2$ in Figure 4.5. In the bigger domain and longer time of integration the system will eventually evolve to travelling wave but we are interested in the finite domain.

4.5.3 Case II : $\chi = 13.2173$

We consider the case when the dimensionless parameter $\chi = 13.2173$ and find the value of parameter δ and γ such that theoretical speed of growth front v_c is 1. Table 4.3 shows the values of dimensionless parameter δ for the corresponding values of parameter γ .

γ	0	1	2	3	4
δ	0.01891	0.05141	0.139760	0.37990	1.03269

Table 4.3: Values of γ and δ for $\chi = 13.2173$

Numerical results of modified Fisher equation (4.3.3) are plotted in Figure 4.6 for parameter values given in Table 4.3. It is clear from the Figure 4.6 that in this case the solution evolves into travelling wave fronts. So in this case the growth term is bigger than the diffusion term. But the diffusion term is not too small because the cells also diffuse very quickly. This feature is evident from the Figure 4.6 because at the edges the front are smooth.

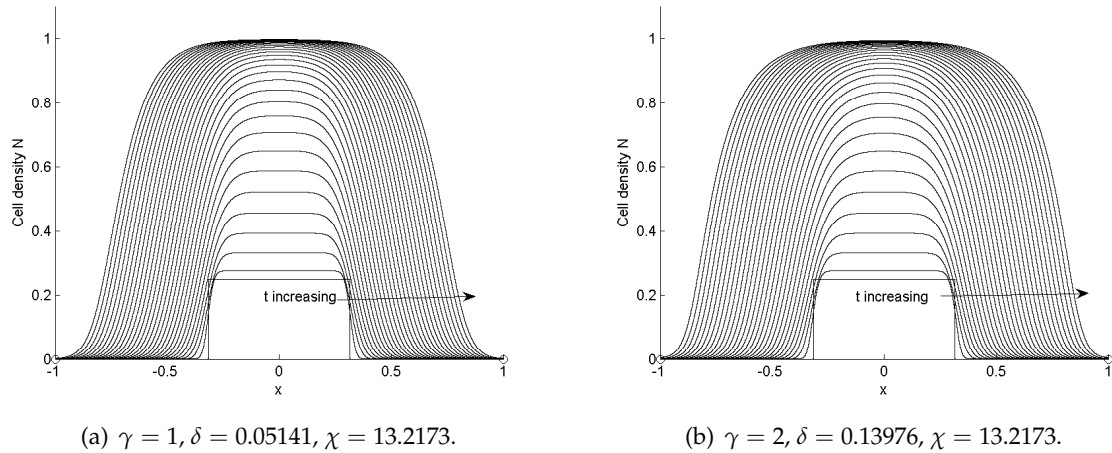


Figure 4.6: Numerical results of profile of cell density N at different times and for different values of γ and δ when $\chi = 13.2173$. N_{init} , Δt and t_{new} are same as in Figure 4.5. In this case the final time is $t = 0.6$.

4.5.4 Case III : $\chi = 132.1739$

Consider the case when the value of dimensionless parameter χ is very high *i.e.* $\chi = 132.1739$ and we find the values of parameters δ and γ such that theoretical speed of growth front v_c is 1. Table 4.4 shows the values of dimensionless parameter δ for corresponding values of parameter γ .

γ	0	1	2	3	4	5
δ	1.891×10^{-3}	5.1414×10^{-3}	0.013976	0.037990	0.103269	0.2807

Table 4.4: Values of γ and δ for $\chi = 132.1739$

In the modified Fisher equation (4.3.3), growth and diffusion are taking place simultaneously. But if the diffusion is very small compared to growth, then first cells will

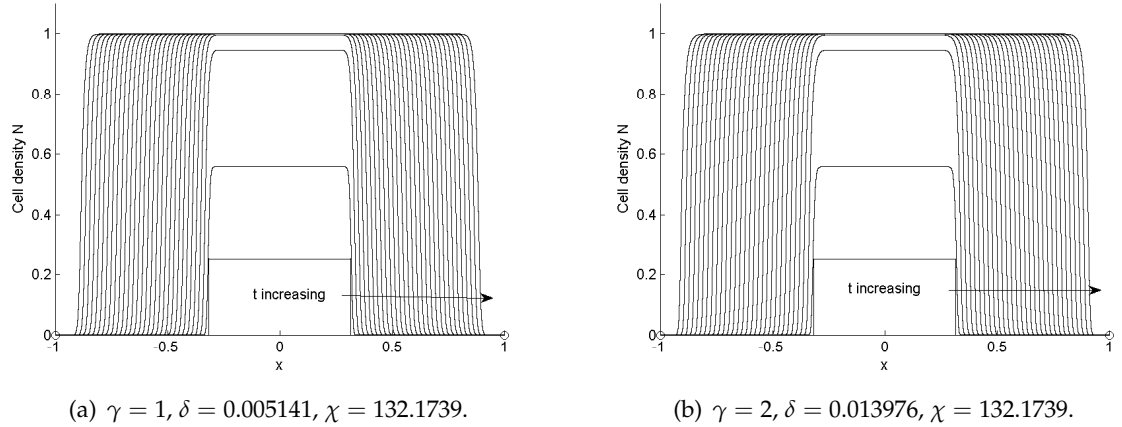


Figure 4.7: Numerical results of profile of cell density N at different times and for different values of γ and δ when $\chi = 132.1739$. N_{init} , Δt and t_{new} are same as in Figure 4.5.

grow quickly and when they reach maximum carrying capacity growth stops and they spread in the domain via diffusion. In the present case the growth term is very big as compared to the diffusion term.

Figure 4.7 shows the numerical solution of the modified Fisher's equation (4.3.3) for $\chi = 132.1739$ and values of parameters γ and δ given in Table 4.4. The wave front takes some time to settle down to a travelling wave, which moves at a constant speed. When the number of cells reaches its maximum limit the proliferation stops and then the cells spread via diffusion in the entire domain. In this case diffusion term is much smaller than the growth term, and due to this reason the shape of the front is very sharp. It is evident from the Figure 4.7 that when the front settles down then it moves with constant speed and shape.

4.5.5 Case IV : $\chi = 0$

If $\chi = 0$ then it represents the case when there is no growth of cells. The number of cells will not increase because of the absence of growth term. In that case for every value of δ the solution will not evolve to travelling wave. Figure 4.8 shows the cell density in the pure diffusion case *i.e.* Fisher equation without the growth term for the same times and parameter values used in Figure 4.6 except in this case $\chi = 0$. The behaviour of the solution is different from the Fisher equation with the growth term. Clearly the solution does not grow due to the absence of growth term and the behaviour of the solution is not wave-like.

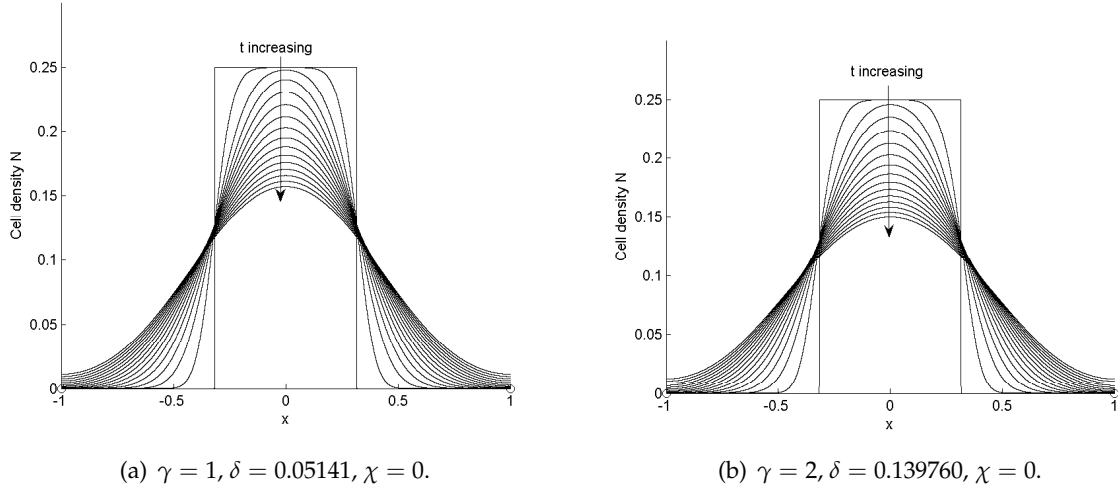


Figure 4.8: Numerical results of profile of cell density N at different time without growth term. N_{init} , Δt and t_{new} are same as in Figure 4.5.

4.6 Numerical minimum wave speed

From the phase plane analysis it is clear that a travelling wave front solution exists for a range of wave speeds $v \geq v_c$. We choose the values of parameters γ and δ such that the theoretical wave speed $v_c = 1$. If diffusion is linear in the modified Fisher equation (4.3.3) then travelling wave move with the minimum wave speed $v = v_c$ (Murray, 1989). In this model $\gamma = 0$ corresponds to linear diffusion. But when the value of $\gamma > 0$ then diffusion is no longer linear. We observe that when diffusion is non-linear then minimum speed of wave front does not always agree with the theoretical wave speed v_c . In Table 4.5 the numerical values of the minimum wave speed v_{min} are given for different values of χ and γ . It is evident from the Table 4.5 that minimum wave speed v_{min} is not 1 for the non-linear diffusion. The difference between theoretical wave speed v_c and minimum numerical wave speed v_{min} is not very large for $\gamma = 0, 1, 2$ but this difference is significant when $\gamma = 3, 4, 5$. v_{min} is significantly greater than v_c if $\gamma \geq 3$.

	$\chi = 13.2173$	$\chi = 132.1739$
γ	v_{min}	v_{min}
0	0.9999	0.9914
1	1.0005	1.0006
2	1.0069	1.0175
3	1.1497	1.1544
4	1.4205	1.4894
5	1.8540	1.8818

Table 4.5: Numerical minimum wave speed v_{min}

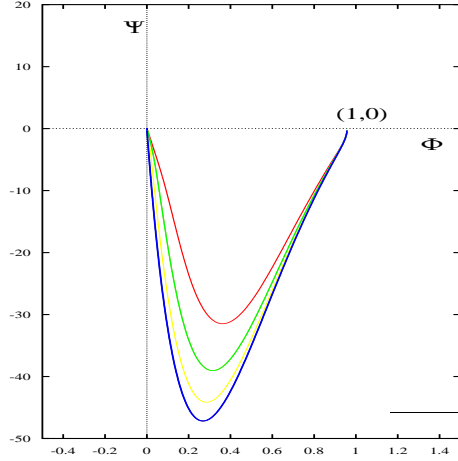


Figure 4.9: Phase plane trajectories of equation (4.4.14) for different values of $v \geq v_c$. The other parameter values are $\chi = 132.1739$, $\gamma = 3$ and $\delta = 0.037990$. Colored lines represents the different values of speed v e.g. $\clubsuit v = 1.15$, $\heartsuit v = 1.2$, $\spadesuit v = 1.3$, and $\diamondsuit v = 1.5$.

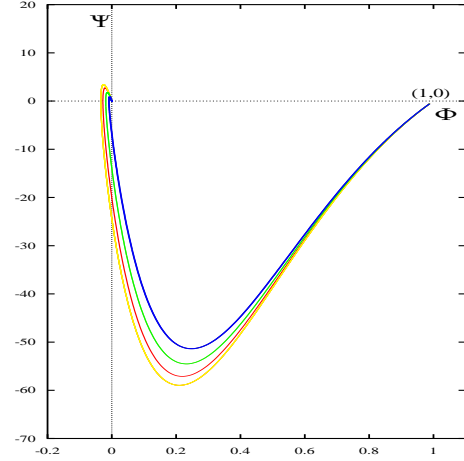


Figure 4.10: Phase plane trajectories of equation (4.4.14) for different values of $v < v_c$. The other parameter values are $\chi = 132.1739$, $\gamma = 3$ and $\delta = 0.037990$. Colored lines represents the different values of speed v e.g. $\heartsuit v = 1$, $\diamondsuit v = 1.02$, $\clubsuit v = 1.05$ and $\spadesuit v = 1.09$.

Figures 4.9 and 4.10 shows the phase plane sketch of the trajectories of equation (4.3.8) for $v \geq v_c$ and $v < v_c$ respectively. We observe from the Table 4.5 that when $\chi = 132.1739$ and $\gamma = 3$ the numerical value of the minimum wave speed $v_{min} = 1.1544$. We see that from Figure 4.9 that when $v \geq 1.15$ then all trajectories from $(1, 0)$ to $(0, 0)$ remain entirely in the region where $\Phi \geq 0$ and $\Phi' \leq 0$ for all wave speed $v \geq 1.15$. Similarly from Figure 4.10 we observe that when wave speed $v < 1.15$ then for all the trajectories from $(1, 0)$ to $(0, 0)$, Φ becomes negative, which is unphysical. $(0, 0)$ is still a stable node. We observe that method of finding v_c by looking at the eigenvalues gives wrong answer. It is beyond the scope of this work to find the analytical formula for the minimum wave speed v_{min} , because the solution depends on the whole trajectory, but we have a very good agreement between numerical results and phase plane analysis.

Figure 4.11 shows the shape of growth front at time $t = 0.3$ for fixed value of χ but different values of γ and δ . It is evident from Figure 4.11 that the speed of the growth front is not the same for all values of parameter γ . The speed of the growth front depends on the value of γ and increases as value of γ increases.

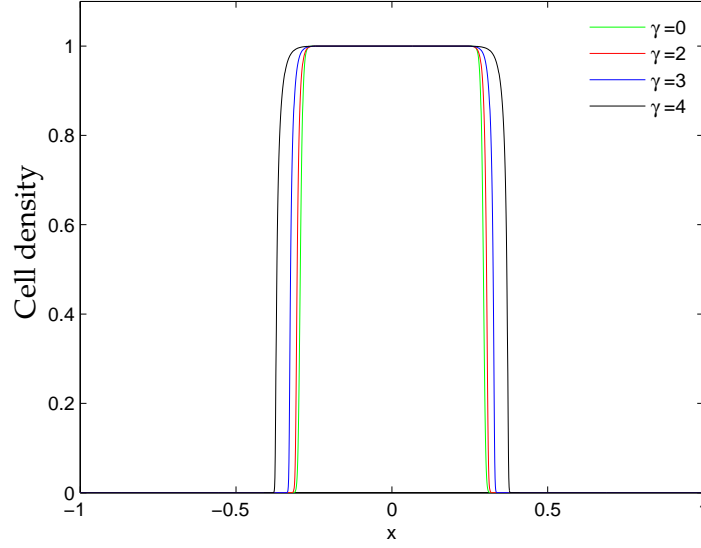


Figure 4.11: Shape of growth front at time $t = 0.3$ for fixed $\chi = 132.1739$ and value of δ for corresponding value of γ are given in Table 4.4. N_{init} , Δt and t_{new} are same as in Figure 4.5.

4.7 Accuracy of numerical method

To check the convergence of our numerical method we calculate v_{min} and N_{total} for different mesh size, internal time step Δt and time of update t_{new} . Table 4.6 shows the values of v_{min} and N_{total} at time $t = 6$ for (a) different mesh size but fixed Δt and t_{new} , (b) different Δt but fixed mesh size and t_{new} (c) different t_{new} but fixed mesh size and Δt . We can see that v_{min} and N_{total} are converging to a stable value for all cases which shows that our numerical method is accurate.

(a) $\Delta t = 0.001, t_{new} = 0.01$.			(b) Mesh size= 1921, $t_{new} = 0.01$.			(c) Mesh size=1921, $\Delta t = 0.001$.		
Mesh size	v_{min}	N_{total}	Δt	v_{min}	N_{total}	t_{new}	v_{min}	N_{total}
30721	1.0203	1.8206	0.0001	1.0183	1.8189	0.01	1.0204	1.8211
1921	1.0204	1.8211	0.001	1.0204	1.8211	0.02	1.0513	1.8667

Table 4.6: Table shows numerical results of v_{min} and N_{total} as a function of time. N_{init} , Δt and t_{new} are same as in Figure 4.5. The other parameter values are $\gamma = 2$, $\delta = 0.013976$, $\chi = 132.173$. Table shows v_{min} and N_{total} at $t = 0.6$ for fixed (a) $\Delta t = 0.001$ and $t_{new} = 0.01$ and different mesh size (b) mesh size and $t_{new} = 0.01$ and different Δt (c) mesh size and $\Delta t = 0.001$ and different t_{new} .

Figure 4.12 shows the total cell density N_{total} as a function of time t_{new} for (a) different mesh size but fixed Δt and t_{new} , (b) different Δt but fixed mesh size and t_{new} (c) different t_{new} but fixed mesh size and Δt . We observe from the Figure 4.12(a), (b) and (c) that our numerical method is convergent for different mesh size and internal time step Δt , and t_{update} .

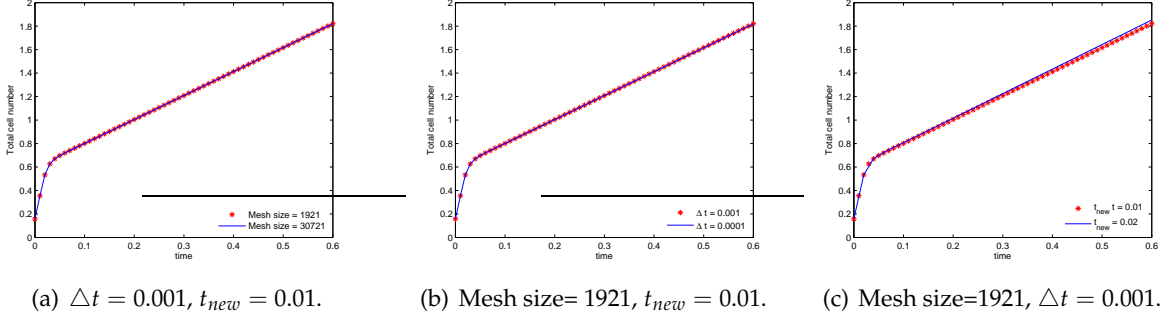


Figure 4.12: Numerical results of total cell density N as a function of time for fixed (a) $\Delta t = 0.001$ and $t_{new} = 0.01$ and different mesh size (b) mesh size and $t_{new} = 0.01$ and different Δt (c) mesh size and $\Delta t = 0.001$ and different t_{new} . Here $\gamma = 2$, $\delta = 0.013976$, $\chi = 132.173$ and N_{init} , Δt and t_{new} are same as in Figure 4.5.

4.8 Two dimensional Fisher equation with density dependent diffusion

Let us consider a porous scaffold of length $2L^*$ in (x^*, y^*) and width $2L^*$ in cartesian co-ordinate system. Initially cells are seeded onto the scaffold. Let us suppose that cell density N^* depends on two spatial variables x^* and y^* and time t^* , *i.e.* $N^* = N^*(x^*, y^*, t^*)$. The Fisher equation with non-linear diffusion coefficient $D^*(N^*)$ in two dimensions can be written as

$$\frac{\partial N^*}{\partial t^*} = \nabla^* \cdot [D^*(N^*) \nabla^* N^*] + \chi^* N^* \left(1 - \frac{N^*}{N_{max}^*} \right), \quad (4.8.1)$$

where $D^*(N^*)$ is density dependent diffusion and is given by equation (4.2.2), χ^* is growth rate and N_{max}^* is maximum carrying capacity. We apply zero flux boundary conditions at all boundaries of the scaffold, in other words we can say that the cells cannot leave the domain. Initial cell density is N_{init}^* . Mathematically we write,

$$\hat{\mathbf{n}} \cdot \nabla^* N^* = 0, \quad \text{at } x^* = \pm L^*, \quad \text{and } y^* = \pm L^*, \quad (4.8.2a)$$

$$N^*(x^*, y^*, 0) = N_{init}^*(x^*, y^*), \quad (4.8.2b)$$

where $\hat{\mathbf{n}}$ is unit outward normal vector.

To reduce the parameters we use the same nondimensionalization as we did for the one dimensional model. In dimensionless form equation (4.8.1) can be written as

$$\frac{\partial N}{\partial t} = \delta \nabla \cdot (D(N) \nabla N) + \chi N (1 - N), \quad (4.8.3)$$

where $D(N) = \exp(\gamma(N - 1))$ and $\gamma = \gamma^* N_{max}^*$. The parameters χ and δ are the dimensionless parameters which are given by equation (4.3.5). Boundary and initial conditions (4.8.2) in dimensionless form becomes

$$\hat{\mathbf{n}} \cdot \nabla N = 0, \quad \text{at } x = \pm 1, \quad \text{and } y = \pm 1, \quad (4.8.4a)$$

$$N(x, y, 0) = N_{init}(x, y). \quad (4.8.4b)$$

Equation (4.8.3) can also be written as

$$\begin{aligned} \frac{\partial N}{\partial t} &= \delta \frac{\partial D(N)}{\partial N} \left[\left(\frac{\partial N}{\partial x} \right)^2 + \left(\frac{\partial N}{\partial y} \right)^2 \right] \\ &+ \delta D(N) \left[\frac{\partial^2 N}{\partial x^2} + \frac{\partial^2 N}{\partial y^2} \right] + \chi N (1 - N). \end{aligned} \quad (4.8.5)$$

We assume that the front is moving along the x -direction. In general the speed v_x of wave may be different from the speed v of plane wave. If a travelling wave solution of equation (4.8.5) exists then $N(x, y, t) = \Phi(\xi = x - vt, y)$, and $N(\xi, y)$ satisfies the equation

$$\begin{aligned} \delta D(\Phi) \left(\frac{\partial^2 \Phi}{\partial \xi^2} + \frac{\partial^2 \Phi}{\partial y^2} \right) &+ \delta \frac{dD(\Phi)}{d\Phi} \left[\left(\frac{\partial \Phi}{\partial \xi} \right)^2 + \left(\frac{\partial \Phi}{\partial y} \right)^2 \right] \\ &+ v_x \frac{\partial \Phi}{\partial \xi} + \chi \Phi (1 - \Phi) = 0 \end{aligned} \quad (4.8.6)$$

If Φ does not depend on y then equation (4.8.6) is a trivial generalization of the one-dimensional equation (4.4.4) with wave speed $v_x = v$. Finding the exact solutions of non-linear models is a challenging task. Several analytical methods have been developed to find the wave solution of one dimensional pure dispersive non-linear system *e.g.* the inverse scattering transform (Novikov, 1984), Lamb's ansatz (Lamb Jr, 1971), the Herota method (Hirota, 1972). Some of these methods may be extended to two dimensional non-linear systems. The solution of the systems including the dissipative losses becomes more complex. Even for the one dimensional case most of the above

mentioned methods do not work. These type of systems can be treated by perturbation theory or numerical investigation.

Finding the exact solution of equation (4.8.5) is a difficult task. There are only few exact solution of (4.8.5) and those solutions are obtained for very simple cases, *e.g.* Petrovskii and Shigesada (2001) considered the early stage of biological invasion based on the Fisher equation. For radially symmetric problems they constructed a self similar solution which is applicable to 1-D, 2-D and 3-D cases. They also assumed that diffusion is homogeneous *i.e.* the diffusion coefficient D is independent of space coordinates, in other words D is constant. They found that solution describes a travelling wave propagation and speed of front is $2\sqrt{\chi D}$. This wave speed agrees with our model if $D(N) = \text{constant}$.

Let us transform equation (4.8.5) into polar coordinates by the transformations

$$x = r \cos(\theta), \quad y = r \sin(\theta) \quad (4.8.7)$$

where

$$r = \sqrt{x^2 + y^2}, \quad \theta = \tan^{-1} \left(\frac{y}{x} \right). \quad (4.8.8)$$

We assume that the cell density N depends only on the distance from the origin, then in polar coordinates equation (4.8.5) can be written as

$$\frac{\partial N}{\partial t} = \delta \frac{\partial D}{\partial N} \left(\frac{\partial N}{\partial r} \right)^2 + \delta D(N) \left[\frac{\partial^2 N}{\partial r^2} + \frac{1}{r} \frac{\partial N}{\partial r} \right] + \chi N(1 - N). \quad (4.8.9)$$

Equation (4.8.9) differs from the 1-D Fisher-Kolmogorov equation 4.3.3 analysed in Sections 4.4 and 4.5 by a new term $\frac{1}{r} \frac{\partial N}{\partial r}$. Equation (4.8.9) does not possess a travelling wave solution, in which the wave spreads out with constant speed v , because of this $1/r$ term. We assume that we are given $N(r, 0)$. N will grow due to the $N(1 - N)$ term since $N < 1$. At the same time N will disperse like a wave due to the diffusion term. On the wave $\partial N / \partial r < 0$ so effectively it reduces the value of source term on right hand side of equation (4.8.9). This effect reduces the speed of an outgoing wave. For large r the term $(1/r)(\partial N / \partial r)$ becomes negligible so the solution will approach asymptotically to the travelling wave front solution moving with speed $v = 2\sqrt{\chi \delta \exp(-\gamma)}$ as in the one-dimensional case.

To find the exact solution of non-linear Fisher equation with non-linear diffusion is very difficult. So we can approximate the solution by numerical investigation. To find

the numerical solution we use commercial software COMSOL, which is based on the finite element solver. The numerical solution gives the cell density $N(x, t)$ at each mesh point after each time unit. To find the speed of the growth front in x and y -direction we take a cross section at $y = 0$ and $x = 0$, respectively, and use the same technique as we did in 1-D case. Table 4.7 shows the speed v_x and v_y of the growth front in the x -direction and y -direction respectively. It is clear from Table 4.7 that the speed of the growth front is approximately same in both directions. The slight difference in wave speeds may be due to numerical calculations, because meshing is not regular in both directions. The wave speed in the 2-D case approximately agrees with the wave speed in the 1-D case.

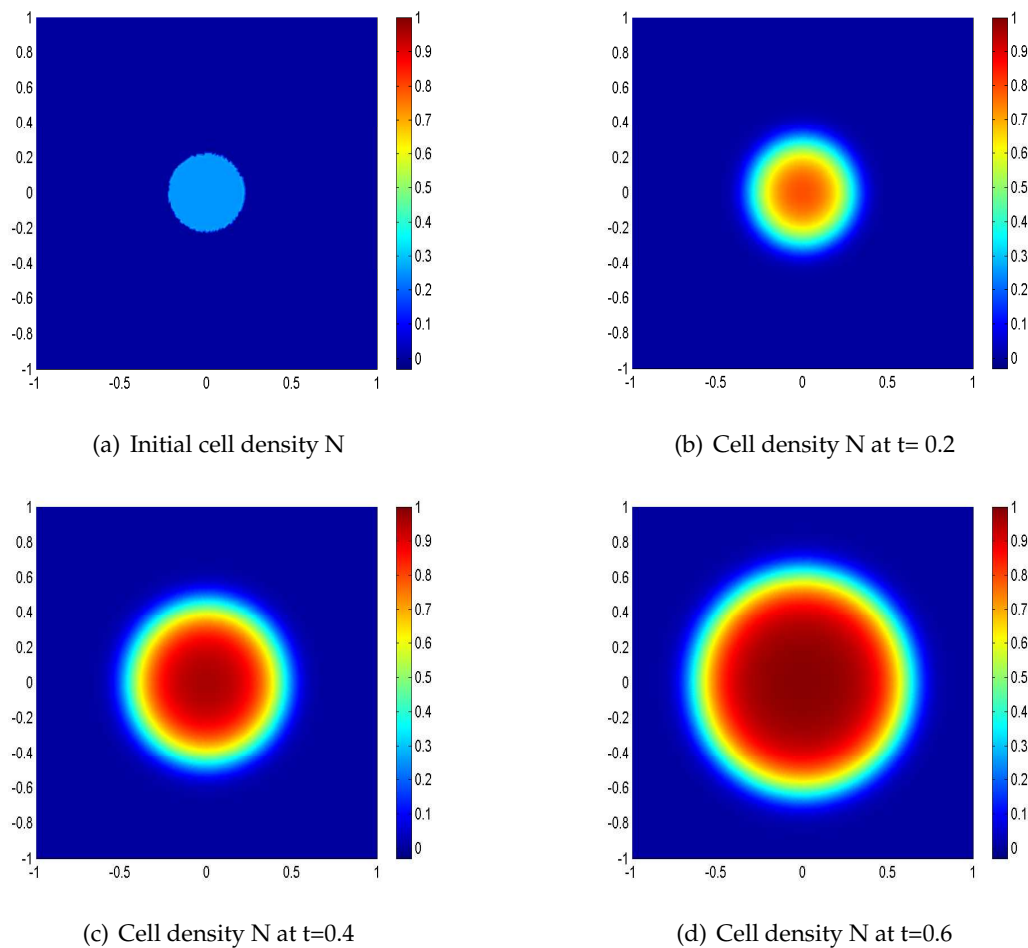


Figure 4.13: Numerical solution of modified 2-D Fisher equation (4.8.5). Color represents the cell density N at different spatial locations for different time. Initial cell density is $N_{init}(x, y) = N_0 H(r^2 - x^2 - y^2)$, where $N_0 = 0.25$ and $r^2 = 0.05$. The values of the parameter used in the simulation are $\gamma = 1$, $\chi = 13.2173$, $\delta = 0.05141$, $\Delta t = 0.001$ and $t_{new} = 0.01$.

Figure 4.13 shows the cell density N at different spatial locations for different time

χ	γ	δ	Speed in x direction v_x	Speed in y direction v_y
13.2173	2	0.13976	1.0065	1.0176
132.1739	2	0.013976	1.0160	1.0186

Table 4.7: Numerical results of minimum wave speed v_{min} of modified two dimensional Fisher equation (4.8.5). The initial conditions and parameters values used in the simulation are same as in Figure 4.13.

units. It is clear from the Figure that cell density N is increasing with time and spreading in the whole domain.

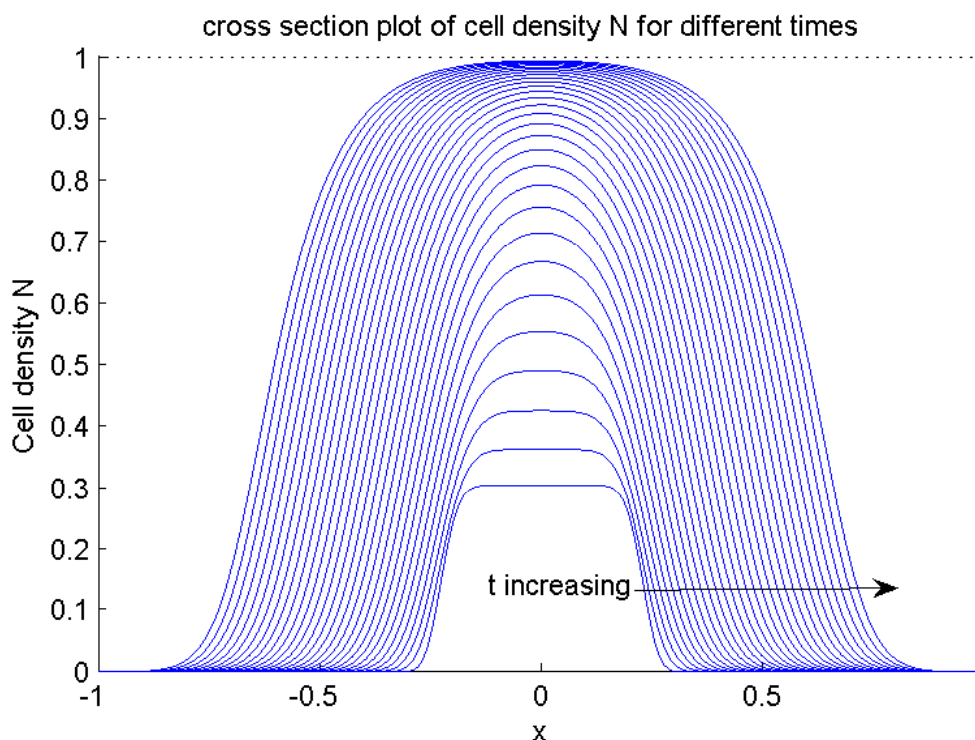


Figure 4.14: Cross section plot $y = 0$ of cell density N for same times and parameter values used in Figure 4.13.

Figure 4.14 shows the cross section plot of cell density N at $y = 0$ for several time units. It is clear from the Figure that cell density N increases with time, when the cell density reaches its maximum limit the proliferation stops and the cells start to spread in the whole domain via diffusion. It is clear from the Figure 4.14 that when wave front settles down it is a travelling wave front. *i.e.* speed and shape of wave front remains

constant for all times.

4.9 Summary and Conclusions

In this Chapter we have modelled the growth of cells in 1-D and 2-D domain subject to uniform availability of nutrients. The growth of cells in the scaffold is governed by a Fisher equation with non-linear diffusion. The diffusion coefficient is modelled as an exponential function of cell density. The Fisher equation captures two features simultaneously, cell growth and diffusion. We have assumed cell growth and diffusion take place simultaneously in such a way that while cells grow in numbers the diffusion is very small and when they reach maximum carrying capacity, cell growth stops and they spread in the whole domain by diffusion. We assume that no cells enter or leave the domain. We apply an initial condition which has compact support. Thus the solution of Fisher equation is travelling wave-like. The main aim of this chapter was to improve the modelling of cell growth in a perfusion bioreactor by including the non-linear cell diffusion. Results of the model give the velocity scale for growing front of cells.

The equation (4.4.4) is highly non-linear so finding the exact solution is a difficult and challenging task. To find a numerical solution for the Fisher equation (4.4.4) we use a finite element solver COMSOL. The cell density $N(x, t)$ can be found at each mesh point. We found that the Fisher equation exhibits a travelling wave like solution. To find the theoretical minimum speed v_c of the growth front in 1-D case we use phase plane analysis. We use eigenvalues analysis to find the speed of growth front. The theoretical speed of the growth front in the 1-D case is $v_c = 2\sqrt{\chi\delta\exp(-\gamma)}$. The front in this case is called a pulled front. The values of parameters γ and δ are chosen in such a way that the theoretical wave speed $v_c = 1$. The wave speed found by numerical method differs from the one found by phase plane analysis for various values of parameter γ (see Section 4.6). The front in this case is called a pushed front. Theoretical wave speed v_c agrees with the numerical results for $\gamma = 0, 1, 2$ but it does not agree for $\gamma > 2$. Thus we will use $\gamma = 2$ in our future modelling. We have verified the approximate minimum wave speed v_c by the phase plane analysis but we do not have a relation to find the minimum wave speed v_{min} analytically when diffusion is non-linear. In general this does not require diffusion to be non-linear, it can happen with linear diffusion and a more complicated growth term (Rothe, 1981, Van Saarloos, 2003).

From numerical results we observe that cells first increase in numbers by cell proli-

feration and reach to maximum carrying capacity. When the cell density reaches its maximum carrying capacity then growth stops and they start to diffuse in the whole domain. The behaviour of the solution is travelling wave like when growth term is bigger than the diffusion term. Initially the shape and speed of the front was not constant but after some time it settles down and moves with constant speed and the shape of the front remains constant.

We have extended the results of the 1-D Fisher equation to 2-D. In 2-D we use a numerical technique to find the cell density $N(x, y, t)$ at each mesh point. We take the cross section of the solution at $x = 0$ or $y = 0$ and find the minimum wave speed in x and y -directions. The minimum wave speed of the growth front in x and y -directions agrees well with the wave speed in the 1-D case. We found that initially the wave moves with high speed and after some time it settles down to a travelling wave and moves without change in shape and speed.

2-D coupled model of fluid flow, nutrient transport and cell growth in a perfusion bioreactor

5.1 Introduction

Each and every tissue or organ is an important part of the human body. Every tissue plays a specific role in the human body in order to run the functions of the body. If a tissue is damaged or lost it can affect the whole body. Certain organs or tissues cannot heal by themselves and they require treatments to restore their functions. In some cases none of the currently available treatments can restore the function of damaged or lost tissue *e.g.* articular cartilage. Tissue engineering offers an alternative and new strategy for the patients requiring the replacement of such tissues. It is a cell based therapy which utilizes the patient's own cells. The cells isolated from the patient are grown in the laboratory so that they multiply in numbers. Then these cells are placed in a biodegradable scaffold that has the mechanical and chemical properties appropriate to the tissue it is replacing. The cell-seeded scaffold is then placed in the bioreactor. The bioreactor provides the correct environment for the growth of cells and to produce the extracellular matrix. The main challenge to grow the tissue in the laboratory is the size of the tissue. To date it has only been possible to grow a functional tissue in the laboratory with a thickness of only a few hundred micrometers. This is due to the constraint of nutrient supply in the inner layers of the scaffold. Mathematical models of nutrient transport and cell growth are a very powerful tool to study the tissue growth outcomes in a bioreactor.

In this Chapter we will describe a coupled mathematical model of nutrient transport and cell growth in a bioreactor. Cell-seeded scaffold is placed in a bioreactor and fluid delivers the nutrients to the cells. When the cells grow and they occupy the empty spaces of the scaffold then the porosity of the scaffold decreases, which means that cell growth affects the quantities such as porosity, permeability and hence flow velocities. We know that the porosity of the material is the fraction of empty spaces in the porous material. So mathematically we define the porosity of the scaffold to be a function of cell density and permeability of scaffold as a function of porosity. The effect of fluid shear stress on nutrient consumption and cell growth rates is also included in the model. The fluid velocity is calculated from Darcy's law for porous media. Once the fluid velocity is known, the distribution of shear stress, nutrient concentration and cell density can be found at each spatial point.

The main aims of this Chapter are

1. To describe the comprehensive mathematical model of nutrient transport and cell growth in a perfusion bioreactor.
2. To include the time dependent porosity changes due to cell growth.
3. To include the effect of fluid shear stress on nutrient uptake and cell growth rates.

In this Chapter we update the model presented in Chapter 3 by including more complicated terms such as the non-linear diffusion, effect of fluid shear stress on cell growth and nutrient consumption rates and a fixed flow rate. We also define the porosity as a function of cell density and represent the permeability as function of porosity. Darcy's law remains same as discussed in Chapter 3.

This Chapter is organized as follows: in Section 5.2 we define the model geometry, in Section 5.3, the dimensional model equations are outlined, in Section 5.3.5 nutrient consumption and cell growth rates are discussed, dimensionless model is outlined in the Section 5.5 and in Section 5.6 parameter values used in the model are discussed.

5.2 Geometry and model constraints

5.2.1 Model geometry

We consider a Cartesian co-ordinate system (x^*, y^*) aligned with the porous scaffold of length $2L^*$ and width $2L^*$. The scaffold extends from $-L^* \leq x^* \leq L^*$ and $-L^* \leq y^* \leq$

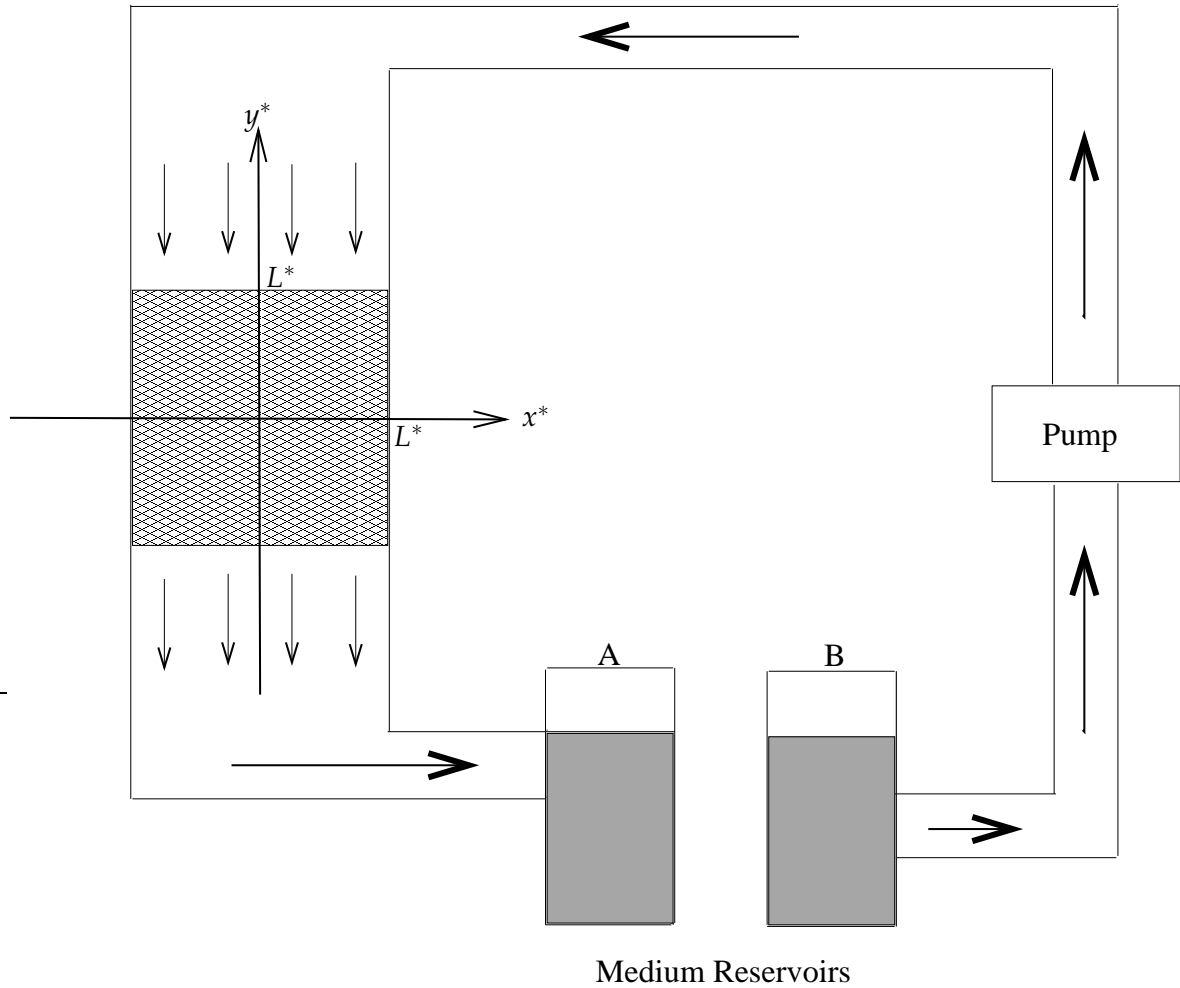


Figure 5.1: Schematic diagram of perfusion bioreactor system. A porous scaffold of length $2L^*$ and width $2L^*$ is placed within the bioreactor. Fresh fluid is drawn from the reservoir B by the actions of the pump. The fluid is then pumped into the porous scaffold. After exiting from the scaffold it returns to the medium reservoir A. Reservoir B is continuously filled with the fresh medium.

L^* . We model the scaffold as a porous material (Bear, 1988), so it is characterized by the usual properties of a porous material (porosity, permeability, tortuosity and pore diameter). We assume that the initial porosity of the scaffold is $\phi_0(x^*, y^*)$ and average pore diameter is $\epsilon^*(m)$. Initially cells are seeded onto the scaffold, which is placed in a perfusion bioreactor.

A simple perfusion bioreactor system is shown in the Figure 5.1. The perfusion bioreactor consist of a porous scaffold, a pump and two reservoirs **A** and **B**. Fresh fluid from reservoir **B** is pumped through the scaffold and is accumulated in reservoir **A**. We assume that a viscous, incompressible and Newtonian fluid of viscosity $\mu^*(Pa.sec)$ enters in the bioreactor through a pipe from reservoir **B**. In front of the pipe a pump

is attached to push the fluid through the scaffold. The fluid is pumped into the porous scaffold at the boundary $y^* = L^*$ and flows out of the scaffold at the boundary $y^* = -L^*$. After exiting from the scaffold the fluid returns in the reservoir **A**. We will also set up the model so that the pump maintains a constant volumetric flow rate through the scaffold.

5.2.2 Model assumptions

We are modelling the growth of cells and transport of nutrients in a bioreactor. Modelling the cell growth in a bioreactor is a complex system. The complete model should include the cell metabolism, growth and death mechanism. The model presented in this Chapter is subject to the following assumptions.

1. Fluid is viscous, incompressible and Newtonian,
2. Cells are immobilized (cells are not moving),
3. Constant total flow rate is maintained through the scaffold (we adjust the pressure drop to keep the flow rate constant),
4. Nutrient diffusion, single cell volume and pore diameter are constant,
5. Gravitational forces acting on the flow are neglected.
6. Heat phenomenon due to metabolic reactions is neglected, because the scaffold is placed in a bioreactor which maintains constant temperature.
7. Cell death due to lack of nutrients and high shear stress is neglected.

5.3 Model equations

We are modelling a coupled system of fluid flow, nutrient transport and cell growth in a perfusion bioreactor. The model consist of three partial differential equations, the first representing flow of fluid through the porous medium, with the velocity denoted by $\mathbf{u}^*(m/sec)$ and pressure denoted by $p^*(kg/m.sec^2)$, the second representing convection and diffusion of nutrients, with the concentration of nutrient denoted by $S^*(moles/m^3)$, and the third representing the cell proliferation, in terms of the cell density $N^*(cells/m^3)$. Nutrients are assumed to move due to convection and diffusion, with a constant diffusion rate $D_s^*(m^2/s)$ and to be consumed by the cells at the rate

G_s^* (moles/ m^3 .sec). Cells are assumed to diffuse with a density dependent diffusion rate $D^*(N^*)$ and they grow in number at a rate Q_n^* (cells/ m^3 .sec).

The shear stress σ^* (kg/ m .sec²) induced by the fluid also has a significant influence on the cell migration and cell differentiation (The process by which a cell becomes specialized in order to perform a specific function is called cell differentiation). Some cells are very sensitive to fluid shear stress. For viable growth some shear stress is necessary but cells may be damaged by the higher levels of shear stress (Whittaker et al., 2009). Therefore it is necessary to calculate the shear stress associated with the flow field. We describe the influence of fluid shear stress on nutrient consumption and the cell growth by the functions $F_s(\sigma^*)$ and $F_n(\sigma^*)$ respectively. These functions are defined later.

5.3.1 Cell feedback equation

We know that porosity is defined as the fraction of open spaces in the porous material. We assume that the cells are seeded onto a porous scaffold of porosity $\phi_0(x^*, y^*)$. As cells, that are initially seeded onto the porous scaffold proliferate (over the time interval Δt^* small enough that cell density changes only by a small amount), they occupy the void spaces in the scaffold so that the scaffold initial porosity $\phi_0(x^*, y^*)$ decreases as cell density increases. Porosity of porous material can be defined by a linear function by using a space filling argument (Coletti et al., 2006). The form of this function is given by

$$\phi(x^*, y^*, N^*) = \phi_0(x^*, y^*) - V_{cell}^* N^*, \quad (5.3.1)$$

where $\phi_0^*(x^*, y^*)$ is initial porosity of the scaffold without cells and V_{cell}^* ($m^3/cell$) is the single cell volume. From equation (5.3.1) porosity can be negative for high values of cell density N^* , which is un-physical. Hence to avoid this problem we define porosity of the scaffold by an exponential function of position and cell density N^* i.e. $\phi = \phi(x^*, y^*, N^*)$. The functional form used to described the porosity is given by,

$$\phi(x^*, y^*, N^*) = \phi_0(x^*, y^*) \exp\left(-\frac{V_{cell}^* N^*}{\phi_0(x^*, y^*)}\right), \quad (5.3.2)$$

Here we assume that the single cell volume is constant. The reason for choosing the porosity as an exponential function of cell density N^* is that the exponential function ensures that porosity will always remain positive. The porosity defined by equation (5.3.2) has linear behaviour for small values of cell density N^* , which agrees with the

function defined by equation (5.3.1).

It is clear from the equation (5.3.2) that in the absence of cells *i.e.* when $N^* = 0$ the porosity of the scaffold is $\phi_0(x^*, y^*)$ and as the cells increase in number then porosity decreases and it is minimum when cell density reaches its maximum carrying capacity N_{max}^* . The porosity of the scaffold varies in the range

$$\phi_0(x^*, y^*) \exp\left(-\frac{V_{cell}^* N_{max}^*}{\phi_0(x^*, y^*)}\right) \leq \phi(x^*, y^*, N^*) \leq \phi_0(x^*, y^*). \quad (5.3.3)$$

We know that the permeability is a measure of the ability of porous material to transmit fluids. Simple dimensional analysis suggest that permeability of the porous material is of the form $k^*(x^*, y^*, N^*) = k_0^* f(\phi)$, where $f(\phi)$ is a dimensionless function of porosity $\phi(x^*, y^*, N^*)$ and k_0^* is a constant. Darcy's law, can easily be derived within the simple capillary theory by Kozeny, in which the porous medium is imagined as a layer of solid material with straight parallel tubes of a fixed cross-sectional shape intersecting the sample. Within this model, the functional form of Kozeny (Kozeny et al., 1996) is used for the permeability $k^*(x^*, y^*, N^*)$.

$$k^*(x^*, y^*, N^*) = k_0^* \phi^3(x^*, y^*, N^*), \quad (5.3.4)$$

where k_0^* is a constant and has dimensions of permeability.

5.3.2 Flow field

Flow of fluid through the porous material is governed by Darcy's law (see Section 2.2) The variations in cell density N^* is a very slow process, and as a result the variations in permeability $k^*(x^*, y^*, N^*)$ will also be slow. The slow variations of permeability $k^*(x^*, y^*, N^*)$ can be captured by a quasi-static approximation, in which Darcy's law instantaneously reaches steady state in response to changes in the cell density. Fluid velocities are assumed to be sufficiently small that inertia can be neglected and also gravitational effects are neglected, so there is no body force term. Therefore we have

$$\mathbf{u}^* = -\frac{k^*(x^*, y^*, N^*)}{\mu^*} \nabla^* p^*. \quad (5.3.5)$$

The continuity equation is

$$\nabla^* \cdot \mathbf{u}^* = 0. \quad (5.3.6)$$

We assume that no fluid flows through the side walls of the scaffold *i.e.* no fluid flux through the boundaries at $x^* = \pm L^*$ and constant pressure conditions are prescribed at the top and bottom boundaries of the scaffold. Mathematically we write

$$\mathbf{u}^* \cdot \hat{\mathbf{n}} = 0 \quad \text{at } x^* = \pm L^*, \quad -L^* \leq y^* \leq L^*, \quad (5.3.7a)$$

$$p^* = p_0^* \quad \text{at } y^* = L^*, \quad -L^* \leq x^* \leq L^*, \quad (5.3.7b)$$

$$p^* = p_1^* \quad \text{at } y^* = -L^*, \quad -L^* \leq x^* \leq L^*, \quad (5.3.7c)$$

where $\hat{\mathbf{n}}$ is the outward unit normal vector to the boundary, p_0^* is the prescribed pressure at top boundary $y^* = L^*$ and p_1^* is the prescribed pressure at bottom boundary $y^* = -L^*$, and we assume that $p_0^* > p_1^*$.

5.3.2.1 Fixed flow rate

In experiments fluid is pumped into the scaffold with a constant flow rate. We do not know the pressure drop between top and bottom boundary of the scaffold. The constant flow rate fixes the pressure drop between top and bottom boundaries. However we notice that the problem is linear in the pressure drop. We can use the constant pressure drop and rescale answer to get the prescribed flow rate. The flow rate u_d^* , across the surface at $y^* = d^*$, where $-L^* \leq d^* \leq L^*$, is given by

$$u_d^* = \frac{1}{2L^*} \int_{-L^*}^{L^*} \frac{k^*(x^*, d^*, N^*)}{\mu^*} \frac{\partial P^*}{\partial y^*} dx^*. \quad (5.3.8)$$

When the cells grow and occupy the scaffold voids then permeability of scaffold decreases, and as a result total fluid flux through the porous material decreases for a fixed pressure drop. The fluid flux continuously decreases with the increase in cell density. Since we have already assumed that nutrients are delivered to the cells by convection and diffusion, if we take Darcy's velocity as the convective velocity for nutrient transport then the convective velocity decreases with decrease in fluid flux. Hence the delivery of nutrients to the cells decrease with the increase in cell density, which influences the cell growth. The growth of cells is proportional to available nutrient concentration. The cell growth will decrease with the decrease in nutrient concentration. To overcome this problem we need to keep the flow rate constant through the scaffold, so to maintain advection of nutrients to the cells.

To keep the flow rate constant we rescale the velocity obtained from Darcy's law. We divide the Darcy's velocity by a constant that ensures that the total flux across every

line of constant y^* is the externally prescribed flux. Let \mathbf{u}_r^* be the rescaled velocity then

$$\mathbf{u}_r^* = \mathbf{u}^* \frac{U_c^*}{u_d^*},$$

where \mathbf{u}^* is the velocity obtained from the Darcy's law solved with fixed pressure drop and u_d^* is the mean velocity at $y^* = d^*$ and U_c^* is the velocity with which fluid is pumped into the scaffold, which is specified externally *i.e.* it is a model parameter.

5.3.2.2 Fluid shear stress

The shear stress experienced by the cells within the individual scaffold pores can be estimated from the rescaled Darcy's velocity \mathbf{u}_r^* . This estimate depends on the porosity, average pore diameter and tortuosity. At the level of this estimate we assume that changes in porosity are made at constant pore diameter and tortuosity. The mean magnitude of the interstitial velocity can be estimated by the typical pore velocity (Whittaker et al., 2009). Let \mathbf{u}_r^* be the mean velocity in the porous material (including pore network and solid material) and U_p^* is the typical velocity in the individual pore then

$$|\mathbf{u}_r^*| = \frac{\phi(x^*, y^*, N^*)}{\tau} U_p^*, \quad (5.3.9)$$

where $\phi(x^*, y^*, N^*)$ is porosity of the porous material. It is clear from the equation (5.3.9) that for constant tortuosity if porosity is small then velocity in the pore has to be fast. For constant porosity if the scaffold is more tortuous then interstitial flow has to be faster to travel the greater distance in the same time. Hence from equation (5.3.9) we can write

$$U_p^* = \frac{\tau}{\phi(x^*, y^*, N^*)} |\mathbf{u}_r^*|, \quad (5.3.10)$$

If the pore Reynolds number is small then the local flow in each pore of the scaffold is modelled by Poiseuille flow which is given by

$$\mathbf{v}_p^*(r^*) = A \left[1 - \left(\frac{2r^*}{\epsilon^*} \right)^2 \right], \quad (5.3.11)$$

where $\mathbf{v}_p^*(r^*)$ is velocity in individual pore, A is constant, ϵ^* is pore diameter and r^* is the radial coordinate. To find the values of constant A we assume that U_p^* is the mean

velocity in the individual pore. Then we have

$$\frac{1}{\pi(\epsilon^*/2)^2} \int_0^{\epsilon^*/2} \mathbf{v}_p^*(r^*) 2\pi r^* dr^* = U_p^*. \quad (5.3.12)$$

Solution of equation (5.3.12) gives $A = 2U_p^*$. Substituting the value of A into equation (5.3.11) we get

$$\mathbf{v}_p^*(r^*) = 2U_p^* \left[1 - \left(\frac{2r^*}{\epsilon^*} \right)^2 \right], \quad (5.3.13)$$

By Newton's law of viscosity the shear stress σ^* is proportional to velocity gradient

$$\sigma^* = \mu^* \left| \frac{\partial \mathbf{v}_p^*}{\partial r^*} \right|. \quad (5.3.14)$$

Substituting the value of velocity \mathbf{v}_p^* from equation (5.3.13) into (5.3.14) we get

$$\sigma^* = \frac{8\mu^* U_p^*}{\epsilon^*}. \quad (5.3.15)$$

Substituting the value of U_p^* from equation (5.3.10) into (5.3.15) we get

$$\sigma^* = \frac{8\mu^* \tau}{\epsilon^*} \frac{|\mathbf{u}_r^*|}{\phi(x^*, y^*, N^*)}. \quad (5.3.16)$$

Equation (5.3.16) represents a relation between the fluid shear stress, Darcy's velocity and porosity of porous material.

5.3.3 Nutrient Transport

Transport of nutrient to the cells is due to convection and diffusion so the dynamics of nutrient concentration is modelled by the convection diffusion equation. Cells require several nutrients to perform their functions. These essential nutrients are delivered to the cells via a fluid usually known as the culture medium. We assume that the cell membranes are completely permeable to this culture medium. Let the total rate of nutrient consumption be G_s^* . The equation governing the transport and consumption of nutrients is given by the continuity equation

$$\frac{\partial S^*}{\partial t^*} + \mathbf{u}_r^* \cdot \nabla^* S^* = D_s^* \nabla^{*2} S^* - G_s^*. \quad (5.3.17)$$

We assume that there is no flux of nutrients through the side boundaries at $x^* = \pm L^*$. If the diffusion coefficient D_s^* is very small then in that case the downstream boundary condition becomes unimportant because it only influences a small boundary layer near $y^* = -L^*$. For numerical convenience we apply an ‘advection dominated’ boundary condition at the bottom boundary $y^* = -L^*$. We assume that advective flux dominates over the diffusive flux at the bottom boundary $y^* = -L^*$, or in other words the flow of nutrients is due to advection not by diffusion. Hence diffusive flux of nutrients through the boundary at $y^* = -L^*$ is zero. This type of boundary condition has also been used by Coletti et al. (2006). At the inlet boundary $y^* = L^*$ we have a bath of nutrients so at the boundary $y^* = L^*$ we consider nutrient concentration is S_0^* . Mathematically we write,

$$\hat{\mathbf{n}} \cdot \nabla^* S^* = 0 \quad \text{at } x^* = \pm L^*, \quad -L^* \leq y^* \leq L^*, \quad (5.3.18a)$$

$$S^* = S_0^* \quad \text{at } y^* = L^*, \quad -L^* \leq x^* \leq L^*, \quad (5.3.18b)$$

$$\hat{\mathbf{n}} \cdot \nabla^* S^* = 0 \quad \text{at } y^* = -L^*, \quad -L^* \leq x^* \leq L^*. \quad (5.3.18c)$$

The form of boundary conditions (5.3.18a) and (5.3.18c) look similar but physically they have different meanings. For fluid flow through the porous scaffold we have already considered the boundary conditions (5.3.7a), which says that no fluid flows through the side walls of the scaffold. Physically boundary condition (5.3.18a) states that there is neither advection nor diffusion through the side walls of the scaffold and boundary condition (5.3.18c) states that at the bottom boundary $y^* = -L^*$ diffusion of nutrients is zero but advection of nutrients is not zero.

5.3.4 Cell Growth

We want to model a system in which change in cell density is due cell proliferation and when the cell density reaches its maximum carrying capacity then proliferation stops and cells start to spread via diffusion in the entire domain. This suggests that we need to consider a logistic growth model in which the cell population spreads via diffusion, so we have a coupled system of reaction kinetics and diffusion. These two features are captured in Fisher’s equation. The Fisher’s equation with non-linear diffusion is discussed in detail in Chapter 4. We have already shown in Chapter 4 that a non-linear diffusion term combined with logistic growth can mimic cell proliferation on a continuum level. The model parameters can be calculated by the growth rate. Hence

the growth of cells is governed by the non-linear Fisher's equation.

$$\frac{\partial N^*}{\partial t^*} - \nabla^* \cdot (D^*(N^*) \nabla^* N^*) = Q_n^*, \quad (5.3.19)$$

where $D^*(N^*)$ represents the non-linear cell diffusion. The cell diffusion is a function of cell density, specifically we assume that

$$D^*(N^*) = D_n^* \exp(\gamma^*(N^* - N_{max}^*)), \quad (5.3.20)$$

where D_n^* is constant, γ^* represents how rapidly the cell diffusion takes place with change in cell density. Equation (5.3.19) is a modified form of the general Fisher equation (Fisher, 1937). In this case we have introduced the diffusion as function of cell density and we have also included the influence of fluid shear stress on growth rate.

We assume that individual cells cannot leave the domain which means zero flux boundary conditions at all the boundaries. Mathematically we write

$$\hat{n} \cdot \nabla^* N^* = 0 \quad \text{at} \quad x^* = \pm L^* \quad \text{and} \quad y^* = \pm L^*, \quad (5.3.21)$$

We suppose that at time $t = 0$ the initial cell density is $N_{init}^*(x^*, y^*)$,

$$N^* = N_{init}^*(x^*, y^*) \quad \text{at} \quad t = 0, \quad (5.3.22)$$

where the form of $N_{init}^*(x^*, y^*)$ depends on the seeding strategy. We will use different choices of $N_{init}^*(x^*, y^*)$ in our simulations.

5.3.5 Nutrient consumption and cell proliferation rates

An important part of modelling is the prescription of the nutrient consumption and net cell growth rate G_s^* and Q_n^* respectively. Let λ^* be the cell proliferation rate per cell. We suppose that the rate of proliferation of cells is a function of nutrient concentration S^* and fluid shear stress σ^* *i.e.* $\lambda^*(S^*, \sigma^*)$ and the rate of nutrient consumption per cell is $\alpha^* \lambda^*(S^*, \sigma^*)$, where α^* is a constant. We assume that the proliferation rate $\lambda^*(S^*, \sigma^*)$ is a separable function of fluid shear stress and nutrient concentration *i.e.* $\lambda^*(S^*, \sigma^*) = F_n(\sigma^*)E(S^*)$. The functions $F_n(\sigma^*)$ and $E(S^*)$ represent the effect of fluid shear stress and nutrient concentration on cell growth rate respectively. We neglect cell death as the growth rate is assumed to be much higher than the death. We assume that the cells proliferate according to the logistic law. Thus the net cell growth

rate $Q_n^* = \lambda^*(S^*, \sigma^*) N^* (1 - N^*/N_{max}^*)$, where N_{max}^* is the maximum carrying capacity. There is significant discussion about the form of the proliferation rate $\lambda^*(S^*, \sigma^*)$ in the literature. In most of the cell growth models the proliferation rate λ^* is a function of nutrient concentration S^* only but only a few models have accounted the effect of fluid shear stress on the cell growth *e.g.* McElwain and Ponzo (1977) used a piecewise linear behaviour, whereas Galban and Locke (1999) used more complex functions such as modified Contois, Moser and nth order heterogeneous models. Coletti et al. (2006) have also used a Contois function to describe the cell growth. Landman and Cai (2007) considered a Heaviside step functional form $H(S^* - S_h^*)$, where S_h^* is the hypoxic threshold for the nutrient concentration. This type of proliferation rate was also used by Lewis et al. (2005). They used an approximation $\lambda^*(S^*) = H(S^*)$ *i.e.* $S_h^* = 0$. Malda et al. (2004a) have used Michaelis-Menton type behaviour. Many of these forms reduce to simple linear behaviour for small values of concentration. The most commonly used functional forms for $E(S^*)$ are linear and Michaelis-Menton functional forms which can be chosen here to describe $E(S^*)$. For simplicity we consider the simple linear behaviour used by Jones et al. (2000) and Lewis et al. (2005), *i.e.* we take $E(S^*) = \beta^* S^*$.

There is not much discussion about the form of $F_n(\sigma^*)$ in the literature. O'Dea et al. (2010) studied the effect of shear stress induced by the flow field on the cell growth. They assumed that at an intermediate level of shear stress, the rates of cell proliferation is increased, for low values of fluid shear stress, the cell proliferation is reduced, and for excessively high shear stresses the cells become damaged (Cartmell et al., 2003). We use the functional form used by O'Dea et al. (2010) to describe the influence of fluid shear stress on the cell growth, which is given by

$$F_n(\sigma^*) = 1 + \left(\frac{k_1 - 1}{2} \right) (\tanh [g^* (\sigma^* - \sigma_{c1}^*)] + 1) - \frac{k_1}{2} (\tanh [g^* (\sigma^* - \sigma_{c2}^*)] + 1), \quad (5.3.23)$$

which approximates the step function behaviour (see Figure 5.2). Here σ_{c1}^* and σ_{c2}^* denotes the threshold values where the cell proliferation is heightened and the zero proliferation phase is entered respectively, the parameter g^* determines the closeness of approximation to the step function behaviour and k_1 is a dimensionless constant that determines the amount of heightened proliferation in the heightened region of stress. Figure 5.2 shows the graphical representation of the function defined by equation (5.3.23). It is clear from Figure 5.2 how the cells progress from the quiescence phase to the proliferative phase and then to the necrotic phase in response to fluid induced shear stress. If the value of parameter g^* is large then the behaviour of the function

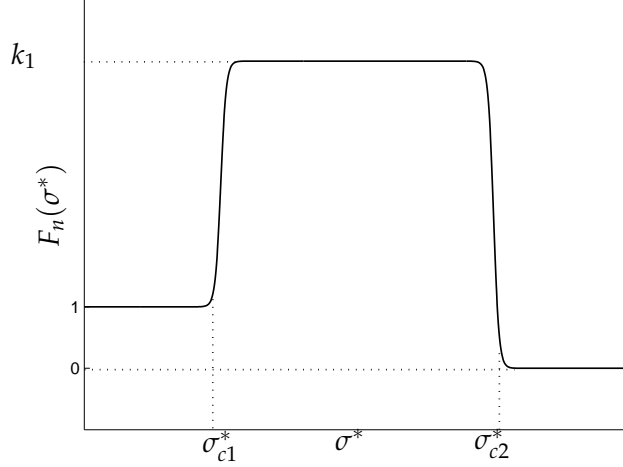


Figure 5.2: Schematic diagram of the progression of cells from quiescence phase to proliferative phase and then to zero proliferation phase.

$F_n(\sigma^*)$ is very close to a step function. We choose this function to describe the effect of fluid shear stress on the cell proliferation.

To consider the influence of fluid shear stress on nutrient consumption rate we assume that up to σ_{c2}^* the nutrient consumption is proportional to cell growth rate. Beyond σ_{c2}^* we assume that cells consume nutrients but they do not grow. Thus we use the functional form of O'Dea et al. (2010) to describe the influence of fluid shear stress on nutrient consumption in the high stress region. Here we assume that for high values of the fluid shear stress the nutrient consumption rate returns to its base line value.

$$F_n(\sigma^*) = 1 + \left(\frac{k_1 - 1}{2}\right) (\tanh [g^* (\sigma^* - \sigma_{c1}^*)] + 1) - \left(\frac{k_1 - 1}{2}\right) (\tanh [g^* (\sigma^* - \sigma_{c2}^*)] + 1), \quad (5.3.24)$$

Figure 5.3 shows the graphical representation of the function defined by equation (5.3.24). It is clear from the Figure 5.3 that for intermediate values of fluid shear stress the nutrient consumption is heightened. So we choose the cell growth rate $\lambda^*(S^*, \sigma^*) = \beta^* F_n(\sigma^*) S^*$, where $\beta^* (m^3 / mole \cdot sec)$ is constant. Thus $Q_n^* = \beta^* F_n(\sigma^*) S^* N^* (1 - N^* / N_{max}^*)$. We assume that the dominant mechanism for cell nutrient consumption is entirely dependent on the cellular growth. We have that $Q_n^* \propto G_s^*$ for $N^* \ll N_{max}^*$ and $\sigma^* < \sigma_{c2}^*$. Hence the nutrient consumption rate $G_s^* = -\alpha^* S^* F_n(\sigma^*) N^*$, where $\alpha^* (m^3 / cells \cdot sec)$ is a constant. However outside these limits the proportionality no longer holds. When $N^* \sim N_{max}^*$ the cell growth slows down but nutrient consumption is high and when $\sigma^* > \sigma_{c2}^*$ cell growth stops but nutrient consumption still continues. We did not use the

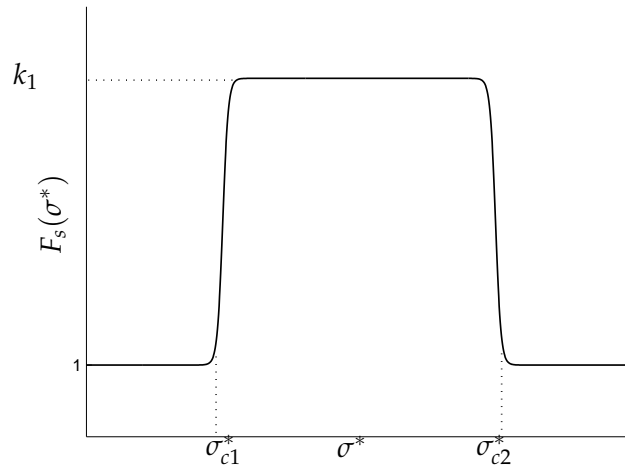


Figure 5.3: Schematic diagram of the progression of nutrient consumption from quiescence phase to proliferative phase and then to zero proliferation phase.

logistic term for nutrient concentration S^* in the expression for nutrient consumption rate G_s^* . The reason is that the logistic term would limit the nutrient concentration S^* and nutrient concentration will not go beyond a limiting value. With the increase in cell density the nutrient consumption increases. Even when cell density reaches its maximum carrying capacity N_{max}^* the cell growth stops but cells would continue to consume nutrients to live.

The summary of dimensional model equations, the boundary and initial conditions is shown in Table 5.1.

Table 5.1: Summary of dimensional model equations, boundary and initial conditions

Equations	Boundary conditions	Initial conditions
$\phi(x^*, y^*, N^*) = \phi_0(x^*, y^*) \exp\left(-\frac{V_{cell}^* N^*}{\phi_0(x^*, y^*)}\right),$ $k^*(x^*, y^*, N^*) = k_0^* \phi^3(x^*, y^*, N^*).$		
<p>Darcy's law</p> $\mathbf{u}^* = -\frac{k^*(x^*, y^*, N^*)}{\mu^*} \nabla^* p^*,$ $\nabla^* \cdot \mathbf{u}^* = 0.$ $u_d^* = \frac{1}{2L^*} \int_{-L^*}^{L^*} \frac{k^*(x^*, d^*, N^*)}{\mu^*} \frac{\partial P^*}{\partial y^*} dx^*, \quad \text{for } -L^* \leq d^* \leq L^*,$ $\mathbf{u}_r^* = \mathbf{u}^* \frac{U_c^*}{u_d^*},$ $\sigma^* = \frac{8\mu^* \tau}{\epsilon^*} \frac{ \mathbf{u}_r^* }{\phi(x^*, y^*, N^*)}.$	$\mathbf{u}^* \cdot \hat{\mathbf{n}} = 0 \quad \text{at } x^* = \pm L^*, \quad -L^* \leq y^* \leq L^*,$ $p^* = p_0^* \quad \text{at } y^* = L^*, \quad -L^* \leq x^* \leq L^*,$ $p^* = p_1^* \quad \text{at } y^* = -L^*, \quad -L^* \leq x^* \leq L^*.$	
<p>Nutrient Transport</p> $\frac{\partial S^*}{\partial t^*} + \mathbf{u}_r^* \cdot \nabla^* S^* = D_s^* \nabla^{*2} S^* - \alpha^* S^* F_s(\sigma^*) N^*,$ <p>where $F_s(\sigma^*)$ is given by equation (5.3.25).</p>	$\hat{\mathbf{n}} \cdot \nabla^* S^* = 0 \quad \text{at } x^* = \pm L^*, \quad -L^* \leq y^* \leq L^*,$ $S^* = S_0^* \quad \text{at } y^* = L^*, \quad -L^* \leq x^* \leq L^*,$ $\hat{\mathbf{n}} \cdot \nabla^* S^* = 0 \quad \text{at } y^* = -L^*, \quad -L^* \leq x^* \leq L^*.$	
<p>Cell growth</p> $\frac{\partial N^*}{\partial t^*} - \nabla^* \cdot (D^*(N^*) \nabla^* N^*) = \beta^* F_n(\sigma^*) S^* N^* \left(1 - \frac{N^*}{N_{max}^*}\right),$ <p>where $D^*(N^*) = D_n^* \exp(\gamma^*(N^* - N_{max}^*))$ and $F_n(\sigma^*)$ is given by equation (5.3.26).</p>	$\hat{\mathbf{n}} \cdot \nabla^* N^* = 0, \quad \text{at } x^* = \pm L^*, \quad y^* = \pm L^*.$	$N^* = N_{init}^*(x^*, y^*),$ <p>at $t^* = 0$.</p>

$$F_s(\sigma^*) = 1 + \left(\frac{k_1 - 1}{2}\right) (\tanh [g^* (\sigma^* - \sigma_{c1}^*)] + 1) - \left(\frac{k_1 - 1}{2}\right) (\tanh [g^* (\sigma^* - \sigma_{c2}^*)] + 1), \quad (5.3.25)$$

$$F_n(\sigma^*) = 1 + \left(\frac{k_1 - 1}{2}\right) (\tanh [g^* (\sigma^* - \sigma_{c1}^*)] + 1) - \frac{k_1}{2} (\tanh [g^* (\sigma^* - \sigma_{c2}^*)] + 1). \quad (5.3.26)$$

5.4 Nondimensionalization

We nondimensionalize all lengths with scaffold length L^* and the permeability with respect to an initial permeability k_0^* , so that

$$\begin{aligned} x^* &= L^*x, & y^* &= L^*y, & \nabla^* &= \frac{1}{L^*}\nabla. \\ k^*(x^*, y^*, N^*) &= k_0^*k(x, y, N). \end{aligned}$$

We nondimensionalize all velocities by the pump velocity U_c^* and pressure by the pressure difference between top and bottom boundaries of scaffold,

$$\mathbf{u}^* = U_c^*\mathbf{u}, \quad \mathbf{u}_r^* = U_c^*\mathbf{u}_r, \quad u_d^* = U_c^*u_d, \quad p^* = (p_0^* - p_1^*)p + p_1^*,$$

where $(p_0^* - p_1^*)$ is the pressure difference between the top and bottom boundaries, and U_c^* is the pump velocity or characteristic velocity scale specified externally.

$$U_c^* = \frac{(p_0^* - p_1^*)k_0^*}{\mu^*L^*} \Rightarrow p_0^* - p_1^* = \frac{U_c^*L^*\mu^*}{k_0^*}. \quad (5.4.1)$$

We nondimensionalize fluid shear stress σ^* , threshold stresses σ_{c1}^* and σ_{c2}^* as follows

$$\sigma^* = \frac{8\tau\mu^*U_c^*}{\epsilon^*}\sigma, \quad \sigma_{c1}^* = \frac{8\tau\mu^*U_c^*}{\epsilon^*}\sigma_{c1}, \quad \sigma_{c2}^* = \frac{8\tau\mu^*U_c^*}{\epsilon^*}\sigma_{c2}. \quad (5.4.2)$$

We nondimensionalize cell density N^* and initial cell density $N_{init}^*(x^*, y^*)$ by the maximum carrying capacity N_{max}^* and nutrient concentration S^* by the initial concentration S_0^* respectively,

$$N^* = N_{max}^*N, \quad N_{init}^*(x^*, y^*) = N_{max}^*N_{init}(x, y), \quad S^* = S_0^*S. \quad (5.4.3)$$

Finally, we nondimensionalize time t^* by velocity of propagation v^* of front (see Chapter 4)

$$t^* = \frac{L^*}{v^*}t, \quad (5.4.4)$$

where $v^* = 2\sqrt{\beta^*S_0^*D_n^*\exp(-\gamma^*N_{max}^*)}$.

5.5 Dimensionless equations and boundary conditions

5.5.1 Cell feedback

The variation of porosity defined by equation (5.3.2) can be written in dimensionless form as,

$$\tilde{\phi}(x, y, N) = \tilde{\phi}_0(x, y) \exp\left(-\frac{\rho N}{\tilde{\phi}_0(x, y)}\right), \quad (5.5.1)$$

where $\rho = V_{cell}^* N_{max}^*$ is a dimensionless parameter which describes how rapidly the porosity is changing. $\tilde{\phi}(x, y, N) = \phi(x^*, y^*, N^*)$ and $\tilde{\phi}_0(x, y) = \phi_0(x^*, y^*)$ represents the porosity in dimensionless variables.

Equation (5.3.4) which represents the relation between porosity and permeability can be written in dimensionless form as,

$$k(x, y, N) = \tilde{\phi}^3(x, y, N). \quad (5.5.2)$$

5.5.2 Flow field

Darcy's law (5.3.5) and the continuity equation (5.3.6) can then be written in dimensionless form as

$$\mathbf{u} = -k(x, y, N) \nabla p, \quad (5.5.3)$$

$$\nabla \cdot \mathbf{u} = 0. \quad (5.5.4)$$

By combining equation (5.5.3) and (5.5.4) we get,

$$\nabla \cdot (k(x, y, N) \nabla p) = 0. \quad (5.5.5)$$

The boundary conditions (5.3.7) in dimensionless form become,

$$\hat{\mathbf{n}} \cdot \nabla p = 0 \quad \text{at } x = \pm 1, \quad -1 \leq y \leq 1, \quad (5.5.6a)$$

$$p = 1 \quad \text{at } y = 1, \quad -1 \leq x \leq 1, \quad (5.5.6b)$$

$$p = 0 \quad \text{at } y = -1, \quad -1 \leq x \leq 1. \quad (5.5.6c)$$

5.5.2.1 Fixed flow rate

The nondimensional form of flow rate u_d^* defined by equation (5.3.8) is given by

$$u_d = \frac{1}{2} \int_{-1}^1 k(x, d, N) \frac{\partial P}{\partial y} dx, \quad (5.5.7)$$

and rescaled velocity \mathbf{u}_r^* defined by equation (5.3.9) in dimensionless form becomes

$$\mathbf{u}_r = \frac{\mathbf{u}}{u_d}. \quad (5.5.8)$$

5.5.2.2 Fluid shear stress

The fluid shear stress defined by equation (5.3.16) in dimensionless form becomes

$$\sigma = \frac{|\mathbf{u}_r|}{\tilde{\phi}(x, y, N)}, \quad (5.5.9)$$

Equations (5.3.24) and (5.3.23), which represent the influence of fluid shear stress on nutrient consumption and cell growth respectively, in dimensionless form becomes

$$\begin{aligned} F_s(\sigma) &= 1 + \frac{k_1 - 1}{2} (\tanh [g (\sigma - \sigma_{c1})] + 1) \\ &\quad - \frac{k_1 - 1}{2} (\tanh [g (\sigma - \sigma_{c2})] + 1), \end{aligned} \quad (5.5.10)$$

$$\begin{aligned} F_n(\sigma) &= 1 + \frac{k_1 - 1}{2} (\tanh [g (\sigma - \sigma_{c1})] + 1) \\ &\quad - \frac{k_1}{2} (\tanh [g (\sigma - \sigma_{c2})] + 1), \end{aligned} \quad (5.5.11)$$

where $g = g^* 8\tau\mu^* U_c^* / \epsilon^*$ is a dimensionless constant.

5.5.3 Nutrient transport equation

The nutrient transport equation (5.3.17) and boundary conditions (5.3.18) can be written in the dimensionless form as,

$$\frac{v^*}{U_c^*} \frac{\partial S}{\partial t} + \mathbf{u}_r \cdot \nabla S = D_s \nabla^2 S - R_s F_s(\sigma) NS, \quad (5.5.12)$$

$$\hat{\mathbf{n}} \cdot \nabla S = 0 \quad \text{at } x = \pm 1, \quad -1 \leq y \leq 1, \quad (5.5.13a)$$

$$S = 1 \quad \text{at } y = 1, \quad -1 \leq x \leq 1, \quad (5.5.13b)$$

$$\hat{\mathbf{n}} \cdot \nabla S = 0 \quad \text{at } y = -1, \quad -1 \leq x \leq 1 \quad (5.5.13c)$$

where

$$D_s = \frac{D_s^*}{U_c^* L^*}, \quad \text{and} \quad R_s = \frac{\alpha^* L^* N_{max}^*}{U_c^*}, \quad (5.5.14)$$

are dimensionless numbers. The parameter D_s is the inverse of the Peclet number and represents the ratio of nutrient diffusion to advection. We assume that the diffusion of nutrients is slow compared to the advective velocity so that the parameter D_s will be small which implies that the Peclet number is high. The parameter R_s represents the rate of nutrient consumption relative to advection. If the characteristic advective velocity U_c^* is high compared to the rate of nutrient consumption then the parameter R_s is small which implies that cells are eating nutrients slowly.

The velocity of the growth front v^* is very small compared to the velocity of the pump U_c^* . So the ratio v^*/U_c^* is a very small number which can be neglected. Hence the quasi-steady approximation of equation (5.5.12) is used *i.e.* the time derivative is neglected. The equation (5.5.12) can be written as

$$\mathbf{u}_r \cdot \nabla S = D_s \nabla^2 S - R_s F_s(\sigma) N S. \quad (5.5.15)$$

5.5.4 Cell growth equation

The cell growth equation (5.3.19) in dimensionless form becomes

$$\frac{\partial N}{\partial t} - \delta \nabla \cdot (D(N) \nabla N) = \beta F_n(\sigma) S N (1 - N), \quad (5.5.16)$$

where $D(N) = \exp(\gamma(N - 1))$ is non-linear cell diffusion, $\delta = D_n^*/L^*v^*$ is a dimensionless number which represents the ratio of the cell diffusion to the speed of the growth front and $\beta = \beta^* L^* S_0^*/v^*$ is a dimensionless number which represents the ratio of the cellular proliferation to the speed of growth front. Boundary conditions (5.3.21) and

initial condition (5.3.22) in dimensionless form can be written as,

$$\begin{aligned}\hat{n} \cdot \nabla N &= 0, \quad \text{at all the four boundaries } x = \pm 1, \quad y = \pm 1, \\ N &= N_{init}(x, y) \quad \text{at } t = 0.\end{aligned}\tag{5.5.17}$$

Dimensionless parameters

The dimensionless parameters in the model are,

$$\begin{aligned}D_s &= \frac{D_s^*}{U_c^* L^*}, & R_s &= \frac{a^* L^* N_{max}^*}{U_c^*}, \\ \beta &= \frac{\beta^* L^* S_0^*}{v^*}, & \delta &= \frac{D_n^*}{v^* L^*}, \\ \rho &= V_{cell}^* N_{max}^*, & \gamma &= \gamma^* N_{max}^*.\end{aligned}$$

The summary of dimensionless model equations, boundary and initial equations are shown in Table 5.2

Table 5.2: Summary of dimensionless model equations, boundary and initial conditions

Equations	Boundary conditions	Initial conditions
Porosity distribution $\tilde{\phi}(x, y, N) = \tilde{\phi}_0(x, y) \exp\left(-\frac{\rho N}{\tilde{\phi}_0(x, y)}\right),$ $k(x, y, N) = \tilde{\phi}^3(x, y, N).$		
Darcy's law $\mathbf{u} = -k(x, y, N) \nabla p,$ $\nabla \cdot \mathbf{u} = 0.$ $u_d = \frac{1}{2} \int_{-1}^1 k(x, d, N) \frac{\partial p}{\partial y} dx, \quad \text{for } -1 \leq d \leq 1$ $\mathbf{u}_r = \frac{\mathbf{u}}{u_d},$ $\sigma = \frac{ \mathbf{u}_r }{\tilde{\phi}(x, y, N)}.$	$\hat{\mathbf{n}} \cdot \nabla p = 0, \quad \text{at } x = \pm 1, \quad -1 \leq y \leq 1,$ $p = 1, \quad \text{at } y = 1, \quad -1 \leq x \leq 1,$ $p = 0, \quad \text{at } y = -1, \quad -1 \leq x \leq 1.$	
Nutrient Transport $\mathbf{u}_r \cdot \nabla S = D_s \nabla^2 S - R_s F_s(\sigma) NS,$ where $F_s(\sigma)$ is given by equation (5.5.18).	$\hat{\mathbf{n}} \cdot \nabla S = 0, \quad \text{at } x = \pm 1, \quad -1 \leq y \leq 1,$ $S = 1, \quad \text{at } y = 1, \quad -1 \leq x \leq 1,$ $\hat{\mathbf{n}} \cdot \nabla S = 0, \quad \text{at } y = -1, \quad -1 \leq x \leq 1.$	
Cell growth $\frac{\partial N}{\partial t} - \delta \nabla \cdot (D(N) \nabla N) = \beta F_n(\sigma) SN(1 - N),$ where $D(N) = \exp(\gamma(N - 1))$ and $F_n(\sigma)$ is given by equation (5.5.19).	$\hat{\mathbf{n}} \cdot \nabla N = 0, \quad \text{at } x = \pm 1, \quad y = \pm 1.$	$N = N_{init}(x, y),$ at $t = 0.$

$$F_s(\sigma) = 1 + \left(\frac{k_1 - 1}{2}\right) (\tanh [g(\sigma - \sigma_{c1})] + 1) - \left(\frac{k_1 - 1}{2}\right) (\tanh [g(\sigma - \sigma_{c2})] + 1), \quad (5.5.18)$$

$$F_n(\sigma) = 1 + \left(\frac{k_1 - 1}{2}\right) (\tanh [g(\sigma - \sigma_{c1})] + 1) - \frac{k_1}{2} (\tanh [g(\sigma - \sigma_{c2})] + 1). \quad (5.5.19)$$

5.6 Parameter values

The model proposed in the previous section includes a number of parameters. Some parameters depend on the cell type and nutrient type and some depend on the bioreactor. Table 5.3 shows the values of the parameters used in the simulations.

5.6.1 Geometric parameters

The values of the geometric parameters such as scaffold length L^* and cell free scaffold characteristics are chosen with reference to experimental system used by Professor David Grant in experiments at the University of Nottingham. The initial porosity $\phi_0 = 0.85$, perfusion velocity $U_c^* = 1.5 \times 10^{-4} m/sec$ and scaffold length $L^* = 0.01m$ are used in these experiments (David Grant, personal communication). The experimental data for initial porosity of scaffold (cell free), tortuosity and permeability are also available from Rose et al. (2004).

5.6.2 Cell parameters

Some quantities such as cell size, density and nutrient uptake rate depend on the cell type cultured in the bioreactor. Our model is a very generalized model and can be applied to any cell type. To compare the model with the experimental data the cells used in the simulations are Murine immortalized rat cell C_2C_{12} .

For their survival cells require several different nutrients that include glucose, oxygen, glutamine, carbon dioxide, ascorbic acid (vitamin C), amino acids, foetal calf serum *etc.* (Sengers et al., 2005). For simplicity we assume that the cell growth is limited by the supply of oxygen only (Malda et al., 2004a). The initial oxygen concentration S_0^* is chosen as $0.2 moles/m^3$, which is much higher than the minimum nutrient concentration required for cell viability.

The single cell volume V_{cell}^* and maximum cell growth rate is taken from Coletti et al. (2006). For C_2C_{12} the maximum oxygen uptake rate $\alpha^* S_0^*$ is presently available neither experimentally nor in the literature. Therefore this value is approximated by using the value for the chondrocyte as used in the literature (Obradovic et al., 2000).

Since cell growth is a very slow process so we assume that the velocity of the growth front v^* is $1mm/day$. The values of parameters γ^* and D_n^* are not available in the literature. We have discussed in detail in Chapter 4 how we choose the values of these parameters.

Table 5.3: Model parameters and values used in the simulation

Parameter	Description	Value	unit
L^*	Scaffold length	0.01	m
U_c^*	Perfusion velocity	2.5×10^{-2}	m/sec
D_s^*	Oxygen diffusion coefficient	1.5×10^{-9}	m^2/sec
V_{cell}^*	Single cell volume	2.5×10^{-18}	$m^3/cell$
N_{max}^*	Maximum carrying capacity	4×10^{17}	$cells/m^3$
S_0^*	Initial oxygen concentration	0.2	$moles/m^3$
$\alpha^* S_0^*$	Maximum oxygen consumption rate	1.86×10^{-18}	$moles/cell.sec$
α^*	-	9.3×10^{-18}	$m^3/cell.sec$
$\beta^* S_0^*$	Maximum cell growth rate	1.52×10^{-5}	$1/sec$
β^*	-	7.6×10^{-5}	$m^3/mole.sec$
v^*	Velocity of growth front	1.15×10^{-8}	m/sec
γ^*	-	5×10^{-18}	$m^3/cell$
D_n^*	-	1.6×10^{-11}	m^2/sec

The values of the threshold shear stresses σ_{c1} and σ_{c2} are not available in literature so we choose the dimensionless values of these parameters directly to be within the range typically found in our computations (see in our calculation in Chapter 6). The parameter g determines the sharpness of stress functions. For high values of parameter g the behaviour stress functions $F_s(\sigma)$ and $F_n(\sigma)$ is like a step function, so are independent of the value of parameter g . Thus we choose reasonably high value of $\tilde{g} = 60$ such that shape of the stress functions $F_s(\sigma)$ and $F_n(\sigma)$ is very close to a step function. Parameter k_1 represents the amount of heightened proliferation in the proliferative region. Again we choose a feasible value for k_1 i.e. $k_1 = 5$.

Table 5.4: Values of dimensionless parameters

Parameter	Formula	Value	Description
D_s	$\frac{D_s^*}{U_c^* L^*}$	6×10^{-6}	Inverse Peclet number
R_s	$\frac{\alpha^* L^* N_{max}^*}{U_c^*}$	1.488	Ratio of nutrient consumption relative to advection
β	$\frac{\beta^* L^* S_0^*}{v^*}$	13.21	Ratio of cellular proliferation to speed of growth front
δ	$\frac{D_n^*}{v^* L^*}$	0.139	Ratio of cellular diffusion to speed of growth front
γ	$\gamma^* N_{max}^*$	2	Constant in non-linear diffusion
ρ	$V_{cell}^* N_{max}^*$	1	Constant in porosity function
σ_{c1}		3	Threshold shear stress for proliferation phase.
σ_{c2}		15	Threshold shear stress for necrotic phase.
k_1		5	amount of heightened proliferation
g		60	Parameter controlling the sharpness of stress functions $F_s(\sigma)$ and $F_n(\sigma)$.

Effect of initial seeding and channeling on cell growth

6.1 Introduction

In this Chapter we discuss the results of the model developed in Chapter 5. First we describe how the model is solved by using the commercial software COMSOL and then we discuss the convergence of numerical method in detail. Since in the model the initial cell density $N_{init}(x, y)$ and initial porosity $\phi_0(x, y)$ depend on the spatial coordinates, we can consider various forms of initial seeding and scaffold design (depending on the initial porosity). We analyze the cell density, nutrient concentration and shear stress at initial time, intermediate time and time close to steady state for various initial seeding strategies and scaffold design. We also consider the effect of perfusion rate on cell density in the final construct.

The model presented in Chapter 5 consists of a coupled system of three partial differential equations, namely Darcy's law, the advection-diffusion equation and a cell growth equation. Darcy's law governs the fluid flow through the porous material. The advection-diffusion equation governs the delivery of nutrients to the cells and the third equation governs the cell growth in the scaffold. A pre-seeded scaffold is placed in the bioreactor and fluid is pumped through the scaffold. We calculate the porosity and permeability of the scaffold for initial cell density. As cells grow with time, the porosity and permeability of the cell-seeded scaffold decreases from its initial value. First we solve Darcy's law (with permeability corresponding to initial cell density) to obtain the fluid velocity. In the model we maintain a constant volumetric flow rate through the scaffold so we divide the Darcy's velocity by a constant that ensures that the total

flux across every line of constant y is the externally prescribed flux. We also calculate the effect of fluid shear stress on nutrient consumption and cell growth rates. We assume that for low and high values of fluid shear stress there is no change in nutrient consumption rate but for intermediate values of shear stress the nutrient consumption rate becomes large. Additionally we assume that low values of fluid shear stress have no effect on cell growth rate, for intermediate values of shear stress cell growth is enhanced and cell growth stops for high values of fluid shear stress (for more details see Sections 1.2 and 5.3.5). We substitute the rescaled velocity as the advective velocity in the advection-diffusion equation to find the nutrient concentration. Then this nutrient concentration is substituted into the cell growth equation to obtain the cell density. We update the effect of cell density on the porosity equation and solve the entire system for the updated cell density. Figure 6.1 shows a schematic diagram of the coupled model equations, showing the three main equations, Darcy's law, advection-diffusion equation and cell growth equation. The corresponding boundary conditions for each equation are given below.

For the flow equation we assume that no fluid flows through the side walls of the scaffold and pressure at inlet and outlet walls of scaffold is constant. Mathematically we write

$$\hat{\mathbf{n}} \cdot \nabla p = 0 \quad \text{at } x = \pm 1, \quad -1 \leq y \leq 1, \quad (6.1.1a)$$

$$p = 1 \quad \text{at } y = 1, \quad -1 \leq x \leq 1, \quad (6.1.1b)$$

$$p = 0 \quad \text{at } y = -1, \quad -1 \leq x \leq 1. \quad (6.1.1c)$$

For the nutrient transport equation we apply no flux (advective and diffusive) conditions at the side walls of the scaffold, constant nutrient concentration at the inlet wall of scaffold and no diffusive flux at the outlet wall of scaffold. Mathematically these conditions can be written as

$$\hat{\mathbf{n}} \cdot \nabla S = 0 \quad \text{at } x = \pm 1, \quad -1 \leq y \leq 1, \quad (6.1.2a)$$

$$S = 1 \quad \text{at } y = 1, \quad -1 \leq x \leq 1, \quad (6.1.2b)$$

$$\hat{\mathbf{n}} \cdot \nabla S = 0 \quad \text{at } y = -1, \quad -1 \leq x \leq 1. \quad (6.1.2c)$$

Finally for the cell growth equation we assume that individual cells cannot leave the domain. Mathematically we write these boundary conditions as

$$\hat{\mathbf{n}} \cdot \nabla N = 0, \quad \text{at all the four boundaries } x = \pm 1, \quad y = \pm 1. \quad (6.1.3)$$

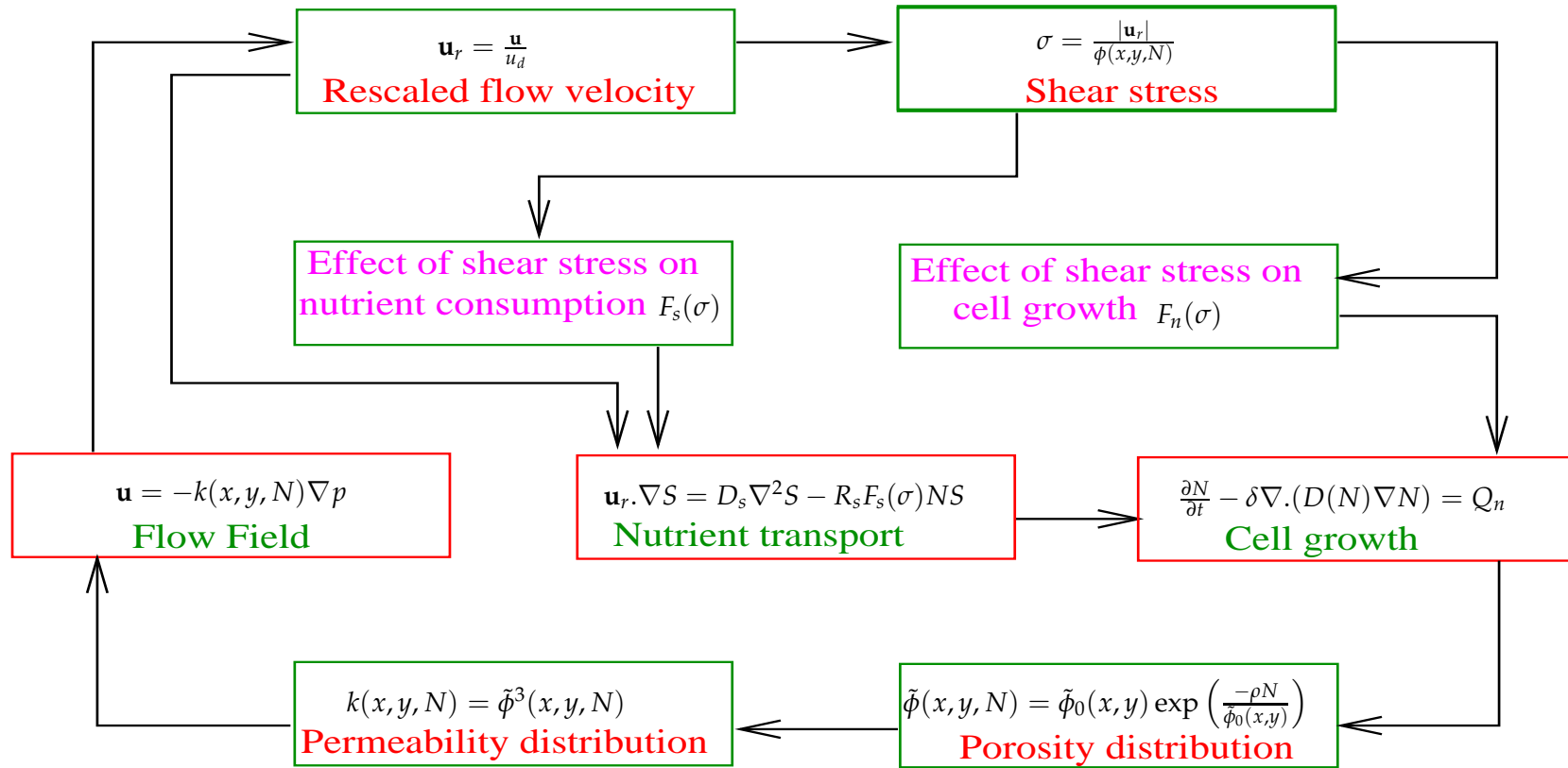


Figure 6.1: Schematic diagram of model equations and solution. All the notations are described in 5 and appendix A

$$u_d = \frac{1}{2} \int_{-1}^1 k(x, d, N) \frac{\partial p}{\partial y} dx, \quad Q_n = \beta F_n(\sigma) S N (1 - N), \quad D(N) = \exp(\gamma(N - 1)), \quad (6.1.4)$$

$$F_s(\sigma) = 1 + \left(\frac{k_1 - 1}{2} \right) (\tanh [g(\sigma - \sigma_{c1})] + 1) - \left(\frac{k_1 - 1}{2} \right) (\tanh [g(\sigma - \sigma_{c2})] + 1), \quad (6.1.5)$$

$$F_n(\sigma) = 1 + \left(\frac{k_1 - 1}{2} \right) (\tanh [g(\sigma - \sigma_{c1})] + 1) - \frac{k_1}{2} (\tanh [g(\sigma - \sigma_{c2})] + 1). \quad (6.1.6)$$

6.2 Solution method

The model consist of three coupled partial differential equations (representing the fluid flow, nutrient transport and cell growth) and an algebraic equation representing the porosity of the porous scaffold. It is a very complicated system which cannot be solved analytically. To solve this coupled system of partial differential equations we use numerical techniques. To solve the model numerically we use the commercially available software COMSOL which is based on the finite element method (for a summary of the basic concepts of the finite element method see appendix C). Solving a coupled system of partial differential equations by COMSOL multiphysics means setting up the underlying equations, material properties and boundary conditions for a given problem using the graphical user interface (GUI) (see appendix B for details of how the model is implemented by using the GUI).

To solve the model numerically the first step is to divide the domain into small elements. Since our geometry is 2-D we divide the domain into small units of simple triangular mesh elements. Since we do not see any sharp gradient in the solution, this encourages us to use a uniform mesh throughout the domain. Thus the mesh is

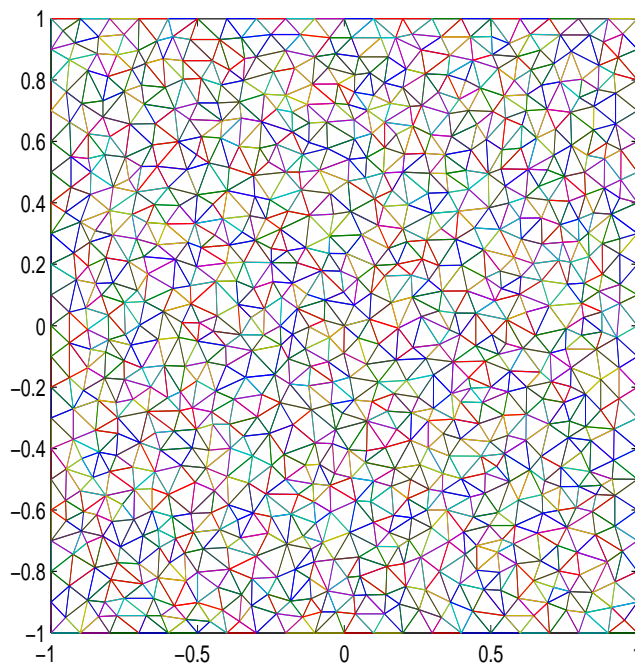


Figure 6.2: Example of a coarse mesh. In this figure there are 851 mesh points, 1600 mesh elements out of which 100 are boundary elements and the system is solved for 9903 degrees of freedom.

uniform in the entire domain and can be refined successively until we get the required convergent results. The refined mesh, that is used for all the calculations, consist of 13001 mesh points and 25600 triangular elements out of which 400 are the boundary elements. The dependent variables are approximated by quadratic shape functions. Since we have three dependent scalar variables, pressure p (velocity is derived from pressure), nutrient concentration S and cell density N , the system is solved for 154803 degrees of freedom, 51601 for each dependent variable. Figure 6.2 illustrates an example of a coarse mesh.

Darcy's law and the advection-diffusion equations are quasi-static equations while the cell growth equation is a time-dependent equation (see Sections 5.3.2, 5.3.3 and 5.3.4). In the model only one equation is time-dependent *i.e.* the cell growth equation. We solve the cell growth equation with step size Δt_{cell} and keep the flow velocity \mathbf{u} and nutrient concentration S fixed till time reaches t_{update} . After time t_{update} we update the cell density in the porosity equation and solve flow and nutrient concentration equations for updated cell density. Thus we can say that the cell growth equation is solved for time $t = 0 : \Delta t_{cell} : t_{update}$, where Δt_{cell} is the step size for the cell growth equation and t_{update} is the time when we update the effect of cell density on the porosity and solve the entire system again. This process continues until the system approaches the steady state. We choose the backward Euler's method for the transient cell growth equation and direct solver (UMFPACK) to solve the linear system of equations.

The success of any numerical method depends on the convergence. To check how reasonable the numerical solution to a given coupled system of partial differential equations is on a given mesh points, a common strategy is to increase the number of mesh points (or decrease the mesh spacing) successively, compute the solution on the finer mesh, and compare the solutions on different number of mesh points. If the solution approaches a stable answer by increasing the number of mesh points or (by decreasing the mesh spacing) then our numerical method is convergent. We check the convergence of our numerical method for various number of mesh points, time step size (for the cell growth equation), and cell update time. We do not know the exact solution of the system but we have discussed the comparison of numerical and analytic solution for constant permeability and uniform initial cell density in Chapter 3.

6.3 Convergence

A numerical method or technique is said to be convergent if it approaches a stable definite value as mesh spacing and time step sizes approach zero. In the present problem to check that our numerical method is convergent we need to choose a suitable number of mesh points, the type of finite element approximation and the time step size for the cell growth equation. The domain of interest is divided into triangular elements. The dependent variables (pressure p , nutrient concentration S and cell density N) can be approximated by linear, quadratic or cubic shape functions. Higher degrees of shape functions give higher degrees of freedom and larger systems of linear equations which need more time for simulation. In this model we choose quadratic shape functions for reasonably smooth solution and shorter simulation time. The mesh is uniform throughout the domain. To show that convergence is achieved we run a series of computations in which the number of mesh points, the step size Δt_{cell} and time t_{update} are varied. This means that convergence depends on three factors number of mesh points, step size, and the time when we update the effect of cell density on porosity. We can fix two factors and vary the third factor to check that the solution approaches a stable value.

6.3.1 Fixed Δt_{cell} and t_{update} and different number of mesh points.

In the first case we keep the step size Δt_{cell} (for the cell equation) and time t_{update} (when we update the effect of cell density on porosity) fixed and calculate the cell density for different number of mesh points. To calculate the total cell number in the scaffold we integrate the cell density N over the entire domain.

$$N_{total} = \int_{-1}^1 \int_{-1}^1 N(x, y) dx dy. \quad (6.3.1)$$

Figure 6.3 shows the total cell number as a function of time for different mesh sizes but fixed step size Δt_{cell} and time t_{update} . We can see from the Figure that total cell number converges to a stable value by increasing the number of mesh points. Figure 6.4 shows the difference between the total cell number for different number of mesh points as a function of time. It is clear that the difference between the total cell numbers for different number of mesh points is approaching to zero which confirms the convergence of numerical method. This suggests that our numerical method converges to a stable value by increasing the number of mesh points.

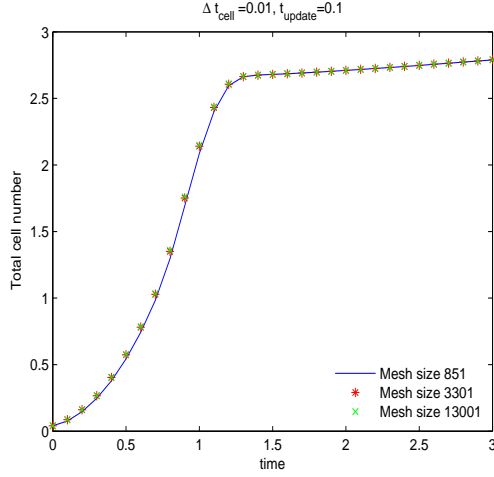


Figure 6.3: Total cell number for different number of mesh points but fixed step sizes Δt_{cell} and time t_{update} . The initial cell density is $N_{init}(x, y) = 0.344H(0.0365 - x^2 - y^2)$. The values of parameters used are $\rho = 1$, $D_s = 6 \times 10^{-6}$, $R_s = 1.488$, $\delta = 0.13976$, $\beta = 13.2173$, $\gamma = 2$, $\sigma_{c1} = 3$ and $\sigma_{c2} = 15$, $g = 60$ and $k_1 = 5$.

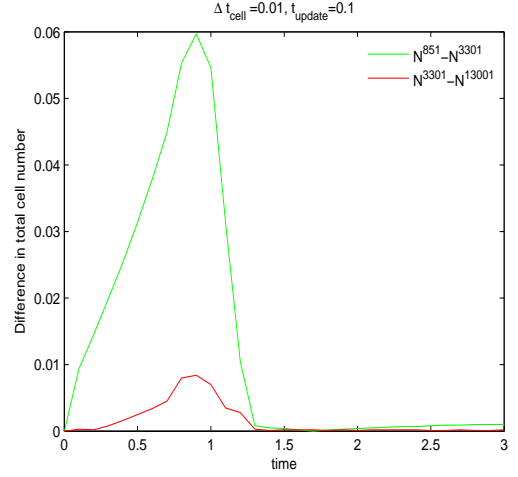


Figure 6.4: Difference between total cell number for different number of mesh points but fixed step size Δt_{cell} and time t_{update} . The green line is the difference between total cell number for mesh points 3301 and 851. The red line is the difference between total cell number for mesh points 13001 and 3301.

At time $t = 3$ which is fairly close to steady state we calculate the difference between the average cell densities for different number of mesh points. If this difference approaches to zero then this will confirm the convergence of numerical method. Let N_i^j represents the cell density at i th mesh point of the domain at time $t = 3$ for mesh size j when both $\Delta t_{cell} = 0.01$ and $t_{update} = 0.1$ are fixed then

$$\begin{aligned} \frac{\sum_{i=1}^j N_i^j}{j} &= 0.6943 \quad \text{when } j = 851 \\ \frac{\sum_{i=1}^j N_i^j}{j} &= 0.6966 \quad \text{when } j = 3301 \\ \frac{\sum_{i=1}^j N_i^j}{j} &= 0.6977 \quad \text{when } j = 13001 \\ \frac{\sum_{i=1}^j N_i^j}{j} &= 0.6980 \quad \text{when } j = 51601. \end{aligned}$$

hence

$$\begin{aligned} \text{abs} \left(\frac{\sum_{i=1}^{851} N_i^{851}}{851} - \frac{\sum_{i=1}^{3301} N_i^{3301}}{3301} \right) &= 0.0023 \\ \text{abs} \left(\frac{\sum_{i=1}^{3301} N_i^{3301}}{3301} - \frac{\sum_{i=1}^{13001} N_i^{13001}}{13001} \right) &= 0.0011 \\ \text{abs} \left(\frac{\sum_{i=1}^{13001} N_i^{13001}}{13001} - \frac{\sum_{i=1}^{51601} N_i^{51601}}{51601} \right) &= 0.0003 \end{aligned}$$

Since these numbers are getting smaller, this suggests convergence of the numerical method.

6.3.2 Fixed number of mesh points and t_{update} and different Δt_{cell} .

In this case we fix the number of mesh points and time t_{update} (when we update the effect of cell density on porosity) and calculate total cell number for different time step sizes Δt_{cell} (for the cell growth equation). Figure 6.5 shows the total cell number when the number of mesh points and t_{update} time are fixed but step sizes Δt_{cell} is varied. It is evident from Figure 6.5 that by decreasing the step size Δt_{cell} total cell number has a stable value, which confirms the convergence of the numerical method with respect to changes in Δt_{cell} .

At time $t = 3$ which is fairly close to steady state we again calculate the difference in cell densities. Let N_i represents the cell density at i th mesh point of the domain at time $t = 3$, when both, number of mesh points= 3301 and $t_{update} = 0.1$ are fixed then

$$\frac{\sum_{i=1}^{3301} N_i}{3301} = 0.6966 \quad \text{when} \quad \Delta t_{cell} = 0.05$$

The average cell density has same value for both $\Delta t_{cell} = 0.01$ or $\Delta t_{cell} = 0.02$ within 9 significant figures. Since the difference between the average cell densities at time $t = 3$ for different step size Δt_{cell} but fixed number of mesh points and time t_{update} is approaching zero so we conclude that numerical method converge to a stable value irrespective of length of step size Δt_{cell} .

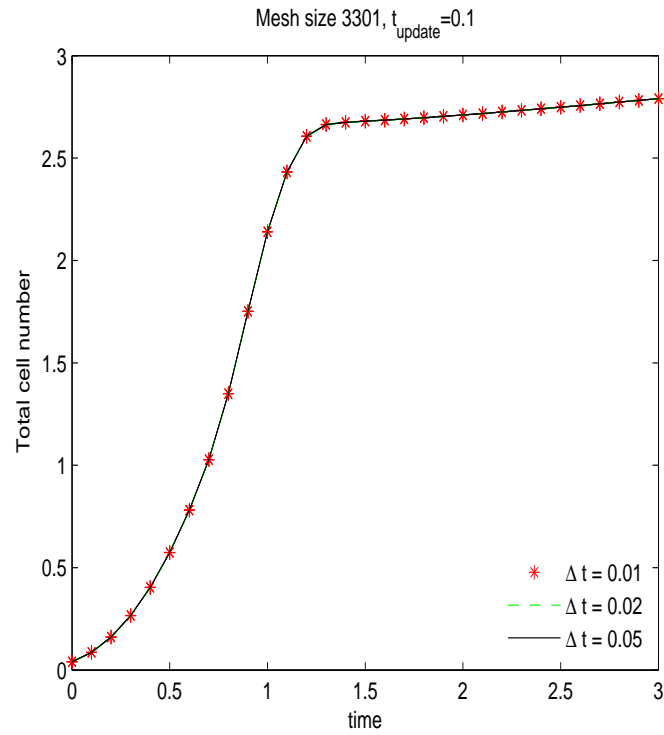


Figure 6.5: Total cell number for different step sizes Δt_{cell} but fixed mesh size and time t_{update} . The initial cell density and parameter values are the same as in Figure 6.3

6.3.3 Fixed number of mesh points and Δt_{cell} and different t_{update} .

In this case we fix the number of mesh points and step size Δt_{cell} and calculate the cell number for different times t_{update} . Figure 6.6 shows the total cell number for various t_{update} when the number of mesh points and step size Δt_{cell} both are fixed. From the Figure 6.6 we see that in order to get the accurate solution t_{update} must be of the order of Δt_{cell} .

Let N_i represents the cell density at the i th mesh point of the domain at time $t = 3$, when both mesh size= 3301 and $\Delta t_{cell} = 0.01$ are fixed, then

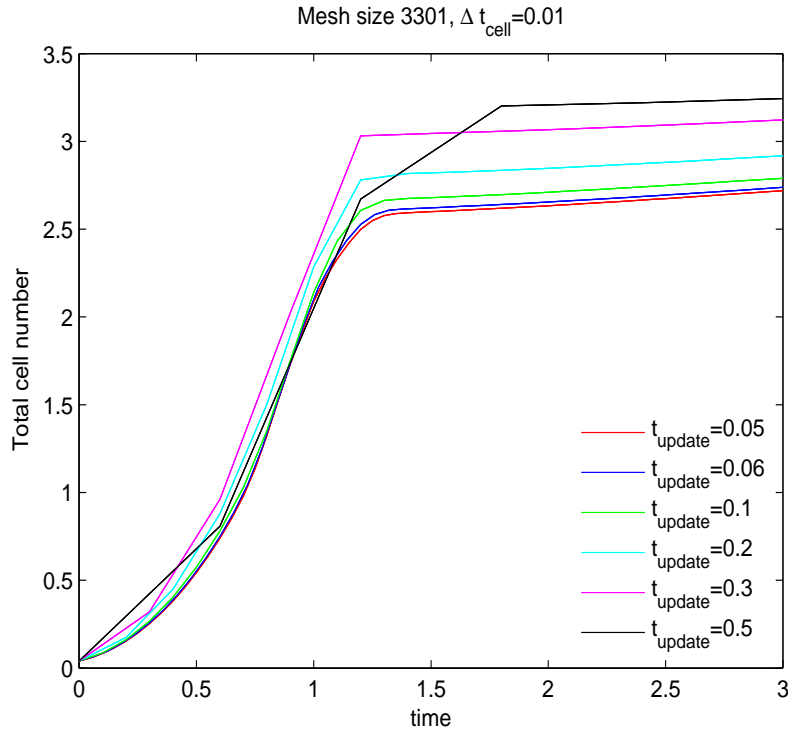


Figure 6.6: Total cell number for different t_{update} but fixed mesh size and step size Δt_{cell} . The initial cell density and parameter values are the same as in Figure 6.3.

$$\frac{\sum_{i=1}^{3301} N_i}{3301} = 0.6787 \quad \text{when } t_{\text{update}} = 0.05$$

$$\frac{\sum_{i=1}^{3301} N_i}{3301} = 0.6835 \quad \text{when } t_{\text{update}} = 0.06$$

$$\frac{\sum_{i=1}^{3301} N_i}{3301} = 0.6966 \quad \text{when } t_{\text{update}} = 0.1$$

$$\frac{\sum_{i=1}^{3301} N_i}{3301} = 0.7287 \quad \text{when } t_{\text{update}} = 0.2$$

$$\frac{\sum_{i=1}^{3301} N_i}{3301} = 0.7799 \quad \text{when } t_{\text{update}} = 0.3$$

$$\frac{\sum_{i=1}^{3301} N_i}{3301} = 0.8174 \quad \text{when } t_{\text{update}} = 0.5$$

hence

$$\begin{aligned} \text{abs} \left(\frac{\sum_{i=1}^{3301}}{3301} [N_i^{t_{update}=0.3} - N_i^{t_{update}=0.5}] \right) &= 0.0375 \\ \text{abs} \left(\frac{\sum_{i=1}^{3301}}{3301} [N_i^{t_{update}=0.1} - N_i^{t_{update}=0.2}] \right) &= 0.0321 \\ \text{abs} \left(\frac{\sum_{i=1}^{3301}}{3301} [N_i^{t_{update}=0.05} - N_i^{t_{update}=0.06}] \right) &= 0.0048 \end{aligned}$$

On the basis of convergence test now we can say that to get convergent results and short simulation time we need to choose the reasonable number of mesh points, time step size Δt_{cell} and frequently update the effect of cells on porosity *i.e.* small t_{update} . So we use 13001 number of mesh points, step size $\Delta t_{cell} = 0.005$, and $t_{update} = 0.01$ in all the subsequent calculations.

Results and discussion

The growth of murine immortalized rat cells C_2C_{12} was simulated using the model proposed in Chapter 5. The evaluation of velocities, cell densities, nutrient concentrations and shear stress was calculated. In the model we can consider different forms of the initial porosity $\phi_0(x, y)$, initial seeding strategy $N_{init}(x, y)$ and effect of flow rate. In Section 6.4 we will present the results of various initial seeding strategies and compare the total cell yield in the final construct. In Sections 6.5 and 6.6 we will discuss the effect of channeling and flow rate on the cell growth. We will propose several scaffold designs depending on the porosity distribution to improve the supply of nutrients to the deeper sections of the scaffold.

6.4 Initial seeding strategy

The fabrication of tissue in the laboratory starts with the attachment of isolated cells to the polymer scaffold. This stage is commonly known as cell seeding. Desired features of cell seeding include a high ratio of attached cells to seeded cells, fast attachment of cells to the scaffold, high cell survival and a uniform spatial distribution in the final construct.

The initial seeding strategy plays an important role in maximizing the total cell number in the final construct. It is believed that a uniform initial distribution of attached cells

to the scaffold lays the foundation for uniform cell growth (Bueno et al., 2007) and non-uniform seeding results in enhanced tissue growth at the periphery of scaffold (Freed et al., 1998). Later we will show that our model contradicts this. We take uniform initial porosity of the scaffold *i.e.* $\phi_0(x, y) = 0.85$, a mesh size of 13001, step size $\Delta t_{cell} = 0.005$ (for the cell growth equation) and we update the cells in the porosity equation after a time 0.01 *i.e.* $t_{update} = 0.01$. We will test different forms of the initial seeding strategies when the initial porosity of scaffold is uniform and the values of all the parameters are fixed. Our aim is to identify the seeding strategy that gives both rapid cell growth and the maximum number of uniformly distributed cells in the final construct.

6.4.1 Uniform initial cell density

Let us consider the case where the initial cell density is uniform everywhere in the entire scaffold. Initially the cell density at each mesh point is 0.01 *i.e.* $N_{init} = 0.01$. Since the scaffold extends from $-1 \leq x \leq 1$ and $-1 \leq y \leq 1$ the total cell number in the entire scaffold is 0.04.

The model was run using the values of dimensionless parameters given in the Table 5.4. Figure 6.7 shows snapshots of the cell density N , nutrient concentration S , the flow field and the shear stress σ at time $t = 0.5$ (first row), $t = 1.5$ (second row) and $t = 2.5$ (third row).

These times corresponds to an early point of a transient solution, a later point in the transient solution and fairly close to the steady state solution respectively. Nutrients are supplied constantly to the cells at the top boundary $y = 1$. The scale for cell density N and nutrient concentration S is $[0..1]$ in Figure 6.7 and will remain the same in all the subsequent figures, but the scale for shear stress may change.

Initially, nutrients penetrate into the entire depth of the scaffold; however, its concentration remains high near the inlet wall. The concentration of nutrients falls off lower down the scaffold as time passes. Initially, cells are uniformly distributed throughout the entire scaffold. As cells grow and occupy the empty spaces in the scaffold pores they consume more nutrients and this depletes the supply of nutrients in the lower region. The cells near the nutrient source have access to more nutrients and grow quickly. Since most of the nutrients are consumed by the cells near the nutrient source however the amount of nutrients available to the cells in the deeper sections of the scaffold is very low and the growth of cells in this region is also slow. After some time the cell distribution becomes non-uniform, giving more cells near the nutrient source and fewer cells away from the nutrient source. With the increase in cell density all the nutrients

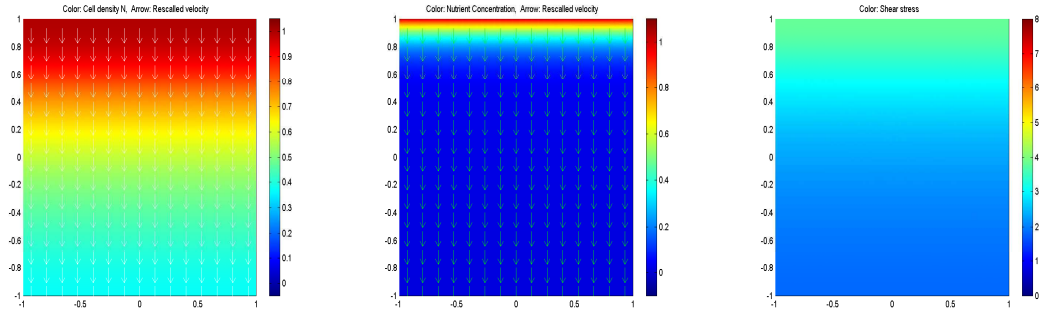
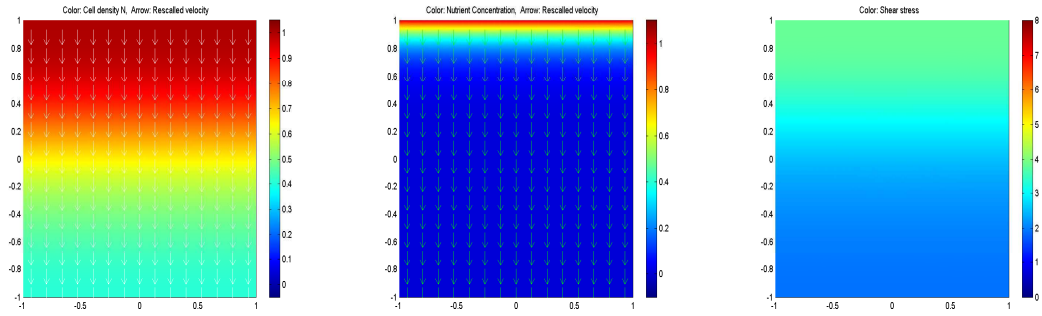
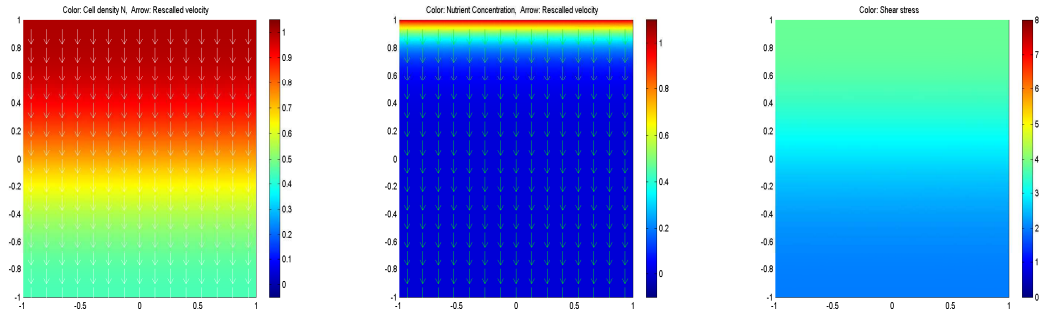
(a) Cell density N and fluid velocity \mathbf{u}_r at $t = 0.5$.(b) Nutrient concentration S and fluid velocity \mathbf{u}_r at $t = 0.5$.(c) Shear stress σ at $t = 0.5$.(d) Cell density N and fluid velocity \mathbf{u}_r at $t = 1.5$.(e) Nutrient concentration S and fluid velocity \mathbf{u}_r at $t = 1.5$.(f) Shear stress σ at $t = 1.5$.(g) Cell density N and fluid velocity \mathbf{u}_r at $t = 2.5$.(h) Nutrient concentration S and fluid velocity \mathbf{u}_r at $t = 2.5$.(i) Shear stress σ at $t = 2.5$.

Figure 6.7: Snapshots of the cell density N , nutrient concentration S , fluid velocity \mathbf{u}_r and the shear stress σ at time $t = 0.5, 1.5, 2.5$ when initial cell density is uniform. The parameter values used in the simulation are given in Table 5.4.

are consumed by cells near the nutrient source and cells in the deeper sections of the scaffold become hypoxic. Due to lack of nutrients the cell growth stops in this region.

We observe that the solution of the system is independent of x . To justify this we consider all the three equations. Firstly, consider the flow equation. We know that initially cells are distributed uniformly in the entire depth of the scaffold and there is no fluid

flux through the side walls of the scaffold so solution of flow equation is independent of x . Likewise the solution of nutrient concentration and cell growth equations is also independent of x . This feature is also evident from the Figure 6.7.

We know that shear stress is directly proportional to velocity and inversely proportional to the porosity of scaffold. The porosity of the scaffold is initially uniform so the flow of fluid through the scaffold is uniform. As more cells grow near the nutrient source the porosity of the scaffold decreases in this region and shear stress increases in this region due to decrease in porosity. This fact is also evident from the Figures 6.7(c), 6.7(f) and 6.7(i).

6.4.2 Central blob

Let there initially be a blob of cells placed at the centre of the scaffold. We expect that cells at the edges of the blob will grow outward and spread into the whole domain. Figure 6.8 shows that initially a blob of cells is placed at the centre of the scaffold. Mathematically we represent the initial cell density by

$$N_{init} = 0.346 \times H(0.0365 - x^2 - y^2),$$

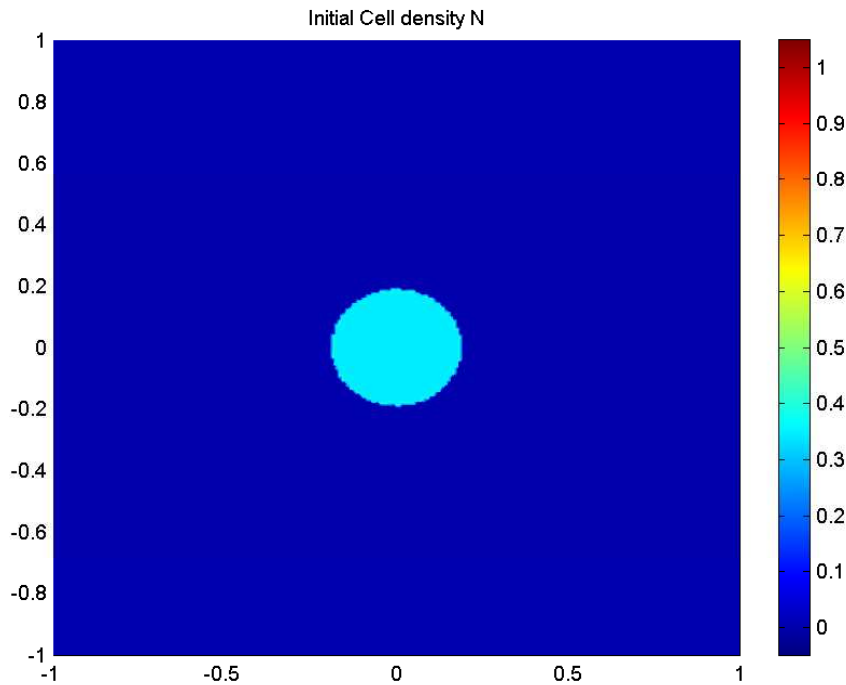
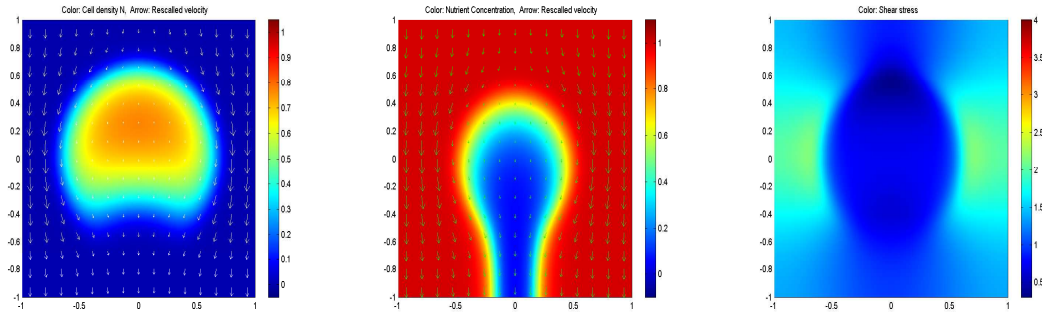


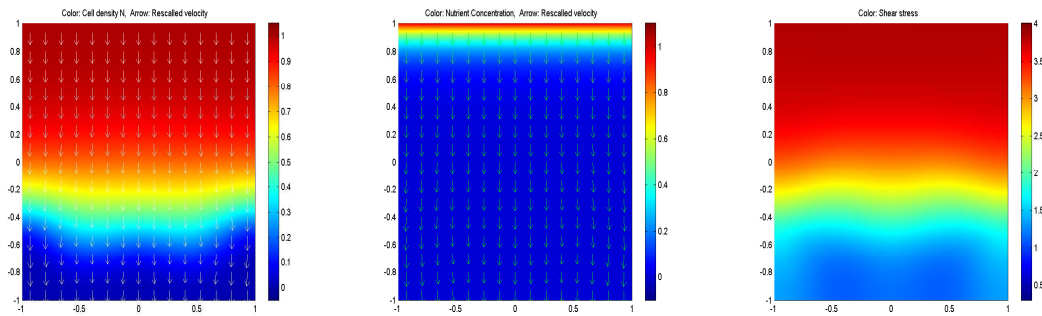
Figure 6.8: Form of initial cell distribution when a blob of cells is placed at the centre of the scaffold. Mathematically $N_{init} = 0.346 \times H(0.0365 - x^2 - y^2)$.

where $H(\cdot)$ is the Heaviside step function. The total cell number in the entire scaffold is again 0.04.

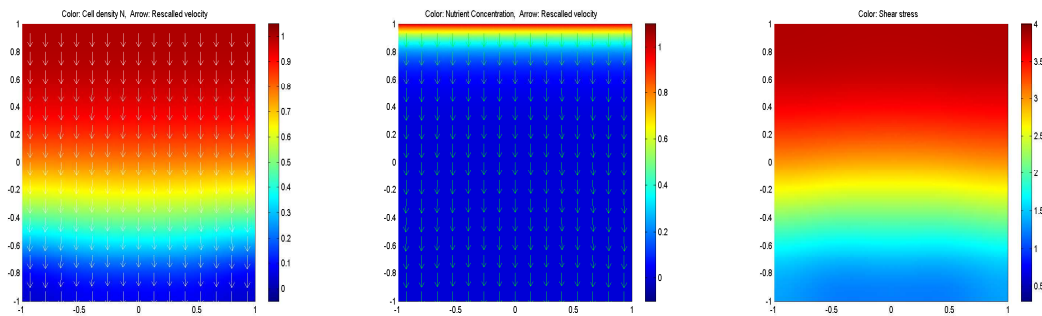
Figure 6.9 shows the same plots as in Figure 6.7 but in this case initially a blob of cells is placed at the centre of the scaffold. Initially the concentration of nutrients is uniform around the edges of the blob. We observe that the cells at the edges of the blob consume nutrients and grow.



(a) Cell density N and fluid velocity \mathbf{u}_r at $t = 0.5$. (b) Nutrient concentration S and fluid velocity \mathbf{u}_r at $t = 0.5$. (c) Shear stress σ at $t = 0.5$.



(d) Cell density N and fluid velocity \mathbf{u}_r at $t = 1.5$. (e) Nutrient concentration S and fluid velocity \mathbf{u}_r at $t = 1.5$. (f) Shear stress σ at $t = 1.5$.



(g) Cell density N and fluid velocity \mathbf{u}_r at $t = 2.5$. (h) Nutrient concentration S and fluid velocity \mathbf{u}_r at $t = 2.5$. (i) Shear stress σ at $t = 2.5$.

Figure 6.9: Snapshots of the cell density N , nutrient concentration S , fluid velocity \mathbf{u}_r and the shear stress σ at time $t = 0.5, 1.5, 2.5$ when initially a blob of cells placed at the centre of scaffold. The parameter values are same as in Figure 6.7.

The cells spread towards the boundaries of the domain. The left and right edges of blob move towards their respective boundaries of the scaffold with equal speed due to symmetry of the problem along $x = 0$. The cells at the top edge of blob (which is near to the nutrient source) grow quickly because cells in this region have a constant supply of nutrients from the top boundary of the scaffold. The cells at the bottom edge of the blob (which is far from the nutrient source) grow very slowly and ultimately stop growing because most of the nutrients are consumed before they reach this edge of the blob. When the cells at the left and right edges of the blob spread and touch their respective boundaries of the scaffold then nutrients will not have an easy path around the cells. There will be no cells in the deeper sections of the scaffold especially in the last quarter of the scaffold. The cells at the far end of the scaffold, away from the nutrient source will be hypoxic and there will be no cell growth in this region. This fact is evident from Figure 6.9. We observe that from Figure 6.9(a) that when the blob of cells is at the centre of the scaffold it forces the fluid to go around the edges of the blob. So fluid will flow with high velocity around the edges of the blob. We observe that the shear stress is high in the regions where the advective velocity is high. The advective velocity is high in the regions where the cell density is low and vice versa. On the other hand when the blob of cells touches the boundaries of the scaffold then in that case fluid must go through the cells. The shear stress is high in the regions where the porosity is low and velocity is uniform. The porosity of the scaffold is low in the regions where the cell density is high.

6.4.3 Off-Centre blob

If we put a blob of cells at the centre of the scaffold then the edge of the blob facing away from the nutrient source grows slowly due to lack of nutrients source and there are few cells in the deeper sections of the scaffold. If we put a blob of cells away from the nutrient source then the cells will spread more uniformly into all the sections of the scaffold. Let us consider the case when a blob of cells is placed on the centre line but away from the nutrient source. Figure 6.10 shows that initially a blob of cells is placed away from the nutrient source. Mathematically we represent the initial distribution of cells by

$$N_{init} = 0.346 \times H(0.0365 - x^2 - (y + 0.5)^2).$$

As before the total cell number in the entire scaffold is 0.04.

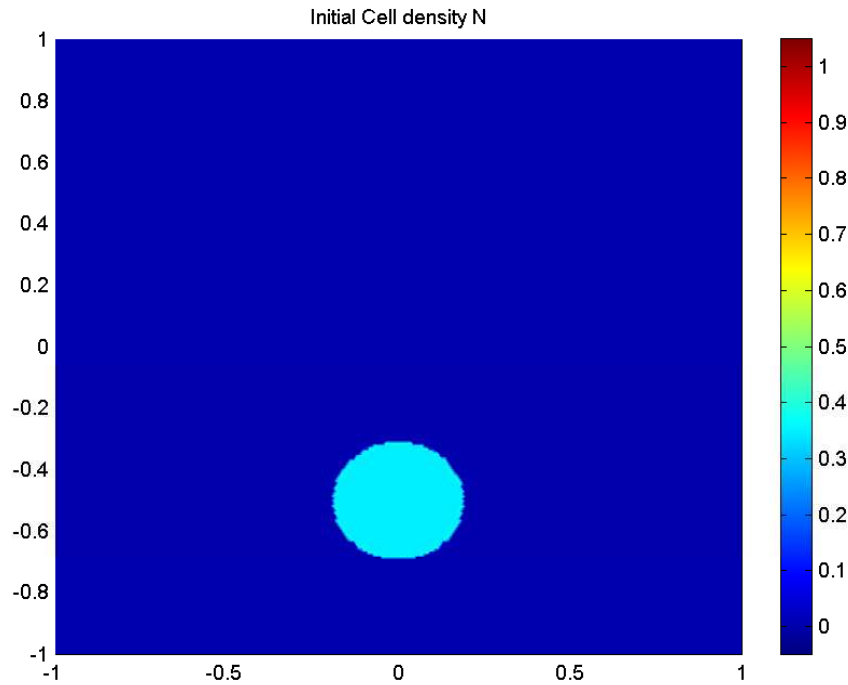


Figure 6.10: Form of initial cell distribution when a blob of cells is placed away from the nutrient source. Mathematically $N_{init} = 0.346 \times H(0.0365 - x^2 - (y + 0.5)^2)$.

Figure 6.11 shows the same plots as in Figure 6.7 but in this case initially a blob of cells is placed away from the nutrient source. We observe that the blob of cells grows towards the nutrient source. After some time the cells spread into the entire domain and are more uniformly distributed compared to the central blob case. Clearly the cell density is high in the upper half of the scaffold and cell density is slightly lower in the lower half of the scaffold. Most of the nutrients are eaten up near the scaffold inlet wall and the nutrient concentration becomes low in deeper sections of the scaffold which results in a lower cell density away from the nutrient source. The width of the region of lower cell density is thinner for this initial seeding than for the centrally placed blob. It is also evident from the Figure that before touching the boundaries of the scaffold the blob of cells forces the fluid to go around the edges of the scaffold. The velocity of fluid is high around the edges of the blob hence shear stress is high in this region. When the blob of cells touches the boundaries of the scaffold the fluid must go through the cells so shear stress is high in the regions where more cells are present or, in other words, we can say that shear stress is high in the regions where porosity is low.

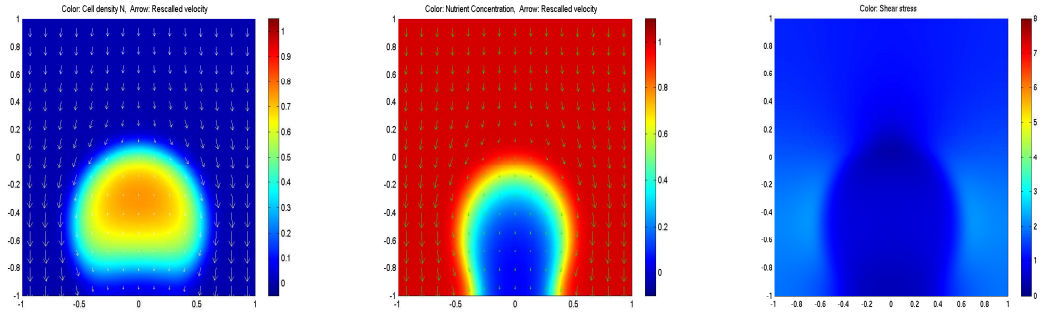
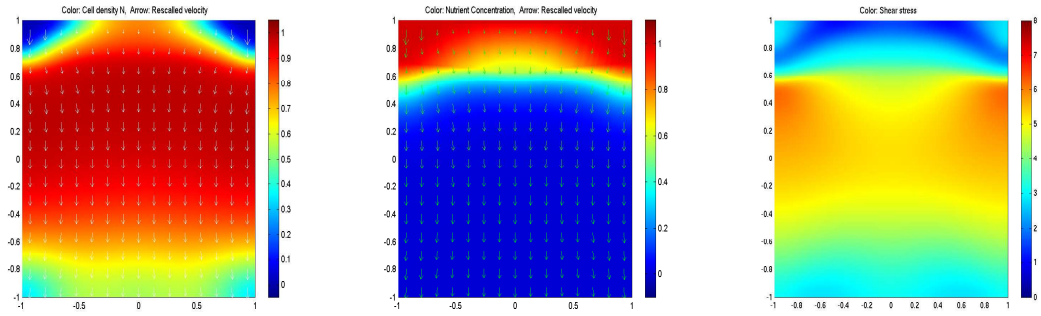
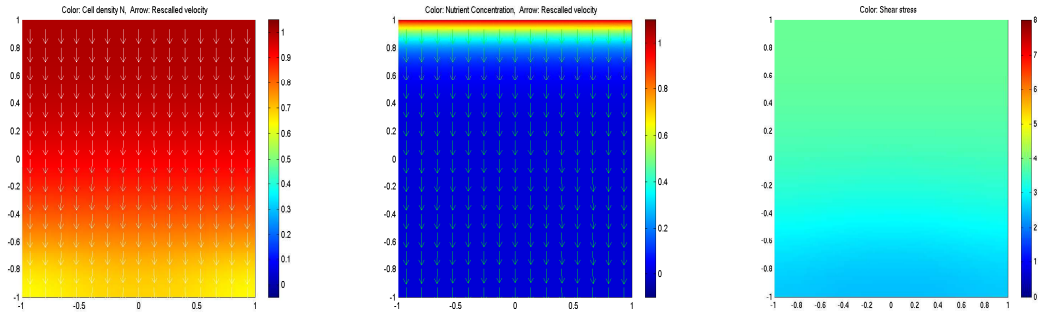
(a) Cell density N and fluid velocity \mathbf{u}_r at $t = 0.5$.(b) Nutrient concentration S and fluid velocity \mathbf{u}_r at $t = 0.5$.(c) Shear stress σ at $t = 0.5$.(d) Cell density N and fluid velocity \mathbf{u}_r at $t = 1.5$.(e) Nutrient concentration S and fluid velocity \mathbf{u}_r at $t = 1.5$.(f) Shear stress σ at $t = 1.5$.(g) Cell density N and fluid velocity \mathbf{u}_r at $t = 2.5$.(h) Nutrient concentration S and fluid velocity \mathbf{u}_r at $t = 2.5$.(i) Shear stress σ at $t = 2.5$.

Figure 6.11: Snapshots of the cell density N , nutrient concentration S , fluid velocity \mathbf{u}_r and the shear stress σ at time $t = 0.5, 1.5, 2.5$ when initially a blob of cells placed away from the nutrient source. The parameter values are the same as in Figure 6.7.

6.4.4 Layer of cells opposite to nutrient source

From the results of the central and off-central blobs we conclude that if we put a layer of cells at the scaffold outlet wall, away from the nutrient source then we can get a more uniform cell distribution in the final construct. Consider the case when initially a layer of cells is placed away from the nutrient source. Figure 6.12 shows the initial

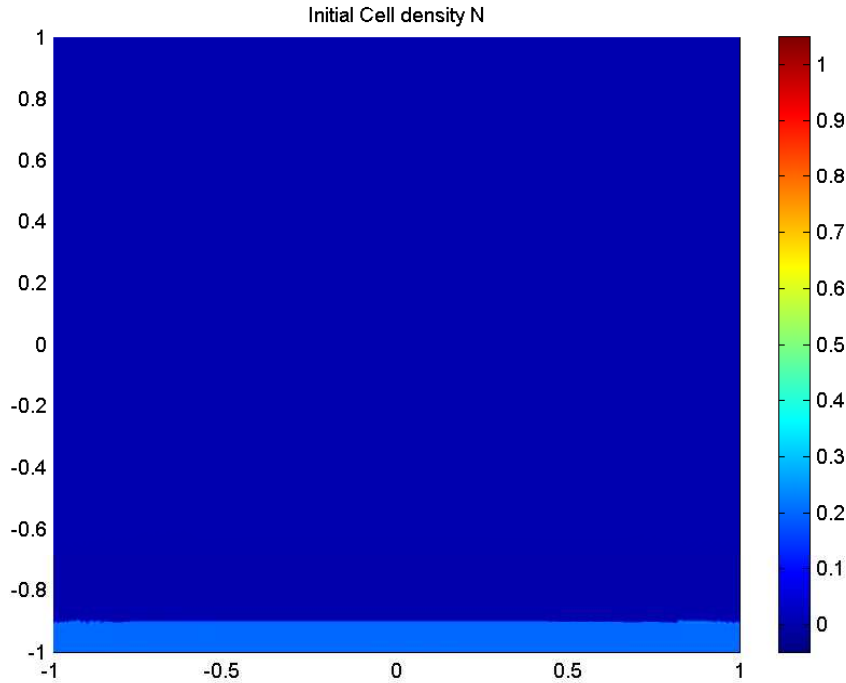


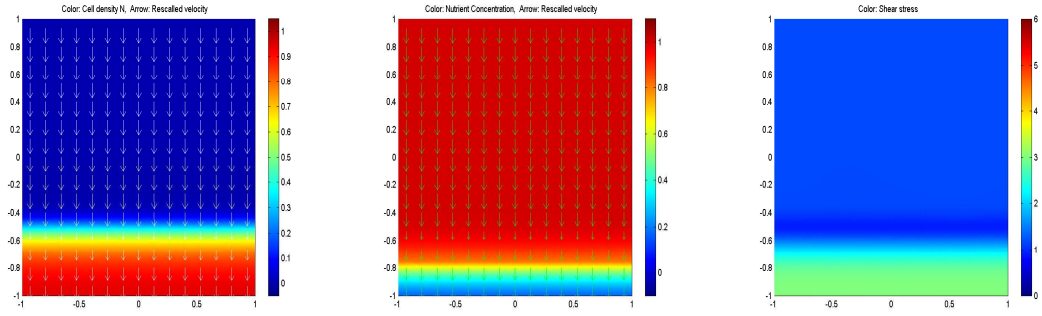
Figure 6.12: Form of initial cell distribution when a layer of cells is placed away from the nutrient source. Mathematically $N_{init} = 0.2 \times H(-0.9 - y)$.

cell density when layer of cells is placed near the scaffold outlet wall away from the nutrient source. Mathematically we represent the layer of cells by

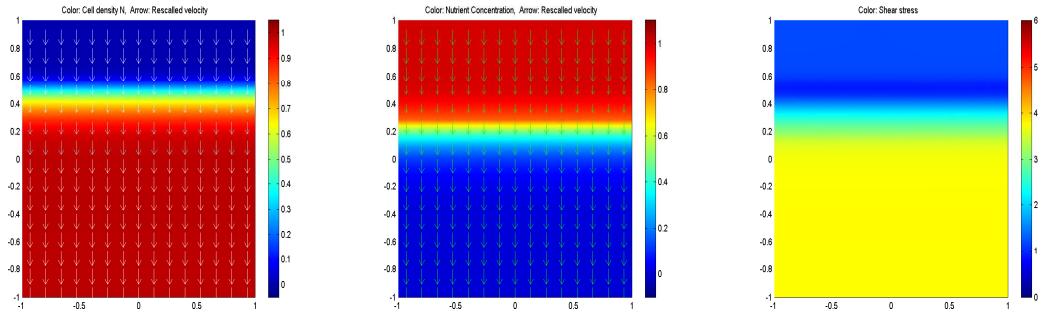
$$N_{init} = 0.2 \times H(-0.9 - y).$$

The total initial cell number in the entire scaffold is again 0.04.

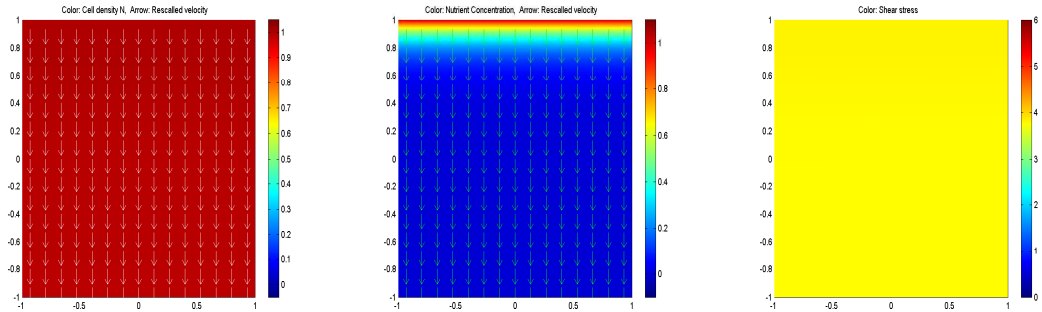
Figure 6.13 shows the same plots as in Figure 6.7 when initially a layer of cells is placed away from the nutrient source. It is evident from the Figure that the cells grow towards the nutrient source and after some time cells have spread uniformly into the entire domain. When cells spread in the entire domain then the nutrient concentration becomes zero in the deeper section of the scaffold. It is also evident that, since the cell density is uniform everywhere the shear stress is also uniform in the entire domain.



(a) Cell density N and fluid velocity \mathbf{u}_r at $t = 0.5$. (b) Nutrient concentration S and fluid velocity \mathbf{u}_r at $t = 0.5$. (c) Shear stress σ at $t = 0.5$.



(d) Cell density N and fluid velocity \mathbf{u}_r at $t = 1.5$. (e) Nutrient concentration S and fluid velocity \mathbf{u}_r at $t = 1.5$. (f) Shear stress σ at $t = 1.5$.



(g) Cell density N and fluid velocity \mathbf{u}_r at $t = 2.5$. (h) Nutrient concentration S and fluid velocity \mathbf{u}_r at $t = 2.5$. (i) Shear stress σ at $t = 2.5$.

Figure 6.13: Snapshots of the cell density N , nutrient concentration S , fluid velocity \mathbf{u}_r and the shear stress σ at time $t = 0.5, 1.5, 2.5$ when initially a layer of cells is placed away from the nutrient source. The parameter values are same as in Figure 6.7.

6.4.5 Layer of cells on all the boundaries of the scaffold

It is not possible for tissue engineers to initially place the cells in the internal region of the scaffold. To be more realistic we initially place the cells on all the boundaries of the scaffold. Figure 6.14 shows the initial distribution of cells on the periphery of the scaffold. Mathematically we represent this type of initial cell distribution by a series of

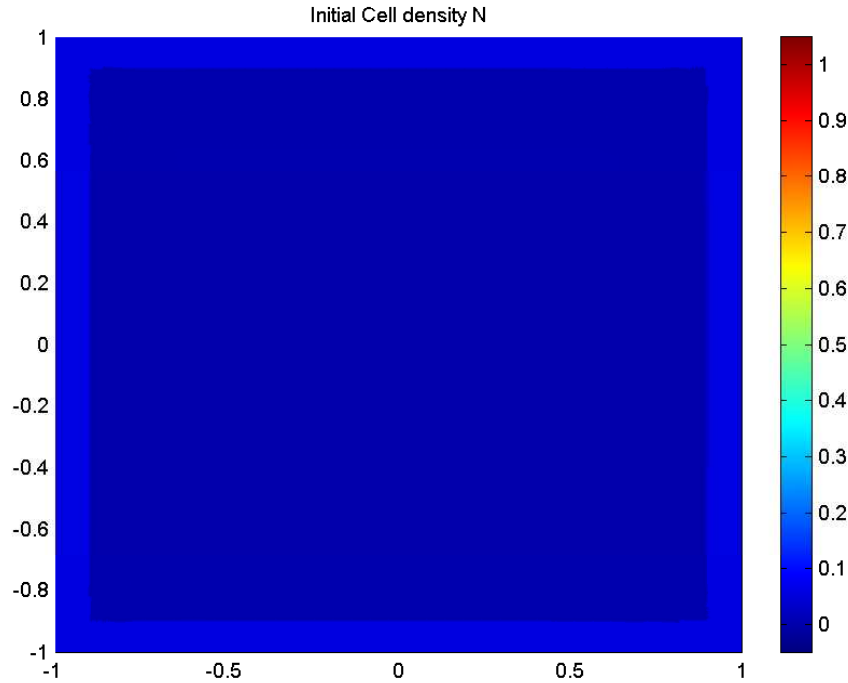


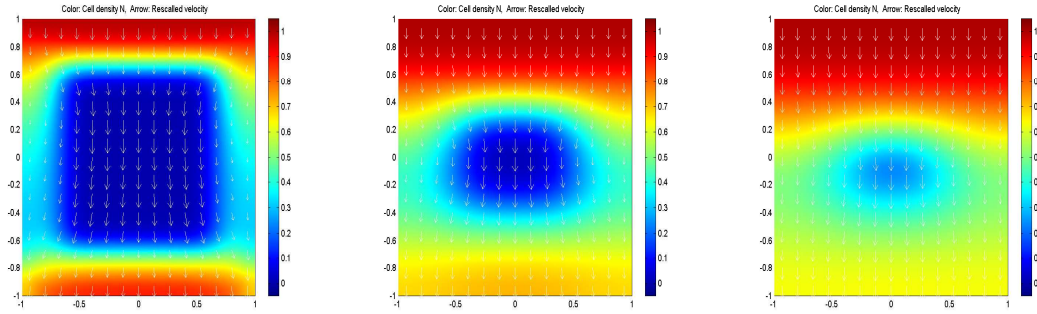
Figure 6.14: Form of initial cell distribution when cells are placed on all the boundaries of the scaffold. Mathematically $N_{init} = 0.05276 \times \min(1, H(-y - 0.9) + H(-x - 0.9) + H(x - 0.9) + H(y - 0.9))$.

Heaviside functions as

$$N_{init} = 0.05276 \times \min(1, H(-y - 0.9) + H(-x - 0.9) + H(x - 0.9) + H(y - 0.9)).$$

The total initial cell number in the entire scaffold is again 0.04.

Figure 6.15 shows the snapshots of cell density N at an early point of transient solution $t = 0.5$, an intermediate point of transient solution $t = 1.5$ and close to steady state at time $t = 2.5$. Initially cells are seeded at the periphery of the scaffold. The cells on the inlet boundary of the scaffold consume nutrients and grow quickly. Cells on the other boundaries have less access to available nutrients so their growth is slow. We observe that the cells grow and move towards the centre of the scaffold. As more cells grow near the inlet wall they block the scaffold pores as a result delivery of nutrients to the internal regions of the scaffold decreases to zero. We also observe that there is no cell growth in the centre of the scaffold due to lack of nutrients. These features are evident from the Figure 6.15.



(a) Cell density N and fluid velocity \mathbf{u}_r at $t = 0.5$. (b) Cell density N and fluid velocity \mathbf{u}_r at $t = 1.5$. (c) Cell density N and fluid velocity \mathbf{u}_r at $t = 2.5$.

Figure 6.15: Snapshots of the cell density N and fluid velocity \mathbf{u}_r at time $t = 0.5, 1.5, 2.5$ when initially layer of cells is placed on the periphery of the scaffold. The parameter values are same as in Figure 6.7.

6.4.6 Layer of cells on three boundaries of scaffold

From the results of initial distribution of cells on the periphery of the scaffold we found that the cells on the inlet walls consume most of the nutrients and grow quickly. As the cell density increases the nutrient consumption increases which causes the depletion

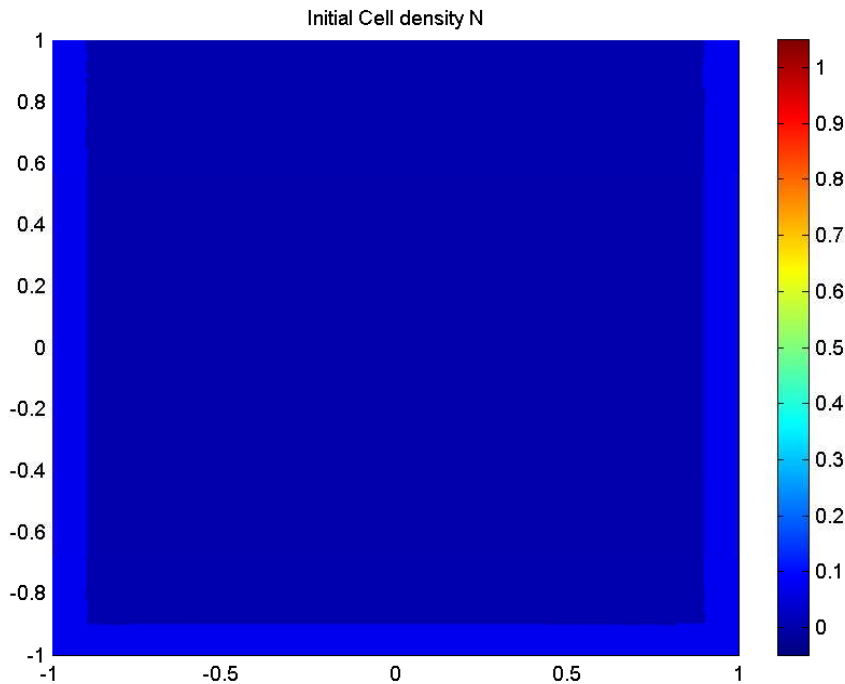
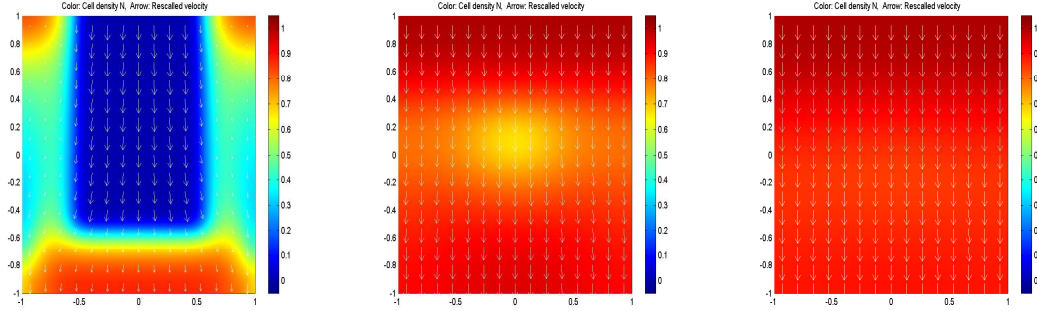


Figure 6.16: Form of initial cell distribution when cells are placed on all the boundaries of the scaffold except the inlet boundary. Mathematically $N_{init} = 0.069216 \times \min(1, H(-y - 0.9) + H(-x - 0.9) + H(x - 0.9))$.

of nutrients in the central sections of the scaffold. To overcome this problem let us consider the case when initially we place the cells on the scaffold boundaries except the inlet boundary. Figure 6.16 shows the initial distribution of cells. Mathematically we represent the initial cell distribution by

$$N_{init} = 0.069216 \times \min(1, H(-y - 0.9) + H(-x - 0.9) + H(x - 0.9)).$$

The total initial cell number in the entire scaffold is again 0.04.



(a) Cell density N and fluid velocity \mathbf{u}_r at $t = 0.5$. (b) Cell density N and fluid velocity \mathbf{u}_r at $t = 1.5$. (c) Cell density N and fluid velocity \mathbf{u}_r at $t = 2.5$.

Figure 6.17: Snapshots of the cell density N and fluid velocity \mathbf{u}_r at time $t = 0.5, 1.5, 2.5$ when initially cells are seeded on all the boundaries of the scaffold except inlet boundary. The parameter values are same as in Figure 6.7.

Figure 6.17 shows the same plots as in Figure 6.15. Initially cells are seeded at the three boundaries of the scaffold and there are no cells on the inlet wall of the scaffold. In this case cells from all the boundaries of the scaffold grow and move towards the centre of the scaffold. When the cells from the side walls of the scaffold reach the centre of the scaffold and block the scaffold pores then the delivery of the nutrients in the internal regions of the scaffold decreases rapidly. Due to decrease in the nutrient concentration in the internal regions of the scaffold, the growth of cells also slows down in these regions. We can observe from the Figure 6.17 that cell density is low in the middle portion of the scaffold.

6.4.7 Layer of cells at side walls of the scaffold

Let us consider the case when initially cells are seeded on the side walls of the scaffold. Figure 6.18 shows the form of initial cell distribution. Mathematically we represent this type of initial cell distribution by

$$N_{init} = 0.1 \times (H(-x - 0.9) + H(x - 0.9)).$$

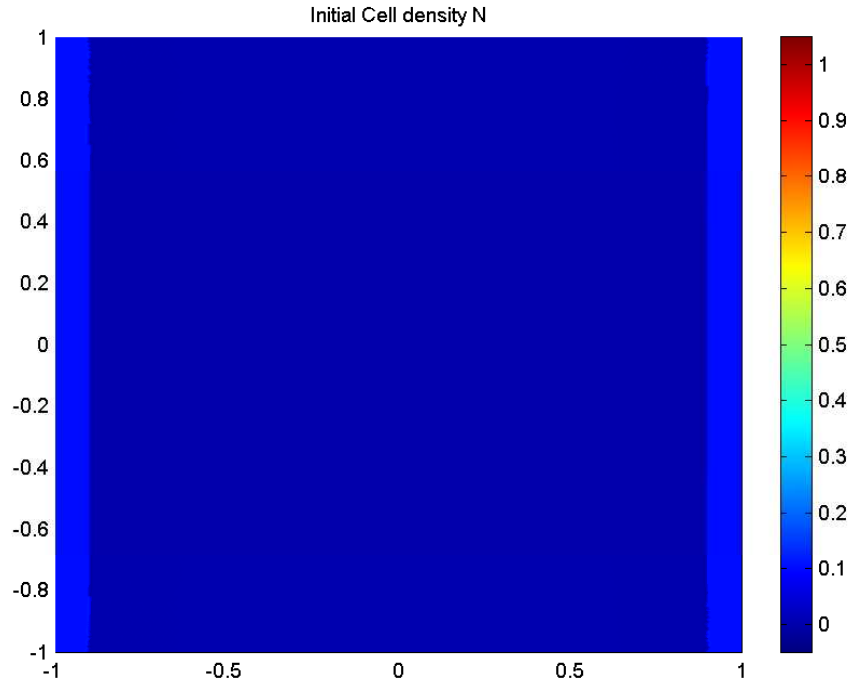
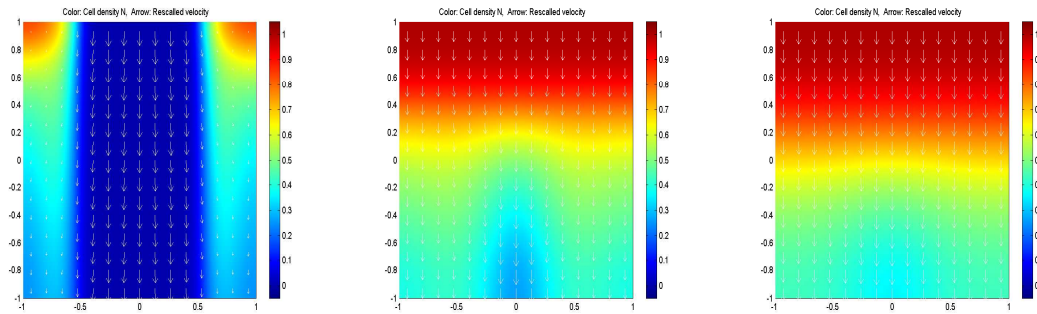


Figure 6.18: Form of initial cell distribution when layers of cells are placed on the side walls of the scaffold. Mathematically $N_{init} = 0.1 \times (H(-x - 0.9) + H(x - 0.9))$.

The total initial cell number in the entire scaffold is again 0.04.

Figure 6.19 shows the same plots as in Figure 6.15. We observe that the cells grow towards the centre of the scaffold. When the cells from both the boundaries reach the centre of the scaffold they block the scaffold pores. The growth of cells near the nutrient source is rapid which causes a decrease in nutrient concentration in the deeper sections



(a) Cell density N and fluid velocity \mathbf{u}_r at $t = 0.5$. (b) Cell density N and fluid velocity \mathbf{u}_r at $t = 1.5$. (c) Cell density N and fluid velocity \mathbf{u}_r at $t = 2.5$.

Figure 6.19: Snapshots of the cell density N and fluid velocity \mathbf{u}_r at time $t = 0.5, 1.5, 2.5$ when initially layer of cells is placed on the side walls of the scaffold. The parameter values are same as in Figure 6.7.

of the scaffold. The cells away from the nutrient source becomes hypoxic and stop growing.

6.4.8 Comparison of results of initial cell seeding strategy

Figure 6.20 shows the time evolution of the total cell number for various initial seeding strategies suggested in this section when the values of threshold shear stresses are $\sigma_{c1} = 3$ and $\sigma_{c2} = 15$. It is evident from Figure 6.20 that initially the total cell number in all the seeding strategies is the same in each case *i.e.* $N_{init} = 0.04$. At fairly close to steady state the total cell number in the scaffold is highest when initially we put a layer of cells away from the nutrient source and lowest when initially we place a layer of cells at all the boundaries of the scaffold.

In the case of the central or off-centre blob initially it is surrounded by a uniform amount of the nutrients. The cells at the edges of the blob grow and spread outwards. The top edge of the blob near the nutrient source grows quickly. The edge of the blob away from the nutrient source grows initially but it stops growing after some time. Since concentration of nutrients near the bottom edge of the blob decreases rapidly so the cells on the bottom edge of the blob grow at slower rate and eventually stop altogether. When the left and right edges of the blob touch the boundaries of the scaffold and block the pores then nutrients cannot reach the cells in the deeper sections of the scaffold. So there is no cell growth in the second half of the scaffold.

When initially we place the cells on the periphery of the scaffold then in that case cells on the inlet wall grow very quickly and block the scaffold pores. The cells in the deeper sections of the scaffold becomes hypoxic and stop growing. To overcome this problem when we remove the cells from the inlet wall then the total cell number in the final construct increases due to the increase in the concentration of nutrients in the internal sections of the scaffold. On the other hand if we put a layer of cells away from the nutrient source then this layer will grow and move towards the nutrient source giving highest cell density in the final construct. The cells are more uniformly distributed in all sections of the scaffold when we put a layer of cells away from the nutrient source. From the results we conclude that if we delay the cell growth near the nutrient source and increase the cell growth away from the nutrient source then we get largest cell yield uniformly distributed in the entire depth of the scaffold. This is because if the cells grow quickly near the inlet wall and consume more nutrients and cells in the deeper sections of the scaffold are depleted. In the case of a central blob when it interacts the side walls of the scaffold then the cells in the deeper sections of the scaffold become

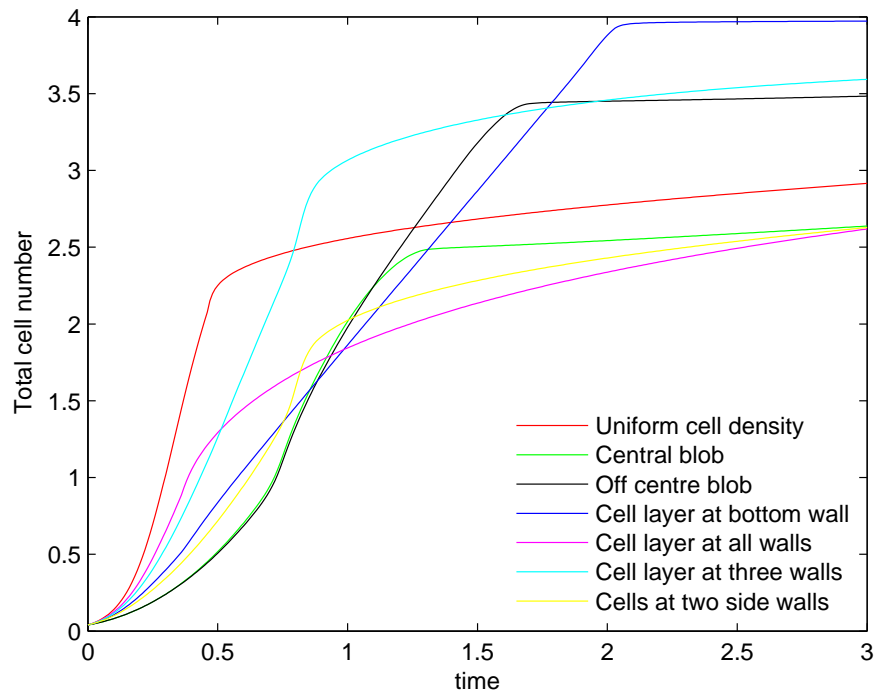


Figure 6.20: Comparison of the time evolution of total cell number for various initial seeding strategies.

hypoxic and do not grow. When we place the cells on all the boundaries of the scaffold then the cells on the inlet boundary grow quickly and do not allow the nutrients to reach into the internal regions of the scaffold but if we remove the cells from the inlet wall then this will improve the nutrient concentration in the internal regions of the scaffold and the total cell yield increases. In the case of a cell layer placed away from the nutrient source, cells grow in the deeper sections of the scaffold and move towards the nutrient source and spread in the entire domain uniformly. These results show that the system is sensitive to initial seeding technique and initial cell density plays an important role in cell distribution and total cell yield in the final tissue construct.

We observe that the growth rate of cells is fastest when cells are distributed uniformly in the entire domain and they reach the quasi-steady state very quickly. Initially the cells and nutrients are uniformly distributed, so cells grow quickly in all sections of the scaffold because of the large surface area of contact between cells and nutrients. However, after a relatively short time the growth of cells decreases in the deeper sections of the scaffold and eventually stops altogether. When more cells grow near the inlet wall, they consume most of the nutrients fed from the inlet wall and block up the pores. The cells in the deeper sections of the scaffold becomes hypoxic and do not grow. We can notice that after time $t = 0.5$ the cell growth becomes extremely slow because cells at

the top are saturated at maximum cell density and cells in the deeper sections are nutrient depleted. The initial growth rate of the off-centre and centre blob is the slowest because of the low surface area. The centre and off-centre blobs have the same initial growth profile because neither blob initially interacts with the scaffold boundaries. However, when at $t = 0.75$ the blob in both the cases touches the boundaries of the scaffold and has cells in the most parts of the scaffold then the growth rate increases a little bit due to increase in surface area. The width of the hypoxic region in the case of centre blob is bigger compared to that of the off-centre blob. In the case of the centre blob, when it grows and touches the boundaries of the scaffold and blocks the pores, the cells in the lower half of the scaffold become hypoxic and give a wide hypoxic layer. But when we put the blob of cells further down, away from the nutrient source, then in that case when it touches the boundaries of the scaffold and blocks the pores the width of hypoxic region will be smaller and upward growth is still possible. The initial growth rate is rapid when we seed the cells on the periphery of the scaffold but it drops down very quickly because the cells on the inlet wall reach maximum carrying capacity and block scaffold pores. The concentration of nutrients in the deeper sections of the scaffold reduces which causes the growth rate to slow down. When initially we seed the cells on the boundaries except the inlet wall we get a reasonably fast growth rate and high cell yield. The growth rate is linear when we put a layer of cells away from the nutrient source because supply of nutrients and surface area of growth front are both constant.

Figure 6.21 shows the comparison of total cell number for various initial seeding strategies when the threshold shear stresses are $\sigma_{c1} = 3$, $\sigma_{c2} = 15$ and $\sigma_{c1} = 2.5$, $\sigma_{c2} = 4.5$. The line color represents the initial seeding technique. We know that when the shear stress reaches σ_{c1} then the cell growth rate increases and when shear stress reaches σ_{c2} then cell growth stops but they still consume nutrients to live. We observe that by decreasing the width of the heightened proliferative region the total cell number also decreases. We can see a quite small change in the total cell number for all seeding strategies. The change is largest in the case of uniform initial cell density.

6.5 Effect of porosity

In the previous Section we have found that the initial seeding strategy plays an important role in the distribution of cells in the final construct. Also nutrient delivery is important to determine the final cell density. In this Section we will discuss the effect of

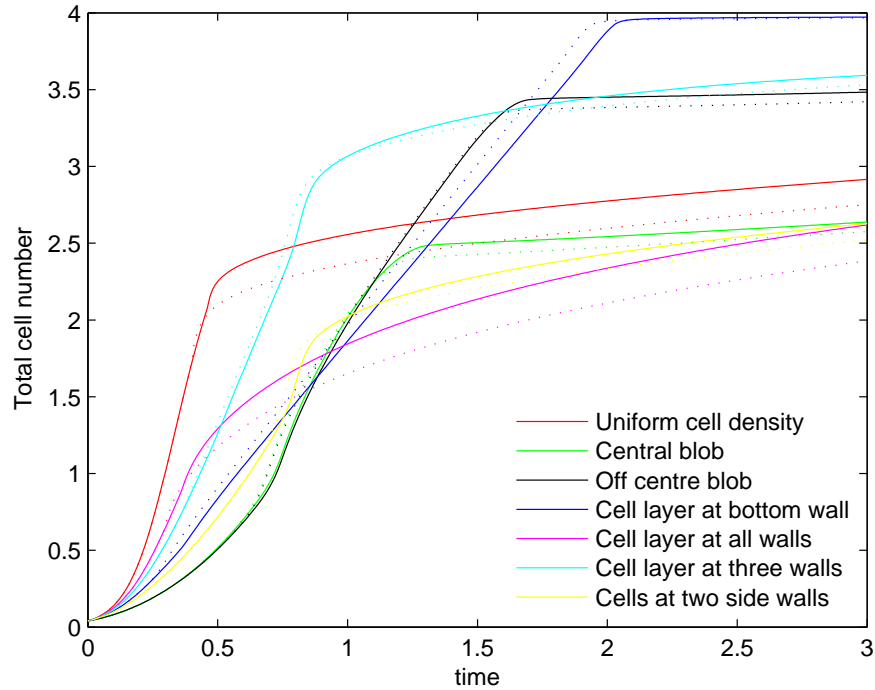


Figure 6.21: Comparison of the time evolution of the total cell number for four different initial seeding strategies. Color represents the different seeding strategies. Solid and dotted lines represent the total cell number when threshold shear stresses are $\sigma_{c1} = 3$, $\sigma_{c2} = 15$ and $\sigma_{c1} = 2.5$, $\sigma_{c2} = 4.5$ respectively.

the initial porosity on the cell distribution and suggest a scaffold design for the initial porosity distribution which improves the delivery of nutrients to the deeper sections of the scaffold. Let us assume that the initial cell density is uniform *i.e.* $N_{init}(x, y) = 0.01$ and initial porosity $\phi_0(x, y)$ is not uniform. We consider different choices of the initial porosity $\phi_0(x, y)$ and scaffold design to compare the cell density N in the final construct.

6.5.1 Adjacent scaffolds of different porosities

Let us consider a scaffold which is less porous in one half and highly porous in the other half. Let the initial porosity $\phi_0(x, y)$ of the left and right half of the scaffold be 0.60 and 0.90, respectively. Figure 6.22 shows a scaffold having different porosities in two halves. Mathematically we can represent the porosity of such a scaffold by the Heaviside step function

$$\phi_0(x, y) = 0.60 + 0.30 \times H(x).$$

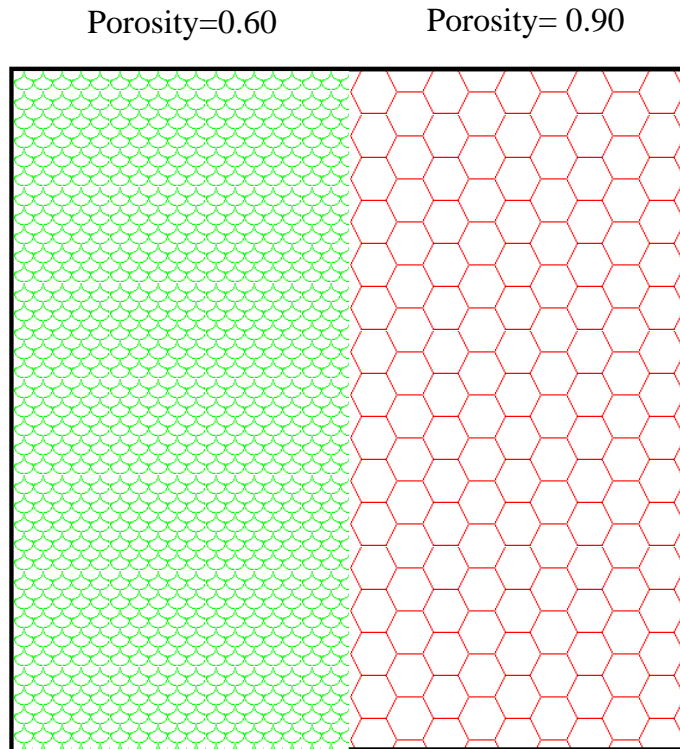
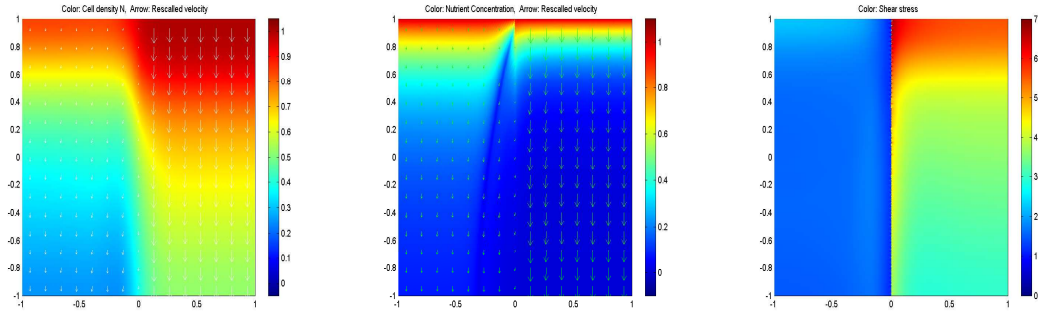
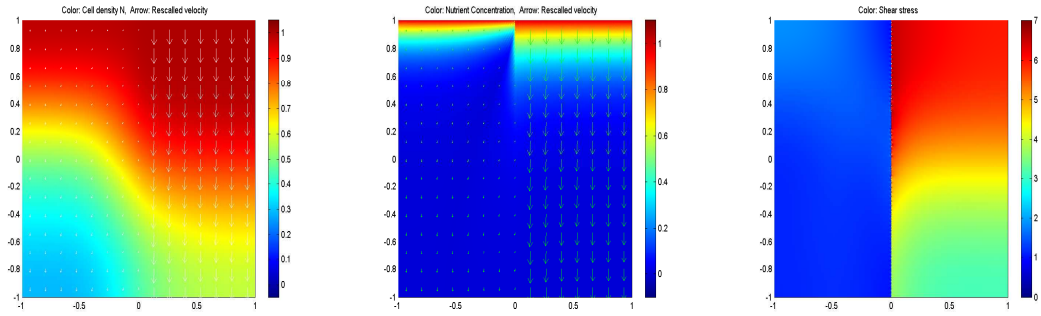


Figure 6.22: Scaffold having different porosity in different regions. Initial porosity of scaffold $\phi_0 = 0.60$ in one half and $\phi_0 = 0.90$ in the other half.

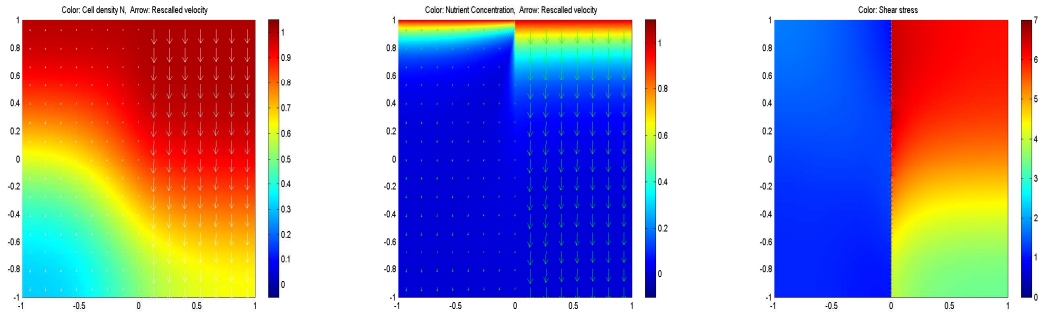
Figure 6.23 shows the same plots as Figure 6.7 when the porosity of the scaffold is different in two halves. We can observe the difference in cell densities in both halves. The cell density is high in the right half where the porosity of the scaffold is high whereas the cell density is low in the left half where the porosity of the scaffold is low. It is evident from the Figure that the concentration of nutrients becomes zero very quickly in the left half due to the low porosity and cells in the deeper sections of the scaffold become hypoxic. On the other hand nutrients can penetrate a further distance from the inlet wall in the right half of scaffold where porosity of scaffold is high. So we conclude that the porosity of the scaffold should be high to deliver nutrients to the deeper sections of the scaffold. The flow is focused in the regions with lowest resistance *i.e.* the high porosity region. The fluid will flow with a high velocity in this region which results in high nutrient concentrations but also high shear stress in this region. So shear stress will be high in the right half of the scaffold where fluid velocity is high.



(a) Cell density N and fluid velocity \mathbf{u}_r at $t = 0.5$. (b) Nutrient concentration S and fluid velocity \mathbf{u}_r at $t = 0.5$. (c) Shear stress σ at $t = 0.5$.



(d) Cell density N and fluid velocity \mathbf{u}_r at $t = 1.5$. (e) Nutrient concentration S and fluid velocity \mathbf{u}_r at $t = 1.5$. (f) Shear stress σ at $t = 1.5$.



(g) Cell density N and fluid velocity \mathbf{u}_r at $t = 2.5$. (h) Nutrient concentration S and fluid velocity \mathbf{u}_r at $t = 2.5$. (i) Shear stress σ at $t = 2.5$.

Figure 6.23: Snapshots of the cell density N , nutrient concentration S , fluid velocity \mathbf{u}_r and the shear stress σ at time $t = 0.5, 1.5, 2.5$ when the initial cell density is uniform and initial porosity of the scaffold is high in one half and low in the other half. The parameter values are the same as in Figure 6.7.

6.5.2 High porosity vertical tubes

To increase the delivery of nutrients to the deeper sections of the scaffold we put three high porosity tubes in the scaffold. The porosity of scaffold is 0.70 and the porosity of the tubes is 0.95. Figure 6.28 shows a scaffold with three high porosity tubes. Mathe-

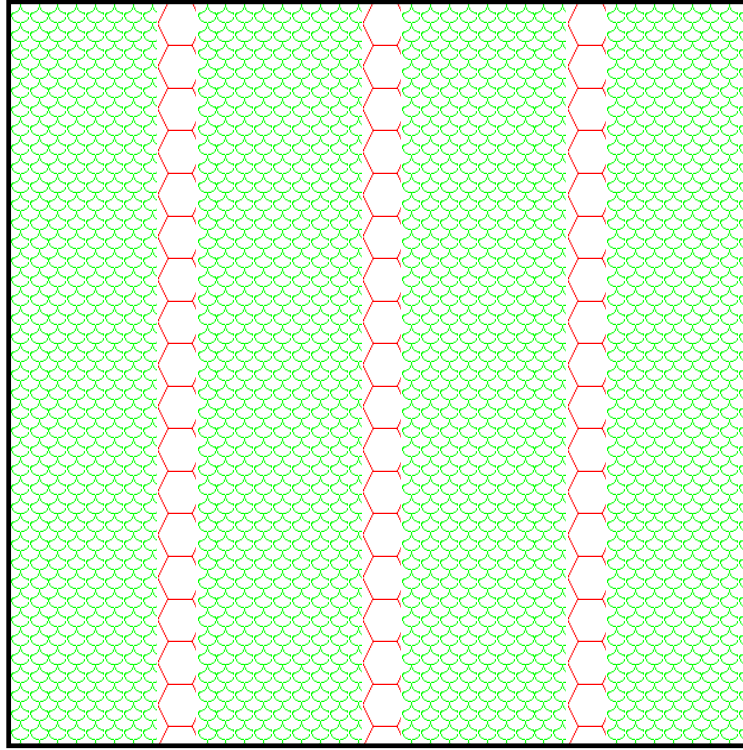


Figure 6.24: Scaffold with three high porosity vertical tubes. Initial porosity of tubes is 0.95 and initial porosity of other sections is 0.70.

matically the porosity of such a scaffold is given by

$$\phi_0(x, y) = 0.70 + 0.25 \times ((H(x + 0.6) - H(x + 0.5)) + (H(x + 0.05) - H(x - 0.05)) + (H(x - 0.5) - H(x - 0.6))).$$

Figure 6.25 shows the same plots as Figure 6.7 when three high porosity, vertical, parallel tubes are inserted into the scaffold. Since the porosity of tubes is high the flow of fluid through these tubes is high which improves the delivery of nutrients in the deeper sections of the scaffold. Nutrients flows through the tubes and diffuse into the low porosity regions to reach in the deeper sections of the scaffold. Due to the delivery of nutrients in the deeper sections of the scaffold, the growth of cells increases in these sections. The initial cell density is uniform in the scaffold. We observe that the growth of cells is still higher near the scaffold inlet wall compared to the other sections of the scaffold due to presence of high nutrient concentration. Due to the high fluid velocity in the parallel tubes the shear stress is very high in the tubes. The cell density still remains lowest in the two lower corners of the scaffold.

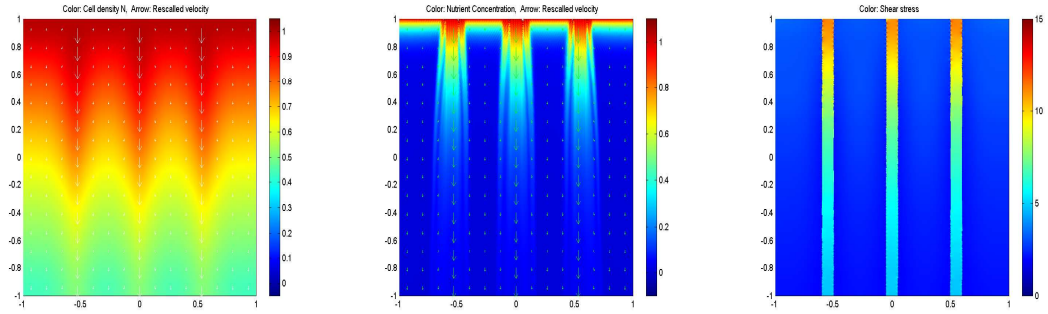
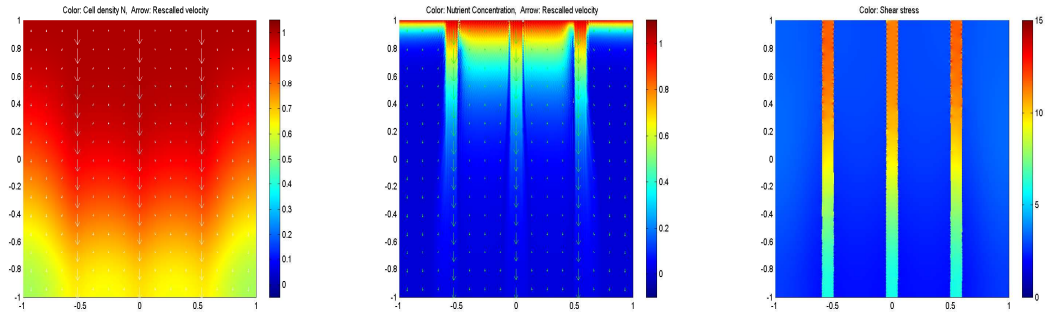
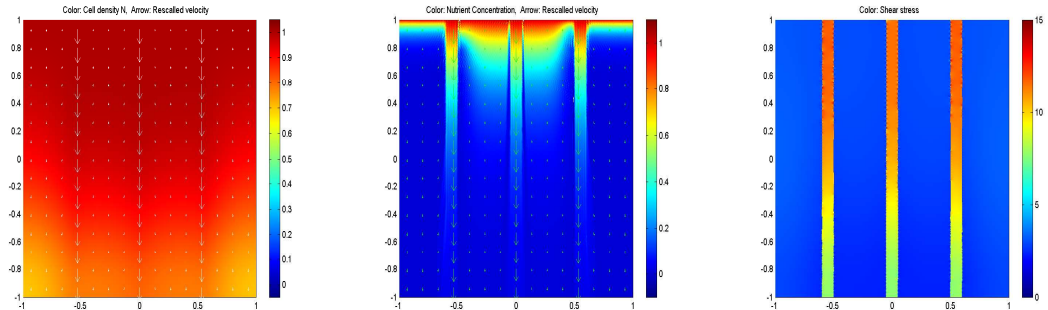
(a) Cell density N and fluid velocity \mathbf{u}_r at $t = 0.5$.(b) Nutrient concentration S and fluid velocity \mathbf{u}_r at $t = 0.5$.(c) Shear stress σ at $t = 0.5$.(d) Cell density N and fluid velocity \mathbf{u}_r at $t = 1.5$.(e) Nutrient concentration S and fluid velocity \mathbf{u}_r at $t = 1.5$.(f) Shear stress σ at $t = 1.5$.(g) Cell density N and fluid velocity \mathbf{u}_r at $t = 2.5$.(h) Nutrient concentration S and fluid velocity \mathbf{u}_r at $t = 2.5$.(i) Shear stress σ at $t = 2.5$.

Figure 6.25: Snapshots of the cell density N , nutrient concentration S , fluid velocity \mathbf{u}_r and the shear stress σ at time $t = 0.5, 1.5, 2.5$ when the initial cell density is uniform and three high porosity vertical parallel tubes are inserted in the scaffold. The parameter values are the same as in Figure 6.7.

6.5.3 High porosity vertical tubes along side walls

In the case of high porosity parallel tubes we observe that the cell growth is slow in the bottom corners of the scaffold. To overcome this problem we slightly modify the design of scaffold and put the two high porosity parallel tubes adjacent to side walls of

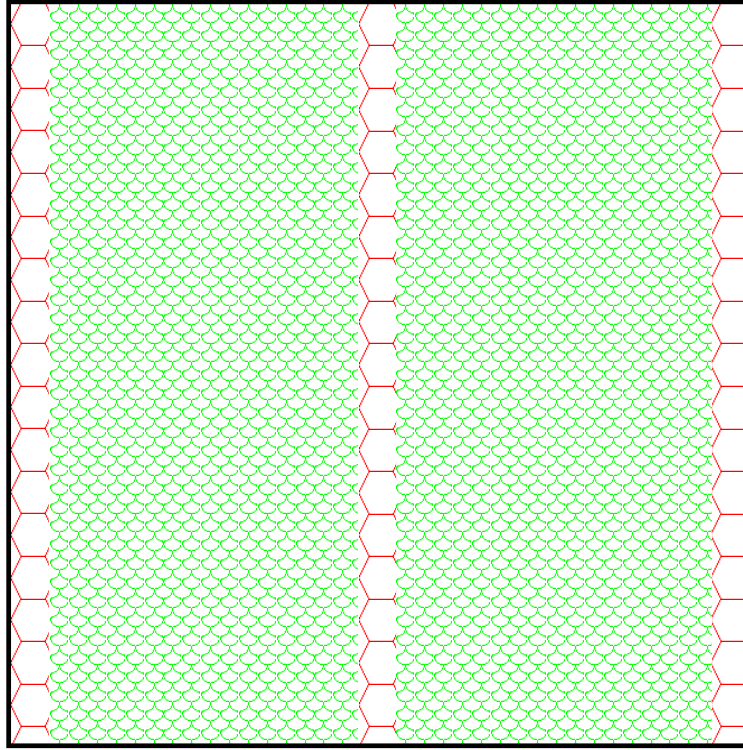


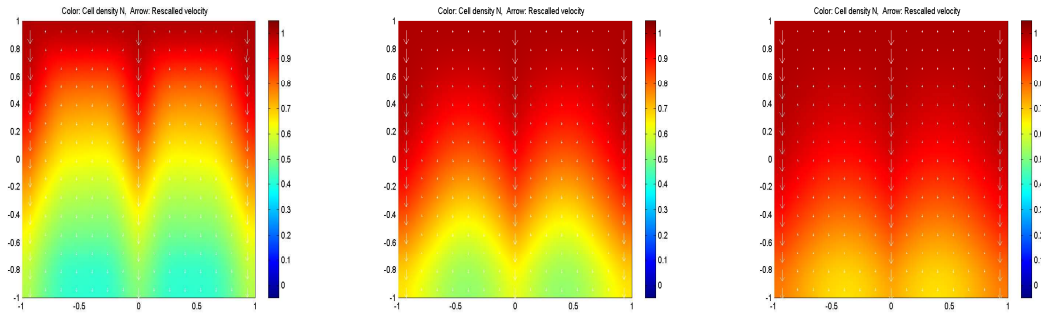
Figure 6.26: Scaffold with three high porosity vertical tubes along side walls. Initial porosity of tubes is 0.95 and initial porosity of other sections of scaffold is 0.70.

the scaffold and one in the middle of the scaffold. Again the porosity of scaffold is 0.70 and the porosity of the tubes is 0.95.

Figure 6.26 shows a scaffold with three high porosity tubes. Mathematically the porosity of such a scaffold is given by

$$\phi_0(x, y) = 0.70 + 0.25 \times ((H(x + 1) - H(x + 0.9)) + (H(x + 0.05) - H(x - 0.05)) + (H(x - 0.9) - H(x - 1))).$$

Figure 6.27 shows the same plots as Figure 6.15 when three high porosity (two adjacent to side walls and one in middle) vertical tubes are inserted into the scaffold. Since the porosity of tubes is high the flow of fluid through these tubes is high which improves the delivery of nutrients in the deeper sections of the scaffold. Since the tubes are adjacent to the side walls, they will deliver the nutrients to deeper sections of the scaffold from only one side. Thus this design does not improve the delivery of nutrients to the deeper sections of the scaffold as a consequence the total cell yield in the final construct does not improve.



(a) Cell density N and fluid velocity \mathbf{u}_r at $t = 0.5$. (b) Cell density N and fluid velocity \mathbf{u}_r at $t = 1.5$. (c) Cell density N and fluid velocity \mathbf{u}_r at $t = 2.5$.

Figure 6.27: Snapshots of the cell density N and fluid velocity \mathbf{u}_r at time $t = 0.5, 1.5, 2.5$ when the initial cell density is uniform and three high porosity vertical tubes are inserted in the scaffold. The parameter values are the same as in Figure 6.7.

6.5.4 High porosity diagonal tubes

To improve the delivery of nutrients in the deeper sections of the scaffold, particularly lower corners, let us consider a scaffold with high porosity diagonal tubes inserted in it. Figure 6.28 shows a scaffold with two high porosity diagonal tubes. Mathematically we represent the porosity of such scaffold by a series of step functions.

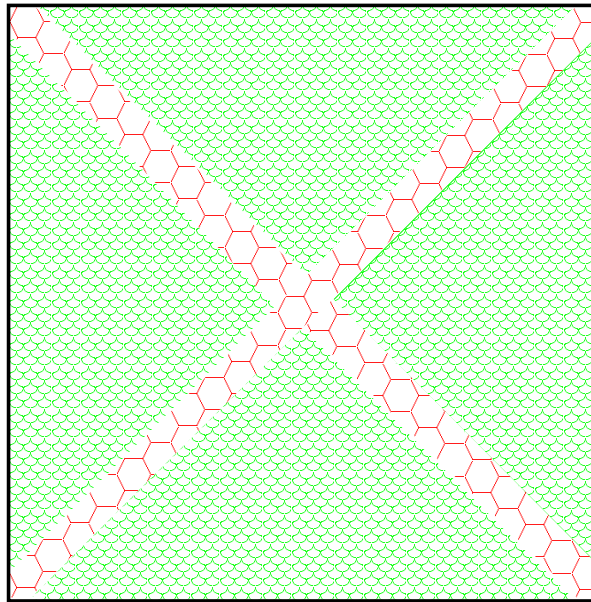
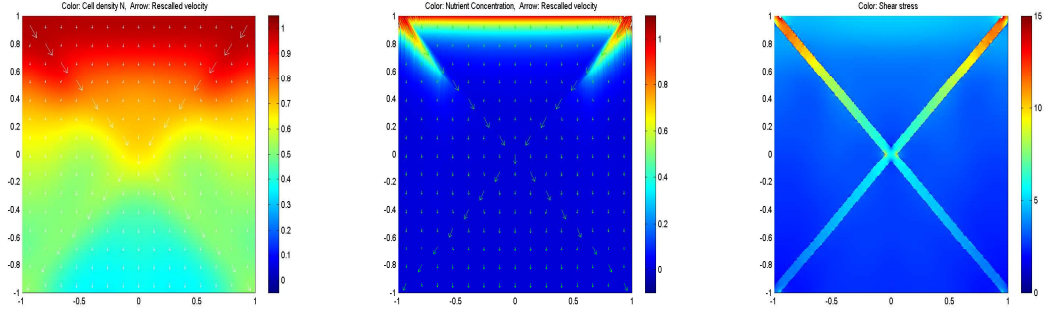
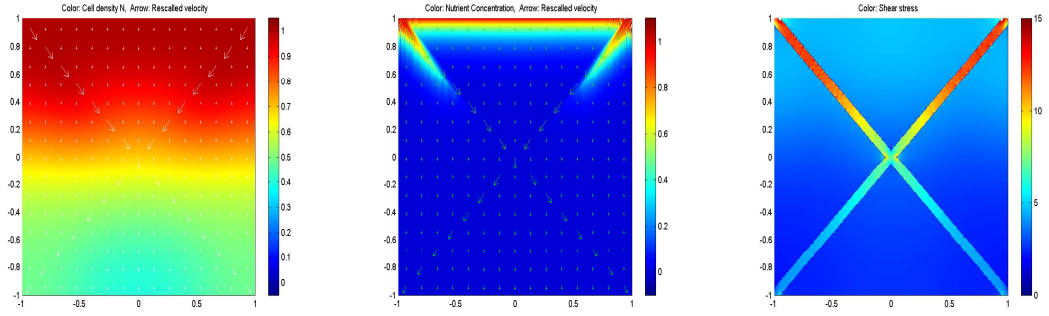


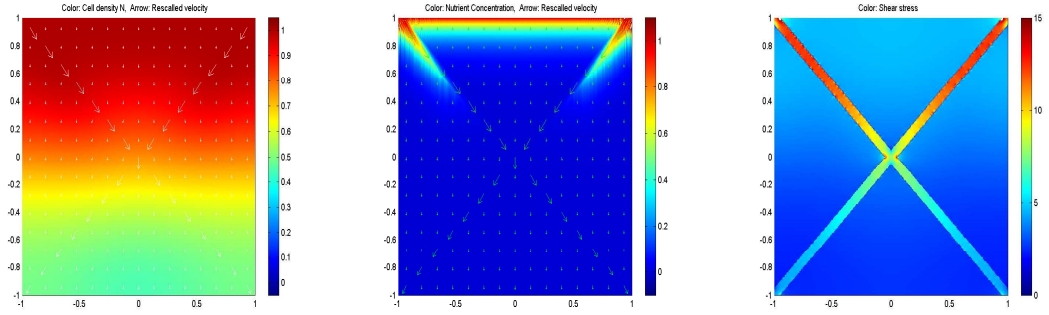
Figure 6.28: Scaffold with high porosity diagonal tubes. Initial porosity of tubes is 0.95 and initial porosity of other sections of scaffold is 0.70.


 (a) Cell density N and fluid velocity \mathbf{u}_r at $t = 0.5$.

 (b) Nutrient concentration S and fluid velocity \mathbf{u}_r at $t = 0.5$.

 (c) Shear stress σ at $t = 0.5$.

 (d) Cell density N and fluid velocity \mathbf{u}_r at $t = 1.5$.

 (e) Nutrient concentration S and fluid velocity \mathbf{u}_r at $t = 1.5$.

 (f) Shear stress σ at $t = 1.5$.

 (g) Cell density N and fluid velocity \mathbf{u}_r at $t = 2.5$.

 (h) Nutrient concentration S and fluid velocity \mathbf{u}_r at $t = 2.5$.

 (i) Shear stress σ at $t = 2.5$.

Figure 6.29: Snapshots of the cell density N , nutrient concentration S , fluid velocity \mathbf{u}_r and the shear stress σ at time $t = 0.5, 1.5, 2.5$ when the initial cell density is uniform and two high porosity diagonal tubes are inserted in the scaffold. The parameter values are the same as in Figure 6.7.

We define the initial porosity of scaffold by

$$\begin{aligned} \phi_0(x, y) = & 0.70 + 0.25 \times \min(1, (H(y - x + 0.05) - H(y - x - 0.05)) \\ & + (H(y + x + 0.05) - H(y + x - 0.05))). \end{aligned}$$

Figure 6.29 shows the the same plots as Figure 6.7 when high porosity diagonal tubes are inserted in the scaffold. We observe that the flow velocity is high in the diagonal tubes but nutrients are not delivered to the deeper sections of the scaffold. Cell growth is high near the scaffold inlet wall due to the high nutrient concentration and the cell growth is low in the deeper sections of the scaffold due to the low nutrient concentration. We observe that this technique is not very efficient for the delivery of nutrients to the deeper sections of the scaffold. Also the shear stress is high in the diagonal tubes due to the high flow velocity.

6.5.5 High porosity diagonal and vertical tubes

Consider the case when two diagonal and a vertical tube are inserted in order to improve the delivery of nutrients to the deeper sections of the scaffold. Figure 6.30 shows the scaffold with two diagonal and one vertical high porosity tubes. Mathematically the initial porosity of such a scaffold can be represented by a series of heaviside step

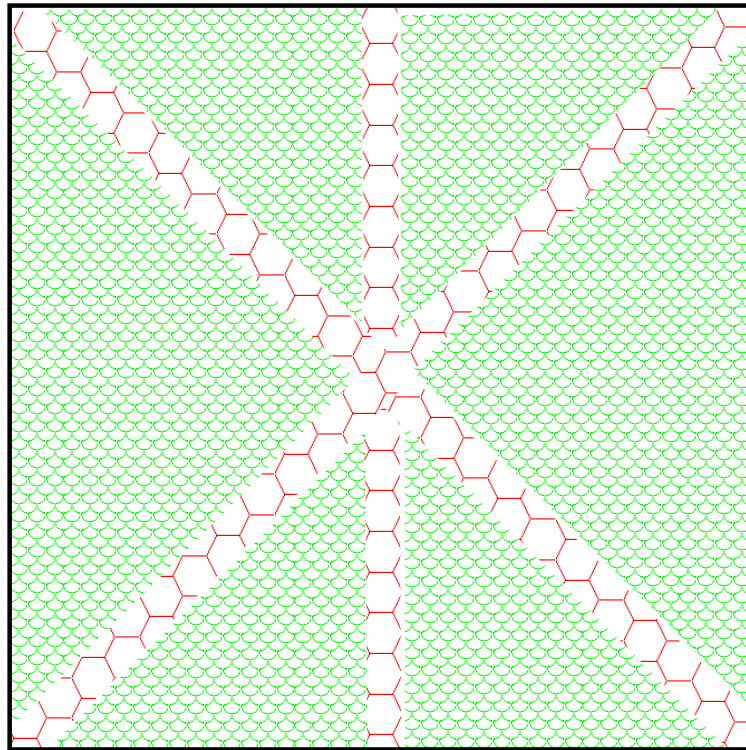
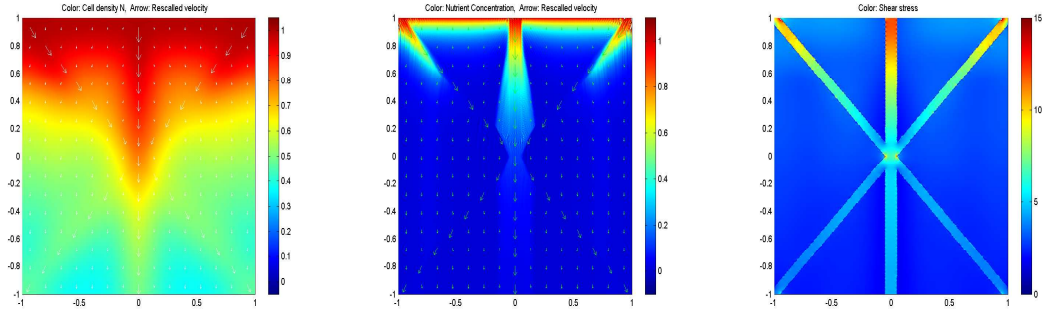


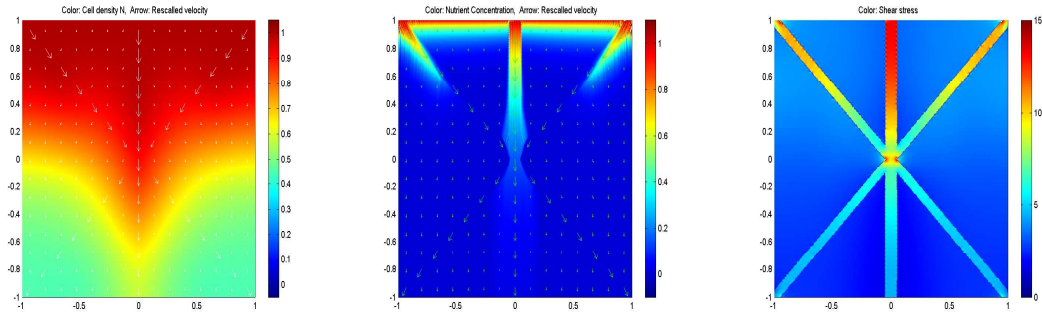
Figure 6.30: Scaffold with high porosity diagonal and vertical tubes. Initial porosity of tubes is 0.95 and initial porosity of other sections of scaffold is 0.70.

functions. We define the initial porosity of the scaffold by

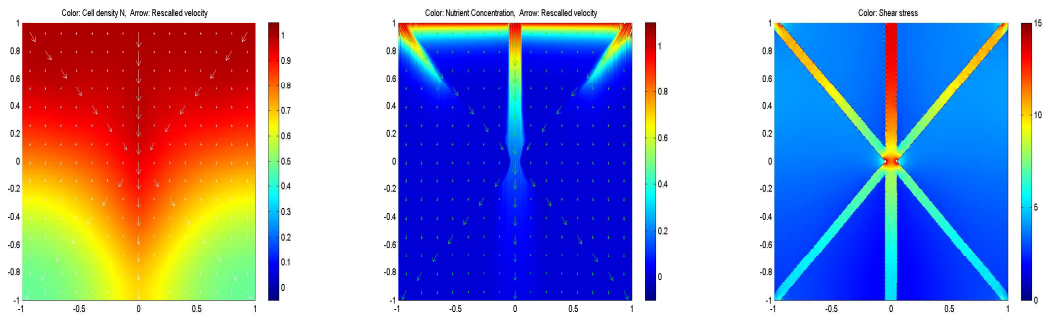
$$\begin{aligned} \phi_0(x, y) = & 0.70 + 0.25 \times \min(1, (H(y - x + 0.05) - H(y - x - 0.05)) \\ & + (H(y + x + 0.05) - H(y + x - 0.05)) + (H(x + 0.05) - H(x - 0.05))). \end{aligned}$$



(a) Cell density N and fluid velocity \mathbf{u}_r at $t = 0.5$. (b) Nutrient concentration S and fluid velocity \mathbf{u}_r at $t = 0.5$. (c) Shear stress σ at $t = 0.5$.



(d) Cell density N and fluid velocity \mathbf{u}_r at $t = 1.5$. (e) Nutrient concentration S and fluid velocity \mathbf{u}_r at $t = 1.5$. (f) Shear stress σ at $t = 1.5$.



(g) Cell density N and fluid velocity \mathbf{u}_r at $t = 2.5$. (h) Nutrient concentration S and fluid velocity \mathbf{u}_r at $t = 2.5$. (i) Shear stress σ at $t = 2.5$.

Figure 6.31: Snapshots of the cell density N , nutrient concentration S , fluid velocity \mathbf{u}_r and the shear stress σ at time $t = 0.5, 1.5, 2.5$ when the initial cell density is uniform and two high porosity diagonal and one vertical tubes are inserted in the scaffold. The parameter values are the same as in Figure 6.7.

Figure 6.31 shows the same plots as Figure 6.7 when two high porosity diagonal tubes and one vertical tube are inserted into the scaffold. We observe that the transport of nutrients increases into the deeper sections of the scaffold due to the vertical tube while delivery of nutrients is not improved due to diagonal tubes. Due to improved delivery of nutrients the cell growth has increased in the deeper sections of the scaffold around the vertical tube. The cell growth is still very low in both left and right corners of the scaffold due to lack of delivery of nutrients. Again the shear stress is very high in the tubes due to the high flow velocity.

6.5.6 Comparison of results of porosity distribution

Figure 6.32 shows a comparison of the time evolution of the total cell number in the domain for uniform initial cell density and five different initial porosities of the scaffold. We can see that the total cell number in the scaffold is largest when three high porosity tubes are inserted in the scaffold. We conclude that when we insert the three high porosity tubes not along the edges in the scaffold the delivery of nutrients improves in the deeper sections of the scaffold. Note that all of the modified scaffolds improve the total

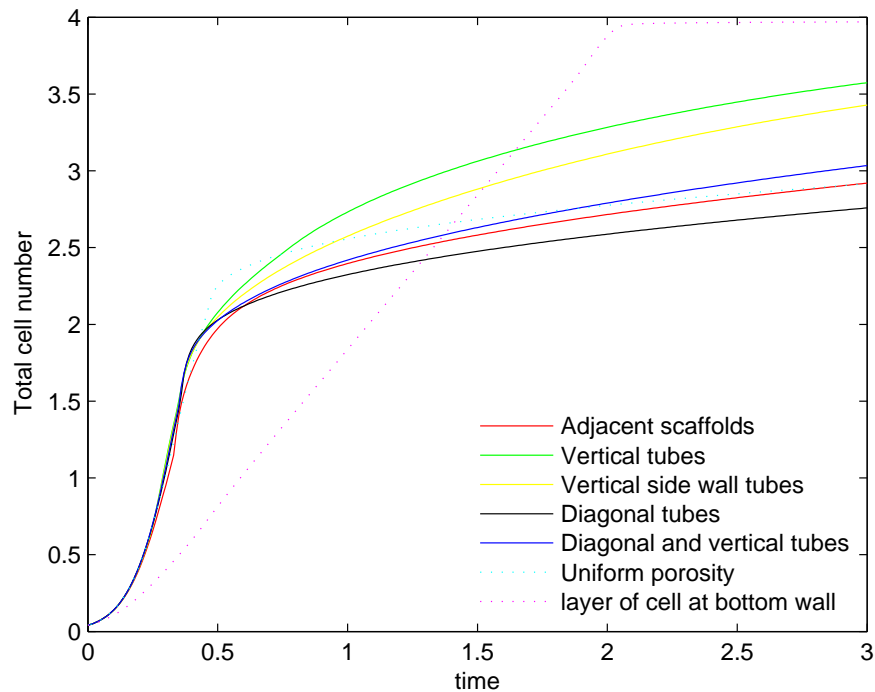


Figure 6.32: Comparison of the time evolution of total cell number for various initial porosities of scaffold. The initial cell density is uniform throughout the scaffold. Dashed curves are our previous results, from Section 6.4.8 included for comparison.

yield. In Figure 6.32 we have also included the data when the initial porosity of the scaffold is uniform but initially a layer of cells is placed away from the nutrient source. From the results of different initial porosity distributions we conclude that to get the highest cell number in the scaffold, initially seeded with uniform cell distribution, we should insert three vertical high porosity tubes not along the side walls in the scaffold. From the Figure 6.32 we observe that to get the fastest growth rate and a high total number of cells we should choose a scaffold with uniform initial cell distribution and three high porosity vertical tubes inserted into it. But if we are not concerned about the growth rate and we want highest number of cells in the scaffold then we should choose a scaffold having uniform initial porosity and initially a layer of cells is placed away from the nutrient source.

6.5.7 Combined effects of initial seeding and initial porosity

In Section 6.4 we have discussed various initial seeding strategies for uniform initial porosity of the scaffold. In each case we chose initial porosity of scaffold to be $\phi_0 = 0.85$. We found that to get the largest cell yield initially we should put the cells on the boundary opposite to the nutrient source (see Figure 6.20). In Section 6.5 we have discussed the various initial porosity distributions when initial cell density is uniform in the scaffold. In each case the average porosity of the scaffold is between 0.70 and 0.75. Since average porosity in Section 6.4 and 6.5 is not the same, results for the total cell yield are not comparable directly.

Now in this Section we study combined effects of initial seeding and initial porosity. We consider a scaffold with three high porosity vertical tubes not along the side walls and initially we put a layer of cells on the bottom boundary. Figure 6.33 shows the comparison of optimal cases for initial seeding, initial porosity distribution and combined effects of initial seeding and initial porosity. The scaffold with three vertical tubes has initial average porosity 0.85. We observe that the total cell yield is approximately the same when initially we put the cells on the bottom boundary and keep the porosity of the scaffold either uniform or insert the three high porosity tubes in it. We conclude that if initially we put the layer of cells at the bottom boundary then by inserting the high porosity tubes do not increase the total cell yield but if the initial cell density is uniform then the high porosity tubes help to improve the total cell yield.

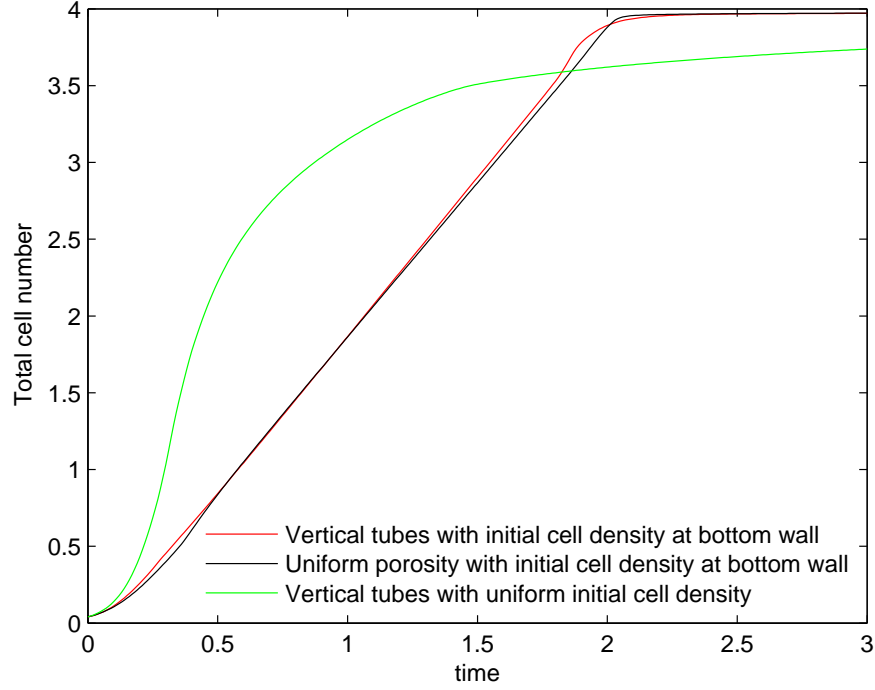


Figure 6.33: Comparison of the time evolution of total cell number for optimal case of initial cell density, initial porosity distribution and combined effects of initial seeding and initial porosity.

6.6 Effect of flow rate on cell growth

The basic model developed in Chapter 5 is a generic model and can be easily manipulated to consider different geometric configurations, cell types, nutrient types and different combination of parameter values. In this Section we will study the effect of flow rate on the cell growth. All the results in Sections 6.4 and 6.5 are calculated for the flow rate $U_c^* = 2.5 \times 10^{-2} m/sec$. Now in this Section we will increase and decrease the flow rate and observe the effect on cell growth. By changing the characteristic flow rate the dimensionless threshold shear stresses σ_{c1} and σ_{c2} will be affected. Clearly by increasing the flow rate the shear stress will increase and *vice versa*. Thus by increasing or decreasing the flow rate the threshold shear stresses will be reached earlier and later respectively. Thus we must keep the dimensional threshold shear stresses fixed and recalculate the dimensionless values. We start by computing the dimensional values. We know from equation (5.4.2) that

$$\sigma^* = \frac{8\tau\mu^*U_c^*}{\epsilon^*}\sigma, \quad (6.6.1)$$

Similarly dimensional threshold shear stresses σ_{c1}^* and σ_{c2}^* are given by

$$\sigma_{c1}^* = \frac{8\tau\mu^*U_c^*}{\epsilon^*}\sigma_{c1}, \quad (6.6.2)$$

$$\sigma_{c2}^* = \frac{8\tau\mu^*U_c^*}{\epsilon^*}\sigma_{c2}. \quad (6.6.3)$$

Table 6.1: Parameter values

Parameter	Description	Value			unit
μ^*	Fluid viscosity	8.4×10^{-4}			$kg/m.sec$
ϵ^*	Pore diameter	6.8×10^{-4}			m
τ	Scaffold tortuosity	2.05			-
U_c^*	Perfusion rate	1.25×10^{-2}	2.5×10^{-2}	5×10^{-2}	m/sec
σ_{c1}		6	3	1.5	-
σ_{c2}		30	15	7.5	-
D_s		1.25×10^{-5}	6×10^{-6}	3×10^{-6}	-
R_s		2.976	1.488	0.744	-

We fix the dimensionless threshold shear stresses σ_{c1} and σ_{c2} and calculate the dimensional threshold shear stresses σ_{c1}^* and σ_{c2}^* from equations (6.6.2) and (6.6.3) for the values of flow rate and dimensionless threshold shear stresses used in Sections 6.4 and 6.5 i.e. $U_c^* = 2.5 \times 10^{-2} m/sec$, $\sigma_{c1} = 3$ and $\sigma_{c2} = 15$. The values of other parameters are given in Table 6.1.

Thus $\sigma_{c1}^* = 1.5194$ and $\sigma_{c2}^* = 7.5971$. When we change the flow rate we calculate the dimensionless threshold shear stresses σ_{c1} and σ_{c2} from equations (6.6.2) and (6.6.3) for fixed values of dimensional threshold shear stresses $\sigma_{c1}^* = 1.5194$ and $\sigma_{c2}^* = 7.5971$. The flow rate U_c^* also appears in the dimensionless parameters D_s and R_s . From equation 5.5.14 we observe that parameters D_s and R_s are inversely proportional to flow rate U_c^* . Thus by increasing the flow rate the values of parameters D_s and R_s will decrease and *vice versa*. The initial cell distribution and initial porosity of the scaffold both are uniform.

6.6.1 High flow rate

Let us consider the case when the flow is $U_c^* = 5 \times 10^{-2} m/sec$ which is twice the flow rate used in Sections 6.4 and 6.5. With this flow rate we calculate the values of parameters D_s and R_s and dimensionless threshold shear stresses σ_{c1} and σ_{c2} . Thus

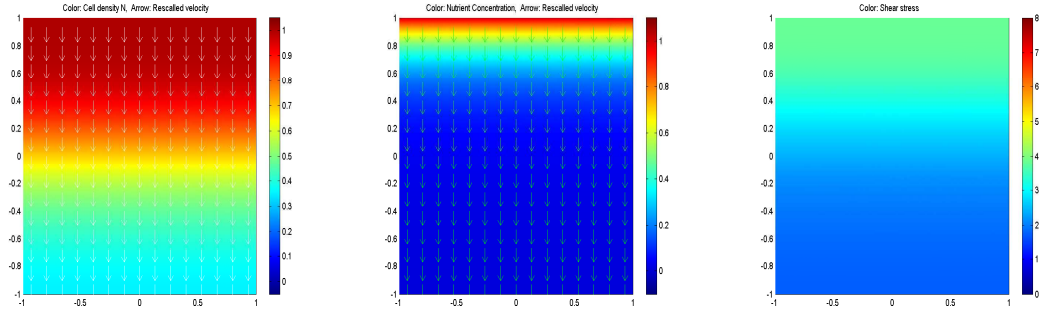
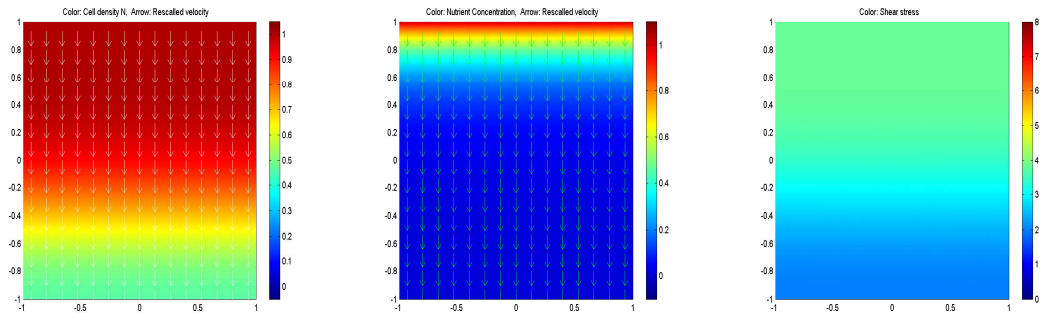
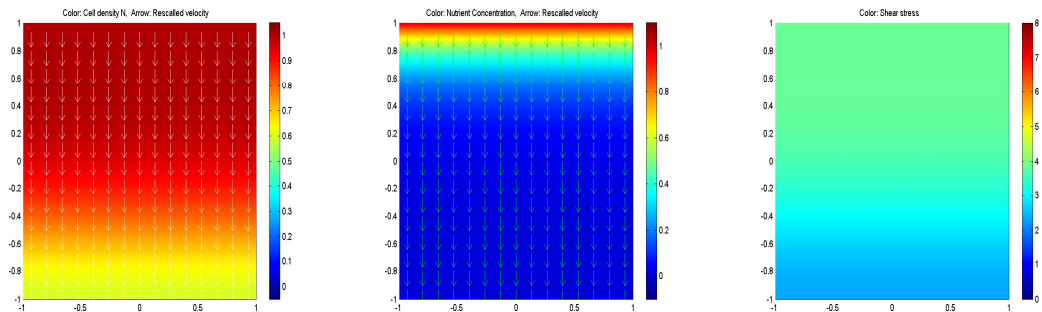
(a) Cell density N and fluid velocity \mathbf{u}_r at $t = 0.5$.(b) Nutrient concentration S and fluid velocity \mathbf{u}_r at $t = 0.5$.(c) Shear stress σ at $t = 0.5$.(d) Cell density N and fluid velocity \mathbf{u}_r at $t = 1.5$.(e) Nutrient concentration S and fluid velocity \mathbf{u}_r at $t = 1.5$.(f) Shear stress σ at $t = 1.5$.(g) Cell density N and fluid velocity \mathbf{u}_r at $t = 2.5$.(h) Nutrient concentration S and fluid velocity \mathbf{u}_r at $t = 2.5$.(i) Shear stress σ at $t = 2.5$.

Figure 6.34: Snapshots of the cell density N , nutrient concentration S , fluid velocity \mathbf{u}_r and the shear stress σ at time $t = 0.5, 1.5, 2.5$ when the initial cell density is uniform and flow rate $U_c^* = 0.05 m/sec$, $D_s = 3 \times 10^{-6}$ and $R_s = 0.744$. The other parameter values are the same as in Figure 6.7.

$D_s = 3 \times 10^{-6}$, $R_s = 0.744$, $\sigma_{c1} = 1.5$ and $\sigma_{c2} = 7.5$. The values of other parameters are given in Table 5.4.

Figure 6.34 shows the same plots as in Figure 6.7. By increasing the flow rate the nutrients penetrate into the internal sections of scaffold which increases the cell growth in these sections. We also observe from the equations 6.6.2 and 6.6.3 the dimensionless threshold shear stresses σ_{c1} and σ_{c2} are inversely proportional to flow rate U_c^* . Hence by increasing the flow rate the values of dimensionless threshold shear stresses σ_{c1} and σ_{c2} will decrease. Also by increasing the flow rate the parameter R_s decreases which means that nutrient consumption reduces. Thus with the reduction in nutrient consumption near the scaffold inlet wall allows the nutrients to penetrate in the deeper sections of the scaffold. We observe that the cell density increases with the increase in flow rate.

6.6.2 Reduced flow rate

Let us consider the case when the flow rate $U_c^* = 1.25 \times 10^{-2} m/sec$ which is half the flow rate used in the Sections 6.4 and 6.5. With the decrease in flow rate the values of parameters D_s and R_s and dimensionless threshold shear stresses σ_{c1} and σ_{c2} increase. Thus $D_s = 1.2 \times 10^{-5}$, $R_s = 2.976$, $\sigma_{c1} = 6$ and $\sigma_{c2} = 30$. The values of other parameters are given in Table 5.4.

Figure 6.35 shows the same plots as in Figure 6.7 for reduced flow rate. By reducing the flow rate the value of the parameter R_s increases which means that most of the nutrients are consumed near the scaffold inlet wall. We observe that the cell density decreases by decreasing the flow rate.

Figure 6.36 shows the comparison of total cell number for various perfusion rates. We observe that when the perfusion rate is high it helps the nutrients to reach a farther distance from the inlet wall. This improves the total cell yield in the final construct. However by reducing the perfusion rate most of the nutrients are consumed near the scaffold inlet wall and cells in the deeper sections of the scaffold becomes hypoxic. This reduces the total cell yield in the final construct. We conclude that by increasing the perfusion rate total cell number in the final construct increases. But we observe from the Figure that when $U_c^* = 1.25 \times 10^{-2} m/sec$ the initial growth rate is slow when compared to the initial growth rate when flow rate $U_c^* = 2.5 \times 10^{-2} m/sec$ but earlier perfusion rate gives a high cell yield in the final construct. The origin of this unusual behaviour is not clear. Also a very high perfusion rate will exceed the second threshold shear stress σ_{c2} and will produce no cell growth.

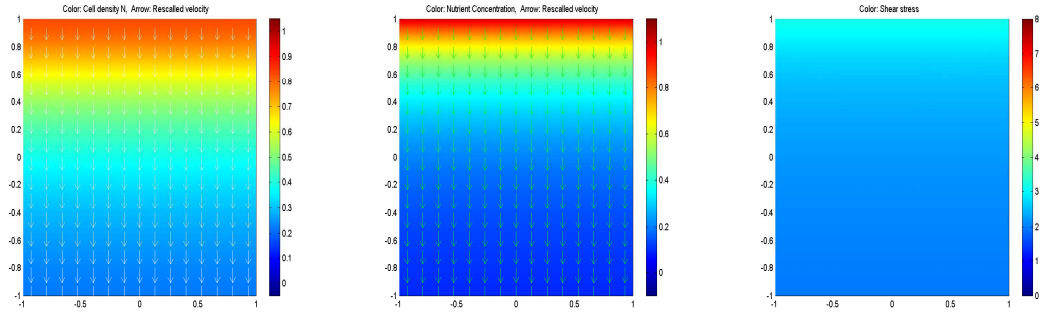
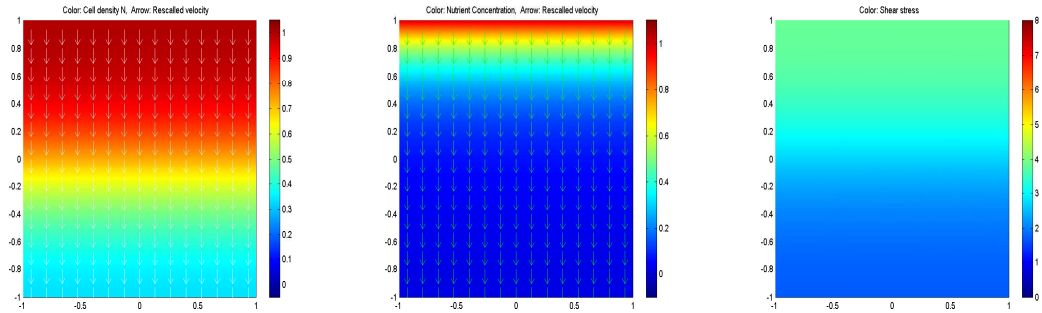
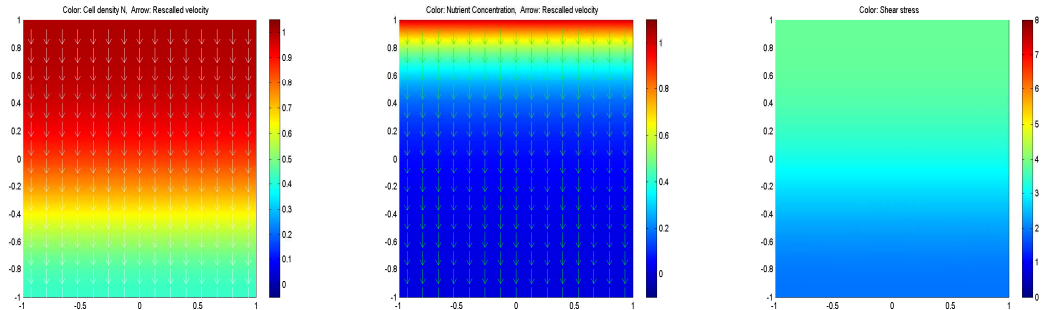
(a) Cell density N and fluid velocity \mathbf{u}_r at $t = 0.5$.(b) Nutrient concentration S and fluid velocity \mathbf{u}_r at $t = 0.5$.(c) Shear stress σ at $t = 0.5$.(d) Cell density N and fluid velocity \mathbf{u}_r at $t = 1.5$.(e) Nutrient concentration S and fluid velocity \mathbf{u}_r at $t = 1.5$.(f) Shear stress σ at $t = 1.5$.(g) Cell density N and fluid velocity \mathbf{u}_r at $t = 2.5$.(h) Nutrient concentration S and fluid velocity \mathbf{u}_r at $t = 2.5$.(i) Shear stress σ at $t = 2.5$.

Figure 6.35: Snapshots of the cell density N , nutrient concentration S , fluid velocity \mathbf{u}_r and the shear stress σ at time $t = 0.5, 1.5, 2.5$ when the initial cell density is uniform and flow rate $U_c^* = 0.0125m/sec$, $D_s = 1.2 \times 10^{-5}$ and $R_s = 2.976$. The other parameter values are the same as in Figure 6.7.

6.7 Summary and conclusions

In this Chapter we have presented the results of the model developed in Chapter 5. We studied the effect of various initial seeding strategies, initial porosities and perfusion rates on the cell growth and nutrient transport in a perfusion bioreactor. We found that

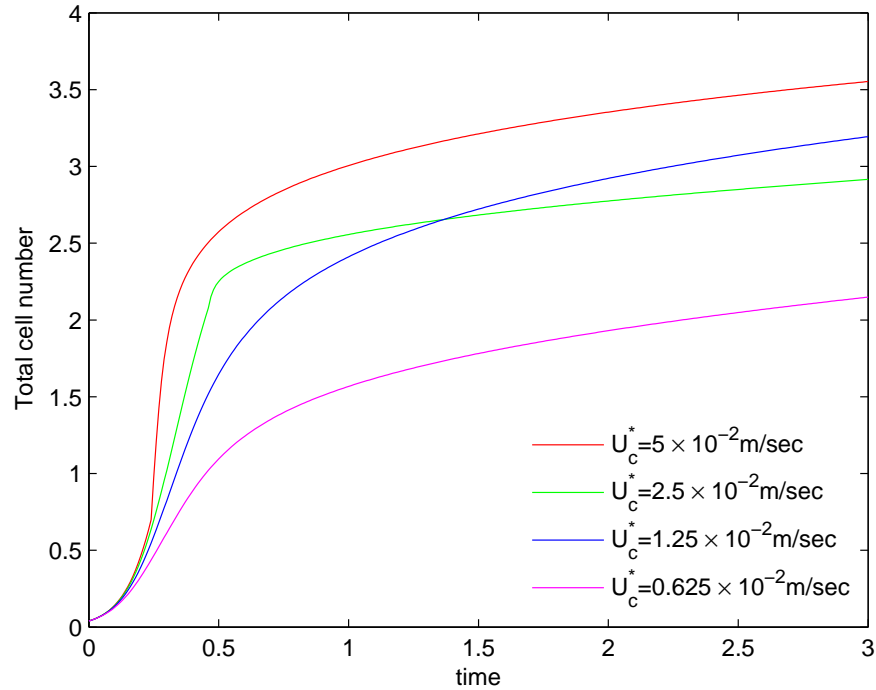


Figure 6.36: Comparison of the time evolution of total cell number for different perfusion velocities. The initial cell density is uniform throughout the scaffold.

the initial cell growth is rapid when initial cell density is uniform and initial cell growth is slowest when initially we place a blob of cells at centre or off-centre of the scaffold. We get a maximum cell yield in the final construct when initially we place a cell layer away from the nutrient source and minimum cell yield when initially we place cells at all walls of the scaffold. The cell growth depends on the surface area of contact between the cells and nutrients. The cell yield depends on the cell growth rate at the entrance compared to the cell growth rate at the exit. To improve the delivery of nutrients in the deeper sections of the scaffold we put high porosity tubes in the various locations of the scaffold. We found that three high porosity vertical tubes not along scaffold edges improve the delivery of nutrients in the deeper sections of the scaffold and hence gives the largest cell number in the final construct. The perfusion velocity also enhances the cell number in the final construct. If the perfusion velocity is high it improves the delivery of nutrients in the deeper sections of the scaffold which enhances the total cell yield in the final construct. A flow rate that is too high will exceed the threshold shear stress σ_{c2} that inhibits the cell growth.

Summary and conclusions

7.1 Summary

In this project we have developed a mathematical model of convective and diffusive transport of nutrients and cell growth in a perfusion bioreactor. The model includes the coupled processes affecting the cell growth in a bioreactor, such as fluid flow through the material, nutrient delivery, cell growth and variation of porosity with cell growth.

In Chapter 2 we modeled the flow of fluid through a porous material, by Darcy's law. We have studied Darcy's law for different permeability distributions and discussed the effect of permeability on flow. We found that the velocity of fluid is high where the permeability of the porous material is high and vice versa. We solved Darcy's law numerically and presented analytic solutions for special cases of permeability. We found that analytic and numerical results agree well.

In Chapter 3 we have developed a simple mathematical model of nutrient transport and cell growth in a perfusion bioreactor. The mathematical model consists of three coupled partial differential equations. Darcy's law governs the fluid flow through the porous material, the advection diffusion equation governs the transport of nutrients to the cells and a reaction diffusion equation governs the cell growth. As cells grow and occupy the empty spaces of the scaffold the permeability of the scaffold decreases, and we describe the variation in permeability by an exponential function of cell density. The cell's nutrient consumption and growth rates are modelled by a linear function of nutrient concentration. The growth of cells is controlled by the logistic law. We solved the model for 2-D geometry by using a commercially available solver COMSOL which employs the finite element method. The model presented in Chapter 3 is very complicated and cannot be solved analytically. To verify the coupling in our numeri-

cal method we employed some simplifying assumptions in order to solve the model analytically. The analytical and numerical results agree well which confirms that the numerical coupling works as expected.

In Chapter 4 we studied the Fisher equation with non-linear cell diffusion, in detail. The diffusion coefficient in this case is non-linear, depending on the density. The form of non-linear diffusion is such that it produces similar behaviour to cell proliferation. This leads us to choose the non-linear diffusion to be an exponential function of cell density. We found a travelling wave solution of the Fisher equation and found the theoretical minimum wave speed of growth front by using an eigenvalue analysis of stationary points. But when we calculate the minimum wave speed numerically we observe that, for highly non-linear diffusion, numerical speed of wave front is greater than the minimum speed growth front found by using the eigenvalue analysis. This shows that the front is a "pushed front" in which the wave speed is determined by non-linear effects. This comparison enables us to choose a form of the non-linear diffusion in which we can predict the cell growth speed.

In Chapter 5 we presented a comprehensive mathematical model of cell growth in a perfusion bioreactor which includes the flow, advective and diffusive transport of nutrients, non-linear cell diffusion and variation of porosity with cell growth. We also include a constant volumetric flow rate constraint and the effect of shear stress on nutrient consumption and cell growth rates in our model. We assume that if the shear stress is very low or very high nutrient consumption is not affected and for intermediate values of shear stress nutrient consumption is enhanced. Similarly for very low values of the shear stress cell growth is not affected and for intermediate values of shear stress cell growth is heightened and for high values of shear stress cell growth becomes zero. The model consists of three coupled partial differential equations. Cell growth is a slow process as compared to transient flow and nutrient fields, so in the model the cell growth equation is transient while Darcy's law and the advection diffusion equation are quasi-static with respect to changes in the cell density. To solve the model initially the scaffold is seeded with cells and placed in the bioreactor. First we calculate the porosity of the scaffold from the porosity equation and then we calculate the permeability (which is a function of porosity) of the scaffold. We use this permeability in Darcy's law to give the fluid velocity. In experiments the total volumetric flow rate is constant. To keep this flow rate constant in the simulations we divide Darcy's law by a constant which ensures the constant volumetric flow rate. We call this constant flow rate the rescaled velocity. We substitute this rescaled velocity as advective velocity in the advection diffusion equation and solve this equation to give the concentration

of nutrients. By substituting the nutrient concentration into the cell growth equation we can calculate cell density. We update the cell density in the porosity equation and solve the entire system again. This process continues until the system gets close to steady state. This coupled system of three partial differential equations and an algebraic equation is solved by the finite element solver COMSOL.

In Chapter 6 we have presented the results of model developed in Chapter 5. We found that system is sensitive to initial seeding and initial porosity. The results are presented for various initial seeding strategies, scaffold designs and perfusion rates. We found that we get a reasonably fast growth rate and largest cell yield when initially we place a cell layer away from the nutrient source. However, on the other hand depending on the scaffold design the total cell yield is largest when we insert the three high porosity vertical tubes in the scaffold away from the scaffold edges. The conclusions of these results are discussed below.

7.2 Conclusions

The main challenges that tissue engineering is facing at present are how to produce a proper nutrient supply to the internal regions of the tissue, uniform cell distribution in the final construct, a large cell yield and rapid growth. From the analysis of the model we observe that these factors are sensitive to the initial cell seeding strategy and initial porosity distribution of the scaffold. The results of the model show that the total cell number in the final construct depends on the initial cell distribution in the scaffold and that the proper supply of the nutrients to the internal regions of the construct depends on the initial porosity distribution of the scaffold.

To understand the mechanism leading to largest cell yield and rapid growth we have tested various initial seeding techniques, including a uniform initial cell distribution, centre and off centre blobs of cells and layers of cells at the walls of the scaffold. Here we keep the initial porosity of the scaffold uniform. From the results of the simulations we observe two important features. Firstly, we observe that if cells have large surface area of contact with the nutrients then their growth is rapid and if the surface area is small the cell growth will be slow. For example when initially cells are distributed uniformly then they have large surface area of contact with the nutrients so they initially grow very quickly giving highest cell growth. On the other hand the initial growth of centre and off centre blobs is slowest due to small area of contact with the nutrients. The initial growth of both the blobs is same because they have the same surface area of

contact with the nutrients before they interact with the boundaries of the scaffold. The initial growth rate of cells will be linear if they have constant supply of nutrients and constant area of contact with the nutrients.

Secondly, we observe that if initially we place the cells away from the nutrient source we get the highest cell yield in the final construct. In other words if we delay the cell growth near the nutrient source and enhance the cell growth away from the nutrient source we get a higher cell number in the final construct. If the initial cell growth is high near the nutrient source then the cells grow quickly due to the constant supply of nutrients. When more cells grow near the inlet wall they consume more nutrients and the cells in the deeper sections of the scaffold become hypoxic and stop growing. To counter this problem initially we should put the cells away from the nutrient source. For example when we move the blob of cells from centre of the scaffold to further down, the total cell number in the final construct increases because in that case the cells grow in the deeper sections of the scaffold and move towards the nutrient source. We get a lowest cell yield when we place the cells layer at all the boundaries of the scaffold. For reasonably fast growth rate and high cell yield we should place the cells on the three walls of the scaffold (no cells on the inlet wall). Tissue engineers like to seed the cells on the periphery of the scaffold so to be more realistic we recommend that if we seed the cells on the three walls of the scaffold then we get the larger cell yield and reasonably fast growth rate.

A common problem tissue engineering is facing is the rapid growth of cells near the nutrient source while the cells in the inner region becomes hypoxic (Rose et al., 2004). This is thought to be due to the limited supply of nutrients in the internal regions of the scaffold. One way of addressing this problem is to incorporate channels in the scaffold to improve the nutrient delivery and hence cell growth in the centre and lower regions of the scaffold. In this thesis to study the delivery of nutrients to the deeper sections of the scaffold we have considered several scaffold designs having different initial porosities. For uniform initial cell seeding and porosity the results of the simulation indicate that the cells in the deeper sections of the scaffold becomes hypoxic very quickly so they do not grow in the deeper sections of the scaffold. The growth of cells can be enhanced in the deeper sections of the scaffold by improving the nutrient delivery. For that we have designed the scaffold in several ways by inserting high porosity tubes into it. These designs include a scaffold with different porosities in two halves, a scaffold with three vertical high porosity tubes, a scaffold with high porosity diagonal tubes and a scaffold with the combination of high porosity diagonal and vertical tubes. We found that we get the largest cell yield when we use a scaffold with three vertical

high porosity tubes away from the scaffold edges. When we put the tubes in the scaffold they improve the delivery of nutrients to the deeper sections of the scaffold. We observe that high porosity vertical tubes, which are also parallel to flow direction, improve the delivery of nutrients to the deeper sections of the scaffold giving the largest cell yield. Tubes at angle to the flow direction are considerably less effective. When we compare the results of the modified scaffold with the results of scaffold having uniform porosity we observe that the modified scaffolds improve the cell yield. *e.g.* for uniform initial cell distribution we consider two scaffolds, one with uniform initial porosity and other with three high porosity tubes inserted into it. The results show that cell number improves in the later case.

There is one major concern in fabricating the scaffolds with aligned channels is that the scaffolds loses its mechanical strength where the part of the main scaffold is removed. But Rose et al. (2004) demonstrated that 13 channels within scaffold ($432\ \mu\text{m}$ in diameter) enhanced the mechanical strength of the scaffold, to almost double when compared to the scaffold with no channels. In this study we have inserted 3 channels in the scaffold thus from the results of Rose et al. (2004) we expect that inserting more channels in the scaffold would increase the nutrient supply to the internal regions of the scaffold and hence cell growth without losing the mechanical strength. Several authors studied the effect of aligned channels in various areas of tissue engineering. Lin et al. (2003) used aligned channels in bone tissue engineering. They used steel rods coated with poly (L-lactide-co-DL-lactide). They generated a porous polymer scaffold with channels measuring $100\ \mu\text{m}$ in diameter when they removed the rods. They found a large amount of viable cells on the periphery of the scaffold but also found some viable cells in the internal regions of the scaffold. Schugens et al. (1996) used such channels in nerve regeneration to provide spatial guidance and increased surface area for neuron growth. Our study shows a positive influence of channels within tissue engineering scaffold on cell growth. This is due to enhanced delivery of nutrients to the centre of the scaffold.

Another feature which is also evident from the results is that the threshold shear stresses also affect the total cell yield in the final construct. The total cell yield depends on the amount of shear stress cells are experiencing and the width of the enhanced proliferation region. We neglect cell death due to high shear stress and assume that for high shear stress the cell growth stops but they do not die. When cells are placed in one region of the scaffold then it forces the fluid to go around the cells so the velocity will be high around the edges and as a result the shear stress will also be high in that region. Once cells spread in the whole domain then the fluid has to pass through the cells

which results in a high shear stress in that region.

We have also studied the effect of perfusion rate on the cell growth. We found that by increasing the perfusion rate the total cell yield in the final construct also increases. However very high flow rates will inhibit the cell growth due to high shear stress. Several authors studied the effect of perfusion on the cell growth. Glowacki et al. (1998) analyzed the effect of perfusion culture through stromal cell-seeded 90% porous type I collagen sponge. They found that the perfusion construct yields more cells especially in the centre of the construct compared to non perfusive constructs.

7.3 Future work

The model presented in this thesis is very complex because it couples many different phenomena. We have therefore employed some simplifying assumptions *e.g.* we have neglected cell death due to lack of nutrients and high shear stress and we did not account for the removal of waste products from the construct. A complete model should include these effects. The general model framework presented in this work is comprehensive and lends itself to a number of expansions and modifications.

Firstly, we can include cell death mechanism in our model. The cell equation could be modified to include cell death term by changing the linear term to $(S - S_c)N$, where S_c is the threshold value of nutrient concentration, so that the linear growth is negative if S is less than the threshold value S_c .

Secondly, we know that the strong shear stress can cause the cell necrosis (Cartmell et al., 2003). Although we have not included cell death due to high shear stress in the model, with slight modification in function F_n we can include cell death phenomena due to high shear stress in our model.

Finally, for the removal of waste products from the construct we need to add an extra advection-diffusion equation in the model with zero flux condition at the top boundary and similarly at the lower boundary. If flow is much larger than to production rate of waste products then the concentration of waste products will be very low.

In the present model we have considered simple 2-D square geometry but we can consider more complicated geometries like cylindrical (axi-symmetric) and more realistic 3-D geometries. For axi-symmetric geometry we need to re-write the model equations in cylindrical coordinates which is again a 2-D model in axi-symmetric coordinates and can be solved by the methods used in Chapter 6. Solving the model in a full 3-D geo-

metry will be a more realistic situation. In principle there should not be any problem to extend the model in 3-D. The 3-D model might be numerically expensive but we have proved that 2-D model converges for quite coarse meshes which encourages us to solve the model in 3-D.

The comparison of the model results with the experimental data would be very interesting. The experiment run by David Grant at the University of Nottingham are still at an early stage, it is difficult to make direct comparison at this stage. The model can be further improved by calibration against relevant experimental measurements. A simpler way to increase the realism of the model developed in Chapter 5 is to work more closely with the biologists to obtain the better estimates of the parameters and more accurate functional forms such as permeability, porosity, non-linear diffusion and mechanotransduction. A well calibrated model will help experimentalists to design scaffolds and understand their results. The mathematical model can provide data of cell density, nutrient concentration and shear stress at each spatial location, to the biologists, which can help them to understand the model and their experiments. We have all relevant coupling in the model, meaning that changes suggested by experimentalists will easily fit into our model framework.

In the model we did not consider the degradation rate of scaffold. In future we can incorporate the scaffold degradation in the model by keeping in mind that the rate of scaffold degradation must coincide with the rate of tissue formation.

Appendices

Notation guide

Symbol	Description	Units
α^*	Nutrient consumption constant	$m^3 / cell.sec$
β^*	Cell growth rate constant	$m^3 / mole.sec$
β	Ratio of cell growth to front velocity when nutrient concentration is not constant	-
χ^*	Maximum cell growth rate	$1/sec$
χ	Ratio of cell growth to front velocity when nutrient concentration is constant	-
γ^*	Parameter in non-linear diffusion	$m^3 / cell$
γ	Dimensionless parameter in non-linear diffusion	-
Γ	Ratio of cell diffusion to cell growth	-
Λ	Dimensionless parameter in stress function	-
ρ	Dimensionless parameter in porosity equation	-
η^*	Blocking parameter in permeability equation	$m^3 / cell$
η	Dimensionless parameter in permeability equation	-
ζ	Travelling wave variable	m
σ^*	Shear stress	$kg/m.sec^2$
σ	Dimensionless shear stress	-
σ_{c1}^*	Threshold shear stress for proliferation phase	$kg/m.sec^2$
σ_{c1}	Dimensionless threshold shear stress for proliferation phase	-
σ_{c2}^*	Threshold shear stress for necrotic phase	$kg/m.sec^2$
σ_{c2}	Dimensionless threshold shear stress for necrotic phase	-
δ	Ratio of cell diffusion to front velocity	-
$\phi(x^*, y^*)$	Porosity in dimensional coordinates	-
$\tilde{\phi}(x, y)$	Porosity in dimensionless coordinates	-

$\phi_0(x^*, y^*)$	Initial porosity in dimensional coordinates	-
$\tilde{\phi}_0(x, y)$	Initial porosity in dimensionless coordinates	-
Φ	Phase plane coordinate	-
Ψ	Phase plane coordinate	-
τ	Tortuosity of porous material	-
ϵ^*	Pore diameter	m
μ^*	Fluid viscosity	$kg/m.sec$
$\bar{\mu}^*$	Effective viscosity	$kg/m.sec$
λ^*	Cell growth rate	$1/sec$
λ_n	Eigenvalues	-
$D^*(N^*)$	Non-linear diffusion function	m^2/sec
D_s^*	Nutrient diffusion coefficient	m^2/sec
D_n^*	Non-linear cell diffusion coefficient	m^2/sec
D_s	Ratio of nutrient diffusion to advection	-
$f^*(x^*)$	Inlet velocity	m/sec
$f(x)$	Dimensionless inlet velocity	-
f_{max}^*	Maximum value of prescribed inlet velocity	m/sec
G_s^*	Net nutrient consumption rate	$moles/sec.m^3$
$g^*(x^*)$	Outlet velocity	m/sec
$g(x)$	Dimensionless outlet velocity	-
g^*	Constant in stress functions	$m.sec^2/kg$
g	Dimensionless constant in stress functions	-
H	Heaviside Step function	-
k_1	Constant in stress functions	-
$k^*(x^*, y^*)$	Permeability	m^2
$k(x, y)$	Dimensionless permeability	-
$k_0^*(x^*, y^*)$	Initial permeability	m^2
$k_0(x, y)$	Dimensionless initial permeability	-
k_c^*	Typical permeability	m^2
L^*	Dimensional length	m
L	Dimensionless length	-
$N^*(x^*, y^*)$	Cell density	$cells/m^3$
$N(x, y)$	Dimensionless cell density	-
N_{max}^*	Maximum carrying capacity	$cells/m^3$
$N_{init}^*(x^*, y^*)$	Initial cell density	$cells/m^3$
$N_{init}(x, y)$	Dimensionless Initial cell density	-

$\hat{\mathbf{n}}$	Outward unit normal vector	-
p^*	Fluid pressure	$kg/m.sec^2$
p	Dimensionless fluid pressure	-
p_0^*	Pressure at top boundary	$kg/m.sec^2$
p_1^*	Pressure at bottom boundary	$kg/m.sec^2$
Q_n^*	Net cell growth rate	$cells/m^3.sec$
r^*	radial coordinate	m
R_s	Ratio of nutrient consumption to advection	-
S^*	Nutrient concentration	$moles/m^3$
S	Dimensionless nutrient concentration	-
S_0^*	Initial nutrient concentration	$moles/m^3$
t^*	Dimensional time	sec
T^*	Typical time scale	sec
t	Dimensionless time	-
t_{update}	Update time for cell density on porosity	-
Δt	Time step size for cell equation	-
\mathbf{u}^*	Darcy's velocity	m/sec
\mathbf{u}	Dimensionless Darcy's velocity	-
\mathbf{u}_r^*	Rescaled velocity	m/sec
\mathbf{u}_r	Dimensionless rescaled velocity	-
U_c^*	Pump velocity	m/sec
U_p^*	Mean pore velocity	m/sec
\mathbf{v}_p^*	Pore velocity	m/sec
u_d^*	Flow rate at surface $y^* = d^*$	m/sec
u_d	Dimensionless flow rate at surface $y = d$	-
v^*	Velocity of growth front	m/sec
V_{cell}^*	Single cell volume	$m^3/cell$
x^*	Dimensional spatial coordinate	m
y^*	Dimensional spatial coordinate	m
x	Dimensionless spatial coordinate	-
y	Dimensionless spatial coordinate	-

COMSOL modelling guide

B.1 Introduction

Mathematical modelling of tissue engineering, an important and new area of research which aims to replace the damaged or diseased body parts due to trauma, accident or age related degeneration. Certain tissues or organs cannot heal satisfactorily by themselves and require treatments to reinstate their functions. In some of the cases non of the available treatments can restore the functions of affected tissue or organ. Tissue engineering can be considered as alternative to organ transplantation. In the present study we have developed a mathematical model that includes the key features of tissue engineering, where cells are grown outside the body in the laboratory. The model includes the growth of cells and transport of nutrients through the porous material. Cells are seeded in a porous scaffold and fluid delivers the nutrients to the cells for their growth. The efficiency of cell growth can be determined by delicate interplay of scaffold design, fluid flow, nutrient convection and cell growth dynamics. The model consist of three coupled equations describing fluid flow, nutrient transport and cell growth in a porous scaffold. This model investigates the fluid velocity through the porous material, concentration of nutrients and cell density at the different spatial points. In the following section we will describe how the COMSOL Multiphysics is implemented on the model using the Graphical User Interface(GUI).

B.2 Modelling using graphical user interface (GUI)

B.2.1 Model Navigator

1. Start COMSOL Multiphysics.

2. In the **Model Navigator**, select **2D** in the **Space Dimension** list.
3. Select **COMSOL Multiphysics > PDE Modes > Classical PDEs > Poisson's Equation** in the list of application modes.
4. Enter **P** in the **Dependent variables** edit field.
5. Select **Multiphysics** and then click **Add** button.
6. Select **COMSOL Multiphysics > Convection and Diffusion > Convection and Diffusion > Steady-state analysis** in the list of application modes.
7. Enter **S** in the **Dependent variables** edit field and click **Add** button.
8. Select **COMSOL Multiphysics > PDE Modes > Classical PDEs > Heat equation** in the list of application modes.
9. Enter **N** in the **Dependent variables** edit field and click **Add** button.
10. Click **OK**.

B.2.2 Options and Settings

Constants

1. From the **Option** menu, choose **Constants**.
2. Enter the following constant table and click **OK**.

Name	ρ	D_s	R_s	β	γ	δ	g	σ_{c1}	σ_{c2}	k_1
Expression	1	6×10^{-6}	1.488	13.2173	2	0.1397	60	3	15	5

Expressions

1. From the **Option** menu, point to **Expressions** and click **Scalar Expressions**.
2. Enter the following list of expressions and click **OK**.

Name	Expression
ϕ_0	Depending on initial porosity
ϕ	$\phi_0 \exp\left(\frac{-\rho N}{\phi_0}\right)$
k	ϕ^3
σ	$\frac{\sqrt{k^2(P_x^2 + P_y^2)}}{u_d}$
F_s	$1 + \frac{k_1 - 1}{2}(1 + \tanh(g(\sigma - \sigma_{c1}))) - \frac{k_1 - 1}{2}(1 + \tanh(g(\sigma - \sigma_{c2})))$
F_n	$1 + \frac{k_1 - 1}{2}(1 + \tanh(g(\sigma - \sigma_{c1}))) - \frac{k_1}{2}(1 + \tanh(g(\sigma - \sigma_{c2})))$
D	$\exp(\gamma(N - 1))$
N_{init}	Depending on initial seeding

Axis setting

1. From the **Option** menu, select **Axis/Grid setting**.
2. On the **Axis** page deselect **Axis equal**.
3. Enter limits for x and y axis *i.e* $x_{min} = -1$, $x_{max} = 1$, $y_{min} = -1$, $y_{max} = 1$ and click **OK**.

B.2.3 Geometry Modelling

1. Click corner aligned rectangle button at the top of draw toolbar.
2. To describe the rectangle's corners, click the left mouse button and drag the cursor from (-1,-1) to (1,1).

B.2.4 Coupling variables

We are modelling a coupled system of fluid flow, nutrient concentration and cell growth. Nutrients are delivered to the cells by advection and diffusion. So with the increase in cell density the porosity and permeability of the porous material decreases as a result fluid velocity through the porous material decreases, which affects the delivery of nutrients to the cells hence cell growth is affected. So to keep the flow rate constant through the porous material we rescale the fluid velocity with the increase in cell density. We calculate the mean velocity u_d at the surface $y = d$ and divide the Darcy's velocity \mathbf{u} obtained from the flow equation by the mean velocity u_d . So we calculate the mean velocity u_d at $y = d$.

1. On the **Option** menu, point to **Integration Coupling Variable** and then click **Boundary Variables**.
2. Select Boundary 3 and enter the variable **name** u_d and **expression** kP_y .
3. Deselect **Global Destination**.
4. Click **Destination** tab.
5. On **Destination** page, select **geom1** in the list of **Geometry** and **subdomain** in the list of **level**.
6. Select subdomain 1.
7. Select **Use selected subdomain as destination** and click **OK**.

B.2.5 Poisson's Equation

Subdomain setting

1. From **Multiphysic** menu choose **Poisson's Equation(Poeq)**.
2. From **Physics** menu point to **Subdomain setting**.
3. On the **Subdomain** page select the menu **Coefficients** and enter k and 0 in c and f edit field respectively.
4. The **init** tab should retain the value zero.

Boundary conditions

1. From the **Physics** menu, choose **Boundary settings**.
2. Specify the boundary conditions according to following table.

Boundary	1,4	2	3
Type	Neumann condition	Dirichlet condition	Dirichlet condition
Equation	$n.(c\nabla p) + q.P = g$	$h.P = r$	$h.P = r$
q	0	-	-
g	0	-	-
h	-	1	1
r	-	0	1

B.2.6 Convection and Diffusion

Subdomain setting

1. From the **Multiphysics** menu, choose **Convection and Diffusion(cd)**.
2. From the **Physics** menu, choose **Subdomain settings**.
3. On the **Subdomain** page select the menu **Coefficients** and enter the following coefficient values,

Coefficient	Value
D	$u_d D_s$
R	$u_d R_s F_s S N$
u	$-k P_x$
v	$-k P_y$

4. The **init** tab should retain the value zero.

Boundary conditions

1. From the **Physics** menu, choose **Boundary settings**.
2. Specify the boundary conditions according to following table.

Boundary	1,4	2	3
Type	Flux	Convective Flux	Concentration
Equation	$n \cdot (D \nabla S - S \mathbf{u}) = N_0$	$n \cdot D \nabla S = 0$	$S = S_0$
S_0	-	-	1
N_0	0	-	-

B.2.7 Heat Equation(hteq)

Subdomain setting

1. From the **Multiphysics** menu, choose **Heat Equation(hteq)**.
2. From the **Physics** menu, choose **Subdomain settings**.

3. On the **Subdomain** page select the menu **Coefficients** and enter the following coefficient values,

Coefficient	Value/Expression
d_q	1
c	D
f	$\beta F_n S N (1 - N)$

4. click **init** tab.
5. Enter initial value N_{init} in the edit field for $N(t_0)$.
6. Click **OK**.

Boundary conditions

1. From the **Physics** menu, choose **Boundary settings**.
2. Press **Ctrl + A** to select all the boundaries.
3. Select **Neumann boundary condition** and enter $q = 0$ and $g = 0$ in the edit field.

B.2.8 Mesh Generation

1. From the **Mesh** menu, choose **Initialize Mesh**.
2. To refine mesh again from the **Mesh** menu, choose **Refine Mesh**.

B.2.9 Computing the solution

1. From the **Solve** menu, choose **Solver Parameters** button.
2. On **Solver Parameters** page click **General** tab, then select **Solver: Time dependent**, **Times: 0 : 0.000001 : 0.00001** and **Linear system solver, Direct(UMFPACK)**.
3. Click **OK**.
4. From the **Solve** menu, choose **Solver Manager** button.
5. Go to **Initial Value** tab.
6. On the **Initial value** page, select **Initial value expression** and **use setting from initial value frame**.

7. Go to **Solve for** tab and highlight **Heat equation** and click **Solve**.
This would give you the initial cell density N .
8. To calculate the total initial cell density in the entire domain on the **Postprocessing** menu click **Subdomain integration** button. On **Subdomain integration** page select subdomain 1 and predefined quantities N . This would give the total initial cell density in the whole domain.
9. On the **Solver Parameters** page select **Solver: Stationary non-linear** and click **OK**.
10. On the **Solver Manager** page go to **Initial Value** tab.
11. On the **Initial value** page, select **Current solution** and **use setting from initial value frame**.
12. Go to **Solve for** tab and highlight **Poisson's Equation** and click **Solve**.
13. Go to **Script** tab and click **Add Current Solver Settings**.
14. Again click **Solve for** tab and highlight **Convection and Diffusion** and click **Solve**.
15. On the **Script** page click **Add Current Solver Settings**.
16. On the **Solver Parameters** page click **General** tab and select **Times: 0 : 0.001 : 0.01** and click **OK**.
17. On the **Solver manager** page click **Solve for** and highlight **Heat equation** and click **Solve**.
18. Go to **Script** tab and click **Add Current Solver Settings**.
19. On the **script** page place **For i=1:10** at the beginning of the solver command and **end** at its end.
20. Select **Solve using a script** check box.

B.2.10 Post processing and visualization

1. Click **Plot parameters** button and select the **Surface** tab.
2. On the **Surface** tab, Select **N(h_{teq})** from the **Predefined quantities** list and click **OK**.

3. Click **Plot parameters** button and select the **Contour** tab.
4. On the **Contour** tab, select **Concentration, S(cd)** from the **Predefined quantities** and enter **10** in the **levels** edit field and click **OK**.
5. Click **Plot parameters** button and select the **Arrow** tab.
6. On the **Arrow** tab, enter kP_x and kP_y in the **x-component** and **y-component** edit field and click **OK**.

B.2.11 Exporting data to COMSOL script or MATLAB

- Select the menu item **File > Save**.
- On the **Save As** page, choose **file name** and **Save in** folder then choose file type **M-file(*.m)** from list of file types.
- To access MATLAB code start **COMSOL Multiphysics with MATLAB** and open **M-file(*.m)**.
- From MATLAB command line, use functions **Postinterp** to compute the numerical values for any expression *e.g* if we want to find cell density N at each mesh point (x, y) after each time step we use $Celldensity = postinterp(fem0, 'N', [x; y]);$

B.2.12 Data Extraction in MATLAB

1. To find the coordinate data of mesh points use command **Points=fem.mesh.p**.
2. To find the x and y coordinates of data points use command **x=Points(1,:)** and **x=Points(2,:)** respectively.
3. To find the values of various variables *e.g* P, S, N, P_x, P_y etc at each mesh point use **Postinterp** command. For example to find the value of pressure at each mesh point we use **Pressure=postinterp(fem,'P',[x,y])**.
4. To save the data after each time unit define a variable **temp= zeros(length(x), t_1)**, where t_1 is the length of loop. If we want to save pressure P after each time step we use command **temp(:,i)=Pressure**. We can repeat this process for each variable.

5. For time dependent variable each time t is subdivided in internal time stepping. To find the data of such variable in the internal time stepping we use the command

```
[t,temp1]=postinterp(fem,'t','N',[x,y],'solnum',1:length(fem.sol.tlist)).
```

Finite element method(FEM)

C.1 Basic concepts

The finite element method is a tool to solve boundary or initial value problems and integral equations. The solution of some ordinary and partial differential equations varies rapidly in some regions and less rapidly in others. In such cases finite difference methods become more cumbersome and inaccurate if the mesh size is not constant. The Finite element method is a good choice for solving the partial differential equations when mesh size is not constant or when solution lacks smoothness.

The approximate solution of a partial differential equation by using finite element problem can be found in four steps.

1. The idea of finite element method is based on the dividing the complicated object into small pieces. First step in the finite element method is to divide the domain of interest into large number of discrete elements. The elements may be 1-D, 2-D (triangular or quadrilateral) or 3-D (tetrahedral, hexahedral). The elements do not have to have the same size. The vertices of the elements are called nodes. The nodes are called the boundary nodes if they lie on the boundary of the domain and interior node otherwise. An element is a boundary element if it possesses two or more boundary nodes and interior element otherwise. The nodes can be numbered locally 1, 2 and 3 it is conventional to use these numbers anticlockwise. Every node can be given a global number and also each element can be assign a number.
2. The next step is to approximate the unknown function (say) $P(x, y)$ by some piecewise polynomial function of order m , which has a continuous derivative of order $(m - 1)$ at each mesh element, that are in general not equal sized. Let $\beta_j(x, y)$

represents a polynomial of order m . The unknown function $P(x, y)$ can be represented by the linear combination of $\beta_j(x, y)$.

$$P(x, y) = \sum_{j=0}^n a_j \beta_j(x, y).$$

The function $\beta_j(x, y)$ has various names in the finite element literature including interpolation functions, shape functions or basis functions. Each base function has a property that it is 1 at one node and zero at all the other nodes *i.e*

$$\beta_j(x_i, y_i) = \begin{cases} 1, & i = j \\ 0, & i \neq j, \end{cases}$$

from which it follows that $a_j = P_j$; this means that the coefficient a_j has exactly the value of $P(x, y)$ at the nodal point (x_i, y_i) , so

$$P(x, y) = \sum_{j=0}^n P_j \beta_j(x, y)$$

3. The next task is to find a variational form for the given problem. Let us consider a general elliptic partial differential equation of the form

$$-\nabla \cdot (a \nabla P) + bP = f(x, y) \quad \text{in } R, \quad (\text{C.1.1})$$

where R is the region in a plane. a, b, f and unknown solution P may be functions of x and y throughout the domain R . The boundary conditions may be Neumann or Dirichlet

$$\vec{n} \cdot a \nabla P + m(x, y)P = h(x, y), \quad (\text{C.1.2})$$

where \vec{n} is outward unit normal. $m(x, y)$ and $h(x, y)$ are the functions defined on the boundary ∂R .

Multiplying equation (C.1.1) by $P(x, y)$ and integrating over the entire domain R we get

$$\int_R [-\nabla \cdot (a \nabla P)P + bP^2] dx dy = \int_R f(x, y)P dx dy$$

Integrate by parts (*i.e* use Green's formula) to obtain

$$\int_R [(a\nabla P) \cdot \nabla P + bP^2] dx dy - \int_{\partial R} [\vec{n} \cdot (a\nabla P)] P ds = \int_R f(x, y) P dx dy.$$

The boundary integral can be replaced by the boundary condition

$$\begin{aligned} \int_R [a(\nabla P)^2 + bP^2] dx dy - \int_{\partial R} [\{h(x, y) - m(x, y)P\}P] ds \\ = \int_R f(x, y) P dx dy \end{aligned} \quad (\text{C.1.3})$$

Equation (C.1.3) is called the variational or weak form of the differential equation. The solution of the differential equation is also the solution of variational form. Let us suppose that

$$\begin{aligned} J(P) &= \int_R [a(\nabla P)^2 + bP^2 - f(x, y)P] dx dy \\ &- \int_{\partial R} [\{h(x, y) - m(x, y)P\}P] ds \end{aligned} \quad (\text{C.1.4})$$

4. In the step four the contribution from each element is assembled to give a large system of equations for the solution. Finally $J(P)$ is minimized with respect to unknown P at all internal and boundary nodes gives a large system of equations which can be solved by any iterative method.

To take a practical approach we implement the four steps of the finite element method on the following example.

C.2 Worked Example

Solve Laplace equation $\nabla^2 P = 0$ in a square region R , given by $-1 \leq x \leq 1$ and $-1 \leq y \leq 1$. Boundary conditions are

$$\begin{aligned} \frac{\partial P}{\partial x} &= 0 \quad \text{at } x = \pm 1, \quad -1 \leq y \leq 1, \\ \frac{\partial P}{\partial y} &= 1 \quad \text{at } y = 1, \quad -1 \leq x \leq 1, \\ \frac{\partial P}{\partial y} &= 1 \quad \text{at } y = -1, \quad -1 \leq x \leq 1. \end{aligned}$$

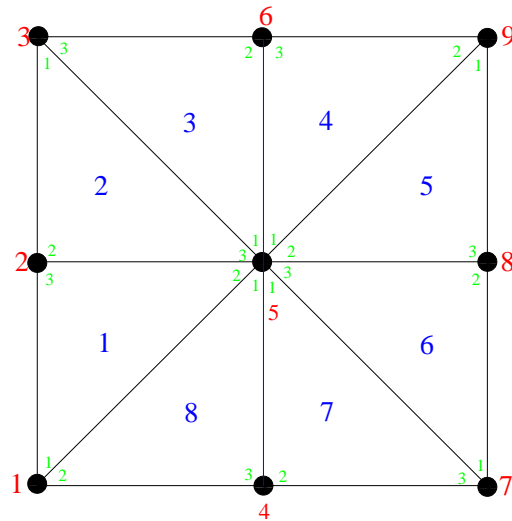


Figure C.1: Discretization of finite element domain

Step 1

Figure (C.1) represents a square region R , $-1 \leq x \leq 1$ and $-1 \leq y \leq 1$. The first step in FEM is to divide the region R into small triangular or rectangular elements. In this case the region R is divided into 8 triangular elements. The local and global node numbers are represented by green and red colors respectively. The element number is represented by blue color.

Step 2

For the present problem we define P over the triangular element in terms of P values at three nodes. Hence a linear form for P will have correct number of degrees of freedom.

$$\begin{aligned}
 P(x, y) &= \alpha_1 + \alpha_2 x + \alpha_3 y \\
 &= \begin{bmatrix} 1 & x & y \end{bmatrix} \begin{bmatrix} \alpha_1 \\ \alpha_2 \\ \alpha_3 \end{bmatrix}
 \end{aligned}$$

We can calculate the three constants by solving the set of three simultaneous equations at each node of the element.

$$P_1 = \alpha_1 + \alpha_2 x_1 + \alpha_3 y_1$$

$$P_2 = \alpha_1 + \alpha_2 x_2 + \alpha_3 y_2$$

$$P_3 = \alpha_1 + \alpha_2 x_3 + \alpha_3 y_3$$

The solution of these equations gives the values of α_1 , α_2 and α_3 in terms of nodal values P_1 , P_2 and P_3 . So we get

$$\begin{aligned} P(x, y) &= \frac{1}{2\Delta} [(a_1 + b_1 x + c_1 y)P_1 + (a_2 + b_2 x + c_2 y)P_2 + (a_3 + b_3 x + c_3 y)P_3] \\ &= \sum_{j=1}^3 P_j \beta_j(x, y) \end{aligned}$$

where

$$\beta_j = \frac{(a_j + b_j x + c_j y)}{2\Delta}, \quad (\text{C.2.1})$$

where

$$\begin{aligned} a_1 &= x_2 y_3 - x_3 y_2, & b_1 &= y_2 - y_3, & c_1 &= x_3 - x_2 \\ a_2 &= x_3 y_1 - x_1 y_3, & b_2 &= y_3 - y_1, & c_2 &= x_1 - x_3 \\ a_3 &= x_1 y_2 - x_2 y_1, & b_3 &= y_1 - y_2, & c_3 &= x_2 - x_1 \end{aligned} \quad (\text{C.2.2})$$

and Δ is area of triangle given by

$$\Delta = \frac{1}{2} \begin{vmatrix} 1 & 1 & 1 \\ x_1 & x_2 & x_3 \\ y_1 & y_2 & y_3 \end{vmatrix}$$

The function β_j defined by equation (C.2.1) is a linear function and its value is 1 at the node j and zero otherwise.

Step 3

For the present problem $a = 1$, $b = 0$, $f = 0$ and $m = 0$ then variational form (C.1.4) reduces to

$$J(P) = \int_R (\nabla P)^2 dx dy - \int_{\partial R} h(x, y) P ds \quad (\text{C.2.3})$$

For the i th element the variational form (C.2.3) can then be written as

$$J^{(i)}(P) = \int_{R^{(i)}} (\nabla P^{(i)})^2 dx dy - \int_{\partial R^{(i)}} P^{(i)} h(x, y) ds, \quad (\text{C.2.4})$$

where

$$P^{(i)}(x, y) = \sum_{j=1}^k P_j^{(i)} \beta_j(x, y) \quad (\text{C.2.5})$$

$$\frac{\partial P^{(i)}(x, y)}{\partial x} = \sum_{j=1}^k P_j^{(i)} \frac{\partial \beta_j(x, y)}{\partial x} \quad (\text{C.2.6})$$

$$\frac{\partial P^{(i)}(x, y)}{\partial y} = \sum_{j=1}^k P_j^{(i)} \frac{\partial \beta_j(x, y)}{\partial y} \quad (\text{C.2.7})$$

Equation (C.2.6) can be written in matrix form as

$$\begin{aligned} \frac{\partial P^{(i)}}{\partial x} &= \begin{bmatrix} P_1^{(i)} & P_2^{(i)} & \dots & P_j^{(i)} \end{bmatrix} \begin{bmatrix} \frac{\partial \beta_1}{\partial x} \\ \frac{\partial \beta_2}{\partial x} \\ \vdots \\ \frac{\partial \beta_j}{\partial x} \end{bmatrix} \\ &= \begin{bmatrix} \frac{\partial \beta_1}{\partial x} & \frac{\partial \beta_2}{\partial x} & \dots & \frac{\partial \beta_j}{\partial x} \end{bmatrix} \begin{bmatrix} P_1^{(i)} \\ P_2^{(i)} \\ \vdots \\ P_j^{(i)} \end{bmatrix} \end{aligned} \quad (\text{C.2.8})$$

$$\left(\frac{\partial P^{(i)}}{\partial x} \right)^2 = (P^{(i)})^T M_{jk}^{(i)} P^{(i)} \quad (\text{C.2.9})$$

where

$$P^{(i)} = \begin{bmatrix} P_1^{(i)} & P_2^{(i)} & \dots & P_j^{(i)} \end{bmatrix}^T \quad (\text{C.2.10})$$

$$M_{jk}^{(i)} = \frac{\partial \beta_j}{\partial x} \frac{\partial \beta_k}{\partial x}. \quad (\text{C.2.11})$$

Similarly

$$\left(\frac{\partial P^{(i)}}{\partial y}\right)^2 = (P^{(i)})^T N_{jk}^{(i)} P^{(i)} \quad (\text{C.2.12})$$

where

$$N_{jk}^{(i)} = \frac{\partial \beta_j}{\partial y} \frac{\partial \beta_k}{\partial y}. \quad (\text{C.2.13})$$

Substituting values from equation (C.2.9), (C.2.12) and (C.2.10) into equation (C.2.4) we get

$$\begin{aligned} J^{(i)} &= \int_{R^{(i)}} (P^{(i)})^T [M^{(i)} + N^{(i)}] P^{(i)} dx dy - \int_{\partial R} h(x, y) P_j^{(i)} \beta_j(x, y) \\ &= (P^{(i)})^T K^{(i)} P^{(i)} - (P^{(i)})^T Q^{(i)} \end{aligned} \quad (\text{C.2.14})$$

where

$$\begin{aligned} K^{(i)} &= \int_{R^{(i)}} [M^{(i)} + N^{(i)}] dx dy \\ &= \int_{R^{(i)}} \left[\frac{\partial \beta_j}{\partial x} \frac{\partial \beta_k}{\partial x} + \frac{\partial \beta_j}{\partial y} \frac{\partial \beta_k}{\partial y} \right] dx dy \end{aligned} \quad (\text{C.2.15})$$

$$Q^{(i)} = \int_{\partial R} h(x, y) \beta_j(x, y) ds. \quad (\text{C.2.16})$$

$K^{(i)}$ is called element stiffness matrix, $P^{(i)}$ is called element generalized coordinate vector and $Q^{(i)}$ is called generalized force vector. The element stiffness matrix has two important properties

1. The stiffness matrix is symmetric, i.e. $K_{jk}^{(i)} = K_{kj}^{(i)}$,
2. The stiffness matrix is positive definite i.e. $(P^{(i)})^T K^{(i)} P^{(i)} > 0$ for any non zero vector $P^{(i)}$.

Substituting the values of basis function from equation (C.2.6) into equation (C.2.15) we get

$$\frac{\partial \beta_j}{\partial x} = \frac{b_j}{2\Delta}, \quad \frac{\partial \beta_j}{\partial y} = \frac{c_j}{2\Delta}. \quad (\text{C.2.17})$$

where $j, k = 1, 2, 3$. The stiffness matrix (C.2.15) is then written as

$$K^{(i)} = \frac{1}{4\Delta} \begin{bmatrix} b_1^2 + c_1^2 & b_1b_2 + c_1c_2 & b_1b_3 + c_1c_3 \\ b_2b_1 + c_2c_1 & b_2^2 + c_2^2 & b_2b_3 + c_2c_3 \\ b_3b_1 + c_3c_1 & b_3b_2 + c_3c_2 & b_3^2 + c_3^2 \end{bmatrix} \quad (\text{C.2.18})$$

From Figure (C.1) substitute the coordinates of nodes of element 1 in equation (C.2.2) to find a's and b's

$$\begin{aligned} a_1 &= 0, & b_1 &= 0, & c_1 &= -1 \\ a_2 &= 1, & b_2 &= 1, & c_2 &= 0 \\ a_3 &= 0, & b_3 &= -1, & c_3 &= 1 \quad \text{and} \quad \Delta = 0.5 \end{aligned}$$

Hence stiffness matrix (C.2.18) becomes

$$K^{(1)} = \frac{1}{2} \begin{bmatrix} 1 & 0 & -1 \\ 0 & 1 & -1 \\ -1 & -1 & 2 \end{bmatrix} = \begin{bmatrix} k_{11} & k_{15} & k_{12} \\ k_{51} & k_{55} & k_{52} \\ k_{53} & k_{52} & k_{22} \end{bmatrix} \quad (\text{C.2.19})$$

Similarly stiffness matrix for element 2 is

$$K^{(2)} = \frac{1}{2} \begin{bmatrix} 1 & -1 & 0 \\ -1 & 2 & -1 \\ 0 & -1 & 1 \end{bmatrix} = \begin{bmatrix} k_{33} & k_{32} & k_{35} \\ k_{23} & k_{22} & k_{25} \\ k_{53} & k_{52} & k_{55} \end{bmatrix} \quad (\text{C.2.20})$$

The elements 3,6,7 are congruent to element 2 and elements 1,4,5,8 are congruent to mirror reflection of element 2. So

$$K^{(1)} = \frac{1}{2} \begin{bmatrix} 1 & -1 & 0 & 0 & 0 & 0 & 0 & 0 & 0 \\ -1 & 2 & 0 & 0 & -1 & 0 & 0 & 0 & 0 \\ 0 & 0 & 0 & 0 & 0 & 0 & 0 & 0 & 0 \\ 0 & 0 & 0 & 0 & 0 & 0 & 0 & 0 & 0 \\ 0 & -1 & 0 & 0 & 1 & 0 & 0 & 0 & 0 \\ 0 & 0 & 0 & 0 & 0 & 0 & 0 & 0 & 0 \\ 0 & 0 & 0 & 0 & 0 & 0 & 0 & 0 & 0 \\ 0 & 0 & 0 & 0 & 0 & 0 & 0 & 0 & 0 \\ 0 & 0 & 0 & 0 & 0 & 0 & 0 & 0 & 0 \end{bmatrix} \quad (C.2.21)$$

In the same way we can calculate the stiffness matrix for each element. Next we need to evaluate the force vector for each element.

$$Q^{(1)} = \int_{-1}^0 h(x,y)\beta_j(x,y)dy = 0, \quad h(x,y) = 0 \quad (C.2.22)$$

$$Q^{(2)} = Q^{(5)} = Q^{(6)} = 0 \quad (C.2.23)$$

Similarly

$$Q^{(3)} = \int_{-1}^0 h(x,y)\beta_j(x,y)dx = \int_{-1}^0 (a_j + b_jx + c_j)dx \quad (C.2.24)$$

$$Q_j^{(3)} = a_j - \frac{1}{2}b_j + c_j \quad (C.2.25)$$

$$Q_1^{(3)} = 0, \quad Q_2^{(3)} = \frac{1}{2}, \quad Q_3^{(3)} = \frac{1}{2} \quad (C.2.26)$$

In the same way we can calculate the force vectors for remaining elements.

Step 4

Next step is to assemble the contribution from each element to produce a large system of equations.

$$\begin{aligned} J &= \sum_{i=1}^9 J^{(i)} \\ &= \sum_{i=1}^9 [(P^{(i)})^T K^{(i)} P^{(i)} - (P^{(i)})^T Q^{(i)}] \end{aligned}$$

So

$$\begin{aligned}
 K &= K^{(1)} + K^{(2)} + K^{(3)} + K^{(4)} + K^{(5)} + K^{(6)} + K^{(7)} + K^{(8)} + K^{(9)} \\
 &= \frac{1}{2} \begin{bmatrix} 2 & -1 & 0 & -1 & 0 & 0 & 0 & 0 & 0 \\ -1 & 4 & -1 & 0 & -2 & 0 & 0 & 0 & 0 \\ 0 & -1 & 2 & 0 & 0 & -1 & 0 & 0 & 0 \\ -1 & 0 & 0 & 4 & -2 & 0 & -1 & 0 & 0 \\ 0 & -2 & 0 & -2 & 8 & -2 & 0 & -2 & 0 \\ 0 & 0 & -1 & 0 & -2 & 4 & 0 & 0 & -1 \\ 0 & 0 & 0 & -1 & 0 & 0 & 2 & -1 & 0 \\ 0 & 0 & 0 & 0 & -2 & 0 & -1 & 4 & -1 \\ 0 & 0 & 0 & 0 & 0 & -1 & 0 & -1 & 2 \end{bmatrix} \quad (C.2.27)
 \end{aligned}$$

Similarly force vector Q is given by

$$Q = \begin{pmatrix} -1 \\ 0 \\ 1 \\ -2 \\ 0 \\ 2 \\ -1 \\ 0 \\ 1 \end{pmatrix} \quad (C.2.28)$$

Once the stiffness matrix J and force vector Q have been assembled, the remaining problem is to find the minimum of the function

$$J = P^T K P - P^T Q \quad (C.2.29)$$

In some cases equation (C.2.29) is minimized directly using a suitable optimization technique, but it is convenient to equate the partial derivatives of J with respect to generalized coordinate to zero which is also the analytic condition for minimum. By using the later technique we get a system of equations

$$KP = Q \quad (C.2.30)$$

This system of equations can be solved by any iterative technique or by using MATLAB software. So the value of unknown function P at each grid point is given by

$$P = \begin{bmatrix} -1 & -1 & -1 \\ 0 & 0 & 0 \\ 1 & 1 & 1 \end{bmatrix} \quad (\text{C.2.31})$$

Hence we can calculate the velocity at each grid point by using $\mathbf{u} = -\nabla P$,

$$u = \begin{bmatrix} 0 & 0 & 0 \\ 0 & 0 & 0 \\ 0 & 0 & 0 \end{bmatrix}, \quad (\text{C.2.32})$$

and

$$v = \begin{bmatrix} -1 & -1 & -1 \\ -1 & -1 & -1 \\ -1 & -1 & -1 \end{bmatrix} \quad (\text{C.2.33})$$

In Figure (C.2) arrow represent the velocity and solid lines represent the pressure contours. It is evident from the Figure (C.2) that pressure is a linear function of y only and the velocity \mathbf{u} is uniform every where.

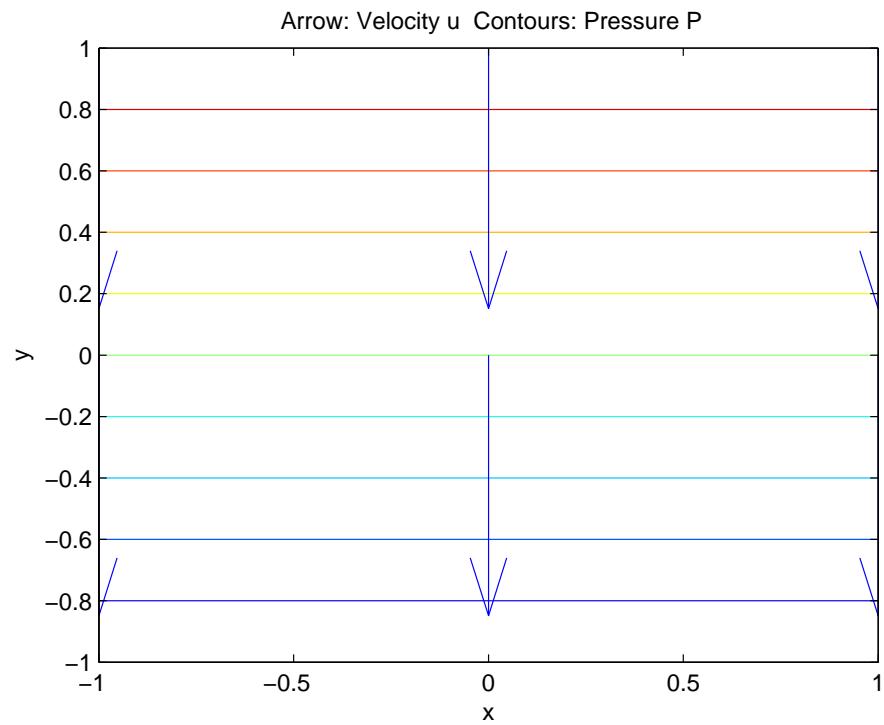


Figure C.2: Finite element solution of flow field and pressure contours

Specific rate equations for microbial growth

Several models have been proposed for predicting the microbial growth as a function of the concentration of single rate limiting substrate. The most widely used models are Monod, Teissier, Moser, Contois and Michaelis Menton. Each model have been used successfully for certain organisms under certain conditions.

D.1 Michaelis-Menton model

The Michaelis-Menton model relates the rate of substrate conversion to the concentration of substrate. It is relevant to situations where very simple kinetics can be assumed, *i.e* there is no contact inhibition.

$$\lambda = \frac{\lambda_{max}C_m}{K_s + C_m},$$

where

λ = Growth rate,

λ_{max} = Maximum growth rate,

C_m = Substrate concentration,

K_m = Michaelis-Menton constant or half saturation constant and have same units as C_m .

More complex models exist for the cases where the assumptions of Michaelis-Menton kinetics are no longer appropriate.

D.2 Moser's Model

Moser's model relates the specific growth rate to the concentration of limiting substrate. Mathematically

$$\lambda = \frac{\lambda_{max} C_m^n}{K_s + C_m^n},$$

where $n \geq 1$, n is the Moser parameter and it represents the ability of cell to absorb the substrate either for metabolic processes or storage and

$$\begin{aligned}\lambda &= \text{Specific growth rate,} \\ \lambda_{max} &= \text{Maximum growth rate,} \\ C_m &= \text{Substrate concentration,} \\ K_s &= \text{Monod's constant or half saturation constant.}\end{aligned}$$

It is an empirical equation and has no mechanistic basis. The equation is only valid for exponential growth.

D.3 Monod's Model

Monod's model is the special form of the Moser's model for $n = 1$

$$\lambda = \frac{\lambda_{max} C_m}{K_s + C_m},$$

D.4 Tiesser's Model

$$\lambda = \lambda_{max}(1 - \exp(-C_m/K_s))$$

D.5 Contois Model

In this growth kinetics rate of growth is dependent not only limiting substrate but also the amount of cells. This type of growth represents the contact inhibition due to over

population of the system. Contois growth kinetics is given as

$$\lambda = \frac{\lambda_{max}C_m}{K_cNV_{cell}N_c + C_m},$$

where

λ = Specific Growth rate,

λ_{max} = Maximum growth rate,

C_m = Substrate concentration,

K_s = Contois parameter,

N = Cell density,

N_c = Single cell density,

V_{cell} = Single cell volume.

Bibliography

- Abbott, A. (2003). Cell culture: Biology's new dimension. *Nature a-z index*, 424(6951):870–872.
- Abercrombie, M. (1970). Contact inhibition in tissue culture. *In Vitro Cellular & Developmental Biology-Plant*, 6(2):128–142.
- Ablowitz, M. and Zeppetella, A. (1979). Explicit solutions of Fisher's equation for a special wave speed. *Bulletin of Mathematical Biology*, 41(6):835–840.
- Akhyari, P., Fedak, P., Weisel, R., Lee, T., Verma, S., Mickle, D., and Li, R. (2002). Mechanical stretch regimen enhances the formation of bioengineered autologous cardiac muscle grafts. *Circulation*, 106(90121):137–142.
- Antonov, E., Bagratashvili, V., Whitaker, M., Barry, J., Shakesheff, K., Konovalov, A., Popov, V., and Howdle, S. (2005). Three-dimensional bioactive and biodegradable scaffolds fabricated by surface-selective laser sintering. *Advanced Materials*, 17(3):327–330.
- Armstrong, N., Painter, K., and Sherratt, J. (2006). A continuum approach to modelling cell–cell adhesion. *Journal of Theoretical Biology*, 243(1):98–113.
- Atala, A., Bauer, S., Soker, S., Yoo, J., and Retik, A. (2006). Tissue-engineered autologous bladders for patients needing cystoplasty. *The Lancet*, 367(9518):1241–1246.
- Babensee, J., McIntire, L., and Mikos, A. (2000). Growth Factor Delivery for Tissue Engineering. *Pharmaceutical Research*, 17(5):497–504.
- Bakker, A., Klein-Nulend, J., and Burger, E. (2004). Shear stress inhibits while disuse promotes osteocyte apoptosis. *Biochemical and Biophysical Research Communications*, 320(4):1163–1168.
- Batchelor, G. (2000). *An introduction to fluid dynamics*. Cambridge University Press.

- Bear, J. (1988). *Dynamics of fluids in porous media*. Dover Publications.
- Bear, J. and Buchlin, J. (1991). *Modelling and applications of transport phenomena in porous media*. Kluwer Academic Publisher.
- Bianco, P., Robey, P., Regeneration, B., and Cells, S. (2001). Stem cells in tissue engineering. *Nature*, 414(6859):118–121.
- Boccaccini, A. and Blaker, J. (2005). Bioactive composite materials for tissue engineering scaffolds. *Expert Review of Medical Devices*, 2(3):303–317.
- Boutilier, R. and St-Pierre, J. (2000). Surviving hypoxia without really dying. *Comparative Biochemistry and Physiology. Part A, Molecular & Integrative Physiology*, 126(4):481–490.
- Brinkman, H. (1949). A calculation of the viscous force exerted by a flowing fluid on a dense swarm of particles. *Applied Scientific Research*, 1(1):27–34.
- Britton, N. (2003). *Essential mathematical biology*. Springer Undergraduate Mathematics Series.
- Bueno, E., Laevsky, G., and Barabino, G. (2007). Enhancing cell seeding of scaffolds in tissue engineering through manipulation of hydrodynamic parameters. *Journal of Biotechnology*, 129(3):516–531.
- Butler, D., Goldstein, S., and Guilak, F. (2000). Functional tissue engineering: The role of biomechanics. *Journal of Biomechanical Engineering*, 122(6):570–575.
- Byrne, H. and Preziosi, L. (2003). Modelling solid tumour growth using the theory of mixtures. *Mathematical Medicine and Biology*, 20(4):341–366.
- Canosa, J. (1969). Diffusion in non-linear multiplicative media. *Journal of Mathematical Physics*, 10(10):1862–1868.
- Carl, E. (1971). Population control in arctic ground squirrels. *Ecology*, 52(3):395–413.
- Cartmell, S. and El-Haj, A. (2005). Chapter 8 : Mechanical bioreactors for bone tissue engineering. *Bioreactors for tissue engineering*, pages 193–209.
- Cartmell, S., Porter, B., García, A., and Guldberg, R. (2003). Effects of medium perfusion rate on cell-seeded three-dimensional bone constructs in vitro. *Tissue Engineering*, 9(6):1197–1203.

- Chapekar, M. (2000). Tissue engineering: challenges and opportunities. *Journal of Biomedical Materials Research Part B: Applied Biomaterials*, 53(6):617–620.
- Chaplain, M. and Stuart, A. (1991). A mathematical model for the diffusion of tumour angiogenesis factor into the surrounding host tissue. *Mathematical Medicine and Biology*, 8(3):191–220.
- Chaplain, M. and Stuart, A. (1993). A model mechanism for the chemotactic response of endothelial cells to tumour angiogenesis factor. *Mathematical Medicine and Biology*, 10(3):149–168.
- Chung, C., Chen, C., Chen, C., and Tseng, C. (2007). Enhancement of cell growth in tissue-engineering constructs under direct perfusion: Modeling and simulation. *Biotechnology and Bioengineering*, 97(6):1603–1616.
- Chung, C., Chen, C., Lin, T., and Tseng, C. (2008). A compact computational model for cell construct development in perfusion culture. *Biotechnology and Bioengineering*, 99(6):1535–1541.
- Cohen, H. (1971). Non-linear diffusion problems. *Studies in Applied Mathematics*, 7:27–63.
- Coletti, F., Macchietto, S., and Elvassore, N. (2006). Mathematical modeling of three-dimensional cell cultures in perfusion bioreactors. *Industrial & Engineering Chemistry Research*, 45(24):8158–8169.
- Cowin, S. (2000). How is a tissue built? *Journal of Biomechanical Engineering*, 122(6):553–569.
- Croll, T., Gentz, S., Mueller, K., Davidson, M., O'Connor, A., Stevens, G., and Cooper-White, J. (2005). Modelling oxygen diffusion and cell growth in a porous, vascularising scaffold for soft tissue engineering applications. *Chemical Engineering Science*, 60(17):4924–4934.
- Curtis, A. and Riehle, M. (2001). Tissue engineering: the biophysical background. *Physics in Medicine and Biology*, 46(4):R47–R65.
- Ellis, M., Jarman-Smith, M., and Chaudhuri, J. (2005). Chapter 1: Bioreactor Systems for Tissue Engineering: A Four-Dimensional Challenge. *Bioreactors for Tissue Engineering*, pages 1–18.

- Fife, P. and McLeod, J. (1977). The approach of solutions of non-linear diffusion equations to travelling front solutions. *Archive for Rational Mechanics and Analysis*, 65(4):335–361.
- Finney, K., Appleton, D., Ince, P., Sunter, J., and Watson, A. (1989). Proliferative status of colonic mucosa in organ culture: 3H-thymidine-labelling studies and computer modelling. *Virchows Archiv. B, Cell pathology*, 56(6):397–405.
- Fisher, R. (1937). The wave of advance of advantageous genes. *Ann. Eugenics*, 7:353–369.
- Fournier, N. and Doillon, C. (1996). Biological molecule-impregnated polyester: an in vivo angiogenesis study. *Biomaterials*, 17(17):1659–1665.
- Frank-Kamenetskii, D. (1955). *Diffusion and heat exchange in chemical kinetics*. Princeton University Press, Princeton, NJ.
- Freed, L., Hollander, A., Martin, I., Barry, J., Langer, R., and Vunjak-Novakovic, G. (1998). Chondrogenesis in a Cell-Polymer-Bioreactor System. *Experimental Cell Research*, 240(1):58–65.
- Freed, L., Marquis, J., Langer, R., and Vunjak-Novakovic, G. (1994). Kinetics of chondrocyte growth in cell-polymer implants. *Biotechnology and Bioengineering*, 43(7):597–604.
- Freed, L. and Vunjak-Novakovic, G. (1995). Cultivation of cell-polymer tissue constructs in simulated microgravity. *Biotechnology and Bioengineering*, 46(4):306–313.
- Freed, L. and Vunjak-Novakovic, G. (1997). Microgravity tissue engineering. *In Vitro Cellular & Developmental Biology-Animal*, 33(5):381–385.
- Galban, C. and Locke, B. (1997). Analysis of cell growth in a polymer scaffold using a moving boundary approach. *Biotechnology and Bioengineering*, 56(4):422–432.
- Galban, C. and Locke, B. (1999). Analysis of cell growth kinetics and substrate diffusion in a polymer scaffold. *Biotechnology and Bioengineering*, 65(2):121–132.
- Girard, P. and Nerem, R. (1995). Shear stress modulates endothelial cell morphology and F-actin organization through the regulation of focal adhesion-associated proteins. *Journal of Cellular Physiology*, 163(1):179–193.

- Glowacki, J., Mizuno, S., and Greenberger, J. (1998). Perfusion enhances functions of bone marrow stromal cells in three-dimensional culture. *Cell Transplantation*, 7(3):319–326.
- Goyeau, B., Lhuillier, D., Gobin, D., and Velarde, M. (2003). Momentum transport at a fluid–porous interface. *International Journal of Heat and Mass Transfer*, 46(21):4071–4081.
- Griffith, L. (2002). Emerging design principles in biomaterials and scaffolds for tissue engineering. *Annals of the New York Academy of Sciences*, 961(1):83–95.
- Griffith, L. and Naughton, G. (2002). Tissue engineering—current challenges and expanding opportunities. *Science(Washington)*, 295(5557):1009–14.
- Gurney, W. and Nisbet, R. (1975). The regulation of inhomogeneous populations. *Journal of Theoretical Biology*, 52(2):441–457.
- Gurney, W. and Nisbet, R. (1976). A note on non-linear population transport. *Journal of Theoretical Biology*, 56(1):249–251.
- Hasirci, V., Berthiaume, F., Bondre, S., Gresser, J., Trantolo, D., Toner, M., and Wise, D. (2001). Expression of liver-specific functions by rat hepatocytes seeded in treated poly (lactic-co-glycolic) acid biodegradable foams. *Tissue Engineering*, 7(4):385–394.
- Hirota, R. (1972). Exact solution of the modified Korteweg-deVries equation for multiple collisions of solution. *Journal of the Physical Society of Japan*, 33(5):1456–1458.
- Holy, C., Shoichet, M., and Davies, J. (2000). Engineering three-dimensional bone tissue in vitro using biodegradable scaffolds: investigating initial cell-seeding density and culture period. *Journal of Biomedical Materials Research Part A*, 51(3):376–382.
- Howard, D., BATTERY, L., Shakesheff, K., and Roberts, S. (2008). Tissue engineering: strategies, stem cells and scaffolds. *Journal of Anatomy*, 213(1):66–72.
- Huang, H., Kamm, R., and Lee, R. (2004). Cell mechanics and mechanotransduction: pathways, probes, and physiology. *American Journal of Physiology- Cell Physiology*, 287(1):C1–C11.
- Hutmacher, D. (2000). Scaffolds in tissue engineering bone and cartilage. *Biomaterials*, 21(24):2529–2543.
- Ikada, Y. (2006a). Challenges in tissue engineering. *Journal of the Royal Society Interface*, 3(10):589–601.

- Ikada, Y. (2006b). *Tissue Engineering: Fundamentals and applications*. Academic Press.
- Isele, W. and Meinzer, H. (1998). Applying Computer Modeling to Examine Complex Dynamics and Pattern Formation of Tissue Growth* 1. *Computers and Biomedical Research*, 31(6):476–494.
- Ives, C., Eskin, S., and McIntire, L. (1986). Mechanical effects on endothelial cell morphology: in vitro assessment. *In vitro cellular & Developmental Biology: Journal of Tissue Culture Association*, 22(9):500–507.
- Jones, A., Byrne, H., Gibson, J., and Dold, J. (2000). A mathematical model of the stress induced during avascular tumour growth. *Journal of Mathematical Biology*, 40(6):473–499.
- Kareiva, P. (1983). Local movement in herbivorous insects: applying a passive diffusion model to mark-recapture field experiments. *Oecologia*, 57(3):322–327.
- Kaur, P. and Potten, C. (1986). Cell migration velocities in the crypts of the small intestine after cytotoxic insult are not dependent on mitotic activity. *Cell and tissue kinetics*, 19(6):601–610.
- Kellner, K., Liebsch, G., Klimant, I., Wolfbeis, O., Blunk, T., Schulz, M., and G"opferich, A. (2002). Determination of oxygen gradients in engineered tissue using a fluorescent sensor. *Biotechnology and Bioengineering*, 80(1):73–83.
- Kim, B., Putnam, A., Kulik, T., and Mooney, D. (1998). Optimizing seeding and culture methods to engineer smooth muscle tissue on biodegradable polymer matrices. *Biotechnology and Bioengineering*, 57(1):46–54.
- Klein-Nulend, J., Van Der Plas, A., Semeins, C., Ajubi, N., Frangos, J., Nijweide, P., and Burger, E. (1995). Sensitivity of osteocytes to biomechanical stress *in vitro*. *FASEB*, 9(5):441–445.
- Kolmogorov, A., Petrovsky, I., and Piskounov, N. (1937). Study of the diffusion equation with growth of the quantity of matter and its applications to a biological problem. *Moscow University Bulletin Math*, 1:1–25.
- Koponen, A., Kataja, M., and Timonen, J. (1996). Tortuous Flow In Porous Media. *Physical Review. E, Statistical Physics, Plasmas, Fluids, and Related Interdisciplinary Topics*, 54(1):406–410.
- Lamb Jr, G. (1971). Analytical descriptions of ultrashort optical pulse propagation in a resonant medium. *Reviews of Modern Physics*, 43(2):99–124.

- Landman, K. and Cai, A. (2007). Cell proliferation and oxygen diffusion in a vascularising scaffold. *Bulletin of Mathematical Biology*, 69(7):2405–2428.
- Langer, R. and Vacanti, J. (1993). Tissue Engineering. *Science*, 260(5110):920–926.
- Lanza, R., Langer, R., and Vacanti, J. (2007). *Principles of tissue engineering*. Academic Press.
- Lappa, M. (2003). Organic tissues in rotating bioreactors: fluid-mechanical aspects, dynamic growth models, and morphological evolution. *Biotechnology and Bioengineering*, 84(5):518–532.
- Lemon, G. and King, J. (2007). Multiphase modelling of cell behaviour on artificial scaffolds: effects of nutrient depletion and spatially non-uniform porosity. *Mathematical Medicine and Biology*, 24(1):57–83.
- Lemon, G., King, J., Byrne, H., Jensen, O., and Shakesheff, K. (2006). Mathematical modelling of engineered tissue growth using a multiphase porous flow mixture theory. *Journal of Mathematical Biology*, 52(5):571–594.
- Lewis, M., MacArthur, B., Malda, J., Pettet, G., and Please, C. (2005). Heterogeneous proliferation within engineered cartilaginous tissue: the role of oxygen tension. *Biotechnology and Bioengineering*, 91(5):607–615.
- Li, Y., Ma, T., Kniss, D., Lasky, L., and Yang, S. (2001). Effects of filtration seeding on cell density, spatial distribution, and proliferation in nonwoven fibrous matrices. *Biotechnology Progress*, 17(5):935–944.
- Lin, A., Barrows, T., Cartmell, S., and Guldberg, R. (2003). Microarchitectural and mechanical characterization of oriented porous polymer scaffolds. *Biomaterials*, 24(3):481–489.
- Loeffler, M., Stein, R., Wichmann, H., Potten, C., Kaur, P., and Chwalinski, S. (1986). Intestinal cell proliferation. I: A comprehensive model of steady-state proliferation in the crypt. *Cell and Tissue Kinetics*, 19(6):627–645.
- Luther, R. (1906). Propagation of chemical reactions in space. *Z. Elektrochem*, 12:596.
- Ma, C., Kumar, R., Xu, X., and Mantalaris, A. (2007). A combined fluid dynamics, mass transport and cell growth model for a three-dimensional perfused bioreactor for tissue engineering of haematopoietic cells. *Biochemical Engineering Journal*, 35(1):1–11.

- Macchiarini, P., Jungebluth, P., Go, T., Asnaghi, M., Rees, L., Cogan, T., Dodson, A., Martorell, J., Bellini, S., Parnigotto, P., et al. (2008). Clinical transplantation of a tissue-engineered airway. *The Lancet*, 372(9655):2023–2030.
- Maguire Jr, J., Coscia, M., and Lynch, M. (1987). Foreign body reaction to polymeric debris following total hip arthroplasty. *Clinical Orthopaedics and Related Research*, (216):213–223.
- Malda, J., Rouwkema, J., Martens, D., le Comte, E., Kooy, F., Tramper, J., Van Blitterswijk, C., and Riesle, J. (2004a). Oxygen gradients in tissue-engineered Pegt/Pbt cartilaginous constructs: Measurement and modeling. *Biotechnology and Bioengineering*, 86(1):9–18.
- Malda, J., Woodfield, T., Van Der Vloodt, F., Kooy, F., Martens, D., Tramper, J., Blitterswijk, C., and Riesle, J. (2004b). The effect of PEGT/PBT scaffold architecture on oxygen gradients in tissue engineered cartilaginous constructs. *Biomaterials*, 25(26):5773–5780.
- Martin, I., Wendt, D., and Heberer, M. (2004). The role of bioreactors in tissue engineering. *Trends in Biotechnology*, 22(2):80–86.
- McElwain, D. and Ponzo, P. (1977). A model for the growth of a solid tumor with non-uniform oxygen consumption. *Math. Biosci*, 35(3-4):267–279.
- Meineke, F., Potten, C., and Loeffler, M. (2001). Cell migration and organization in the intestinal crypt using a lattice-free model. *Cell Proliferation*, 34(4):253–266.
- Middleton, J. and Tipton, A. (2000). Synthetic biodegradable polymers as orthopedic devices. *Biomaterials*, 21(23):2335–2346.
- Montroll, E. and West, B. (1979). On an enriched collection of stochastic processes. *Fluctuation Phenomena*, 66:61.
- Mooney, D., Kaufmann, P., Sano, K., Schwendeman, S., Majahod, K., Schloo, B., Vacanti, J., and Langer, R. (1996). Localized delivery of epidermal growth factor improves the survival of transplanted hepatocytes. *Biotechnology and Bioengineering*, 50(4):422–429.
- Morel, D., Marcelpoil, R., and Brugal, G. (2001). A proliferation control network model: the simulation of two-dimensional epithelial homeostasis. *Acta Biotheoretica*, 49(4):219–234.
- Murray, J. (1977). *Lectures on non-linear-differential-equation models in biology*. Oxford University Press.

- Murray, J. (1989). *Mathematical Biology*.
- Myers, J. and Krebs, C. (1974). Population cycles in rodents. *Scientific American*, 230(6):38.
- Nimni, M. (1997). Polypeptide growth factors: targeted delivery systems. *Biomaterials*, 18(18):1201–25.
- Novikov, S. (1984). *Theory of solitons: the inverse scattering methods*. Springer.
- Obradovic, B., Meldon, J., Freed, L., and Vunjak-Novakovic, G. (2000). Glycosaminoglycan deposition in engineered cartilage: Experiments and mathematical model. *AIChE Journal*, 46(9):1860–1871.
- O’Dea, R., Waters, S., and Byrne, H. (2008). A two-fluid model for tissue growth within a dynamic flow environment. *European Journal of Applied Mathematics*, 19(06):607–634.
- O’Dea, R., Waters, S., and Byrne, H. (2010). A multiphase model for tissue construct growth in a perfusion bioreactor. *Mathematical Medicine and Biology*, 27(2):95.
- Okubo, A. (1980). Diffusion and ecological problems: Mathematical models. *Springer-Verlag, Berlin(Frg)*. 1980., 10.
- Osborne, J., Walter, A., Kershaw, S., Mirams, G., Fletcher, A., Pathmanathan, P., Gavaghan, D., Jensen, O., Maini, P., and Byrne, H. (2010). A hybrid approach to multi-scale modelling of cancer. *Philosophical Transactions of the Royal Society A: Mathematical, Physical and Engineering Sciences*, 368(1930):5013.
- Palsson, E. (2001). A three-dimensional model of cell movement in multicellular systems. *Future Generation Computer Systems*, 17(7):835–852.
- Palsson, E. and Othmer, H. (2000). A model for individual and collective cell movement in *Dictyostelium discoideum*.
- Pathmanathan, P., Cooper, J., Fletcher, A., Mirams, G., Murray, P., Osborne, J., Pitt-Francis, J., Walter, A., and Chapman, S. (2009). A computational study of discrete mechanical tissue models. *Physical Biology*, 6(3):6001.
- Patience, C., Takeuchi, Y., and Weiss, R. (1997). Infection of human cells by an endogenous retrovirus of pigs. *Infection*, 3(3):282–286.
- Petrovskii, S. and Shigesada, N. (2001). Some exact solutions of a generalized Fisher equation related to the problem of biological invasion. *Mathematical Biosciences*, 172(2):73–94.

- Rose, F., Cyster, L., Grant, D., Scotchford, C., Howdle, S., and Shakesheff, K. (2004). In vitro assessment of cell penetration into porous hydroxyapatite scaffolds with a central aligned channel. *Biomaterials*, 25(24):5507–5514.
- Rose, F. and Oreffo, R. (2002). Bone Tissue Engineering: Hope vs Hype. *Biochemical and Biophysical Research Communications*, 292(1):1–7.
- Rothe, F. (1981). Convergence to pushed fronts. *Rocky Mountain Journal of Mathematics*, 11(4):617–634.
- Saltzman, W. (2004). *Tissue Engineering: Principles for the design of replacement organs and tissues*. Oxford university press.
- Sánchez-Garduño, F. and Maini, P. (1994). Existence and uniqueness of a sharp travelling wave in degenerate non-linear diffusion Fisher-KPP equations. *Journal of Mathematical Biology*, 33(2):163–192.
- Schugens, C., Maquet, V., Grandfils, C., Jérôme, R., and Teyssie, P. (1996). Biodegradable and macroporous polylactide implants for cell transplantation: 1. Preparation of macroporous polylactide supports by solid-liquid phase separation. *Polymer*, 37(6):1027–1038.
- Scientific American, S. e. (1999). The Promise of Tissue Engineering. *Scientific American Magazine*.
- Sengers, B., Van Donkelaar, C., Oomens, C., and Baaijens, F. (2005). Computational study of culture conditions and nutrient supply in cartilage tissue engineering. *Biotechnology Progress*, 21(4):1252–1261.
- Sherratt, J. (2000). Wavefront propagation in a competition equation with a new motility term modelling contact inhibition between cell populations. *Proceedings of the Royal Society of London. Series A: Mathematical, Physical and Engineering Sciences*, 456(2002):2365–2386.
- Sherratt, J. and Murray, J. (1990). Models of epidermal wound healing. *Proceedings: Biological Sciences*, 241(1300):29–36.
- Skellam, J. (1991). Random dispersal in theoretical populations. *Bulletin of Mathematical Biology*, 53(1):135–165.
- Stephanopoulos, G., Aristidou, A., Nielsen, J., and service, S. O. (1998). *Metabolic Engineering: Principles and Methodologies*. Academic Press.

- Stock, U. and Vacanti, J. (2001). Tissue Engineering: Current State and Prospects. *Annual Review of Medicine*, 52(1):443–451.
- Tabata, Y., Nagano, A., and Ikada, Y. (1999). Biodegradation of hydrogel carrier incorporating fibroblast growth factor. *Tissue Engineering*, 5(2):127.
- Tilman, D. and Kareiva, P. (1997). *Spatial ecology: the role of space in population dynamics and interspecific interactions*. Princeton Univ Press.
- Tuckwell, H. (1988). *Introduction to theoretical neurobiology: Non-linear and stochastic theories*. Cambridge University Press.
- Van Leeuwen, I., Mirams, G., Walter, A., Fletcher, A., Murray, P., Osbourne, J., Varma, S., Young, S., Cooper, J., Doyle, B., et al. (2009). An integrative computational model for intestinal tissue renewal. *Cell Proliferation*, 42(5):617–636.
- Van Saarloos, W. (2003). Front propagation into unstable states. *Physics Reports*, 386(2-6):29–222.
- Vunjak-Novakovic, G., Obradovic, B., Bursac, P., Langer, R., and Freed, L. (1998). Dynamic cell seeding of polymer scaffolds for cartilage tissue engineering. *Biotechnology Progress*, 14(2):193–202.
- Walter, A. (2009). *A Comparison of Continuum and Cell-based Models of Colorectal Cancer*. PhD thesis, The University of Nottingham, UK.
- Waters, S., Cummings, L., Shakesheff, K., and Rose, F. (2006). Tissue growth in a rotating bioreactor. Part I: mechanical stability. *Mathematical Medicine and Biology*, 23(4):311–337.
- Wendt, D., Marsano, A., Jakob, M., Heberer, M., and Martin, I. (2003). Oscillating perfusion of cell suspensions through three-dimensional scaffolds enhances cell seeding efficiency and uniformity. *Biotechnology and Bioengineering*, 84(2):205–214.
- Whang, K., Tsai, D., Nam, E., Aitken, M., Sprague, S., Patel, P., and Healy, K. (1998). Ectopic bone formation via rhBMP-2 delivery from porous bioabsorbable polymer scaffolds. *Journal of Biomedical Materials Research*, 42(4):491–499.
- Whitaker, M., Quirk, R., Howdle, S., and Shakesheff, K. (2001a). Growth factor release from tissue engineering scaffolds. *Journal of Pharmacy and Pharmacology*, 53(11):1427–1437.

- Whitaker, M., Quirk, R., Howdle, S., and Shakesheff, K. (2001b). Growth factor release from tissue engineering scaffolds. *Journal of Pharmacy and Pharmacology*, 53(11):1427–1437.
- Whittaker, R., Booth, R., Dyson, R., Bailey, C., Chini, L., Naire, S., Payvandi, S., Zimei, R., Woollard, H., Cummings, L., et al. (2009). Mathematical modelling of fibre-enhanced perfusion inside a tissue-engineering bioreactor. *Journal of Theoretical Biology*, 256(4):533–546.
- Woods, H., Silva, M., Nouvel, C., Shakesheff, K., and Howdle, S. (2004). Materials processing in supercritical carbon dioxide: surfactants, polymers and biomaterials. *Journal of Materials Chemistry*, 14(11):1663–1678.
- You, J., Yellowley, C., Donahue, H., Zhang, Y., Chen, Q., and Jacobs, C. (2000). Substrate deformation levels associated with routine physical activity are less stimulatory to bone cells relative to loading-induced oscillatory fluid flow. *Journal of Biomechanical Engineering*, 122(4):387–393.
- You, L., Cowin, S., Schaffler, M., and Weinbaum, S. (2001). A model for strain amplification in the actin cytoskeleton of osteocytes due to fluid drag on pericellular matrix. *Journal of Biomechanics*, 34(11):1375–1386.